



Thermal fluctuations of a stationary out-of-equilibrium system

Alex Fontana

► To cite this version:

Alex Fontana. Thermal fluctuations of a stationary out-of-equilibrium system. Astrophysics [astro-ph]. Université de Lyon, 2020. English. NNT : 2020LYSE1168 . tel-03325266

HAL Id: tel-03325266

<https://theses.hal.science/tel-03325266>

Submitted on 24 Aug 2021

HAL is a multi-disciplinary open access archive for the deposit and dissemination of scientific research documents, whether they are published or not. The documents may come from teaching and research institutions in France or abroad, or from public or private research centers.

L'archive ouverte pluridisciplinaire **HAL**, est destinée au dépôt et à la diffusion de documents scientifiques de niveau recherche, publiés ou non, émanant des établissements d'enseignement et de recherche français ou étrangers, des laboratoires publics ou privés.



N° d'ordre NNT : 2020LYSE1168

THESE DE DOCTORAT DE L'UNIVERSITE DE LYON

opérée au sein de
l'Université Claude Bernard Lyon 1

École Doctorale ED52
(Physique et Astrophysique)

Spécialité de doctorat: Physique statistique

Soutenue publiquement le 01/10/2020, par :
Alex Fontana

Thermal fluctuations in an out-of-equilibrium system

Devant le jury composé de :

Cagnoli Gianpietro, Professeur des Universités, ILM	<i>Président</i>
Berthier Ludovic, Directeur de recherche CNRS, Laboratoire Charles Coulomb	<i>Rapporteur</i>
Cohadon, Pierre François, Maître de Conférence, Laboratoire Kastler Brossel	<i>Rapporteur</i>
Conti Livia, Chercheuse INFN Padova, National Laboratories of Legnaro	<i>Examinatrice</i>
Del Fatti Natalia, Professeure des Universités, UCBL	<i>Examinatrice</i>
Galliou Serge, Professeur, ENSMM, Institut FemtoST	<i>Examineur</i>
Seidelin Signe, Maitresse de conférence, Institut Néel	<i>Examinatrice</i>
Bellon Ludovic, Chargé de Recherche CNRS, ENS de Lyon	<i>Directeur de thèse</i>

Abstract

Résumé de la thèse

L'objectif de cette thèse est une étude théorique et expérimentale des propriétés du bruit thermique hors d'équilibre, dans le but de comprendre si nous pouvons étendre les outils de la physique statistiques aux systèmes hors équilibre. En particulier, nous montrons comment étendre le Théorème de Fluctuation-Dissipation (FDT) à des systèmes soumis à un profil spatial de température, donc dans un état de non équilibre stationnaire (NESS). Étant donné que les fluctuations thermiques ne peuvent pas être décrites par une seule température grâce au théorème d'équipartition, nous montrons comment elles sont prescrites par le profil de température pondéré par la dissipation mécanique locale.

Nous testons cette prédiction dans divers micro-leviers en silicium, en créant une forte différence de température (plusieurs centaines de degrés) entre la base et la pointe. Dans une expérience en particulier, la base est maintenue à température cryogénique, plaçant ainsi le cantilever aussi loin de l'équilibre que physiquement possible. Nous mesurons alors les fluctuations thermiques de l'échantillon ainsi que leur dissipation, montrant comment ces deux quantités sont parfaitement interprétées par notre cadre théorique. Le même résultat est également vérifié pour un oscillateur macroscopique en aluminium. Une analyse minutieuse des propriétés statistiques du bruit thermique démontre enfin que nos résultats sont robustes, et un algorithme de tri des données expérimentales est proposé. Une méthode simple pour estimer les incertitudes de mesures finalement proposée.

Thesis abstract

The goal of this thesis is a theoretical and experimental study of the non-equilibrium properties of thermal noise, with the purpose of understanding whether we can extend certain statistical physics tools to non-equilibrium systems. In particular, we show how we can extend the Fluctuation-Dissipation Theorem (FDT) to systems subjected to a stationary spatial temperature profile, thus in a Non-Equilibrium Steady State (NESS). Since thermal fluctuations cannot be described by a single temperature through the Equipartition Theorem, we show how they are then prescribed by the temperature profile weighted by the local mechanical dissipation.

We test this prediction in various silicon micro-cantilevers, creating a strong temperature difference of hundreds of degrees between the base and the tip. In one experiment in particular, the base is held at cryogenic temperatures, thus placing the cantilever as far from equilibrium as physically possible. We then measure the thermal fluctuations of the sample alongside their dissipation, showing how these two quantities are perfectly construed by our theoretical framework. The same is also verified for a macroscopic aluminum oscillator. A careful analysis of the statistical properties of thermal noise finally demonstrates that our results are robust, and a sorting algorithm of the experimental data is proposed. A simple method to estimate the uncertainties of the measurements is finally given.

Résumé substantiel

Le bruit thermique est un phénomène microscopique, causé par l'échange d'énergie entre les systèmes physiques et leur environnement. Normalement indétectable en raison de la faible amplitude intrinsèque des fluctuations, il devient saillant lorsque la taille du système considéré atteint l'échelle micro et nanométrique, ou que la sensibilité requise augmente. Dans ces cas-là en effet, les fluctuations, généralement négligeables, deviennent une source majeure de bruit. Une caractérisation complète de ce phénomène devient donc primordiale.

L'un des principaux outils statistiques en notre possession pour décrire le bruit thermique est le célèbre Théorème de Fluctuation-Dissipation (FDT), de H. Callen et T. Welton. Cette relation relie l'amplitude des fluctuations thermiques d'une observable à la puissance qu'il dissipe dans le bain thermique environnant et à la température de ce dernier. Ceci n'est néanmoins valable que pour un système en équilibre thermique.

Lorsque nous considérons un objet dans un état de non-équilibre, le FDT ne parvient pas à prédire les fluctuations thermiques de l'observable. La plupart des systèmes physiques que nous rencontrons dans la vie quotidienne (nous y compris) sont hors équilibre. Certains d'entre eux sont suffisamment proches de l'équilibre pour que nous puissions supposer que le FDT est valable, mais ce n'est souvent pas le cas. Les cellules biologiques, les verres et les systèmes soumis à un flux de chaleur constant, par exemple, nécessitent une description adaptée afin de prévoir leurs fluctuations thermiques. Dans cette thèse, nous nous intéressons en particulier aux systèmes en État Stationnaire Hors d'Équilibre (NESS), causé par un profil de température sur leur longueur. Le but est de proposer une extension du FDT pour les systèmes en NESS, et de la vérifier expérimentalement en étudiant le bruit thermique d'un micro-levier en silicium et d'un oscillateur macroscopique en aluminium.

Nous proposons une extension minimale du FDT pour les systèmes soumis à une différence de température. Alors qu'en équilibre, le principe d'équipartition lie les fluctuations thermiques à la température unique du bain thermique, notre FDT étendu montre que la température de fluctuation du système est prescrite par le profil de température pondéré par la dissipation d'énergie mécanique locale. Pour simplifier, nous prévoyons qu'un système dans un NESS présente un bruit thermique proportionnel à l'endroit où la dissipation est prépondérante. Nous montrons comment calculer la Densité Spectrale de Puissance (PSD) des résonances du levier lorsqu'il est dans un NESS, à la fois pour ses modes de flexion et de torsion. Nous associons ensuite à chaque mode une température de fluctuation, qui représente la véritable température de non-équilibre de chaque résonance, à comparer avec la température moyenne du système.

L'étape suivante consiste à tester le cadre théorique que nous développons en étudiant les fluctuations d'un micro-levier. Nous le plaçons dans une chambre à vide avec sa base thermalisée à température ambiante et son embout chauffé par un laser. Nous créons ainsi une différence de température de plusieurs centaines de degrés sur sa longueur, et nous mesurons les fluctuations thermiques de chaque mode de résonance. De plus, la quantification des angles de perte de chaque mode donne une estimation de la dissipation dans le système. Nous étudions trois échantillons dans ces conditions.

Nous montrons que le bruit thermique hors d'équilibre du premier échantillon est indépendant du profil de température imposé au système. Alors que la température moyenne du levier augmente, les fluctuations sont à peu près constantes à leur valeur à température ambiante. Nous observons donc un fort *déficit* de fluctuations. Nous interprétons ce phénomène grâce à notre FDT étendu, qui indique que le système est alors dominé par les pertes à l'encastrement. En effet, dans ce cas, la seule température importante est celle à la

base, qui est constante et donne donc des fluctuations constantes. Cette affirmation est vérifiée grâce aux angles de perte mesurés, qui sont également indépendants de la température.

Le deuxième échantillon présente un revêtement et une géométrie différente par rapport au premier. Son bruit thermique hors d'équilibre montre dans ce cas une dépendance marquée de la température, les températures de fluctuation étant de l'ordre de la température moyenne. La dissipation est également influencée, ce qui montre que dans ce cas l'échantillon est dominé par un amortissement distribué. Grâce à un ajustement des angles de perte, nous sommes alors en mesure de prédire théoriquement les températures de fluctuation avec notre FDT étendu : le résultat correspond bien aux résultats expérimentaux, ce qui montre la puissance de notre cadre théorique.

Le troisième échantillon a la même géométrie que le précédent mais est dépourvu de revêtement. Le comportement observé est néanmoins très similaire : le bruit thermique et la dissipation augmentent avec la température moyenne, simplement avec des angles de perte environ 10 fois plus faibles que dans le cas précédent. Cela montre que cet échantillon présente également une dissipation distribuée. En plus, nous démontrons que dans le cas précédent le substrat contribue à l'amortissement total, bien que dans une moindre mesure par rapport au revêtement. Avec cet échantillon également, une prédiction théorique de la fluctuation représente bien les mesures.

Dans tous ces cas, la base du levier est placée à température ambiante, de sorte que la différence de température maximale que nous pouvons atteindre se situe entre celle-ci et le point de fusion. Le FDT hors d'équilibre est ainsi vérifié dans cette plage de température. Afin de le tester pour *toutes* les températures, nous plaçons un levier dans un cryostat et atteignons presque le point de fusion à son extrémité. Nous créons ainsi la plus grande différence de température qu'il peut supporter, et nous mesurons son bruit thermique. Grâce à une estimation précise de la température moyenne du cantilever, nous démontrons que le système présente une forte absence de fluctuations. En effet, les températures de fluctuation sont des dizaines de fois inférieures à la température moyenne, bien qu'elles ne soient pas exactement constantes. La dissipation mesurée est cohérente avec cette image, montrant comment l'amortissement de ce levier est la combinaison de pertes à l'encastrement et de pertes réparties, la première provoquant le déficit de bruit et la seconde la faible dépendance à la température. Le FDT étendu est ainsi vérifié jusqu'à ses limites physiques.

La dernière expérience prend en considération un oscillateur macroscopique en aluminium dans l'expérience NETN, à Padoue. Dans ce cas également, l'objectif du groupe dirigé par L. Conti est d'imposer un NESS dans le système et de mesurer le bruit hors équilibre. Le but dans ce cas est de vérifier si notre description s'applique également à un objet macroscopique, ce qui pousserait la validité du FDT étendu à des échelles plus grandes. En effet, les résultats précédents de ce groupe ne peuvent pas être expliqués dans notre cadre, et il y a donc une forte curiosité à tester si un comportement universel existe en non-équilibre. J'ai passé un mois dans ce laboratoire, où j'ai assemblé un nouveau dispositif de mesure expérimental et effectué quelques mesures de non-équilibre. Tout d'abord, j'ai réussi à améliorer sensiblement la sensibilité de l'instrument autour des résonances de l'oscillateur. Deuxièmement, les mesures de bruit thermique montrent un accord parfait avec le FDT étendu : les températures de fluctuation sont en effet très proches de la température moyenne du système, ce qui s'explique par un amortissement distribué. Les angles de perte mesurés confirment finalement cette image, montrant comment notre description est en effet valable aussi pour un objet macroscopique.

Toute la discussion précédente est basée sur une supposition, à savoir que les signaux mesurés sont en effet du bruit thermique, c'est-à-dire une force stochastique cédant de

l'énergie au système. Nous la testons alors, en montrant d'abord les propriétés statistiques des fluctuations thermiques et en les vérifiant ensuite dans les données expérimentales grâce à une détection synchrone. Nous montrons initialement qu'il n'y a pas de différence qualitative entre une distribution à l'équilibre et une distribution hors équilibre pour les coefficients de Fourier dans les spectres. En plus, nous sommes capables de discerner si certains événements ne sont pas dus au bruit thermique en nous basant sur la fonction de densité de probabilité (PDF) échantillonnée. Nous discutons ensuite de la PDF des spectres expérimentaux, en démontrant comment une PSD est en général Γ -distribuée autour de la moyenne. Ensuite, un algorithme original de tri des spectres expérimentaux est proposé, où les mesures en dehors d'un certain seuil de la PDF attendue sont exclues. Les techniques permettant de contourner les éventuels problèmes liés à la définition d'une moyenne sont examinées. Enfin, la PDF du bruit thermique est également récupérée, et une deuxième méthode de tri possible est suggérée.

En raison de l'importance capitale de la mesure de la dissipation dans cette thèse, nous utilisons une méthode d'ajustement non biaisée afin de définir une procédure d'ajustement. À partir de là, nous discutons d'une manière innovante de vérifier la robustesse des ajustements et de calculer les incertitudes des paramètres d'ajustement.

Les autres contributions notables sont : un étude minutieux de la sensibilité d'une détection du bruit technique grâce à une technique de levier optique ; l'estimation du point de mesure et du rayon du faisceau laser sur un levier grâce à des mesures de bruit ; l'ajout d'une correction du FDT pour la torsion d'un levier en tenant compte des contraintes longitudinales.

Acknowledgments

This thesis is the culmination of three amazing years. It is hard for me to quantify or even put in words the growth I underwent, from the professional and the human point of view. In this time span, I had the opportunity to perform high-precision experiments, show the results in conferences, have challenging discussions, travel, drink a lot of coffee, meet great people, celebrate their birthdays, and live a happy life. For these reasons, I would like to thank the people who made this journey so special.

I would firstly like to thank you, Ludovic. None of this would have happened if I hadn't had the luck to meet you. Thank you for giving me this opportunity and guiding me throughout the years. As Richard once said, "he is just the best". Well, I agree. Your brilliance, intuition, and experience as a researcher are paralleled by your human kindness. Thank you Ludovic, from the bottom of my heart.

Naturally, I would like to thank the laboratory, the ENS of Lyon, and the UCBL1 for giving me all the tools in order to successfully complete this period. Vincent, you helped me at the beginning of my path; we tried to assemble a 8-quadrant photodiode detection which was a bit an overkill, but it was fun and it got me going. For all the kindness and the help throughout the years, thank you. Artyom, thank you for your expertise, your help when I needed a component for my experiments, or simply for a little chat. Jorge, you are really someone special. Kind, hard-working, you are always ready to help others. Thank you for what you did for me and for the beers at the Foyer. Thierry, there is such a good ambiance in the laboratory thanks to your keen management, so thank you. Similarly, thanks to Jean-Christophe. I would also like to thank Fatiha, Camille, Laure, Laurence et Nadine for their fundamental help and courtesy. Also, a big thank you to F. Ropars and P. Metz of the atelier d'électronique; D. Le Tourneau, M. Moulin, F. Vittoz and O. Razezassia for the atelier de mécanique; and H. Barroux and D. Duperray of the service d'informatique.

Of course, I express my gratitude to my jury for agreeing to read this document and for participating in the discussion: L. Berthier, P-F. Cohadon, G. Cagnoli, L. Conti, N. Del Fatti, S. Galliou, and S. Seidelin. In particular, thank you Livia for hosting me for one month in your laboratory in Padua, where I was able to participate in your experiment and to learn so much. It was truly an inspiring experience, and I am looking forward to visiting again. Thanks also to G. Ciani, for the same reasons.

I cannot forget the members of the Informatics Departments of the UCBL1, all of whom helped me throughout my teaching years. After one week in France, I began teaching C++ in French, a (maybe two) language(s) I didn't master at the time. At the beginning it was tricky, but thanks to E. Perna, A. Meyer, M. Lefevre, E. Galin, and E. Desseree I managed to have a great time, learn a lot and possibly help some students. I am really grateful to you all for your help, suggestions, and kindness.

I would also like to thank the people at LMA for the time I spent in their laboratory. The welcoming environment, the professionalism, and the kindness of its members greatly

helped me throughout this thesis. In particular, Massimo, Lorenzo, Laurent, Jérôme, and Christophe thank you for your kindness and expertise.

Other people helped me throughout the years, and I would like to thank you here: Giannamaria, thank you for the help and for the good chats we had, including a fun climbing session in Buenos Aires; Giorgio, thank you for the time spent together and for the contributions to this thesis; you are great, and you have a bright future ahead of you! Jennifer, thank you for all the help and the conversations in Padua; it was a pleasure to meet you! Special mention goes to Giovanni and LucaVioletto, two of my best friends at the university, to whom I owe gratitude for their loyalty and help. I wish you the best: you deserve it.

Next, friends and fellow PhD students at the lab: wow. You welcomed me and had the patience to wait for my spaghetti French (I am quoting from Alex(2) here) to develop into something intelligible, standing my direct Frenchification of Italian words, with a whole cacophony resulting in the process. Thanks to the senators Valentin, Jérôme, Vincent for the coffee breaks, the company, but most importantly "40 c'est 40" which is now carved in my brain forever. A special thanks to you Géraldine, from taking the time to let me finish my first slow sentences in French to teaching me how to snowboard. Similarly, thanks to Timothée for your kindness and friendship (and an unlucky plant). Also, thanks to Lucas for being a good friend and the best climbing buddy one can desire, always pushing me to my (pretty low) limits. Thank you Lucile for coming with me to Iguazú, el lugar mas lindo del mundo. In general, thanks to Salambô, Clément, Barbara, David, Ariane, Raphaël, Hélène, Lavi, Dario, Marco, and many more for the beautiful moments spent together.

Among the category of friends and colleagues: Richard. Words don't do your friendship justice. You are one of the first people I met in Lyon, and your friendship has always been so dear to me. I'm so glad I met you; thank you for being, simply, *un ami magnifique*. Similarly, Alex(2), my twin in all but the hair color. Thank you for all the time spent together, be it having a beer at the river or in Ventimiglia, playing Catan, or eating sushi. Also, thank you for the encouragement and for your advice. You two are my best friends in Lyon, and may this continue in the future!

Cómo podría olvidar mi club chileno? Marcelo, thank you for teaching me Spanish Chilean, the adventures at the climbing gym, the jokes and the company. You are a good friend! Yeraldinne, Cristobal, thank you too for letting me know all the nuances of the word "wea," for the evenings together and (Yeraldinne) for always asking me politely to stay when I wanted to leave "early". Again, Matias, Clément, Valentina and Ignacio, but also the whole VIP team with David, Aneta, Ester, Paola, Olivier, Angélique, and Mathilde: thank you all for the wonderful memories. Also, thanks to you Chiara for your joy and company (and letting me win at 7 Wonders from time to time).

A special thanks to my b.r.o. Amedeo, to Tomàs, Enrico, Riccardo, Marta, Gianluca, Baron, Edoardo, Alain, Tia, Alberto, C.A., Anna, Nico, Albi for welcoming me when I come back to Italy and for being the best friends one can desire. Also, thanks to my Achsoo friends and to Pablo for keeping the flame of our Erasmus friendship alive. In addition, thank you Naomi for being simply wonderful, from the bottom of my heart.

I would also like to thank the Kichenassamy family for welcoming me in the beginning of this journey.

Last but not least, thank you mom and dad for being supportive, nice, weird, lovely, and just great parents. Dad, thank you for making me discover places around our home that I would have never imagined and for always being there for a laugh. Mom, thank you for



FIGURE 1: Ludovic's group: from left to right, Jorge, Batiste, Richard, Ludovic, Salambô, me.

caring so much, and for being an extraordinary woman and the best person I know. Also thanks to my brother, uncles, and cousins, for being more than just family.

Contents

Abstract	iii
Acknowledgments	vii
1 General introduction	1
2 Thermal noise	7
2.1 Thermal fluctuations	7
2.1.1 First observations	7
2.1.2 Fluctuation-Dissipation Theorem	9
2.1.3 Simple Harmonic Oscillator	10
2.2 Equilibrium thermal fluctuations of a micro-cantilever	12
2.2.1 Deflection	13
Euler-Bernoulli model	13
FDT	16
2.2.2 Torsion	17
Saint-Venant's model	18
FDT	19
Barr's model	21
2.3 Non equilibrium thermal fluctuations	21
2.3.1 Non-equilibrium FDT	22
2.3.2 Fluctuation temperature measurement	24
Appendices	25
2.A Energy dissipation in a cantilever	25
2.A.1 Viscous dissipation	25
2.A.2 Internal dissipation	25
Stress-strain relations	26
Dynamics	27
Energy considerations	29
Examples	30
Local properties of internal dissipation	31
2.A.3 Clamping dissipation	32
2.A.4 Discussion	33
3 Thermal noise of a micro-cantilever	35
3.1 Experimental setup	35
3.1.1 Micro-cantilevers	37
3.1.2 Experimental setup	38
3.1.3 Displacements	38
3.2 Temperature of the cantilever	39
3.2.1 Theoretical framework	39
3.2.2 Uniform temperature	43

3.2.3	Apparent temperature	43
3.3	Experimental procedure	44
3.4	Results	45
3.4.1	C100	45
	Thermal fluctuations	46
	Dissipation	46
	Discussion	46
3.4.2	C30C	51
	Thermal fluctuations	51
	Dissipation	51
	Discussion	53
3.4.3	C30	57
	Thermal fluctuations	57
	Dissipation	57
	Discussion	59
3.5	Conclusions	59
Appendices		65
3.A	Calibration	65
3.A.1	Photodetector	65
3.A.2	Laser spot influence	67
3.A.3	Large spot case	68
	Deflection	69
	Torsion	71
3.A.4	Estimation of x_0 and R_0	72
3.A.5	Calibrated spectra	74
3.B	Fluctuation temperatures and uncertainties	75
3.C	Ruling out external noise contributions	76
3.C.1	Background electronic noise contribution	76
3.C.2	Laser power fluctuations	77
3.C.3	Self-oscillations	78
4	Thermal noise of a micro-cantilever in cryogenic environment	83
4.1	Experimental setup	84
4.1.1	CryoQPDI	84
4.1.2	Displacements	86
4.2	Temperature of the cantilever	86
4.2.1	Apparent temperature calibration	86
4.2.2	Average temperature from simulated temperature profile	88
4.3	Experimental procedure	92
4.4	Results	93
4.4.1	Thermal fluctuations	93
4.4.2	Dissipation	94
4.4.3	Discussion	94
4.5	Conclusions	99
Appendices		101
4.A	Sensitivity of the QPDI	101
4.B	Temperature estimations	103
5	Thermal noise of a macroscopic oscillator	109

5.1	Experimental setup	110
5.1.1	Jones calculus	111
5.1.2	Input area	113
5.1.3	Sensing area	113
5.1.4	Analysis area	114
5.1.5	Phase and displacement	115
5.1.6	Real life implementation	115
5.1.7	Calibration	116
5.1.8	Displacements	117
5.2	Heating	118
5.3	Experimental procedure	119
5.3.1	Experimental procedure	119
5.3.2	Analysis procedure	120
5.4	Results	122
5.4.1	Improvements of the detection	122
5.4.2	Thermal fluctuations	122
5.4.3	Dissipation	124
5.4.4	Discussion	124
5.5	Conclusions	126
Appendices		129
5.A	Alignment and optimization of the interferometer	129
5.A.1	Alignment of the interferometer	129
5.A.2	Optimisation of the interferometric signal	131
5.B	Noise sources	132
5.C	Sensitivity and statistical uncertainties on T^{fluc}	133
5.D	Dependency on pressure	133
5.E	Open questions and insights	135
5.E.1	Open questions	135
5.E.2	Insight on possible explanations	137
6	Statistical properties of thermal noise	139
6.1	Statistical properties of noise	140
6.1.1	Random force F	140
6.1.2	Deflection δ	142
6.1.3	Lock-in amplifier	143
	Ideal case $\Delta f = 0$	144
	General case $\Delta f \neq 0$	145
6.2	Experiment	145
6.2.1	Self-oscillations	146
6.2.2	Equilibrium case	148
6.2.3	Non-equilibrium case	148
6.2.4	Comparison with the measured areas	151
6.2.5	Discussion	154
6.3	Statistical properties of the PSD	154
6.3.1	Statistical distribution of the PSD	155
6.4	Spectra selection	158
6.4.1	Threshold	159
6.4.2	Analysis procedure	160
	Representative average	160
	Non-representative average	160

	Frequency dependent average	161
6.4.3	Discussion	162
6.5	Statistical properties of the area	163
6.5.1	Area selection	164
6.5.2	Distribution of T^{fluc}	164
6.6	Statistical properties of the fit	165
6.6.1	Uncertainty of the fit parameters	167
6.6.2	Discussion	168
6.7	Conclusions	170
7	General conclusions	173

List of Abbreviations

AOM	A cousto- O ptic M odulator
DOF	D egree O f F reedom
EM	E quation of M otion
EP	E quipartition P rinciple
ET	E instein T elescope
FDT	F luctuation D issipation T heorem
GOF	G oodness O f F it
GW	G ravitational W aves
LNL	L aboratori N azionali di L egnaro
NESS	N on E quilibrium S teady S tate
NETN	N on E quilibrium T hermal N oise
PDF	P robability D ensity F unction
PSD	P ower S pectrum D ensity
SNR	S ignal to N oise R atio

Chapter 1

General introduction

An unperturbed dissipative system in contact with a thermal bath for a long time is usually considered to be in thermal equilibrium. In this situation, the Equipartition Principle (EP) states that every microscopic degree of freedom possesses on average an energy $k_B T/2$, where k_B is the Boltzmann constant and T the temperature of the bath. Let us consider the simple case of a mass attached to a spring presenting some form of damping. The mass oscillates around its mean value, dissipating energy in the environment, which in return transfers on average the same amount to the mass, yielding a total balance of zero. This concept was formalized by Callen and Welton in the Fluctuation-Dissipation Theorem (FDT) [25], which creates a precise formulation of the link between the dissipation process, the temperature of the system, and its thermal fluctuations (a.k.a. thermal noise).

The amplitude of these oscillations is generally tiny and usually goes unnoticed. Macroscopic systems are normally subject to many kinds of external and internal perturbations, completely obscuring the action of the surrounding thermal bath. In many instances, however, this is not true. For example, microelectromechanical systems (MEMS) require a careful study of thermal noise, since it is often the limiting factor in their sensitivity [78]. In biology, cellular membranes show thermal fluctuations whose characterisation is paramount in order to understand the bioelectro-magnetism [99] and survival of cells *in vitro* [58]. Nowadays, a relatively new field requires this kind of knowledge: Gravitational Waves (GWs) detection. In these experiments, technology is pushed to its limits in order to gain the possibility of measuring the extremely weak GWs signals. One of the factors prescribing further advances in resolution is the thermal noise contribution of the test masses in the detectors [53]. Numerous other technological applications or physical phenomena can be listed, as thermal fluctuations become salient with the decreasing of the system size or the increasing of the measurement sensitivity. Understanding it is thus fundamental.

Whilst the FDT constitutes an excellent framework for systems in thermal equilibrium, there is no guarantee that it could be used for non-equilibrium systems. Non-equilibrium is a state to which we refer to in many contexts in physics, but also in biology, cosmology and economy, to name a few. In physics, examples range from living systems [48], aging materials [22], and systems subject to a heat flux [79, 29]. As before, the research of possible non-equilibrium effects in the thermal noise of the GWs collaboration has recently been a prolific subject [29, 64].

We say that a system is considered in equilibrium when, after enough time from a previous potential perturbation, the macroscopic quantities we use to identify it are relaxed to a specific value, which we call equilibrium value. In this work, the macroscopic quantity we are interested in is the temperature, hence, restricting the previous definition, a system is in thermal equilibrium when it reaches the temperature of the surrounding environment. A

classification of non equilibrium arises when considering the time duration involved. A system put in contact with a thermal reservoir will relax towards its equilibrium temperature. On the other hand, a system which is placed in contact with two thermal baths at different temperatures and left there will never be able to relax towards one equilibrium value, and it is thus in a Non-Equilibrium Steady State (NESS), which is the main topic of this thesis. In this case, the non-equilibrium system is in contact with two equilibrium ones (the baths). A third state is when the baths are themselves out of equilibrium, which is the case of a balloon in the atmosphere, or in the case of active matter, where there is no relaxation value to start with.

In this thesis, we thus study a system which is placed in a NESS, with one end of it kept at a reference constant temperature T^{\min} and the other end at a constant higher temperature T^{\max} . In this case, a temperature profile $T(x)$ is established along the longitudinal direction x , hindering the definition of a global temperature of the system. In fact, the whole system has not *one* temperature at which it can be considered, but rather a whole field of it. As an approximation, a unidimensional system in a NESS can be considered as a collection of N masses m_i each at a certain temperature T_i . The mass at one end ($x = 0$) is at $T = T^{\min}$, and the one at the other end ($x = L$) at T^{\max} . A classic example of this is the Fermi-Pasta-Ulam-Tsingou chain [39], however many authors have studied out-of-equilibrium systems from a theoretical and experimental point of view [11, 10, 61, 52, 42].

Since the systems we discuss in this thesis are mechanical ones, fluctuations of mechanical observables are the key. As stated previously, for a generic degree of freedom, the equilibrium T becomes $T(x)$ in a NESS, and the EP hypotheses are not longer valid. Nonetheless, thermal fluctuations are a macroscopic observable, and thus it is possible to associate a non-equilibrium temperature to them. We generally refer to them as T^{fluc} : we simply apply the EP ignoring the actual NESS of the system. Whilst we define T^{fluc} more precisely in the next section, we stress here the fact that this quantity embodies the thermal noise of the system in consideration regardless of its actual state. Its measurement is therefore one of the main goals of this thesis.

In order to characterize an out-of-equilibrium T^{fluc} , it is important to compare it to the meaningful temperatures of the system. In the case of this thesis, there are three obvious ones: the minimal temperature T^{\min} , the maximal temperature T^{\max} , and the average temperature T^{avg} . For simplicity's sake, let us suppose $T(x)$ is linear, so that T^{avg} is the temperature at the center of the system, i.e. $T^{\text{avg}} = T(L/2)$. Let us then imagine we measure T^{avg} and a fluctuation temperature T^{fluc} ; we can then define three macro-behaviors: if $T^{\text{avg}} \approx T^{\text{fluc}}$, there is no quantitative difference between this system in a NESS and the same in equilibrium at T^{avg} from the fluctuations' point of view. In other words, placing the sample in contact with the two reservoirs at T^{\min} and T^{\max} and thus with a temperature profile along it, or in contact with one single bath at T^{avg} gives the same outcome. On the other hand, if $T^{\text{fluc}} > T^{\text{avg}}$, the fluctuations yield a higher temperature with respect to the one dictated by the average temperature. In this case, we say the system shows an excess of fluctuations with respect to equilibrium. The opposite is also possible: if $T^{\text{fluc}} < T^{\text{avg}}$, we have a lack of fluctuations.

The temperature of an object in an out-of-equilibrium state is a prolific topic of statistical physics, as it seems that fluctuations, and thus fluctuation temperatures, of diverse systems behave substantially differently [31]. In non-equilibrium experiments, higher fluctuations are often the case [29, 30], which is supported by theoretical predictions [52], whilst sometimes the system is indistinguishable from one in equilibrium [79]. Weaker fluctuations have also been observed in experiments such as the ones in this thesis [42, 41, 40].

Whilst experimental bounds are weak (we can imagine that at least $T^{\text{fluc}} \geq T^{\text{min}}$), a theoretical prediction of the fluctuations is needed to further construe the experimental outcomes. One remarkable result [36] shows that for a hot brownian particle, the fluctuation temperature is:

$$T^{\text{fluc}} = \int dx T(x) w^{\text{diss}}(x) \quad (1.1)$$

with w^{diss} the normalised mechanical energy dissipation in the sample. The oscillation temperature of the object is thus the temperature profile weighted by the spatial dependency of the dissipation. This has also been the case shown in previous experiments in our group [42, 79], as we believe it hints to a possible general trend of non-equilibrium systems. We derive this formula and draw its consequences in our experiments in the next chapters.

Motivation

The goal of this thesis is to measure and to characterise the non-equilibrium fluctuations of various mechanical systems thanks to the extension of the FDT, which leads to eq. 1.1. In order to do so, we proceed in two directions: experimental and theoretical.

We analyse the thermal noise of various micro-cantilevers in contact with a thermal bath at room temperature, showing their fluctuations depend on their local dissipation function. We then test our extended FDT at its temperature-wise limits, placing a cantilever at cryogenic temperatures and reaching the melting point at its tip. Next, we further scrutinise the FDT with the characterisation of the non-equilibrium thermal noise of a macroscopic oscillator.

In order to construe the results, we then develop the extended FDT for all the measurable degrees of freedom of the system, and a simple model for the dissipation function in order to theoretically predict T^{fluc} . Furthermore, we take great care in the characterisation of thermal noise from a statistical point of view, which is then applied in order to sort the experimental data.

Relevance for the GWs community

Due to the possible relevance of this thesis in the GWs detection realm, we believe it is worth showing this in details. We therefore briefly introduce the current state of the GWs facilities and then focus on our contributions on the subject.

There are currently three operative detectors in the world: the LIGO collaboration [2] that has two facilities in the USA and the Virgo collaboration in Italy [3]. In both these collaborations, important developments have been made, spanning from the geometry of the suspension system [24, 9] to the study of the best materials for test masses and coatings [46, 8]. The state-of-the-art setup for the last stage of suspension is represented by monolithic fused silica fibers [32], which show excellent thermal noise properties. We can distinguish three main sources of thermal noise: the coating of the test mass, its bulk, and the system adopted to suspend it.

The non-equilibrium behavior of these systems can arise from the power deposited by the very intense laser beams hitting the mirrors [63]. The most recent advances on the coatings [4] target an absorption coefficient of 1 ppm, which combined with the 3 MW of incoming power leads to ≈ 3 W of deposited heat. This energy needs to be transferred through the system in order to avoid raising the temperature of the test mass, thus increasing thermal noise and reducing sensitivity. If this is not the case, a temperature difference ΔT is present along the suspension system, therefore prompting a NESS.

In this context, our study is a perfect test bench for this possible phenomenon. Measuring the non-equilibrium fluctuations of the cantilever leads to a study of the possible non-equilibrium effects of a ΔT on the thermal noise, and thanks to our extended FDT its theoretical prediction. Anticipating the results of Chapter 3 (also shown in [42, 40]), we show that a ΔT does not necessarily represent a nuisance, depending on the local dissipation of the system considered.

Next, a new generation of detectors has recently appeared: KAGRA, currently in the testing phase in Japan [6]. This collaboration is focused on bringing the detectors to cryogenic temperatures. Indeed, since thermal noise is proportional to the temperature, cooling down the detectors is bound to reduce the impact of this noise source on the measurements. Inevitably, this requires a brand new characterization of materials for the aforementioned components of the detectors. Researchers chose to use sapphire mirrors suspended by sapphire blades, due to this material's superior properties at low temperatures with respect to silica.

The Einstein Telescope (ET) [93], a new underground facility currently under study by a European collaboration, also aims at lowering thermal noise thanks to cryogenics. The research of the materials to be used in the suspension system involves sapphire and a third material: silicon. At around 20 K, silicon has a zero in its thermal expansion, thus eliminating the thermoelastic contribution to the total noise.

The recent proposal of LIGO Voyager [4] consists of various upgrades to the LIGO facility, including cooling down the detector at 123 K. In fact, at this temperature, a second minimum of thermal expansion eliminates the thermoelastic noise. Silicon is preferred over sapphire due to the possibility of keeping the detector at higher temperatures with respect to the ≈ 20 K needed to retrieve similar noise properties with sapphire.

The challenge with low temperatures is now not only the possible effects of a ΔT , but also the fact that the thermal noise properties of the selected material need to be optimised for the chosen temperature. In these conditions, the first effect can be even more dramatic than at room temperature: in KAGRA, when the temperature of the mirror is raised from 20 to 23 K (15%), the sensitivity is predicted to decrease by 8 % [96]. KAGRA, ET, and the LIGO Voyager proposal adopt two different strategies: the first two use a conductive circuit to the heat sink, while the second suggests a radiative one. The advantage of the first one is that the temperature can be lower; however, the suspension ribbons must be thick, therefore potentially increasing noise. The opposite is true for the second: since the temperature must be higher, thus increasing the thermal noise of the mirrors, nonetheless reducing the contribution of the suspension. In both approaches, there is a common agreement that a temperature gradient along the suspension blades, or ribbons, is again undesirable.

In this case, our previous studies [42, 40] regarding non-equilibrium noise do not consider a system in a cryogenic environment, and their conclusions may not apply. For this reason, the cryogenic experiment presented in this thesis can represent an interesting test bench for the suspension systems for the aforementioned detectors. Indeed, we show that the conclusions we reach at room temperature can be extended at low temperature, showing how a ΔT may leave the thermal noise of the system roughly unchanged. Furthermore, our sample being made of pure silicon, this experiment represents an important test in assessing the cryogenic non-equilibrium properties of the material for the future ET facility.

Outline

This thesis is divided into 5 main chapters : we first introduce the theoretical background, then describe 3 sets of experiments (cantilevers at room temperature, cantilevers at cryogenic temperature, and macroscopic oscillator), and finally present a general study of the statistical properties of thermal noise, in and out of equilibrium. Each chapter is followed by its own appendices that contain further details on the matter but can safely be omitted for a global reading of the document.

In Chapter 2, we formally introduce the concept of thermal fluctuations of a system, from its early detection to the mathematical description embedded in the FDT. We then show how we can express the action of the thermal bath on a silicon micro-cantilever, prompting oscillations we can divide in two categories: deflection and torsion. The FDT for a cantilever in thermal equilibrium is then retrieved. In the second part, we show a natural extension of this description for a cantilever subjected to a temperature difference along its length [64, 40]. In particular, we show how even in a NESS, we can associate a fluctuation temperature with the system, thanks to an extended EP. In the appendix, we finally discuss the dissipation of a micro-cantilever, developing the necessary tools which will be used in the following parts.

In Chapter 3, we concentrate on the measurement and characterisation of the non-equilibrium thermal noise of various micro-cantilevers using the optical lever technique [60]. We quantify the fluctuations and the dissipation of three samples with different geometries and characteristics, all in contact with a thermal reservoir at room temperature at their clamped end and heated at several hundreds of degrees more at their free end. We then demonstrate how it is possible to *predict* the observed noise based on simple assumptions about the observed dissipation and our extension of the FDT. This description is proven extremely robust, since it allows us to characterise all three samples which show very different behavior under a heat flux. A global view of the different non-equilibrium behavior of the cantilevers is then given in the conclusions. In the appendixes, we discuss a complete and innovative manner to retrieve the sensitivity of the optical lever measurements. Moreover, we show how we can retrieve the probing position and laser waist through the measured thermal noise.

In Chapter 4, we push the previous description to the physical extremes, placing a cantilever in contact with a cryogenic thermal bath on one side and almost reaching the melting point on the other. In this experiment, the system is virtually as far from equilibrium as possible, with a temperature difference on the order of thousands of degrees along the length of the cantilever. In this condition, the temperature field of the cantilever is arduous to characterise; thus we develop a method based on numerical simulations. The thermal fluctuations are retrieved thanks to interferometric detection [87], and we prove the validity of our non-equilibrium FDT in these extreme conditions as well. In spite of difficult interpretation, we also show the dissipation of the cantilever at increasing temperatures. Finally a discussion concludes the chapter.

In Chapter 5, we focus on a macroscopic system, the Non-Equilibrium Thermal Noise (NETN) project in the group of L. Conti [29]. Over a period of one month, I installed a new interferometric detection system and performed some measurements on an aluminum oscillator in a NESS. We start by discussing the oscillator and the new detection system installed, then we show the results of the measurements. While the previous results of the group show a drastic increase in fluctuations with respect to the average temperature of the oscillator, we show that no such phenomenon is found in our measurements. Our data indicate a perfect agreement with our extended FDT, showing how it can be thus applied to a macroscopic object, hinting at its possible generality. Moreover, we show how the new detection system has sensibly improved the Signal to Noise Ratio (SNR) of the detection. After a discussion

and a comparison with the previous results of the group, in the appendixes we examine the alignment of the interferometer and the open questions regarding the system.

In Chapter 6, we tackle a hypothesis underlying the whole thesis, which is the nature of the measured signals we interpret as thermal noise. We show that the expected probability distributions of the Fourier coefficients of the spectrum is a Gaussian, and we verify it thanks to a lock-in amplifier technique. We then show that there is no measurable difference between the statistical distribution of an equilibrium system and an out-of-equilibrium system, which is paramount in defining concepts such as the average and the variance. Then, we discuss the statistical properties of the spectra themselves, showing how they are Γ -distributed around their average. Using this information, we propose an innovative sorting algorithm to exclude polluted signals from an ensemble of spectra and show how we apply it to the measured signals. Next, we calculate the statistical distribution of the thermal fluctuations, showing how it can be safely confounded with a Gaussian, and we propose a second sorting algorithm. In the last section, we examine the fit procedure used throughout the thesis in order to retrieve the dissipation, showing how thanks to an unbiased minimising algorithm and a simulation we can check that the retrieved values are unbiased and associate them with an uncertainty. Finally, a discussion concludes this part.

Lastly, we summarise the results obtained in this thesis in some general conclusions.

Chapter 2

Thermal noise

This chapter concentrates on the study of the nature of thermal noise, starting from its early characterisation until the current state-of-the-art. We introduce the concept of thermal fluctuations of an observable and how they are linked to the dissipation of the system thanks to the Fluctuation Dissipation Theorem (FDT). We then expand the initial description of the oscillations of a single degree of freedom in contact with a thermal bath into the motion of a silicon micro-cantilever. We then show how we can expand this concept for out-of-equilibrium systems, formally introducing the concepts of a fluctuation temperature T^{fluc} .

The first part briefly introduces the concept of thermal fluctuations from its first experimental observations and the theoretical instruments dedicated to its characterization. In particular, we introduce the FDT for a system in thermal equilibrium with its surroundings.

The second part concentrates on applying these concepts to the physical system we are interested in throughout this thesis, a silicon micro-cantilever. We recover the equations of motion of the two families of modes of the cantilever, deflection and torsion, and all the meaningful quantities in order to compute the FDT in this case.

The last part is dedicated to the study of thermal noise in an out-of equilibrium situation. We briefly recall the concept of non-equilibrium and the definition of a fluctuation temperature in this case. An out-of-equilibrium version of the FDT is finally developed.

2.1 Thermal fluctuations

Thermal noise is a property common to all objects having a non-zero temperature. In an experiment, it manifests itself as tiny fluctuations around the mean value of an observable, to which we are going to refer as ζ . Although it goes usually unnoticed, its importance becomes salient when measurements made on the physical system under examination need to be extremely precise, in particular when the size of the system becomes small.

In this section we briefly introduce the first experimental observations of thermal fluctuations and their theoretical interpretation. We introduce the FDT and then apply these concepts in an example, the Simple Harmonic Oscillator (SHO).

2.1.1 First observations

The first studies regarding thermal fluctuations date back to the 19th century, when R. Brown first observed pollen immersed in water [20]. The botanist observed how organelles, expelled by the pollen grains, would exhibit a continuous jittery motion, which appeared

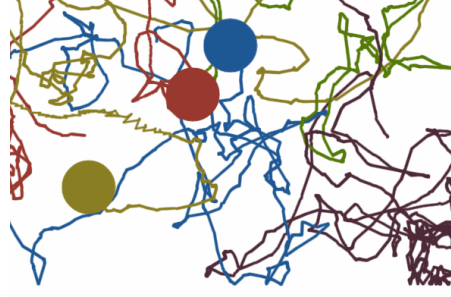


FIGURE 2.1: Brownian motion: some particles are subjected to a random force, which makes them drift with jittery trajectories [77].

to be random. It would take roughly 80 years before A. Einstein would model the aforementioned particles interacting with surrounding molecules, giving a first theoretical justification to what was later named called Brownian motion [34]. Let us suppose that some particles are left in a certain position ξ_0 in a fluid at a temperature T , which exerts a force F on them. Supposing that the only relevant direction of the system is along the x axis, the second law of thermodynamics imposes that for any shift dx of the fluid, the variation of free energy needs to be zero in order for the fluid to be in equilibrium. This imposes that the force F is balanced by the pressure of the fluid, and it allows us to calculate the diffusion coefficient of the fluid $D = \mu k_B T$, with μ the mobility of the fluid and k_B the Boltzmann constant. The author then demonstrates how the density of particles is normally distributed, and thus also the displacements of the particle $\xi(t)$ around its initial value ξ_0 . The variance of this distribution is $2Dt$, with t the time after the particles deposition, which means that on average a particle travels a distance of $\sqrt{2Dt}$. Therefore, it is demonstrated that the mean square displacement of a particle in contact with a fluid is proportional to the temperature of the latter:

$$\langle \xi^2 \rangle = 2Dt = 2\mu k_B T t \quad (2.1)$$

where $\langle \rangle$ represents the ensemble average. The tools developed throughout the article are then used to infer the value of the Avogadro number and the size of atoms. Macroscopic quantities are then shown to be derived from the collective motion of a great number of particles.

A few years later, J. Perrin experimentally demonstrated Einstein's predictions [89], showing with unparalleled precision the strength of the aforementioned analysis. Amongst the various results of his career, the estimation of the Avogadro number represents a milestone in the study of thermodynamics, which also lead to the consolidation of the Atomistic theory.

As atomistic particles, macroscopic objects are subject to Brownian motion as the combination of the fluctuations of all the individual particles composing it. A particularly interesting example is the Brownian motion of electrons in an electrical circuit, first observed by J. B. Johnson [59] and interpreted by H. Nyquist [82]. In this thesis, the thermal fluctuations of the charge carriers inside a resistance R yield a constant exchange of power between the components of the circuit. Let the voltage be our observable $\xi = V$. If we divide the circuit in N networks n , for each n we have a typical length and hence a typical time of vibration, the inverse of which sets a resonance frequency f_n . The authors demonstrate that for each frequency:

$$\langle V_n^2 \rangle = 4k_B T R_n \Delta f_n \quad (2.2)$$

with Δf_n the frequency bandwidth around f_n . This formula relates the mean square voltage

in the circuit with the temperature (as seen in eq. 2.1) and the value of the resistance, which is the dissipative component of the circuit. In the last part of the article of Nyquist [82], it is suggested that the analysis performed can be linked to the mean square displacement of molecules in a gas, hinting at the possibility of this theory and Einstein's being two versions of a unique explanation of thermal fluctuations.

The key is represented by the acclaimed Fluctuation-Dissipation Theorem, demonstrated by H. B. Callen and T. A. Welton [25]. This powerful theoretical framework assembles the clues laid down by the previous works and shows that in general the fluctuations of an observable ξ in equilibrium with the surrounding thermal bath at a temperature T have an amplitude proportional to T and to the inverse of the response function of the system G to a perturbation F . We discuss this in details in the next section.

2.1.2 Fluctuation-Dissipation Theorem

Let us imagine a system characterized by an Hamiltonian \mathcal{H} , which can be divided in one part that does not interact with the environment and another part which represents the exchanges with the thermal bath \mathcal{H}^{int} . If the latter is in the form:

$$\mathcal{H}^{\text{int}} = F(t)\xi \quad (2.3)$$

i.e. the perturbation is linear in the observable, we know from the linear response theory that the value of ξ at a certain time t is influenced not only by the value of the force F at t , but also from its past history. The expectation value of ξ at a t is thus:

$$\langle \xi(t) \rangle = \xi_0 + \int_{-\infty}^t d\tau F(\tau)\chi(t-\tau) \quad (2.4)$$

where we suppose that the perturbation has been acting for a long time. The susceptibility χ is defined as the inverse of the response function $G = 1/\chi \equiv F(\omega)/\xi(\omega)$ of the system to the perturbation. We define $\omega = 2\pi f$ the natural angular frequency and $\xi(\omega), F(\omega)$ the Fourier transformations of $\xi(t), F(t)$.

Next, let us imagine we record the signal $\xi(t)$ for some time \mathcal{T} . We can define the Power Spectrum Density (PSD) of the observable as:

$$\mathcal{S}_\xi(\omega) = \lim_{\mathcal{T} \rightarrow \infty} \frac{1}{\mathcal{T}} \langle \xi(\omega)\xi^*(\omega) \rangle \quad (2.5)$$

with the asterisk denoting the complex conjugate. This closely resembles an autocorrelation function of the observable:

$$C_{\xi\xi}(\tau) = \langle \xi(t)\xi(t+\tau) \rangle \quad (2.6)$$

as it is easy to see that they are Fourier pairs:

$$\mathcal{S}_\xi(\omega) = \int_{-\infty}^{+\infty} e^{i\tau\omega} C_{\xi\xi}(\tau) d\tau = C_{\xi\xi}(\omega) \quad (2.7)$$

The classical form of the FDT [25] then states that:

$$\mathcal{S}_\xi(\omega) = \frac{2k_B T}{\pi\omega} \text{Im} [\chi(\omega)] \quad (2.8)$$

The strength of this relation is that it encompasses the aforementioned examples (Brownian motion, Johnson-Nyquist noise) in one framework, showing how the knowledge of the

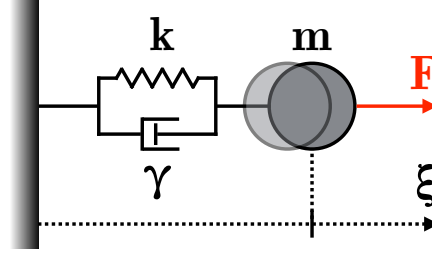


FIGURE 2.2: Simple Harmonic Oscillator.

response function of the system and of the temperature prescribes the amplitude of the fluctuations of an observable.

In this thesis, we are going to use a second form of eq. 2.8, proposed by the inspiring work of Y. Levin [69], who approached the theorem from an experimental point of view. In fact, let us imagine that we want to measure the fluctuations of an object, say a mechanical one for simplicity, at a certain frequency ω . We then mentally apply an oscillating force F linearly coupled to the displacement ξ through the Hamiltonian (eq. 2.3) at this frequency: $F = F_0 \cos \omega t$. This driving force, together with the system's internal forces and its energy dissipation mechanism, yields the evolution of the observable $\xi(t)$. Now, the imaginary part of the susceptibility in eq. 2.8 can be linked to the average dissipated power that this oscillatory force feeds into the system W^{diss} :

$$\text{Im} [\chi(\omega)] = \frac{1}{\omega} \frac{W^{\text{diss}}}{|F(\omega)|^2} \quad (2.9)$$

with $|F(\omega)|^2 = F_0^2/2$. Substituting this into eq. 2.8 gives Levin's version of the FDT:

$$\mathcal{S}_\xi(\omega) = \frac{4k_B T}{\pi \omega^2} \frac{W^{\text{diss}}}{F_0^2} \quad (2.10)$$

This form of the FDT is particularly advantageous because it explicitly shows that the fluctuations of the observable are proportional to the power dissipated by the system when acted on by the force F . We will show that eq. 2.10 is particularly convenient when we want to describe a system with more than one degree of freedom (DOF), i.e. observable.

We now proceed to apply the FDT in a simple example, to show the equivalence of the two definitions of the FDT, in order to then continue with the case of a silicon micro-cantilever.

2.1.3 Simple Harmonic Oscillator

Since in this thesis we are interested in mechanical systems, we consider a Simple Harmonic Oscillator (SHO) immersed in a thermal bath at temperature T , which is shown in fig. 2.2. The physical system is a mass m attached to a spring of stiffness k which presents some form of damping quantified by the quantity γ . Whilst we refer to Appendix 2.A to disclose the possible nature of γ , it is sufficient to know that it allows the oscillator to transfer some of its energy to the environment.

The first task is to define what we intend for this observable to be in thermal equilibrium with the surrounding thermal bath. Via the zeroth law of thermodynamics, the oscillator is in equilibrium with the environment if, on average, it has the same temperature T . The EP

thus tells us:

$$k\langle \xi^2 \rangle = k_B T \quad (2.11)$$

Since our system has just one DOF, it also embeds all the energy of the oscillator in its fluctuations $\langle \xi^2 \rangle$. Therefore, in order for the system to be in equilibrium it must oscillate with this variance around its mean value $\xi_0 = 0$. Doing so, the mass cedes energy to the surrounding thermal bath. If no mechanism is there to invert this process, the oscillator would stop its motion after losing all of its initial energy. The force F (the one acting on the particles described by Einstein) is then the action of the environment transferring energy back to the system, such that on average the total energy of the mass is conserved. We can express this balance through the Langevin equation:

$$m\ddot{\xi}(t) + k\xi(t) + \gamma\dot{\xi}(t) = F(t) \quad (2.12)$$

where the dot represents one temporal derivative, and we express the dissipation as proportional to the velocity of the mass m .

In order to illustrate the mechanical transfer function of the oscillator $G(\omega)$, and thus the susceptibility $\chi(\omega)$, we Fourier transform eq. 2.12:

$$[-m\omega^2 + k + i\gamma\omega] \xi(\omega) = F(\omega) \quad (2.13)$$

For an oscillatory force $F = F_0 \cos \omega_0 t$, it comes naturally that the displacement can be modeled by a similar function $\xi(\omega) = \xi_0 \cos(\omega_0 t + \varphi)$, with a phase φ . It is then easy to derive the dispersion relation and from this to display that the system is resonant at $\omega_0 \equiv \sqrt{k/m}$. It is then possible to define the quality factor $Q \equiv m\omega_0/\gamma$ of the oscillator.

In order to apply the FDT, we must show that the observable ξ is linearly coupled to the force F through the Hamiltonian. Once F acts on the system, the infinitesimal work δW the force makes on the system causes a displacement $\delta \xi$, so it is: $\delta W = F\delta \xi$. For a reversible transformation, the energy exchange is all contained in the work exchange so that $\delta \mathcal{H} = \delta W = F\delta \xi$. Hence:

$$\frac{\partial \mathcal{H}}{\partial \xi} = F \quad (2.14)$$

which demonstrates how the displacement and the thermal force are linearly coupled by the Hamiltonian. In this case, the FDT can be applied, and from eq. 2.8 we get:

$$\mathcal{S}_\xi(\omega) = \frac{2k_B T}{\pi\omega} \text{Im}[\chi(\omega)] = \frac{4k_B T}{k\omega_0} \frac{1/Q}{(1-u^2)^2 + (u/Q)^2} \quad (2.15)$$

where $u \equiv \omega/\omega_0$.

The FDT allows us to predict the oscillations of an observable starting from the mechanical model of the system. If we want to calculate the total energy of ξ , we can integrate eq. 2.15 over all frequencies:

$$\langle \xi^2 \rangle \equiv \int_0^\infty d\omega \mathcal{S}_\xi(\omega) = \frac{k_B T}{k} \quad (2.16)$$

which yields the EP. As expected, one DOF on average possesses an energy $k_B T$.

Let us then show that eq. 2.15 can be obtained from Levin's version of the FDT. We apply a force $F = F_0 \cos \omega t$, so that the position is:

$$\xi(\omega) = \chi(\omega)F(\omega) = \chi(\omega)F_0\delta^D(\omega) \quad (2.17)$$

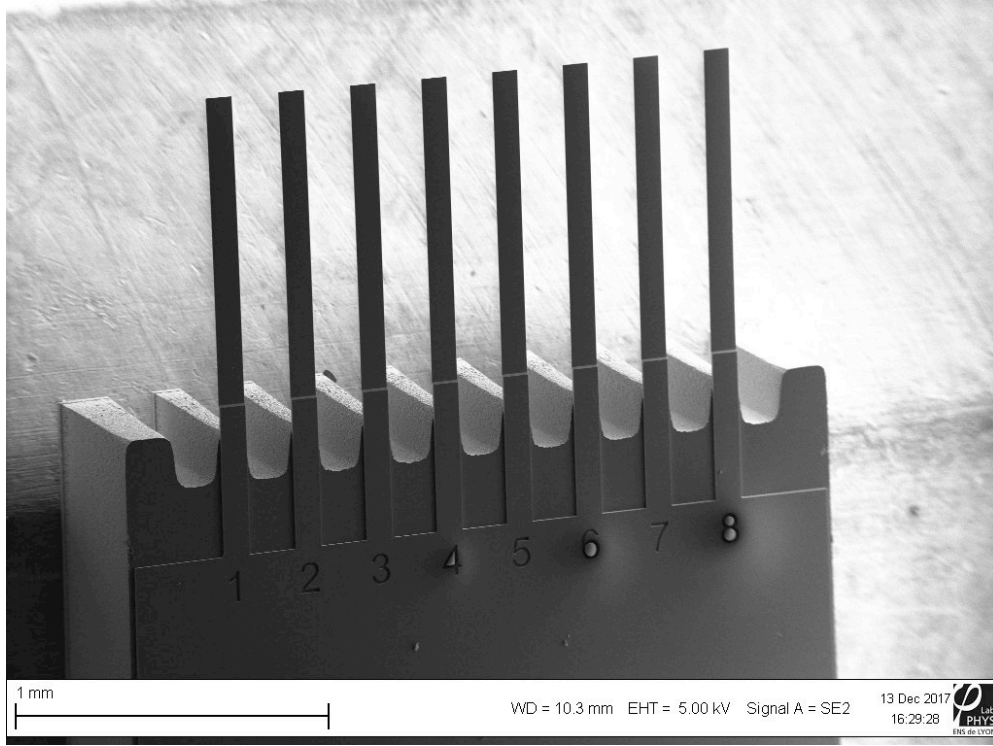


FIGURE 2.3: Example of cantilever array [76]. SEM Image by V. Dolique.

with δ^D the Dirac's delta function. Then:

$$\xi(t) = \text{Re} [\chi(\omega)] F_0 \cos \omega t + \text{Im} [\chi(\omega)] F_0 \sin \omega t \quad (2.18)$$

The dissipated power then is:

$$W^{\text{diss}} = \langle F(t) \dot{\xi}(t) \rangle = \frac{F_0^2}{2} \omega \text{Im} [\chi(\omega)] = \frac{F_0^2}{2} \frac{\omega^2}{k\omega_0} \frac{1/Q}{(1 - u^2)^2 + (u/Q)^2} \quad (2.19)$$

Plugging this into eq. 2.10 leads again to eq. 2.15. As expected, for this example at least, the two versions of the FDT yield the same result. Nevertheless, we believe the second to be an extremely intuitive way to construe the theorem, directly showing the link between the fluctuations of an observable and its dissipation. In this thesis, we henceforth refer to eq. 2.10 when applying the FDT, for two main reasons: as said, it is more intuitive and directly links the energy of the system to its PSD, and in Sec. 2.3 we show that an out-of-equilibrium extension is straightforward.

2.2 Equilibrium thermal fluctuations of a micro-cantilever

A micro-cantilever, such as the ones in fig. 2.3, is a thin silicon beam which in this thesis is usually $500 \mu\text{m}$ long, between $30 - 100 \mu\text{m}$ large, and $1 - 3 \mu\text{m}$ thick. One end of the cantilever is clamped to a macroscopic chip, whilst the other is free to vibrate.

In this section, we discuss the theoretical framework that describes the motion of a cantilever under the action of the surrounding thermal bath, in order to apply then the FDT and predict its thermal noise spectrum. We consider the sample in thermal equilibrium, the extension of which is given in the following section.

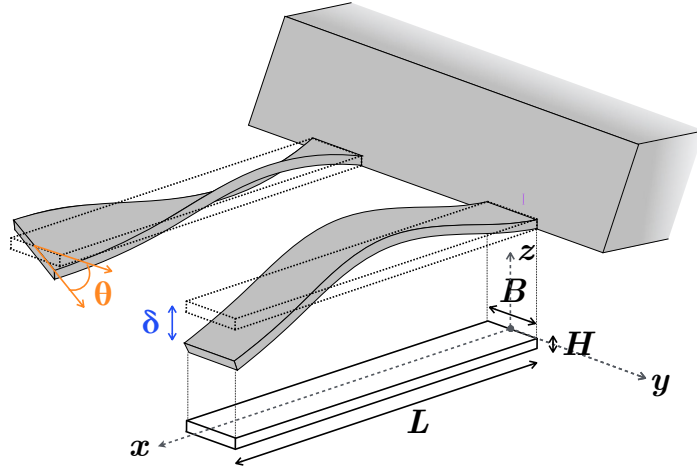


FIGURE 2.4: Motions of the cantilever: the second mode of deflection δ (blue) and torsion θ (orange) is shown. We can see how δ is the movement of the sample in the vertical direction z , whilst θ occurs in the $y - z$ plane, at least in a first approximation.

There are two important deformations that characterize the motion of the cantilever - its deflection and its torsion - which are further divided into eigenmodes of vibration. In fig. 2.4, we show an example of a flexural and a torsional mode of one cantilever. Throughout this document, we refer to the deflection as δ , each mode of which is labeled by an index n . In the same way, the torsional angle θ is divided into modes which are labeled by the letter m . We set x as the axis along the length of the cantilever, y the one across its width and z the direction normal to its surface. The deflection then occurs in the z direction, whilst the torsion occurs around the x -axis.

In the next sections we discuss the theoretical frameworks describing the deflection and the torsion of a cantilever. As part of this information can be found in [15, 84], we refer to these works for further details.

2.2.1 Deflection

In order to describe the vertical displacement of a cantilever, we model it as a clamped-free beam in the Euler-Bernoulli framework [68].

Euler-Bernoulli model

The deflection is considered purely in the z -direction, and thus depends solely on the longitudinal coordinate and the time: $\delta(x, t)$. As we will see, this approach leads to a normal modes description, which will result in each one closely approximated by a harmonic oscillator as in the previous section. For a cantilever of length L , width B , and thickness H , the Equation of Motion (EM) of the system is:

$$m \frac{\partial^2 \delta(x, t)}{\partial t^2} + \frac{\partial^2}{\partial x^2} \left(\frac{L^4}{3} k(x, t) \frac{\partial^2 \delta(x, t)}{\partial x^2} \right) = F(x, t) \quad (2.20)$$

where m is the mass and k the static stiffness of the cantilever, defined as:

$$k = \frac{3YI}{L^3} \quad (2.21)$$

with Y the Young modulus and $I = BH^3/12$ the second moment of area of the sample. The stiffness k contains the rigidity of the system and its dissipation process, the form of which will later be discussed in Appendix 2.A. Finally, the generalized force F represents the usual thermal force. We can express the same equation in the Fourier space:

$$\begin{aligned} [-m\omega^2 + \mathcal{L}] \delta(x, \omega) &= F(x, \omega) \\ \mathcal{L} &\equiv \frac{\partial^2}{\partial x^2} \left(\frac{L^4}{3} k \frac{\partial^2}{\partial x^2} \right) \end{aligned} \quad (2.22)$$

The solution of this EM is found imposing $F = 0$ and using the separation of variables:

$$\delta(x, t) = \phi(x) \delta(t) \quad (2.23)$$

which after reinsertion in eq. 2.20 yields the system:

$$\begin{aligned} -m \frac{d^2 \delta(t)}{dt^2} &= \alpha^4 \delta(t) \\ \mathcal{L} \phi(x) &= \alpha^4 \phi(x) \end{aligned} \quad (2.24)$$

Here α^4 has the dimensions of a stiffness. We now impose the boundary conditions of a clamped-free beam:

$$\begin{aligned} \phi(x=0) &= 0 & \left. \frac{d\phi(x)}{dx} \right|_{x=0} &= 0 \\ \left. \frac{d^2 \phi(x)}{dx^2} \right|_{x=L} &= 0 & \left. \frac{d^3 \phi(x)}{dx^3} \right|_{x=L} &= 0 \end{aligned} \quad (2.25)$$

in order to derive the solution for the spatial component of the displacement:

$$\phi_n(x) = \left(\cos\left(\alpha_n \frac{x}{L}\right) - \cosh\left(\alpha_n \frac{x}{L}\right) \right) - \frac{\cos(\alpha_n) + \cosh(\alpha_n)}{\sin(\alpha_n) + \sinh(\alpha_n)} \left(\sin\left(\alpha_n \frac{x}{L}\right) - \sinh\left(\alpha_n \frac{x}{L}\right) \right) \quad (2.26)$$

Whilst this is the usual solution of the Euler-Bernoulli formalism with a constant stiffness, thus with $\mathcal{L} \propto \partial^4 / \partial x^4$, it is possible to show that it is valid also in the case where k depends weakly on x and t [41]. In this thesis, this can be considered the case, since the stiffness depends on x mostly through its Young modulus Y , which depends weakly on temperature ($\sim 10^{-6} \text{ K}^{-1}$).

The normalised spatial wave numbers $\alpha_1 = 1.875$, $\alpha_2 = 4.694, \dots$ $\alpha_n = (2n - 1)\pi/2$ are the n^{th} root of:

$$\cos \alpha_n \cosh \alpha_n = 1 \quad (2.27)$$

The spatial eigenmodes ϕ_n form an orthonormal basis along the cantilever:

$$\frac{1}{L} \int_0^L dx \phi_n(x) \phi_{n'}(x) = \delta_{nn'}^K \quad (2.28)$$

with δ^K the Kronecher's delta. In fig. 2.4, we report the $n = 2$ mode of deflection, and in fig. 2.5 we show the shape of these functions for higher mode numbers. The temporal part of eq. 2.24 is swiftly solved:

$$\delta_n(t) = \delta_n \cos(\omega_n t) \quad (2.29)$$

with δ_n the amplitude of the oscillation and ω_n the natural angular frequency of the resonance. In order to close the system of eq. 2.24, α_n and ω_n are linked through the dispersion

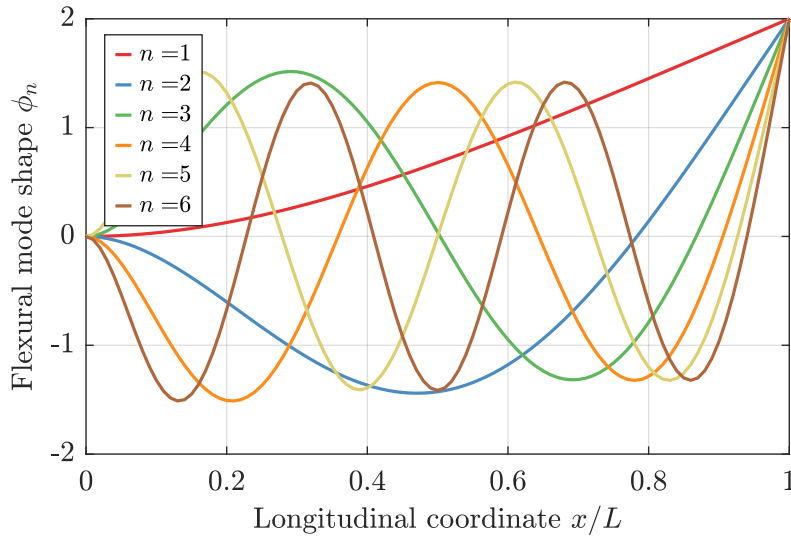


FIGURE 2.5: Flexural normal modes of a cantilever spanning from 1 to 6.

relation, which is the solution to the equation:

$$[-m\omega^2 + \mathcal{L}] \delta_n(\omega) \phi_n(x) = 0 \quad (2.30)$$

which gives the dispersion relation:

$$m\omega_n^2 = \frac{\alpha_n^4}{3} k \equiv k_n \quad (2.31)$$

As said, the functions $\phi_n(x)$ and $\delta_n(t)$ are solutions of the EM (eq. 2.20) in absence of the thermal force $F(x, t)$. In order to find the solution for $F \neq 0$, we expand $\delta(x, \omega)$ and $F(x, \omega)$ on the orthogonal basis of the functions ϕ_n :

$$\begin{aligned} \delta(x, \omega) &= \sum_{n=1}^{\infty} \delta_n(\omega) \phi_n(x) & \delta_n(\omega) &= \frac{1}{L} \int_0^L dx \delta(x, \omega) \phi_n(x) \\ F(x, \omega) &= \sum_{n=1}^{\infty} F_n(\omega) \phi_n(x) & F_n(\omega) &= \frac{1}{L} \int_0^L dx F(x, \omega) \phi_n(x) \end{aligned} \quad (2.32)$$

Projecting eq. 2.22 on this basis, we get:

$$[-m\omega^2 + k_n] \delta_n(\omega) = F_n(\omega) \quad (2.33)$$

The cantilever can thus be conceived as an infinite sum of oscillators. As we remark in Appendix 2.A, we can in addition consider them as independent if some conditions are met. Firstly, the energy dissipation mechanism (and thus the coupling with the thermal bath) cannot be too effective. This is translated in practice as a measurement of the quality factor Q_n of the resonance, which, being the inverse of the strength of the dissipation, needs to be very high. In all the experiments presented in this thesis, Q_n is on the order of thousands or more. Secondly, we would like the resonances to be well separated in frequency. It is then useful to compute the frequency repartition of the modes: from the dispersion relation (eq. 2.31) we can see that the theoretical resonance frequency $f_n = \omega_n/2\pi$ of a mode n is

thus related to the one of the first mode:

$$f_n = \frac{\alpha_n^2}{\alpha_1^2} f_1 \quad (2.34)$$

For example, the second resonance mode is at a frequency roughly 6 times the frequency of the first mode, the third at 17.5 times, and so on and so forth. Each resonance is then a low-dissipation oscillator well separated in frequency from the others. Therefore, one mode can be considered an independent oscillator, i.e. an observable for which we can predict the spectrum through the FDT.

FDT

As shown in Sec. 2.1.2, in order to apply the FDT to the deflection of the cantilever we need to show how δ is linearly coupled to F . The case is slightly different with respect to the SHO case (see Sec. 2.1.3), since the system in question is spatially extended. To calculate the infinitesimal work δW the force makes when displacing the cantilever, we need to integrate its contribution along the sample:

$$\delta W = \int_0^L dx F(x, t) \delta[\delta(x, t)] = \sum_{n=1}^{\infty} F_n(\omega) \delta[\delta_n(\omega)] \quad (2.35)$$

using eq.s 2.28 and 2.59. For a reversible transformation, $\delta \mathcal{H} = \delta W$ and:

$$\frac{\delta \mathcal{H}}{\delta[\delta_n]} = F_n \quad (2.36)$$

We see that the amplitude of each mode n is linearly coupled to the Hamiltonian through the amplitude of the correspondent component of the thermal force F_n . The FDT of each mode then reads:

$$\mathcal{S}_{\delta_n}(\omega) = \frac{2k_B T}{\pi \omega^2} \frac{1}{L} \int_0^L dx \frac{W_n^{\text{diss}}(x, \omega)}{|F_n(\omega)|^2} \quad (2.37)$$

In order to proceed, we need to retrieve the dissipated power W_n^{diss} occurring in the cantilever. As we discuss in Appendix 2.A, we believe that the meaningful description for the dissipation in a micro-cantilever in the experiments we performed is related to the internal dissipation of the material. We then assume a stiffness of shape:

$$k = k^r + i k^i \quad (2.38)$$

where $k^i = k^r \varphi$ represents the internal damping of the material, and φ is the loss angle. As we show in Appendix 2.A, we can thus calculate the dissipated power:

$$\begin{aligned} W_n^{\text{diss}}(x, \omega) &= \omega \varphi(x, \omega) U_n^{\text{max}}(x, \omega) \\ U_n^{\text{max}}(x, \omega) &= \frac{L^4}{3} k^r(x, \omega) \left| \delta_n(\omega) \frac{\partial^2 \phi_n(x)}{\partial x^2} \right|^2 \end{aligned} \quad (2.39)$$

The FDT reads:

$$\mathcal{S}_{\delta_n}(\omega) = \frac{2k_B T}{\pi \omega} \frac{L^4}{3} \frac{1}{L} \int_0^L dx k^i(x, \omega) \phi_n''(x)^2 \left| \frac{\delta_n(\omega)}{F_n(\omega)} \right|^2 \quad (2.40)$$

with ' denoting the spatial derivative. In order to proceed, we can apply some simplifications. Whilst in general k depends on the frequency, its variations are slow compared to the

resonance frequencies, so we can replace $k(x, \omega)$ with its value at ω_n :

$$k(x, \omega) \approx k(x, \omega_n) \quad (2.41)$$

The same concept can be applied to the loss angle φ , in this case also because each mode is extremely peaked at the resonance frequency. Finally, we recognize the susceptibility of mode n in the last quantity of eq. 2.40:

$$\chi_n^2 = \left| \frac{\delta_n(\omega)}{F_n(\omega)} \right|^2 = \frac{1}{(k^r(\omega_n) - m\omega^2)^2 + k^i(\omega_n)^2} \quad (2.42)$$

with:

$$\begin{aligned} k^r(\omega_n) &= \frac{L^4}{3} \frac{1}{L} \int_0^L dx k^r(x, \omega_n) \phi_n''(x)^2 \\ k^i(\omega_n) &= \frac{L^4}{3} \frac{1}{L} \int_0^L dx k^i(x, \omega_n) \phi_n''(x)^2 \end{aligned} \quad (2.43)$$

which arises from the dispersion relation (eq. 2.31). Eq. 2.40 then becomes:

$$\mathcal{S}_{\delta_n}(\omega) = \frac{2k_B T}{\pi\omega} \frac{k^i(\omega_n)}{(k^r(\omega_n) - m\omega^2)^2 + k^i(\omega_n)^2} \quad (2.44)$$

We can now appreciate the similarity of the spectrum of a normal mode of the cantilever and the PSD of a simple oscillator (eq. 2.15):

$$\mathcal{S}_{\delta_n}(\omega) = \frac{2k_B T}{\pi\omega k_n} \frac{1/Q_n}{(1 - u^2)^2 + (1/Q_n)^2} \quad (2.45)$$

with $Q_n \equiv 1/\varphi_n$ and $u \equiv \omega/\omega_n$. We would retrieve the same exact form if we defined $Q_n \equiv \omega_n/\varphi_n$ instead. Finally, we can retrieve the EP. Integrating over all frequencies eq. 2.44 we find:

$$\langle \delta_n^2 \rangle = \int_0^\infty d\omega \mathcal{S}_{\delta_n}(\omega) = \frac{k_B T}{k^r(\omega_n)} \quad (2.46)$$

As we show in the following chapters, the experimental spectrum \mathcal{S}_δ is composed of a certain number of detectable modes, and in order to retrieve the mean square displacement of each one, we restrict our integral to a certain frequency interval $\Delta\omega_n$ around each resonance frequency ω_n . As mentioned, the resonances are highly peaked around ω_n , so we can write:

$$\langle \delta_n^2 \rangle = \int_0^\infty d\omega \mathcal{S}_{\delta_n}(\omega) \approx \int_{\omega_n \pm \Delta\omega_n} d\omega \mathcal{S}_\delta(\omega) \quad (2.47)$$

2.2.2 Torsion

The torsion of a cantilever beam is the rotation of the cantilever around its longitudinal axis x . From a displacement point of view, it corresponds to a deflection in the z coordinate of a quantity $\delta(x, t) = y\theta(x, t)$, with θ the torsional angle and y the transverse direction. This quantity can be modeled as a clamped-free beam in the Saint-Venant framework [33, 68].

Saint-Venant's model

The EM of the torsion of the cantilever is:

$$I \frac{\partial^2 \theta(x, t)}{\partial t^2} - \frac{\partial}{\partial x} \left(L \kappa(x, t) \frac{\partial \theta(x, t)}{\partial x} \right) = \Gamma(x, t) \quad (2.48)$$

with $I = mB^2/12$ the inertial moment of the beam and

$$\kappa = \frac{SBH^3}{3} \quad (2.49)$$

its torsional stiffness, with S the shear modulus. In this case, the thermal noise is represented by a generalized torque Γ , which is defined with respect to the longitudinal axis. We can express the EM in Fourier space:

$$\begin{aligned} [-I\omega^2 - \mathcal{L}] \theta(x, \omega) &= \Gamma(x, \omega) \\ \mathcal{L} &\equiv \frac{\partial}{\partial x} \left(L \kappa \frac{\partial}{\partial x} \right) \end{aligned} \quad (2.50)$$

The unperturbed solution is swiftly found imposing $\Gamma = 0$ and supposing the separation of variables:

$$\theta(x, t) = \theta(t) \phi(x) \quad (2.51)$$

which results in the equations:

$$\begin{aligned} -I \frac{d^2 \theta(t)}{dt^2} &= \alpha^2 \theta(t) \\ \mathcal{L} \phi(x) &= \alpha^2 \phi(x) \end{aligned} \quad (2.52)$$

We then impose the boundary conditions of zero torsion at the clamped end and zero torque at the free end:

$$\phi(x=0) = 0 \quad \left. \frac{d\phi(x)}{dx} \right|_{x=L} = 0 \quad (2.53)$$

and we derive the solution for the mode shape:

$$\phi_m(x) = \frac{\alpha_m}{L} \sin \left(\alpha_m \frac{x}{L} \right) \quad (2.54)$$

Again, this solution is strictly valid if the torsional stiffness is independent of x , but since we are dealing with a weak dependency this approximation holds. The wave numbers are $\alpha_m = (2m-1)\pi/2$ and the spatial eigenmodes ϕ_m form an orthonormal basis along the cantilever:

$$\frac{1}{L} \int_0^L dx \phi_m(x) \phi_{m'}(x) = \delta_{mm'}^K \quad (2.55)$$

In fig. 2.4, we report the $m = 2$ mode of torsion, and in fig. 2.6 we show the shape of these functions for higher mode numbers. Similarly to the flexural case, the temporal solution is then:

$$\theta_m(t) = \theta_m \cos(\omega_m t) \quad (2.56)$$

In the same fashion as the flexural case, we retrieve the dispersion relation as the solution of:

$$[-I\omega^2 + \mathcal{L}] \phi_m(x) = 0 \quad (2.57)$$

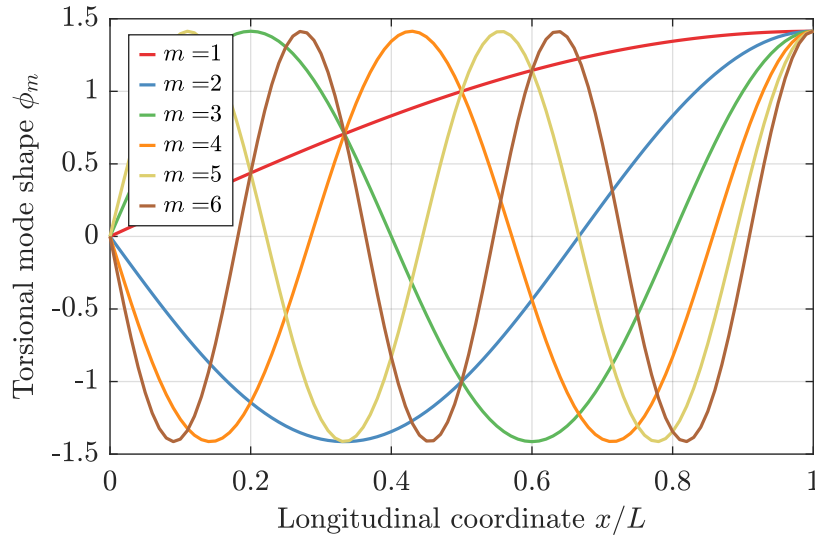


FIGURE 2.6: Torsional normal mode of a cantilever spanning from 1 to 6.

yielding:

$$I\omega_m^2 = \kappa L \alpha_m^2 \equiv \kappa_m \quad (2.58)$$

In order to solve eq. 2.48 for the torque $\Gamma \neq 0$, we expand the angle $\theta(x, \omega)$ and $\Gamma(x, \omega)$ on the basis formed by the functions ϕ_m :

$$\begin{aligned} \theta(x, \omega) &= \sum_{m=1}^{\infty} \theta_m(\omega) \phi_m(x) & \theta_m(\omega) &= \frac{1}{L} \int_0^L dx \theta(x, \omega) \\ \Gamma(x, \omega) &= \sum_{m=1}^{\infty} \Gamma_m(\omega) \phi_m(x) & \Gamma_m(\omega) &= \frac{1}{L} \int_0^L dx \Gamma(x, \omega) \end{aligned} \quad (2.59)$$

Projecting eq. 2.50 on this basis, we get:

$$[-I\omega^2 + \kappa_m] \theta_m(\omega) = \Gamma_m(\omega) \quad (2.60)$$

As in the flexural case, the quality factors of the resonances are on the order of thousands at least, and the frequency separation:

$$f_m = \frac{\alpha_m}{\alpha_1} f_1 \quad (2.61)$$

reveals that the frequency of the second resonance is at 3 times the one of the first, the third at 5 times, and so on and so forth. We can therefore also consider the torsional motion of the cantilever as sum of infinite independent oscillators.

FDT

It is easy to show that the same reasoning of Sec. 2.2.1 can be repeated to demonstrate that the torsional angle θ is linearly coupled to the twisting momentum Γ through the Hamiltonian, and we can thus apply the FDT to each mode m :

$$\mathcal{S}_{\theta_m}(\omega) = \frac{2k_B T}{\pi \omega^2} \frac{1}{L} \int_0^L dx \frac{W_m^{\text{diss}}(x, \omega)}{\Gamma_m^2} \quad (2.62)$$

As for the flexural case, we describe the dissipation as a complex modulus of elasticity:

$$\kappa = \kappa^r + i\kappa^i \quad (2.63)$$

with $\kappa^i = \kappa^r \varphi$ and φ the corresponding torsional loss angle. Since the maximum energy, i.e. the moment of maximum strain, corresponds to the potential energy of the cantilever, it is easy to show that it is:

$$\begin{aligned} W_m^{\text{diss}}(x, \omega) &= \omega \varphi(x, \omega) U_m^{\text{max}}(x, \omega) \\ U_m^{\text{max}}(x, \omega) &= L\kappa^r(x, \omega) \left| \theta_m(\omega) \frac{\partial \phi_m(x)}{\partial x} \right|^2 \end{aligned} \quad (2.64)$$

The FDT then reads:

$$\mathcal{S}_{\theta_m}(\omega) = \frac{2k_B T}{\pi\omega} \frac{1}{L} \int_0^L dx L\kappa^i(x, \omega_m) \phi_m'(x)^2 \left| \frac{\theta_m(\omega)}{\Gamma_m(\omega)} \right|^2 \quad (2.65)$$

In this case, the resonances are also extremely peaked in the resonance frequency, so that we can drop the dependency on the frequency of the stiffnesses and consider only its value at the resonance ω_m . We then calculate the susceptibility:

$$\chi_m^2 = \left| \frac{\theta_m(\omega)}{\Gamma_m(\omega)} \right|^2 = \frac{1}{(\kappa^r(\omega_m) - m\omega^2)^2 + \kappa^i(\omega_m)^2} \quad (2.66)$$

with:

$$\begin{aligned} \kappa^r(\omega_m) &= \frac{1}{L} \int_0^L dx L\kappa^r(x, \omega_m) \phi_m'(x)^2 \\ \kappa^i(\omega_m) &= \frac{1}{L} \int_0^L dx L\kappa^i(x, \omega_m) \phi_m'(x)^2 \end{aligned} \quad (2.67)$$

as solutions of the dispersion equation. Inserting χ_m^2 into eq. 2.65 yields the torsional FDT:

$$\mathcal{S}_{\theta_m}(\omega) = \frac{2k_B T}{\pi\omega} \frac{\kappa^i(\omega_m)}{(\kappa^r(\omega_m) - I\omega^2)^2 + \kappa^i(\omega_m)^2} \quad (2.68)$$

We remark that the spectrum of a torsional mode has the same shape as the flexural mode, and can be thus be rewritten in a similar way as the SHO, with the appropriate parameters:

$$\mathcal{S}_{\theta_m}(\omega) = \frac{2k_B T}{\pi\omega} \frac{1/Q_m}{(1 - u^2)^2 + (1/Q_m)^2} \quad (2.69)$$

with $Q_m \equiv 1/\varphi_m$. Finally, integrating over all frequencies we can therefore retrieve the EP:

$$\langle \theta_m^2 \rangle = \int_0^\infty d\omega \mathcal{S}_{\theta_m}(\omega) = \frac{k_B T}{\kappa^r(\omega_m)} \quad (2.70)$$

Similarly to the flexural modes, we retrieve the mean square torsional angle from the experimental spectrum \mathcal{S}_θ as:

$$\langle \theta_m^2 \rangle = \int_0^\infty d\omega \mathcal{S}_{\theta_m}(\omega) \approx \int_{\omega_m \pm \Delta\omega_m} d\omega \mathcal{S}_\theta(\omega) \quad (2.71)$$

with $\Delta\omega_m$ a small interval around the resonance frequency ω_m .

Barr's model

The Saint-Venant model fails to correctly interpret the torsion of the cantilever for high mode number [15]. This theory only takes into account only stresses in the plane of the cross section of the cantilever, neglecting both longitudinal stresses and inertia that arise due to warping. A refined theory, in which inertia corrections and longitudinal stresses are taken into account, is proposed by Barr [13]. The EM is:

$$\begin{aligned} & \frac{YB^3H^3L}{36} \frac{\partial^4 \theta(x,t)}{\partial x^4} - \left(1 + \frac{Y}{S}\right) \frac{IH^2}{3} \frac{\partial^4 \theta(x,t)}{\partial t^2 \partial x^2} + \frac{4HI^2}{B^3LS} \frac{\partial^4 \theta(x,t)}{\partial t^4} - \\ & - \kappa L \frac{\partial^2 \theta(x,t)}{\partial x^2} + I \frac{\partial^2 \theta(x,t)}{\partial t^2} = \Gamma(x,t) \end{aligned} \quad (2.72)$$

where, for the sake of simplicity, we do not express the spatial and temporal dependency of the quantities. Whilst in the second line, we recognize the Saint-Venant model (eq. 2.48), the first contains the correction terms. The spatial fourth derivative of the torsional angle term represents the longitudinal stress, whilst the mixed derivative terms symbolise the longitudinal inertia, which also yields the fourth derivation in time term. This equation is strictly valid for an isotropic material, but it has been shown that the results are valid for an orthotropic crystal if a plan normal to the cantilever axis is also a symmetry plane of the material [35], which is the case in our experiments.

This equation is still solved by eq. 2.54, yielding a corrected dispersion relation:

$$\frac{YB^3H^3L}{36} \alpha_m^4 - \left(1 + \frac{Y}{S}\right) \frac{IH^2}{3} \omega_m^2 \alpha_m^2 + \frac{4HI^2}{B^3LS} \omega_m^4 - \kappa L \alpha_m^2 + I \omega_m^2 = 0 \quad (2.73)$$

It is also possible to express a correction to the FDT seen before. In this case, since a potential energy is not clearly identifiable, we proceed to calculate the power directly from its stress-strain relation:

$$W = \sigma \dot{\epsilon} \quad (2.74)$$

with ϵ being the strain and σ the stress, linked through the modulus of the material M : $\sigma = M\epsilon$ (see Appendix 2.A for details). W is expressed in the case that we can neglect the longitudinal inertia terms. Whilst it is possible to perform the calculation in the general case, the final result would be difficult to construe. Furthermore, as reported by Barr, for most cantilevers longitudinal stress terms are much more important than the inertia ones. The energy thus reads:

$$U_m^{\max}(x, \omega) = L\kappa^r(x, \omega) \left(\left| \theta_m(\omega) \frac{\partial \phi_m(x)}{\partial x} \right|^2 + \frac{Y}{S} \frac{B^2}{12} \left| \theta_m(\omega) \frac{\partial^2 \phi_m(x)}{\partial x^2} \right|^2 \right) \quad (2.75)$$

From eq.s 2.73 and 2.75 it is then possible to express a corrected version of the FDT of eq. 2.68 involving this new term. For typical values of geometry and moduli, this new term adds a 2% to the energy for $m = 1$, 20% for $m = 2$ and becomes more important than the first term for $m = 4$, which demonstrates the importance of this term.

2.3 Non equilibrium thermal fluctuations

As mentioned, when the system cannot be considered in thermal equilibrium, there is no guarantee that what is discussed in the previous section is valid. In our case, we are interested in systems with a temperature profile along their lengths $T(x)$, thus where a single

temperature T cannot be chosen. Nonetheless, since the systems we are interested in are oscillating mechanical objects, fluctuations are the key. In the case of the cantilever, our observables are the flexural and torsional normal modes amplitudes. In equilibrium, these are related to the temperature through the EP:

$$T = \frac{k_n \langle \delta_n^2 \rangle_{\text{EQ}}}{k_B} = \frac{\kappa_m \langle \theta_m^2 \rangle_{\text{EQ}}}{k_B} \quad (2.76)$$

Whereas T has no meaning in a NESS, thermal fluctuations are still measurable, and it is possible to account for the small variations in the stiffnesses. Since the fluctuations are a collective phenomenon, they are the expression of the processes going on in the whole cantilever. Therefore, it should be possible to find an extended version of the EP in the form:

$$\begin{aligned} T_n^{\text{fluc}} &= \frac{k_n \langle \delta_n^2 \rangle_{\text{NESS}}}{k_B} \\ T_m^{\text{fluc}} &= \frac{\kappa_m \langle \theta_m^2 \rangle_{\text{NESS}}}{k_B} \end{aligned} \quad (2.77)$$

with T^{fluc} the temperature the system would have if its oscillations were measured in equilibrium and if eq. 2.76 were used to estimate it. In other words, the measured non-equilibrium fluctuations $\langle \delta_n^2 \rangle_{\text{NESS}}$, $\langle \theta_m^2 \rangle_{\text{NESS}}$ are considered to be taken in equilibrium, and a temperature is calculated through the equilibrium EP. In this case, we cannot expect every mode to yield the same temperature: indeed, each resonance is a different thermometer, and we have as many thermometers as the modes we record.

In order to characterize an out-of-equilibrium T^{fluc} , we compare it to the meaningful temperatures of the system, which are: the temperature at the clamped end T^{min} , the temperature at the tip T^{max} , and the average temperature T^{avg} . Often, we can estimate the latter as:

$$T^{\text{avg}} = T^{\text{min}} + \frac{T^{\text{max}} - T^{\text{min}}}{2} \equiv T^{\text{min}} + \frac{\Delta T}{2} \quad (2.78)$$

i.e., if the temperature profile $T(x)$ is linear. As mentioned in the introduction, depending on whether T^{fluc} is equal, greater or lower to T^{avg} , we have an equivalent equilibrium system, one showing an excess or a lack of fluctuations.

In the next section, we derive an expression for T^{fluc} , which will lead to eq. 1.1.

2.3.1 Non-equilibrium FDT

In the case of the cantilever, we need to begin our description from the equilibrium FDT discussed in Sec. 2.2.1. Let us consider the flexural modes:

$$\mathcal{S}_{\delta_n}(\omega) = \frac{2k_B T}{\pi \omega^2} \frac{1}{L} \int_0^L dx \frac{W_n^{\text{diss}}(x, \omega)}{|F_n(\omega)|^2} \quad (2.79)$$

As previously stated, if the system is out of equilibrium, this relation is not necessarily valid, as the temperature T is now dependent on x . As shown in [64], the natural extension of the FDT for a system in a NESS is:

$$\mathcal{S}_{\delta_n}(\omega) = \frac{2k_B}{\pi \omega^2} \frac{1}{L} \int_0^L dx T(x) \frac{W_n^{\text{diss}}(x, \omega)}{|F_n(\omega)|^2} \quad (2.80)$$

In the aforementioned article the authors show how it is possible to consider a system presenting a temperature gradient as a sum of oscillators: each one is at a specific temperature

and has with its own dissipation. Levin's form of the FDT [69] is then minimally extended, summing (or, in the limit of continuous systems, integrating) the contributions of all the oscillators. We note that this form of the FDT is the one used in a previous study in our group [42], where only the derivation is different.

From this, deriving the extended EP is straightforward: proceeding as in the equilibrium case, we integrate eq. 2.80 over the frequencies:

$$\begin{aligned}
 \langle \delta_n^2 \rangle &= \int_0^\infty d\omega \mathcal{S}_{\delta_n}(\omega) \\
 \frac{k_B T_n^{\text{fluc}}}{k_n^r} &= \int_0^\infty d\omega \frac{2k_B}{\pi\omega^2} \frac{1}{L} \int_0^L dx T(x) \frac{W_n^{\text{diss}}(x, \omega)}{|F_n(\omega)|^2} \\
 T_n^{\text{fluc}} &= \frac{1}{L} \int_0^L dx T(x) \int_0^\infty d\omega \frac{2k_n^r}{\pi\omega^2} \frac{W_n^{\text{diss}}(x, \omega)}{|F_n(\omega)|^2} \\
 &\equiv \frac{1}{L} \int_0^L dx T(x) w_n^{\text{diss}}(x)
 \end{aligned} \tag{2.81}$$

where we used the definition of T^{fluc} of eq. 2.77 and finally express it as eq. 1.1. While it is clear that the quantity w_n^{diss} is proportional to a dissipated energy, we need to show that it is normalised. A simple argument is to imagine the system in equilibrium: in this case $T_n^{\text{fluc}} = T$ and $T(x) = T$, and thus:

$$\frac{1}{L} \int_0^L dx w_n^{\text{diss}}(x) = 1 \tag{2.82}$$

When the system is out of equilibrium, this needs to be assessed. Let us first note that any effect of the temperature gradient on $w_n^{\text{diss}}(x)$ will be a second order effect for T_n^{fluc} , which is already proportional to $T(x)$. Moreover, the mechanical response of the cantilever is only slightly modified by the temperature gradient, since the maximum frequency shift (and so the stiffness) registered is in the percent range. To a very good approximation, $w_n^{\text{diss}}(x)$ can thus be considered as the normalised dissipation of mode n . We can express this function in a more handy way, developing the terms inside it:

$$\begin{aligned}
 w_n^{\text{diss}} &= \int_0^\infty d\omega \frac{2k_n^r}{\pi\omega^2} \frac{W_n^{\text{diss}}(x, \omega)}{|F_n(\omega)|^2} \\
 &= \frac{L^4}{3} \int_0^\infty d\omega \frac{2k_n^r}{\pi\omega} k^i(x, \omega) \phi_n''(x)^2 \left| \frac{\delta_n(\omega)}{F_n(\omega)} \right|^2 \\
 &= k^i(x, \omega_n) \phi_n''(x)^2 \frac{L^4}{3} \int_0^\infty d\omega \frac{2k_n^r}{\pi\omega} \left| \frac{\delta_n(\omega)}{F_n(\omega)} \right|^2
 \end{aligned} \tag{2.83}$$

The last part of this integral is independent of x , and it could be evaluated using eq. 2.42. However, since w^{diss} is normalised, we can simply make the normalisation explicit:

$$w_n^{\text{diss}} = \frac{k^i(x, \omega_n) \phi_n''(x)^2}{\frac{1}{L} \int_0^L dx k^i(x, \omega_n) \phi_n''(x)^2} \tag{2.84}$$

where the dissipative nature of this quantity emerges from the presence of the loss angle inside the imaginary stiffness $k_n^i = k_n^r \phi_n$.

The same procedure can be applied to the torsional modes: eq. 2.62 becomes:

$$S_{\theta_m}(\omega) = \frac{2k_B}{\pi\omega^2} \frac{1}{L} \int_0^L dx T(x) \frac{W_m^{\text{diss}}(x, \omega)}{\Gamma_m^2} \quad (2.85)$$

which yields:

$$\begin{aligned} T_m^{\text{fluc}} &= \frac{1}{L} \int_0^L dx T(x) \int_0^\infty d\omega \frac{2\kappa_m^r}{\pi\omega^2} \frac{W_m^{\text{diss}}(x, \omega)}{|\Gamma_m(\omega)|^2} \\ &= \frac{1}{L} \int_0^L dx T(x) w_m^{\text{diss}}(x) \end{aligned} \quad (2.86)$$

with:

$$w_m^{\text{diss}} = \frac{\kappa^i(x, \omega_m) \phi'_m(x)^2}{\frac{1}{L} \int_0^L dx \kappa^i(x, \omega_m) \phi'_m(x)^2} \quad (2.87)$$

The definition of the fluctuation temperatures as the temperature profile weighed by a normalised dissipation yields an important theoretical constraint on the fluctuations: T^{fluc} should be bounded by the minimum temperature of the system T^{min} and the maximum T^{max} . In this range, the local dissipation function prescribes the fluctuations. Throughout this thesis, we construe the measured T^{fluc} with the theoretical predictions shown in this section, trying to link the dissipation with the fluctuations, possibly independently by measuring the loss angles φ . Whilst this quantity is experimentally accessible, what we measure is a global quantity which reflects the state of the whole system. In order to predict the behavior of T^{fluc} following eq. 1.1, a spatial (and thus a temperature) dependency on φ would be necessary. As we are going to show, sometimes it is possible to have a clear connection, mostly when the temperature profile is linear. We refer to the next chapters for further details.

2.3.2 Fluctuation temperature measurement

As mentioned, the fluctuation temperatures defined in eq. 2.77 quantify the thermal content of each mode of the cantilever through an extension of the equilibrium EP. In order for this definition to be effective, though, it requires an accurate calibration of the thermal content $\langle \delta_n^2 \rangle$ and $\langle \theta_m^2 \rangle$. A more handy definition arises if we first measure the fluctuations in an equilibrium state, for which we know eq. 2.76 is valid, and the fluctuations relate to the equilibrium temperature T_{EQ} . A comparison of the two gives:

$$\begin{aligned} T_n^{\text{fluc}} &= \beta_n^2 \frac{\langle \delta_n^2 \rangle_{\text{NESS}}}{\langle \delta_n^2 \rangle_{\text{EQ}}} T_{\text{EQ}} & \beta_n &= \frac{\omega_{n,\text{NESS}}}{\omega_{n,\text{EQ}}} \\ T_m^{\text{fluc}} &= \beta_m^2 \frac{\langle \theta_m^2 \rangle_{\text{NESS}}}{\langle \theta_m^2 \rangle_{\text{EQ}}} T_{\text{EQ}} & \beta_m &= \frac{\omega_{m,\text{NESS}}}{\omega_{m,\text{EQ}}} \end{aligned} \quad (2.88)$$

where the β coefficients account for the small changes in stiffness between the two cases (on the order of the percent). In doing so, the fluctuation temperatures are self-calibrated and they are directly related to the equilibrium temperature. Nevertheless, the tradeoff in this case is that one must make sure that the sensitivity of the measurement is constant between the equilibrium and the NESS measurement. Since this depends of the experiment, it will be discussed in each case separately in the following chapters.

Appendix

2.A Energy dissipation in a cantilever

We discuss here the various models that can explain how a cantilever dissipates its energy, focusing then on the ones we believe relevant in this thesis.

2.A.1 Viscous dissipation

A common kind of dissipation is linked to the interactions of the cantilever with the surrounding fluid, hence a viscous dissipation [94, 98, 15]. As an example we can consider Stokes' law for a sphere of radius R immersed in a liquid of viscosity μ :

$$F^{\text{diss}} = 6\pi\mu R v \equiv \gamma \dot{\xi} \quad (2.89)$$

with v the velocity of the sphere. Viscous dissipation is commonly referred to using the symbol γ , and it is the kind of dissipation we used as an example in Sec. 2.1.3 discussing a simple oscillator. In the cantilever case this corresponds to writing the complex stiffnesses as:

$$\begin{aligned} k &= k' + i\omega\gamma \\ \kappa &= \kappa' + i\omega\gamma \end{aligned} \quad (2.90)$$

with k', κ' their real part and the second term representing the dissipation, proportional to the velocity. We remember the definition of the quality factor of each resonance:

$$Q_n = \frac{m\omega_n}{\gamma} \quad (2.91)$$

We do not believe viscous dissipation to be pertinent in describing the damping in our experiments. In fact, during all the measurements the sample is always placed in a vacuum chamber at very low pressure $p \leq 10^{-2}$ mbar, rendering the action of a viscous drag negligible [71].

2.A.2 Internal dissipation

Another source of dissipation is what is usually referred to as the internal dissipation of the material. A displacement of the cantilever generates internal stresses, which in turn induce some dissipation in the material. In order to characterize this phenomenon we follow [81, 7] in deriving the stress-strain relations for an anelastic solid. Note that we use the notation of the aforementioned references, in particular in the definition of an elastic, anelastic and viscoelastic material.

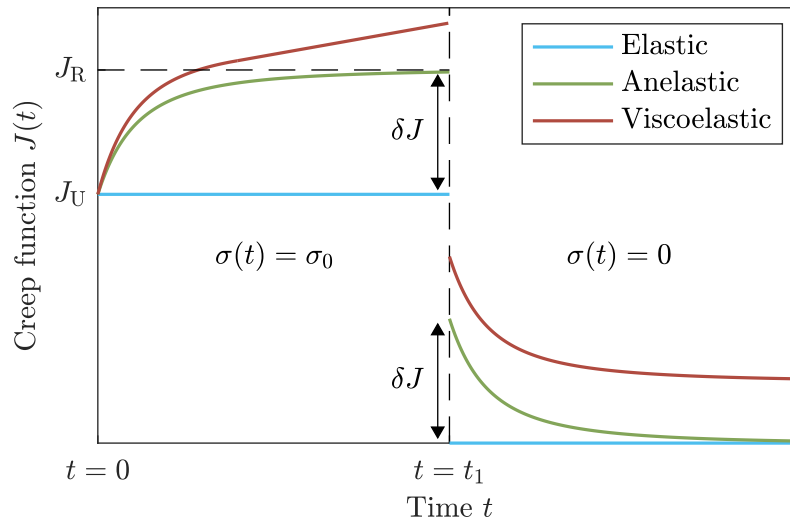


FIGURE 2.A.1: Differences between elastic, anelastic and viscoelastic solid. In the first case (cyan) a stress $\sigma(t)$ imposed at $t = 0$ yields an immediate response in the creep function J , and when this is removed at $t = t_1$ the system goes back to its original state. A anelastic solid (green) takes some time to relax to a certain value J_R , and when the stress is removed a certain time is similarly needed to reach the initial value. The viscoelastic solid (red) never relaxes when a stress is imposed, but rather its J shows a linear growth. When the stress is removed, J relaxes to a different value with respect to its initial one.

Stress-strain relations

Let us first consider a perfectly elastic material which is subject to a stress σ a strain ϵ . Hooke's law states:

$$\begin{aligned}\sigma &= M\epsilon \\ \epsilon &= J\sigma\end{aligned}\tag{2.92}$$

where the modulus of elasticity M and the compliance J are inversely proportional: $M = 1/J$. We take the following as a definition of elasticity: one material for which one strain corresponds to just one stress and vice-versa, plus when perturbed its response function is linear and instantaneous.

Relaxing the last condition yields the concept of anelasticity. This means that once a stress (or a strain) is applied the conjugate variable takes a non-zero time to relax towards its designed value. Loosening the first condition instead defines a viscoelastic material: once a stress (or a strain) is applied, and then removed, the system does not recover its state before the perturbation. We show the differences of these processes in fig. 2.A.1.

Let us take a material which is subject to a time-dependent stress $\sigma(t)$. Following Hooke's law, it experiences a strain $\epsilon(t)$. If the stress is not too great, we can describe $\epsilon(t)$ following a linear theory:

$$\epsilon(t) = \int_{-\infty}^t d\tau j(t-\tau)\sigma(\tau)\tag{2.93}$$

Let us consider the simple case where we apply a constant stress at $t = 0$, $\sigma(t) \equiv \sigma_0\theta(t)$ with $\theta(t)$ the Heaviside function. We can therefore recall eq. 2.92 and find the compliance:

$$J(t) = \frac{\epsilon(t)}{\sigma_0} = \int_{-\infty}^t d\tau j(t-\tau)\tag{2.94}$$

We define the initial value of $J(t)$ as the unrelaxed compliance J_U , correspondent to an elastic system since no time for relaxation is allowed: $J(0) \equiv J_U$. On the other side, as we can see in fig. 2.A.1, an anelastic material experiences a creep, which is the reason $J(t)$ is often referred to as the creep function. After a certain time, the system relaxes towards an equilibrium value, called the relaxed compliance and defined as its asymptotic value $J_R \equiv J(\infty)$. The difference $\delta J = J_R - J_U$ represents the difference between an elastic and an anelastic solid under a constant stress. A different situation arises when a viscoelastic solid is considered: the creep function increases linearly with time.

Let us imagine to remove the stress at a time $t = t_1$. The elastic solid immediately relaxes to its initial equilibrium value, whilst the anelastic reaches in no time the value $\sigma_0 \delta J$ and it needs some time to eventually reach the initial value. A similar effect arises in the viscoelastic case, where the final value of the compliance is not the initial one, since the contribution to the strain during the steady-state phase cannot be reverted.

Whilst such an experiment imposes an external stress and measures the strain of the system, a similar one can be performed the other way around. If we create a strain to a solid, the internal forces would act to bring the system back into an equilibrium situation. As in eq. 2.95 we can write:

$$\sigma(t) = \int_{-\infty}^t d\tau m(t - \tau) \epsilon(\tau) \quad (2.95)$$

if the perturbation is again small. For a constant strain applied at $t = 0$, $\epsilon(t) \equiv \epsilon_0 \theta(t)$ we define the modulus function $M(t)$:

$$M(t) = \frac{\sigma(t)}{\epsilon_0} = \int_{-\infty}^t d\tau m(t - \tau) \quad (2.96)$$

Again, we can define the unrelaxed modulus M_U as the value of the modulus at $t = 0$ and the relaxed modulus M_R as its asymptotic value at $t = \infty$. Since there is a unique relation between stress and strain, these moduli are related to the respective compliances:

$$M_U = 1/J_U \quad M_R = 1/J_R \quad (2.97)$$

and whilst we can similarly define the quantity $\delta M = M_R - M_U$, there is no inverse proportionality between this quantity and δJ . In fact, it is easy to show that $\delta M = \delta J / (J_U J_R)$. From this description we can see that the physical meaning of the modulus function is the same of a spring: when this is extended, thus creating a strain, M prescribes how the system pulls back the spring towards equilibrium.

Dynamics

The experiment described above runs on long times (seconds or more), and we might be interested in the dynamics of the system. Hence, let us imagine that we apply a periodic stress or strain on the sample, with period $\mathcal{T} = 2\pi/\omega$ and with ω the frequency of the cycle. Let us start with an externally imposed stress and the consequent strain:

$$\begin{aligned} \sigma(t) &= \sigma_0 e^{i\omega t} \\ \epsilon(t) &= \epsilon_0 e^{i\omega t + \varphi} \end{aligned} \quad (2.98)$$

where φ is the phase retardation of the strain when the stress is applied (which is zero for an elastic material). The compliance $J = \epsilon/\sigma$ is then a complex quantity:

$$J(\omega) = |J| e^{i\varphi(\omega)} \quad (2.99)$$

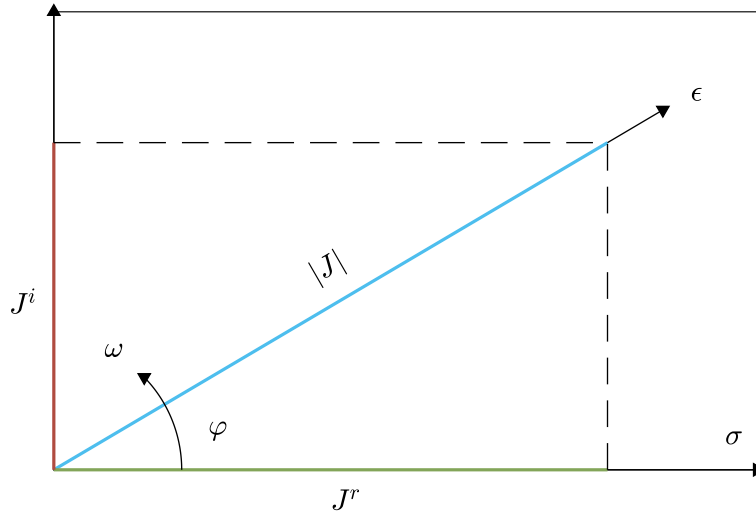


FIGURE 2.A.2: Complex creep function. The creep function J can be imagined as a vector of magnitude $|J| = \sqrt{(J^r)^2 + (J^i)^2}$ aligned with the strain ϵ . There is an angle φ between ϵ and the strain σ , representing the retardation of the first with respect to the latter. Since σ is applied at a frequency $f = \omega/2\pi$, we can depict this as if the two vectors rotated around the origin with an angular velocity ω .

where we let φ depend on the frequency for sake of generality and $|J| = \epsilon_0/\sigma_0$. A practical notation is to rewrite the second of eq.s 2.98 as:

$$\epsilon(t) = (\epsilon^r + i\epsilon^i)e^{i\omega t} \quad (2.100)$$

where ϵ^r is the component in phase with the stress and ϵ^i the one in quadrature. The same notation can be used then to express the compliance:

$$J(\omega) = J^r + iJ^i \quad \tan \varphi = J^i/J^r \quad (2.101)$$

The quantities J^r and J^i are sometimes referred to as the storage and loss compliance, respectively, the reason for which will be clear shortly. In fig. 2.A.2 we show the relations between the quantities we discussed.

In a similar way we can do a stress relaxation experiment. We can impose an external periodic strain on the system and let the internal forces dynamically relax towards equilibrium:

$$\begin{aligned} \sigma(t) &= \sigma_0 e^{i\omega t + \varphi} \\ \epsilon(t) &= \epsilon_0 e^{i\omega t} \end{aligned} \quad (2.102)$$

In this case we can similarly define a complex modulus $M = \sigma/\epsilon$:

$$M(\omega) = M^r + iM^i \quad \tan \varphi = M^i/M^r \quad (2.103)$$

Comparing these quantities with the creep ones we can see that $M^i/M^r = J^i/J^r$ and $M(\omega) = 1/J(\omega)$, so that the complex modulus and the compliance result reciprocal. Nonetheless, this is not necessarily true for their real and complex pairs. In fact, this is assured only if $\varphi^2 \ll 1$, which would imply $\tan \varphi \approx \varphi$. As reported in [81], this is normally the case in crystals. Thus, since $M^i \ll M^r$ and $J^i \ll J^r$ the magnitude of the compliance and the modulus can be

confused with their real parts $|J| = J^r, |M| = M^r$, hence $J^r = 1/M^r$.

A complete description of the functions $J(\omega)$ and $M(\omega)$ is beyond of the scope of this section. We briefly notice that a system satisfying the behavior of fig. 2.A.1 is the so-called three-parameter Voigt-type spring, and writing its EM results in the renowned Debye equations for an anelastic solid [81].

Energy considerations

Let us consider a stress experiment, such as a periodic strain $\epsilon(t)$ (with period $\mathcal{T} = 2\pi/\omega$) is imposed on the system and we let the stress forces $\sigma(t)$ relax towards equilibrium. Thanks to the Debye equations, it is possible to demonstrate that the dissipated power is:

$$W^{\text{diss}} = \sigma(t)\dot{\epsilon}(t) \quad (2.104)$$

where $\dot{\epsilon}$ is the time derivative of the strain. In a whole period \mathcal{T} this is:

$$E^{\text{diss}} = \int_0^{\mathcal{T}} dt \dot{\epsilon} \sigma \quad (2.105)$$

Recalling eq.s 2.103 and 2.102:

$$\begin{aligned} \epsilon &= \text{Re} \left[\epsilon_0 e^{i\omega t} \right] \\ \sigma &= \text{Re} \left[\sigma_0 e^{i\omega t + \varphi} \right] \\ \sigma &= (M^r + iM^i)\epsilon \end{aligned} \quad (2.106)$$

we can calculate the dissipated energy:

$$\begin{aligned} E^{\text{diss}} &= \epsilon_0^2 \omega \left(M^i \int_0^{\mathcal{T}} dt \sin^2 \omega t - M^r \int_0^{\mathcal{T}} dt \sin \omega t \cos \omega t \right) \\ &= \pi \epsilon_0^2 M^i \end{aligned} \quad (2.107)$$

This equation means that the energy dissipation is proportional to the imaginary component of the modulus and the square of the maximum displacement ϵ_0 . In a similar way, we can estimate the maximum stored energy U^{max} . This is defined as an integral:

$$U^{\text{max}} = \int_{t_1}^{t_2} dt \dot{\epsilon} \sigma \quad (2.108)$$

where t_1 is chosen when the stress is zero $\sigma(t) = 0$, which corresponds to $\tan(\omega t_1) = M^r/M^i = 1/\varphi$. Since φ is very small, we can approximate $\omega t_1 \approx \pm\pi/2$. Conversely, t_2 represents the instant when the strain is maximum, which corresponds to a zero in its derivative $\dot{\epsilon} = 0$. This means $\sin \omega t_2 = 0$ and thus $t_2 = k\pi/\omega$ with $k \in \mathbb{Z}$. Thus, choosing $k = 0$:

$$\begin{aligned} U^{\text{max}} &= \epsilon_0^2 \omega \left(M^i \int_{-\frac{\pi}{2\omega}}^0 dt \sin^2 \omega t - M^r \int_{-\frac{\pi}{2\omega}}^0 dt \sin \omega t \cos \omega t \right) \\ &= \frac{1}{2} \epsilon_0^2 (M^r + M^i/2) \approx \frac{1}{2} \epsilon_0^2 M^r \end{aligned} \quad (2.109)$$

since $M^i \ll M^r$. We can thence relate the dissipated energy to the maximum one U^{\max} per cycle :

$$\begin{aligned} E^{\text{diss}} &= 2\pi\epsilon_0^2 \frac{M^i}{M^r} U^{\max} \\ &= 2\pi\varphi U^{\max} \end{aligned} \quad (2.110)$$

Finally, the dissipated power of the system is:

$$W^{\text{diss}}(\omega) = \omega\varphi U^{\max} \quad (2.111)$$

Since the loss energy is proportional to the maximum available energy through the angle φ , this is often referred to as loss angle, or internal friction of the material. Owing to the generality of the last equation, we remark that the same expression would be found if we applied a periodic stress letting the strain lag behind. We finally define the quality factor as:

$$Q = \frac{1}{\varphi} \quad (2.112)$$

Examples

We want now to apply these equations to a familiar system before being able to show that they can be used for the cantilever. Let imagine another SHO, with the position ξ of the mass being prescribed by the elastic force F_e , defined:

$$F_e = c_1 \sigma^{\max} \quad \xi = c_2 \epsilon^{\max} \quad (2.113)$$

If the system is perfectly elastic, the force the mass exerts on the spring is:

$$F_e = \frac{c_1}{c_2} \frac{\sigma^{\max}}{\epsilon^{\max}} \xi = \frac{c_1}{c_2} M \xi \equiv k \xi \quad (2.114)$$

where $c_1 M / c_2 \equiv k$, the stiffness of the spring. On the other side, if the spring is anelastic, this relation becomes $F_e = (k^r + ik^i) \xi$, with the imaginary part of the stiffness that is inherited by the complex modulus M . Let us then recall the EM for an oscillator (eq. 2.13):

$$[-m\omega^2 + k] \xi(\omega) = F(\omega) \quad (2.115)$$

where we imagine a force $F = F_0 e^{i\omega t}$ which modulates the displacement $\xi = \xi_0 e^{i\omega t + \varphi}$. Again finding $\omega_0 = \sqrt{k^r / m}$ as the resonance frequency of the system, we can calculate the energies:

$$\begin{aligned} U^{\max} &= \frac{1}{2} k^r \xi_0^2 \\ W^{\text{diss}} &= \omega \varphi U^{\max} \\ &= \frac{1}{2} \omega \varphi k^r \xi_0^2 \end{aligned} \quad (2.116)$$

This example shows that eq.s 2.109 and 2.111 apply to a resonant system with one degree of freedom. We want to show now that these results can be safely applied to a spatially extended system, with the prominent example being a micro-cantilever. In this case, in fact, the system has a distributed inertia and an infinite number of degrees of freedom, thus resonance modes. The salient point in showing that these differences do not influence the final result is a theorem we quote from [81]:

So long as the internal friction is small, the vibration shape of a specimen is essentially unchanged (to first order) by the presence of internal friction, or by a small departure of the vibration frequency from the natural frequency of the system.

The meaning of this statement is that a small perturbation, such as a small internal dissipation, on the elastic moduli, does not significantly change the normal mode shape $\phi_{n,m}(x)$. Since the significance of a normal mode function is that all the points of the cantilever oscillating at the corresponding frequency are in phase, such that all are zero and all are max at the same time, the theorem says that this is not changed by the internal dissipation. Therefore, since close to a resonance the motion of one point prescribes all the others through the mode shape, the cantilever can be considered an independent oscillator, or a system with one degree of freedom. The most important result is that we can treat the internal dissipation of each mode independently, and eq.s 2.109 and 2.111 can be applied to each resonance. We need solely the parameters k^r and φ (in addition to m in case we want to calculate the kinetic energy).

Let us show an example through the first flexural mode. We write the displacement:

$$\delta(x, t) = \delta_1 \phi_1(x) \cos \omega_1 t \quad (2.117)$$

We thus calculate the maximal stored energy of the system, following eq. 2.105:

$$\begin{aligned} U_1^{\max} &= \int_0^L dx \int_{t_1}^{t_2} dt \dot{\epsilon} \sigma \\ &= \frac{1}{2} \int_0^L dx M^r(x) (\epsilon^{\max}(x))^2 \end{aligned} \quad (2.118)$$

where ϵ^{\max} is the maximum strain. It is possible to show that:

$$U_1^{\max} = \frac{1}{2} \delta_1^2 \int_0^L dx k^r(x) (\phi_1''(x))^2 \quad (2.119)$$

with k^r defined in eq. 2.31.

With this result we can therefore apply the equations for U^{\max} and W^{diss} for each resonance, proven we are able to express their maximal stored energy. Whilst this is easy to compute when a potential energy can be clearly identified, it can be difficult otherwise (see Sec. 2.2.2).

Local properties of internal dissipation

In order to conclude this section, let us discuss the possible causes of internal damping. In fact, the loss angle reflects a *global* property of the cantilever, which is a spatially extended object. In describing its mechanical loss function $w^{\text{diss}}(x)$, though, we need to assess its *local* properties.

In the literature, a main candidate is usually the thermoelastic effect. In this case, temperature differences in the material causes strains, which leads to dissipation. Judging from [18, 26, 72], the contribution of this effect in our experiments is to be discussed. Firstly, pure torsional modes are not affected by thermoelastic losses [72] since they do not create local volume changes in the material. Secondly, for flexural modes it is known [104] that the first resonance mode accounts for almost all the contributions of this noise source. Since in this thesis we cannot analyse this resonance (see Chapter 3), we cannot put this to a test. Furthermore, the observed quality factors cannot be explained solely thanks to this internal

damping, because depending on the specific case they should be hundreds of times higher than the measured ones. We then exclude this as the main contributor to internal losses.

The main component is then possibly related to defects in the crystal. Albeit a model able to theoretical predict the quality factors in this case is beyond the scope of this thesis, it is common to explain the measured loss angles through a local distribution of defects in the material [81]. This theory is particularly fit to describe our cantilevers [42], thus in the next chapters of this thesis we will refer to a density of defects when describing the local dependency of $w^{\text{diss}}(x)$. An example where this function is localised is discussed in the next section.

2.A.3 Clamping dissipation

Yet another source of dissipation is linked to the contact of the cantilever with the chip to which it is monolithically attached. As discussed in ref. [51], dissipation at the clamped end of micro-cantilevers might be an important factor prescribing the final quality factor of the resonances. A vibrating shear force transmits energy from the sample to the chip, and the corresponding elastic waves give raise to dissipation. In order to account for it, in ref. [51] the authors derive a handy formula predicting the quality factor Q^{theo} of the flexural resonances of the cantilever:

$$Q_n^{\text{theo}} = A(\nu) \frac{1}{(\alpha_n b_n)^2} \left(\frac{L}{H} \right)^3 \quad (2.120)$$

with

$$A(\nu) = \frac{0.24(1-\nu)}{(1+\nu)c} \quad b_n = \frac{\sin \alpha_n - \sinh \alpha_n}{\cos \alpha_n + \cosh \alpha_n} \quad (2.121)$$

Here ν is the Poisson ratio of the material and $c \approx 0.336$ for $\nu = 0.28$. The dissipation due to the shear forces interacting with the chip is thus proportional to the 3rd power of the ratio between the length and the thickness of the cantilever.

As we show in the next chapter, this dissipation mechanism might explain some of our experimental results. In particular, one sample with a ratio of $L/H = 500$ yields the quality factors shown in Table 2.A.1.

Mode n	1	2	3	4	5	6	7	8
Quality factor $Q_n^{\text{theo}}/10^5$	260	22	8	4	2.5	1.7	1.2	0.9

TABLE 2.A.1: Clamping losses quality factors.

Whilst the first resonance is almost always undetectable in our experiment, we can compare our results with this theoretical prediction for the higher modes. We will show in the next chapter that a clamping dissipation is the conclusion for one of our samples, and a vibrating shear force could be the cause of it.

A second source of losses at the clamped end of the cantilever might be the presence of defects in this point. As discussed in the previous section, a local density of defects at $x = 0$ can yield a similar effect as a vibrating shear force. In fact, whilst most of the cantilevers described in this thesis are fabricated from a single crystal silicon wafer, hence theoretically devoid of internal defects, this cannot be avoided close to the monolithically clamped end. Indeed, at this point, the chemical etching performed to create the cantilever left a transition between the thin beam and the macroscopic chip, thus possibly a concentrated density of defects.

2.A.4 Discussion

The dissipation of a cantilever is a delicate yet lively subject, due its importance for example in Atomic Force Microscopy (AFM) and MEMS [86]. As seen, many experiments and theoretical models contribute to the subject, a part of which we reported in the present section. A physical system usually shows various concurring forms of dissipation, so that its final quality factor reads:

$$\frac{1}{Q} = \sum_i \frac{1}{Q_i} \quad (2.122)$$

thus a contribution from all the i forms of dissipation. It often happens that one phenomenon dominates over the others, which simplifies the description. Throughout this thesis we will show how, from the measured loss angles and their dependency on the temperature, we can associate a certain dissipation process to a specific system. Thanks to this, we can estimate the local mechanical energy dissipation $w^{\text{diss}}(x)$, which in turn describes the thermal fluctuations of the system. We discuss this separately for each cantilever in the next chapters.

Chapter 3

Thermal noise of a micro-cantilever

In the previous chapter, we showed the theoretical models used to describe the in and out-of-equilibrium thermal noise of a micro-cantilever. In the present one, we apply these concepts measuring the thermal fluctuations of three samples, two of which are also studied in [42, 40]. Micro-cantilevers are particularly suited for the study of thermal noise for various reasons. As we show in the next sections, they are small enough to display measurable mechanical fluctuations, and they are large enough to have a strongly non-uniform temperature profile along their lengths. In this way, we can create an important NESS (with temperature difference of hundreds of degrees) and measure the thermal noise of several resonance modes. In fact, it is also interesting that the micro-cantilevers show a wide range of detectable resonances, with each corresponding to a potentially different thermometer. We believe these to be then the perfect test bench for our extended FDT. The common ground of the experiments presented in this chapter is the experimental setup used to retrieve the fluctuations and the temperature of the clamping end of the cantilever, $T = 300$ K.

The first part focuses on the characterization of the experimental setup, describing the various samples explored and the motivation behind this characterisation. The measuring system used to retrieve thermal fluctuations is displayed.

The second part discusses the temperature of the cantilevers when they are heated at their free end. A simple argument based on the redshift of the resonance frequencies is used to extract the maximal and average temperatures of the samples.

The third part shows the results obtained in the different experiments and their theoretical interpretation. We show the fluctuation temperatures with respect to the average temperature of the system, construing the findings with the help of the measured loss angles.

The last part summarises this chapter and discusses the outcome of the experiments. Perspectives for future work and applications are mentioned.

3.1 Experimental setup

The experimental setup is depicted in fig. 3.1.1. The physical system under study is a silicon micro-cantilever, where thermal noise is measured close to its free end with the optical lever technique [60, 75]. A red laser beam (633 nm) is focused with normal incidence on the cantilever, and its reflection is collected with a 4-Quadrant photodiode. A green laser (532 nm) focused close to its free end acts instead as the heater, creating a temperature profile along the sample. In fig. 3.1.2, we show a picture taken during one of the experiments. The cantilever, in vacuum at 5×10^{-6} mbar, is monolithically clamped to its macroscopic chip which is thermalised at room temperature T^{\min} .

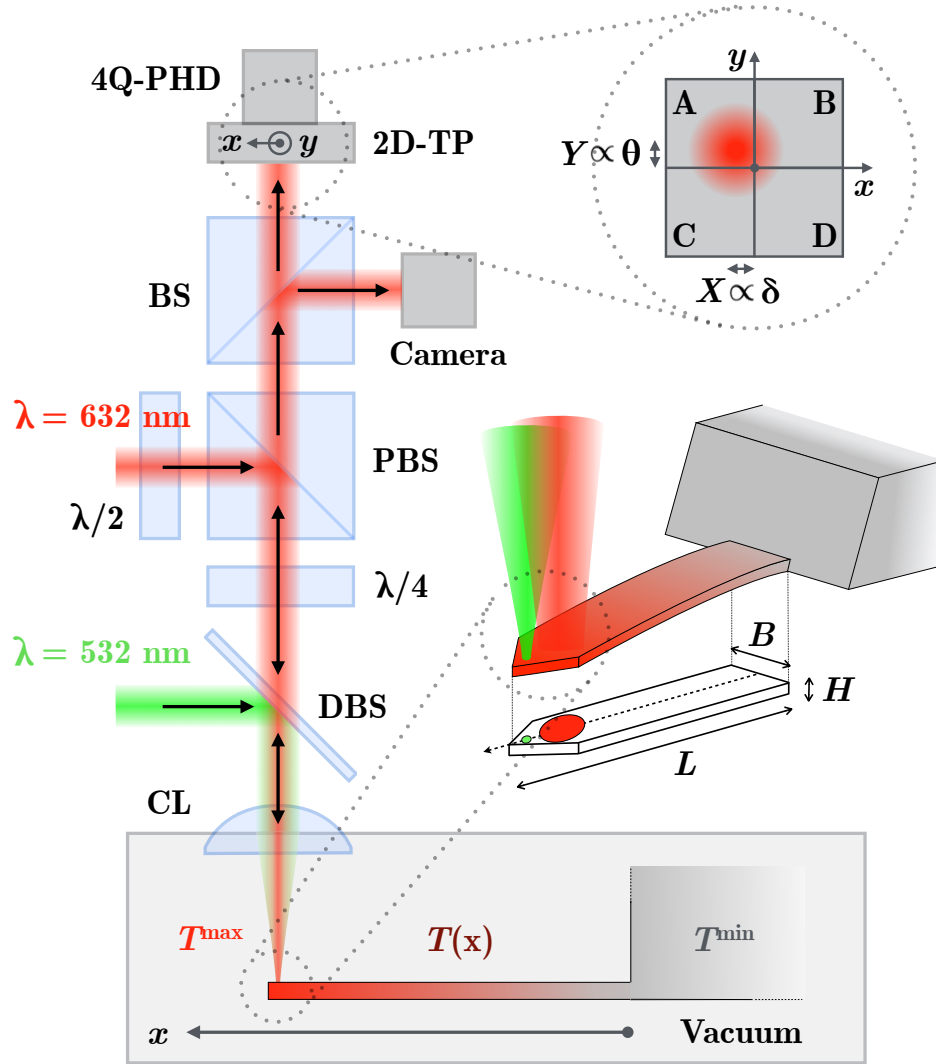


FIGURE 3.1.1: Experimental setup: the deflection and torsion of a cantilever are captured thanks to the optical lever technique. The red laser beam (1 mW at 633 nm), focused on the cantilever tip, is reflected towards the 4-Quadrants photodiode (4Q-PHD). This sensor records the temporal signals of deflection $\delta(t)$ and torsion $\theta(t)$. A motorised 2D translation platform (2D-TP) controlling the position of 4Q-PHD in these directions is used in the calibration. A green laser beam (0 to 10 mW at 532 nm) focused close to the tip of the triangular end of the cantilever acts as the heater. A camera is used to visualise the position of both lasers on the sample (see fig. 3.1.2). The cantilever, in vacuum at 5×10^{-6} mbar, is monolithically clamped to its macroscopic chip, which is thermalised at room temperature T^{\min} .

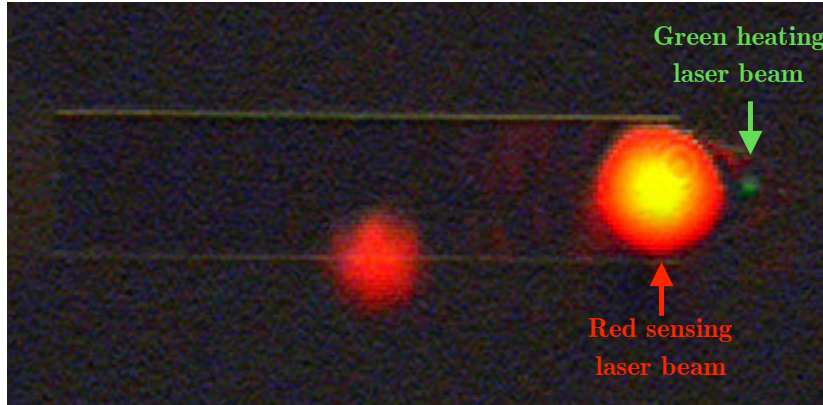


FIGURE 3.1.2: Picture taken during an experiment with a C100 sample. The cantilever is visible only by reflection of light on its edges. The red laser probe is shined close to the triangular tip of the cantilever, with a waist diameter roughly equal to the width of the sample, in order to maximise the sensitivity. The heating green laser is focused even closer to the tip, to avoid an overlap of the two beams and thus mutual interferences. The red spot in the center of the picture is a ghost reflection, so it is actually not present on the cantilever.

3.1.1 Micro-cantilevers

The physical system consists of silicon micro-cantilevers of typical length $L = 500 \mu\text{m}$, with width B and thickness H depending on the sample. In this chapter, we present the results of three different cantilevers, each with its own specific geometry and features.

The first sample is a $B = 100 \mu\text{m}$ wide and $H = 1 \mu\text{m}$ thick silicon cantilever (Nanoworld Arrow TL-8 [80]), with a triangular free end such as the one reported in fig. 3.1.1. This sample is of particular interest because it is the same sample studied in the previous NESS experiments in the group [41, 42]. In these works, in fact, only weak flexural fluctuations are measured, with the cantilever being almost insensitive to the temperature profile alongside it from the fluctuations point of view. The purpose of reexamining this system is twofold: to check previous results in order to strengthen their claims, and to expand the analysis to the torsional modes in order to examine a possible universal behavior. Part of the results related to this sample are available in ref. [40]. We refer to this sample as C100.

The second sample is a $B = 30 \mu\text{m}$ wide and $H = 2.67 \mu\text{m}$ thick silicon cantilever (BudgetSensors AIOTL [21]) with a Tantara (TaO_2) coating on its surface, also with a triangular tip at its end. This sample is also the same one used in some past experiments of the group [42], which shows how its behavior is substantially different with respect to C100. Indeed, thermal fluctuation seem to be strongly influenced by the temperature profile in the system, increasing with the non-equilibrium average temperature. In this chapter, we develop a simple theoretical model which explains why these two samples show different results. We refer to this sample as C30C.

The third sample has the same specifics of C30C, but it is without coating. The goal of this measurement is to check whether the results of C30C are solely due to the coating, or if the substrate plays a similar role in prescribing the thermal fluctuations. We refer to this cantilever as C30.

All but the second sample are commercially fabricated. The sample C30C was obtained adding a TaO_2 coating to a C30 sample, which was performed in the Laboratoire des Matériaux Avancés (LMA) in Lyon, France. The procedure of coating is carefully depicted for

example in [87]. We hereby summarise the characteristics of the different samples in Table 3.1.1.

Name	Width [μm]	Thickness [μm]	Coating
C100	100	1	/
C30C	30	2.67 + coating	TaO ₂
C30	30	2.67	/

TABLE 3.1.1: Experimental samples presented in this chapter and their characteristics. They share a common length $L = 500 \mu\text{m}$.

3.1.2 Experimental setup

As illustrated in fig. 3.1.1, the red laser (1 mW at 633 nm) enters the system through a half-wave plate ($\lambda/2$) which tunes its polarisation so that after passing through the polarising beam splitter (PBS), all light is directed towards the cantilever. It then passes through a quarter-wave plate ($\lambda/4$), a dichroic beam splitter (DBS), and a converging lens (CL, focal length $f_{CL} = 30 \text{ mm}$) which focuses the beam on the cantilever tip. The waist diameter is tuned to roughly $100 \mu\text{m}$ to maximize sensitivity [49]. The lens is also used as the light port to the vacuum chamber. Light is reflected back on the same path from the cantilever. The second passage through the $\lambda/4$ rotates the polarisation perpendicular to the initial one, and therefore the return beam passes straight through the PBS. A final beam splitter (BS) divides it towards an optical camera, used to position the lasers on the cantilever, and the 4-Quadrants photodiode (4Q-PHD). A motorised 2D translation platform (2D-TP) controlling the position of 4Q-PHD in these directions is used in the calibration step (see Appendix 3.A for details).

The green laser beam (0 to 12 mW at 532 nm) focused close to the tip of the cantilever acts as the heater. It is directed towards the cantilever by the DBS and through the lens. Part of the intensity is absorbed and creates a heat flux, and another part is reflected and runs through the same path out of the system. The two lasers spots do not overlap in order to avoid mutual disturbances (see fig. 3.1.2). We discuss the temperature of the cantilever under the action of the heater in Sec. 3.2.

3.1.3 Displacements

The photodetector captures four power signals, which combined give two contrasts C_x, C_y (along the x and y axes respectively) which are proportional to the angle of the beam upon reflection on the cantilever. The contrast C_x leads to the calibrated flexural angle ϑ (in rad), which can be converted to the deflection δ (in meters), whilst the contrast C_y to the torsional angle θ (in rad). We discuss this in detail in Appendix 3.A. Computing the PSD, we identify the normal modes of the cantilever (see fig. 3.1.3 and 3.1.4). The spectra are shot noise limited and the thermal noise-driven resonance peaks show a high signal to noise ratio. Throughout this thesis, the PSD is calculated through the Welch method, with an overlap of 50 %. In general, the number of points in the Fourier transformation are chosen so that the resulting PSD is averaged at least 8 times. We discuss this more in detail in Chapter 6.

Typical measurements allow us to explore a wide range of frequencies, where the observable number of modes depends on the geometry of the sample. In the case of C100, this is up to 11 flexural and 8 torsional modes, whilst for the C30 cantilever we can detect up to 5 flexural and 2 torsional modes. In order assure we correctly identify the resonances, we

simulate the cantilever's eigenmodes in COMSOL [28]. Indeed, due to the imperfect orientation of the photodetector, torsional signals are visible in the flexural PSD and vice versa (see fig. 3.1.3-3.1.4), and the simulation helps us qualitatively distinguish the two motions, especially at high frequency where amplitudes are intrinsically small and vanish close to nodes. Another important contribution of this test is to prove we can access all the resonances in the available frequency range: this is indeed true except for one lateral mode (oscillations in the $x - y$ plane), undetectable with our setup.

Due to experimental constraints, in this chapter, some modes are excluded from the analysis. Flexural mode 1 is often discarded because of self-oscillations (see Appendix 3.C.3), whilst some modes can be undetectable due to the probing point being close to a node of sensitivity (see Appendix 3.A.2 for details).

3.2 Temperature of the cantilever

As mentioned in the previous chapter (see Sec. 2.3), in order to characterize the thermal fluctuations of the cantilever, we quantify them with a fluctuation temperature T^{fluc} . This needs then to be confronted to the meaningful temperatures of the system, which are the temperature of the clamping T^{min} , the temperature at the heating point T^{max} and finally the average temperature T^{avg} . In the experiments presented in this chapter, the temperature of the clamping is the same as the environment $T^{\text{min}} \approx 300$ K due to the cantilever being attached to a macroscopic chip thermalised at this temperature. We then suppose T^{min} to be constant. More delicate is the case of the maximal and average temperature, the latter being defined in general as:

$$T^{\text{avg}} = \frac{1}{L} \int_0^L dx T(x) = T^{\text{min}} + \frac{1}{L} \int_0^L dx \Delta T(x) \quad (3.1)$$

with ΔT the temperature difference between the tip and the clamped end. In our experiments, neither T^{min} nor T^{avg} are directly measurable. Nevertheless, as in [5, 42], we can estimate the temperature of the cantilever through the resonance frequency shifts of its normal modes. In fact, when heated, the cantilever experiences a change in stiffness, becoming softer, mostly due to the temperature dependence of the Young modulus Y and the thermal expansion l .

Following [91], we develop the theoretical model that defines how we can map the frequency shifts of the resonances to the temperature of the cantilever. We then focus on the cases where there is a uniform temperature T , and subsequently we extend this description for case where a temperature profile $T(x)$ exists, i.e. a NESS.

3.2.1 Theoretical framework

Let us focus on the deflection of the cantilever δ , which is described by the Euler-Bernoulli formalism. As seen, for mode n driven to a large amplitude δ_n , we can write:

$$\delta(x, t) = \delta_n \cos(\omega_n t) \phi_n(x) \quad (3.2)$$

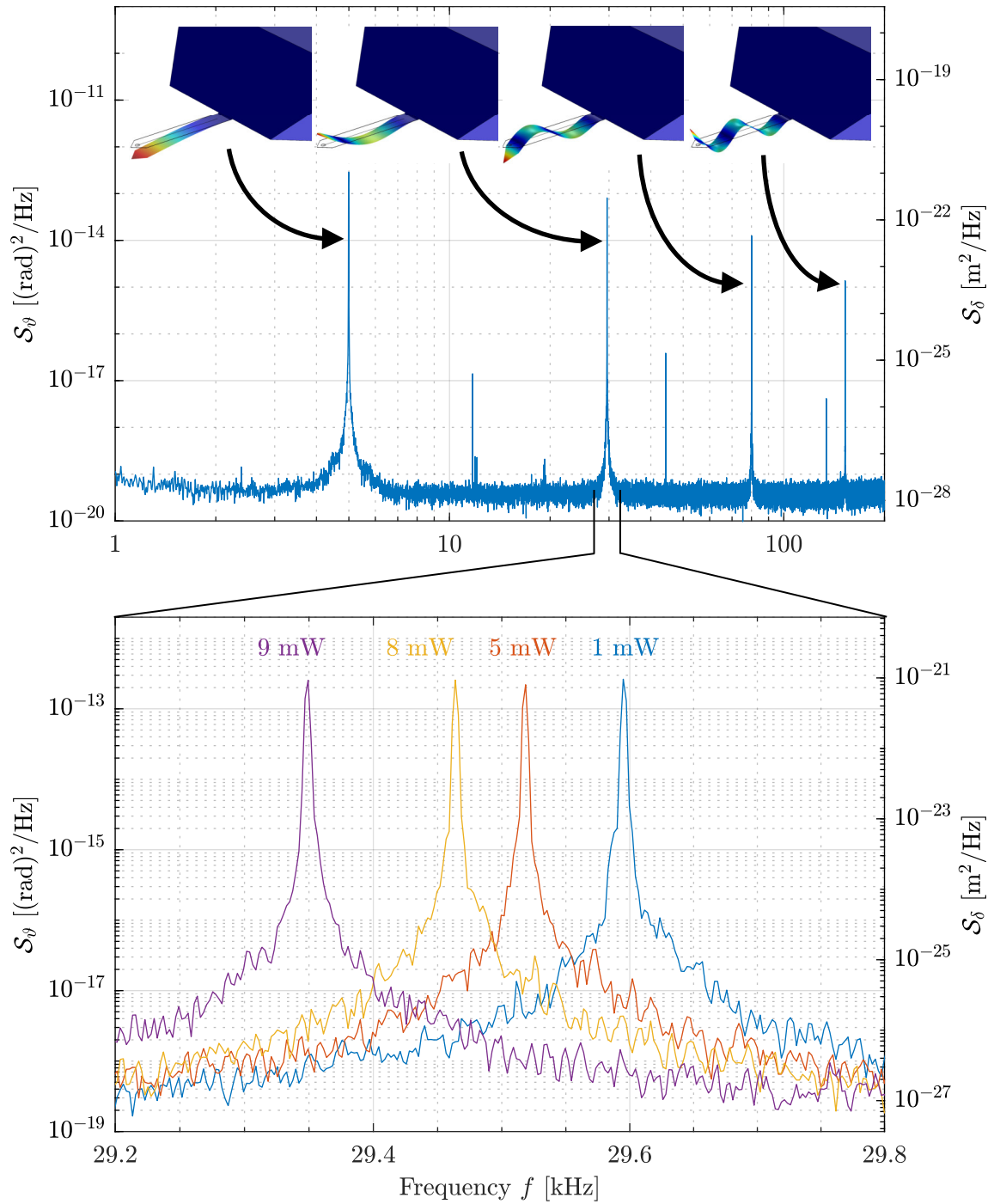


FIGURE 3.1.3: PSDs of the thermal noise-induced deflection of the cantilever. In the upper plot, each resonance mode is identified as a sharp peak with a quality factor in the range of tens of thousands. The modes can safely be considered decoupled and each can be treated as a simple harmonic oscillator. In the lower figure, a zoomed in section around the second flexural resonance shows how the resonance is redshifted with the laser power increasing. This phenomenon is used to compute the imposed ΔT . The shapes of the modes are simulated in COMSOL, yielding resonance frequencies very close to the ones found in our experiment and in agreement with the Euler-Bernoulli description. The left axis of the plots corresponds to the measured flexural angles θ by the optical lever detection (in rad^2/Hz), while the right axis corresponds to its conversion for deflection δ (in m^2/Hz , using mode 2 sensitivity).

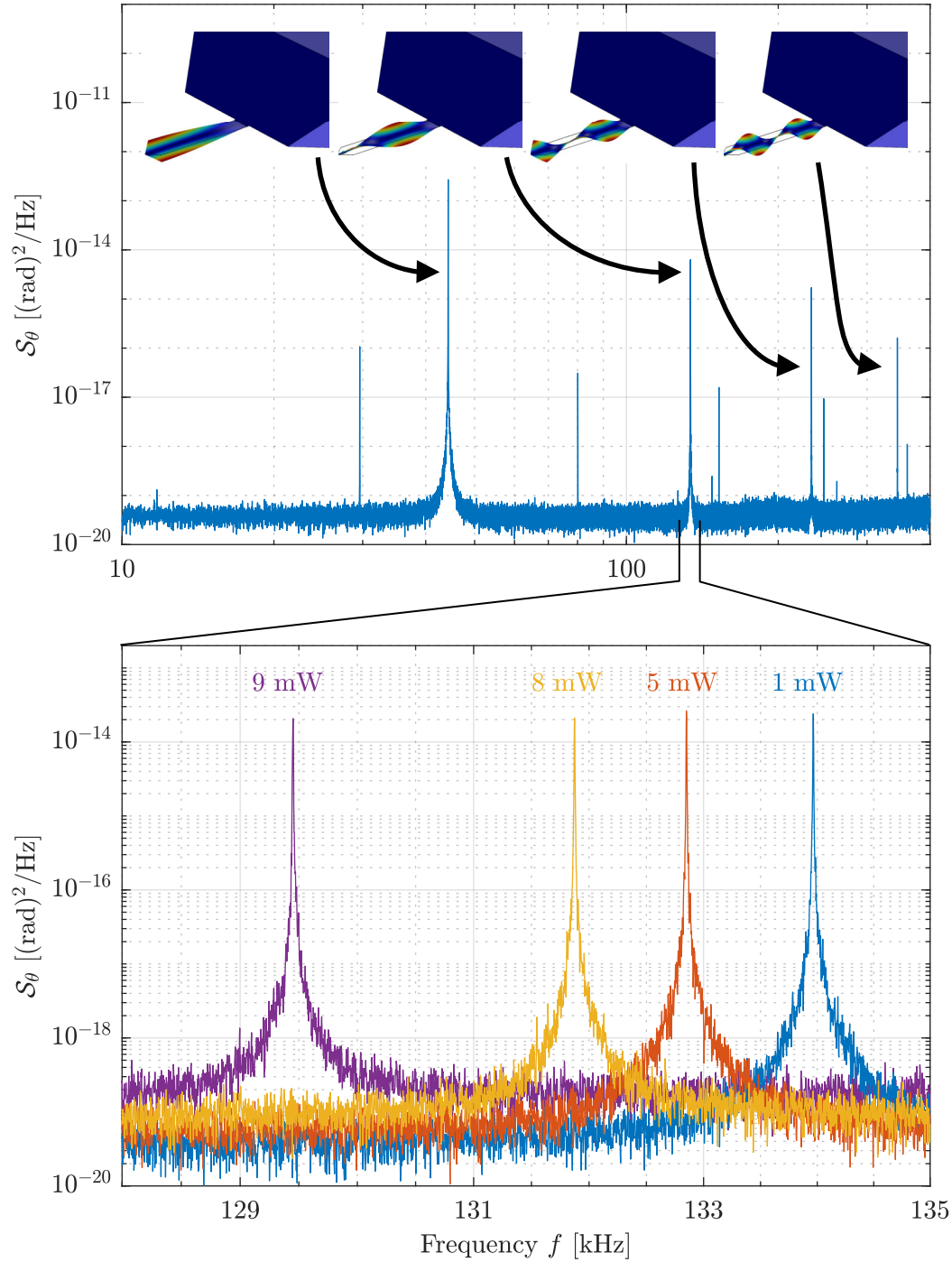


FIGURE 3.1.4: PSDs of the thermal noise-induced torsion of the cantilever. In the upper plot, each resonance mode is identified as a sharp peak with a quality factor in the range of tens of thousands. In the lower figure, a zoomed in section around the second torsional resonance shows how the resonance is redshifted with the laser power increasing, comparatively more with respect to deflection modes. With the model currently at hand, ΔT cannot be calculated with enough precision through torsional frequency shift. The simulated frequencies of the resonances agree quite accurately with the experiment, whereas for the higher modes the analytical Saint-Venant model deviates from the observation.

with ω_n the resonance frequency and ϕ_n the mode shape (see eq. 2.26). As seen in Sec. 2.2.1, we can define the total potential energy U^p and kinetic energy E^k of the cantilever:

$$\begin{aligned} U^p(t) &= \frac{1}{L} \int_0^L dx LYI \left| \frac{\partial^2 \delta(x,t)}{\partial x^2} \right|^2 \\ E^k(t) &= \frac{1}{L} \int_0^L dx m_c \left| \frac{\partial \delta(x,t)}{\partial t} \right|^2 \end{aligned} \quad (3.3)$$

where again Y is the Young modulus, I the second moment of area, and m_c the mass of the cantilever, with all of them in principle dependent on the longitudinal coordinate x . As seen, each resonance can be considered an independent oscillator, thus, since on average kinetic and potential energy coincide (for the EP), for each mode we can write $\langle U_n^p \rangle = \langle E_n^k \rangle$, or:

$$\int_0^L dx LYI \phi_n''(x)^2 = \omega_n^2 \int_0^L dx m_c \phi_n(x)^2 \quad (3.4)$$

From this, the resonance frequency is deduced:

$$\omega_n^2 = \frac{\int_0^L dx LYI \phi_n''(x)^2}{\int_0^L dx m_c \phi_n(x)^2} \quad (3.5)$$

The next step is to retrieve, when the temperature varies, the change of this quantity $\Delta\omega_n \equiv \omega_n - \omega_n^0$, with ω_n^0 the resonance frequency at a reference temperature. On the right hand side of the previous equation, we can distinguish two different dependencies on the temperature: the Young modulus changes because the cantilever gets softer, whilst the mass density and the second moment of area vary because so do the dimensions of the sample. In order to simplify the problem, let us show that the second contributions can be safely neglected. The temperature dependences of $Y(T)$ and thermal expansion $l(T)$ are tabulated [50, 102], and they are highly non-linear at low temperature. Nevertheless, if we restrict ourselves at $T \geq 295$ K, which is the case of the experiments presented in this chapter, a linear approximation yields normalised slopes:

$$\alpha_Y \equiv \frac{1}{Y_0} \frac{\Delta Y}{\Delta T} = -64.2 \times 10^{-6} \text{ K}^{-1} \quad \alpha_l \equiv \frac{1}{l_0} \frac{\Delta l}{\Delta T} = 2.6 \times 10^{-6} \text{ K}^{-1} \quad (3.6)$$

where Y_0, l_0 are the respective values at the reference temperature. Therefore, the Young modulus variation is roughly 25 times more important than thermal expansion at room temperature. Since this is true at all temperatures, we assume $\alpha_l = 0$ from now on. It is of course possible to relax this hypothesis with little if no difference on the final result. Hence, we write:

$$2\Delta\omega_n\omega_n^0 = \frac{IL \int_0^L dx \Delta Y \phi_n''(x)^2}{m_c \int_0^L dx \phi_n(x)^2} \quad (3.7)$$

with $\Delta Y = Y(T) - Y_0$. This equation yields:

$$\frac{\Delta\omega_n}{\omega_n^0} = \frac{1}{2} \frac{\int_0^L dx \frac{\Delta Y(T)}{Y_0} \phi_n''(x)^2}{\int_0^L dx \phi_n''(x)^2} \equiv f_n(T) \quad (3.8)$$

after simplifications. The functions f_n are controlled by the temperature dependence of the Young modulus $Y(T)$, where T depends in principle on x .

3.2.2 Uniform temperature

Let us study the cantilever at a uniform temperature $T^{\text{avg}} = T$. In this case, eq. 3.8 further simplifies, yielding:

$$\frac{\Delta\omega_n}{\omega_n^0} = \frac{1}{2} \frac{\Delta Y}{Y_0} = f(T) \quad (3.9)$$

where f is mode independent and dictated solely by $Y(T)$. At the temperatures considered, we can describe this function with the ansatz [100]:

$$f(T) \equiv c_1 T e^{-c_2/T} \quad (3.10)$$

with the tabulated values [50]: $c_1 = 4.7 \times 10^{-5} \text{ K}^{-1}$ and $c_2 = 317 \text{ K}$.

It is important to note that this relation is valid solely for a *silicon* cantilever, therefore not for the coated sample. For the C30C case, we have two Young moduli to consider: the one of the substrate and the one of the coating. The result of the interaction of the two materials with the temperature change being not trivial, it is therefore best to rely on a calibration of f . Since C30C is the same sample shown in [41], we report here the linear calibration coefficient found by the authors:

$$f_{\text{C30C}}(T) \approx \frac{1}{2} \alpha_{Y,\text{C30C}} T \quad (3.11)$$

with $\alpha_{Y,\text{C30C}} = -113 \times 10^{-6} \text{ K}^{-1}$ representing the Young modulus linear dependency of the substrate-coating system.

We can therefore use these functions to infer the temperature T^{avg} of the cantilever from a frequency shift measured at equilibrium:

$$T^{\text{avg}} = f^{-1} \left(\frac{\Delta\omega_n}{\omega_n^0} \right) \quad (3.12)$$

3.2.3 Apparent temperature

When the system is out of equilibrium, a temperature profile $T(x)$ is present along the cantilever. Since eq. 3.8 does not simplify, f^{-1} no longer yields T^{avg} from a measured non equilibrium frequency shift. We can nevertheless interpret this as an *apparent* temperature, that is the temperature we would associate to a system in thermal equilibrium if we measured the same $\Delta\omega_n/\omega_n^0$:

$$T_n^{\text{app}} \equiv f^{-1} \left(\frac{\Delta\omega_n}{\omega_n^0} \right) \quad (3.13)$$

T_n^{app} and T^{avg} tend to coincide when particular requirements are met: as shown in [5], for a linear temperature profile $T(x) = T^{\text{min}} + x\Delta T$, linear Young modulus temperature dependence $\Delta Y/Y^0 = 2f(T) = \alpha_Y \Delta T$ and sufficiently high mode number $n \geq 5$, eq. 3.8 yields:

$$\frac{\Delta\omega_n}{\omega_n^0} \approx \frac{\alpha_Y}{2} \int_0^1 dx T(x) \Leftrightarrow T_n^{\text{app}} \approx T^{\text{avg}} \quad (3.14)$$

Indeed, for sufficiently high modes n , the curvature ϕ_n'' is spread all over the cantilever, thus becoming not influent on the frequency shift. The proximity of T^{app} and T^{avg} depends on the deviation from the aforementioned approximations.

In order to test the possible discrepancy between T^{app} and T^{avg} , it is possible to simulate the temperature profile of the cantilever solving Fourier's law in the presence of a laser power source. From this, we could get the average temperature T^{avg} (plugging $T(x)$ into

eq. 3.1) and the synthetic frequency shift, using eq.s 3.10 and 3.8. Nevertheless, as shown in [91, 5] for the geometries and temperature ranges considered, $T_n^{\text{app}} \approx T^{\text{avg}}$ is a good approximation if $n \geq 5$. This is not possible in the case considered in the following chapter, though, where the base of the cantilever is thermalised at cryogenic temperatures. In this extreme case, we will show how the apparent temperature is still a good approximation, overestimating the average temperature of not more than 40 K.

From now on, in this chapter, we are going to consider equivalent the temperature retrieved through the resonance mode shifts T^{app} and the average one T^{avg} , simply referring to it as the latter.

3.3 Experimental procedure

Once the cantilever is placed in the vacuum chamber and the pressure is around 5×10^{-6} mbar, we align the experimental setup as in fig. 3.1.1. Through camera observations, we place the two laser beams close to the tip of the cantilever and verify the signal collected by the photodiode. Retrieving the contrasts C_x, C_y , we can then use the 2D-TP to center the sensor with respect to the probing laser, simply finding the point where approximately $C_x, C_y = 0$. This is done in order to avoid losing some signal due to the laser beam being close to the outer edge of the device (see Appendix 3.A for details). Once this is assured, the experiment procedure follows two main steps, which we call S_{EQ} and S_{NESS} . These depend on the power of the heating laser P shined on the cantilever, whilst the probing laser is kept constant at around 1 mW.

The first step S_{EQ} corresponds to an equilibrium case, where the cantilever is irradiated with a low power ($P \approx 1$ mW) so that the temperature gradient is small. The second S_{NESS} is a non-equilibrium case, where we shine the sample with increasing power. Each step is further divided into two steps; let us call them s_{cal} and s_{meas} .

During s_{cal} , the photodiode is moved with an automated procedure thanks to the 2D-TP, first along the x and then in the y -direction, in order to calibrate the sensor for the C_x and C_y signals. In this way, for each step of laser power we retrieve the calibration curve of the sensor, which we discuss in Appendix 3.A. The contrasts C_x and C_y are measured for roughly 1 s, and their average is registered. Then the platform is moved again. With roughly 20 points per contrast, s_{cal} usually lasts less than one minute. At the end, the photodiode is brought back to its initial position.

The following step s_{meas} consists of measuring the displacements δ, θ through the contrasts C_x and C_y . With a sampling frequency of $f_s = 2.5$ MHz and 5×10^6 points acquired, the acquisition time per measured signal is $t_s = 2$ s. Whilst the total number of signals per power changes between the experiments, it is usually between 40 and 75. Taking into consideration also the time to write the data to the disk, the usual duration of this step is thus between 5 and 10 minutes.

The next step S_{NESS} follows the same principles, with a larger laser power P in order to create a NESS. This step is repeated at increasing power until the maximal power is reached, which is usually around 10 mW. Then, P is gradually lowered in order to create a two-side power ramp. This is done for two reasons: firstly, we look for possible modifications of the material which would result in some hysteresis, for example in the resonance frequency of the modes; secondly, we want to check whether the behavior of the thermal noise changes when slowly increasing the temperature or vice-versa.

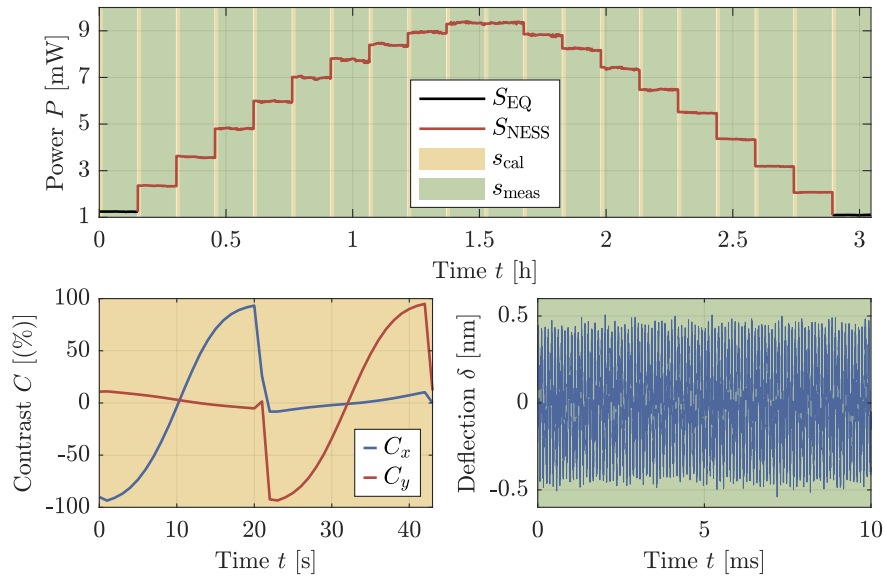


FIGURE 3.3.1: Experimental procedure. In the upper figure, the heating laser power is first set at a low power $P \leq 1$ mW in order to measure the thermal fluctuations in equilibrium, which is the step we call S_{EQ} (black line). Next, the power is slowly increased in the S_{NESS} phase (red line), until reaching a maximum around 9 mW. Each step is divided into a first calibration step s_{cal} (yellow shaded area) and a measurement step (green shaded area). In the lower figures, on the left we show the recorded mean values of the contrasts C_x, C_y whilst moving the photodiode, which calibrates the setup at each power. On the right, we show an example of result of the measurement phase, i.e. a deflection temporal signal (after post-analysis calibration).

We summarize the procedure of the first two S_{EQ} , S_{NESS} steps in Table 3.3.1, and we illustrate a typical measurement sequence in fig. 3.3.1, which is the one used in the C100 experiment.

Steps	S_{EQ} ■		S_{NESS} ■	
	s_{cal} ■	s_{meas} ■	s_{cal} ■	s_{meas} ■
Measured quantities	C_x, C_y	δ, θ	C_x, C_y	δ, θ
Power P [mW]	≤ 1		2-10	

TABLE 3.3.1: Experimental procedure.

3.4 Results

In this section, we present the measured fluctuation temperatures of the three cantilevers and the relative loss angles. Through these two quantities we then try to construe the experimental outcome in light of the theoretical framework developed in the previous chapter. We consider one cantilever at a time.

3.4.1 C100

As mentioned, the sample here considered is the one for which the results can also be found in [40]. With respect to this reference, we add a study of the loss angle of the resonances.

In this experiment, 10 laser powers between 0.8 – 9 mW on a double ramp are imposed near the tip of the cantilever, thus allowing us to probe a maximum temperature T^{\max} going from 330 K up to 1000 K and then back down. Each power step consists of 75 measurement, which yields a total of 750 measured spectra. We record up to 11 flexural and torsional modes, with $n = 1$ being plagued by self-oscillations (see Appendix 3.C.3) and thus discarded. Furthermore, mode 5 is excluded in both motions due to the probing point being on a node of sensitivity, and modes 9 – 11 are similarly not displayed due to their high systematic uncertainty (see Appendix 3.A).

Thermal fluctuations

The fluctuation temperatures can be found in fig. 3.4.1. With T^{avg} increasing, the flexural fluctuation temperature T_n^{fluc} is roughly constant for the first resonances (2 to 4), and it increases slightly for the higher ones. This apparently different behavior of the modes is nevertheless within the error bars, and it should be considered with caution. Since all T^{fluc} show lower values than T^{avg} , we experience a lack of fluctuation with respect to an equilibrium system with the same T^{avg} . These results thus confirm the findings in ref. [42], where a strong lack of fluctuations in a similar sample is observed for the first four resonances. In this section, we extend the previous study for higher modes, with the dearth of fluctuations being a common characteristic of all the observed flexural modes.

The torsional fluctuation temperatures T_m^{fluc} further assesses this phenomenon: the thermal noise is unaffected by the temperature rise in the system for these observables as well. Looking at COMSOL simulations, we verify that we have probed all the existing modes (but one) in the explored frequency range, showing that they all present lower fluctuations than equilibrium. Therefore, this behavior appears to be a general feature for the C100 sample.

Dissipation

We report in fig.s 3.4.2 and 3.4.3 the measured loss angles φ of the resonances. The flexural modes show a loss angle roughly independent of the non-equilibrium increase of the average temperature, a sign that the dissipation processes are almost unchanged between the equilibrium measurements and the NESSes. Indeed, φ_n varies at most by 15 % throughout the whole measurement. It is also remarkable that all but one mode show similar values, $\varphi_n \approx 2 \times 10^{-5}$. It is not clear why mode 6 exhibits a different value, roughly 2 times higher than the rest of the analysed resonances; nevertheless the value is also roughly independent of T^{avg} in this case. The loss angles are obtained through a fit around the resonance frequency, and they always yield a $\chi^2 \leq 2$ (see details of the fit procedure in Chapter 6).

The torsional resonances yield a similar outcome. The loss angles φ_m are roughly independent of the average temperature, as they show similar values with respect to the flexural ones. We note that modes 6 to 8 tend to show values around 20 % higher than the first resonances, which reflects the fact that the dissipation may be slightly more effective for these modes. Also in this case, only fits with a $\chi^2 \leq 2$ are taken into account.

Discussion

As we show, thermal noise appears not to be perturbed by the presence of an important temperature gradient along the length of the cantilever. We have in fact that $T^{\text{fluc}} \approx T^{\min}, \forall T^{\max}$ we impose on the system. In order to construe these findings, we express the theoretical

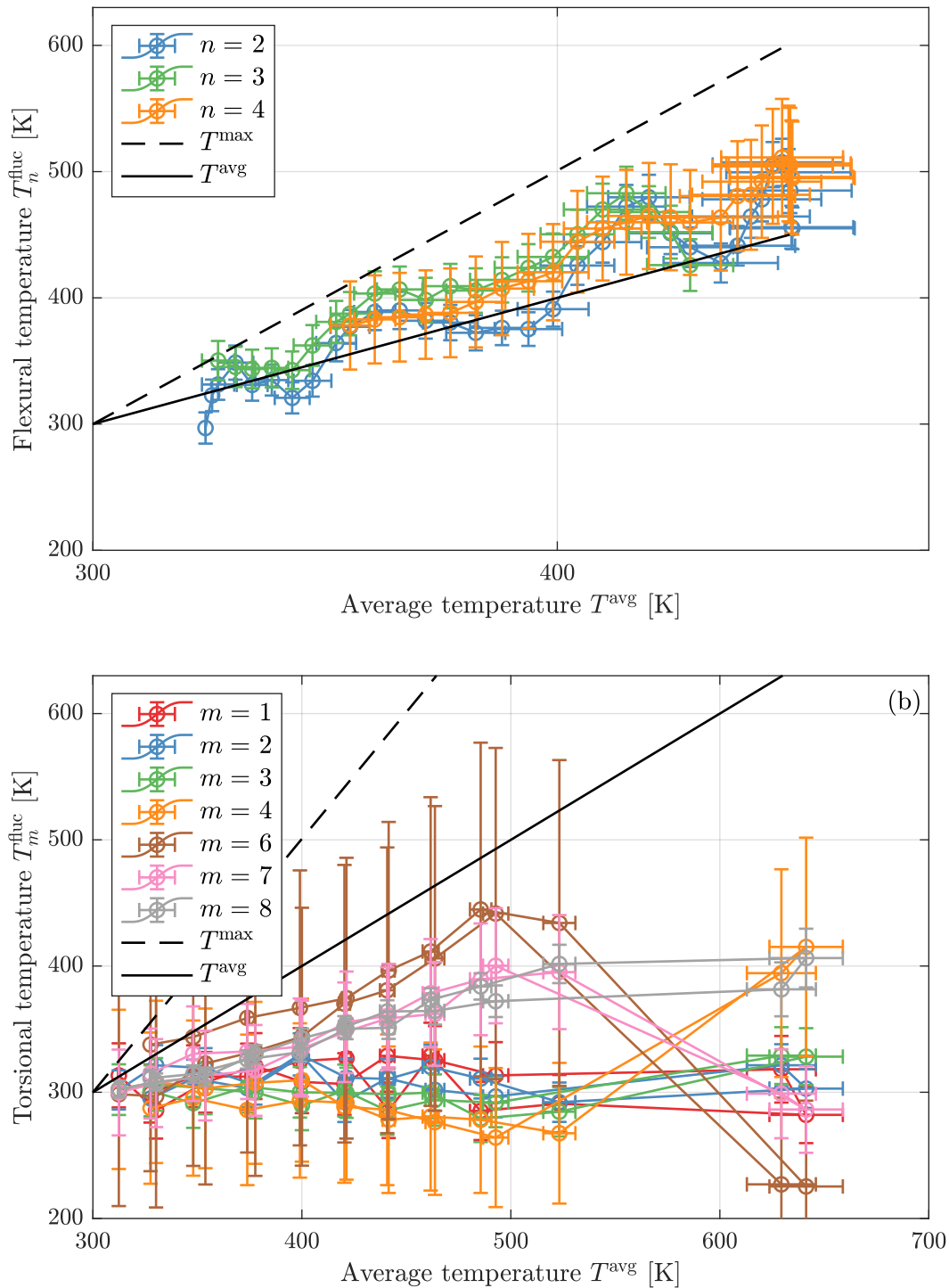


FIGURE 3.4.1: Fluctuation temperature vs. average temperature. In figure (a), the flexural T_n^{fluc} is shown with respect to T^{avg} . The black line represents the equilibrium temperature, i.e. the fluctuations an object would show had it been in thermal equilibrium with a thermal bath at T^{avg} . All the modes lie below this line, as if there was a dearth of thermal noise. Furthermore, we note how they are also much lower than the maximal temperature of the system, represented by the black dashed line. The modes shown span from 2 to 8, excluding mode 5 because of the laser probe being on a node. In figure (b), the same scenario is shown for the torsional degrees of freedom (and mode 5 is omitted for the same reason). The apparent crossover between mode 4 and 6 at the highest T^{avg} is interpreted as a small drift in the laser position, see Appendix 5.C for details in computing T^{fluc} and uncertainties.

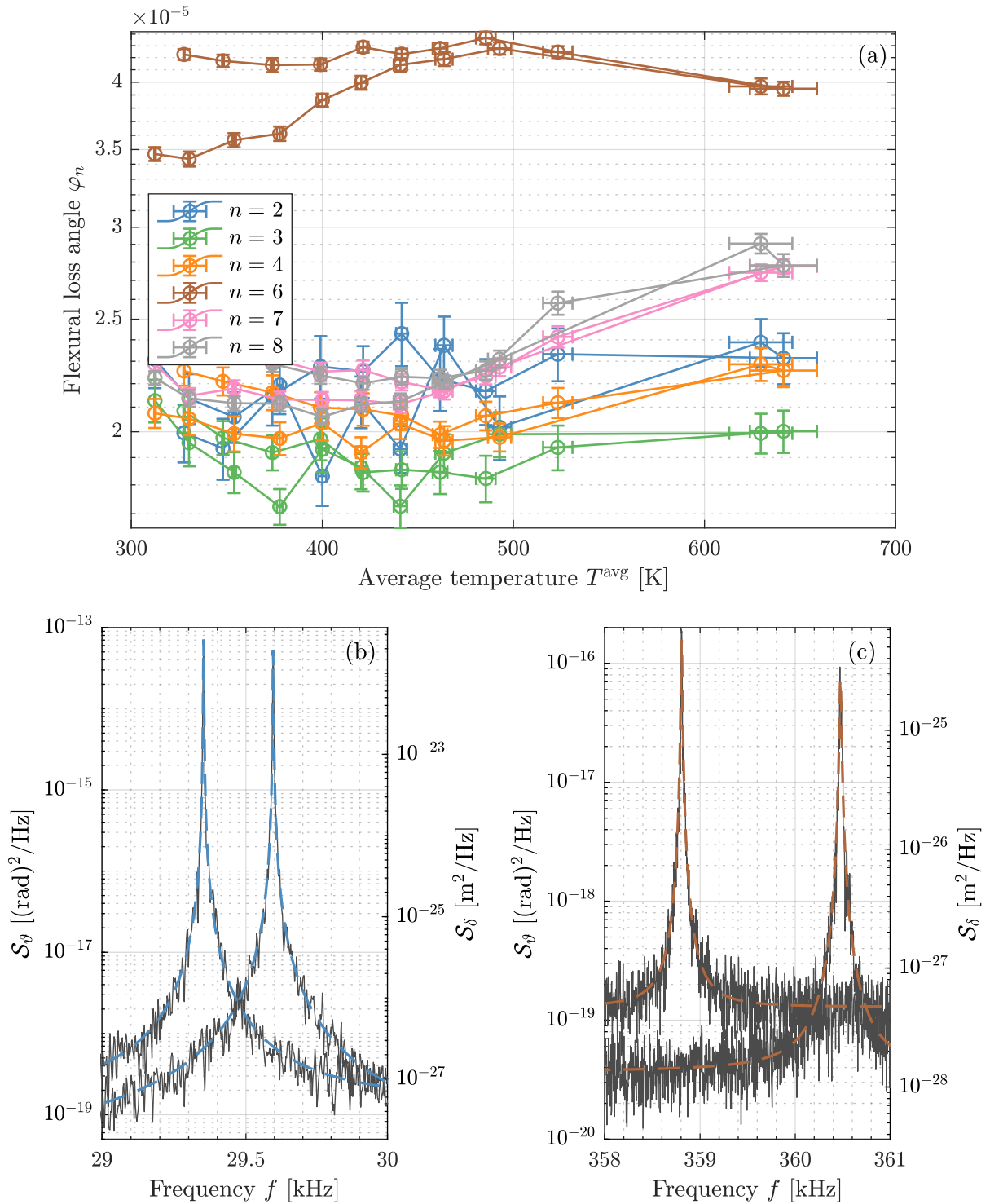


FIGURE 3.4.2: In (a) the flexural loss angles φ_n are shown with respect to the average temperature of the system. With an equilibrium value around 2.3×10^{-5} for all but $n = 6$ (roughly 40 % higher), φ_n changes at most of 15 % at increasing T^{avg} , which we interpret as the expression of the dissipation being independent on the temperature difference ΔT . In (b) the resonance peaks in equilibrium and in a NESS for $n = 2$ are shown, with the former being at higher frequency with respect to the latter. We report also the fits of the data, visually showing how the dissipation does not seem to change from one case to the other. In (c) the same is displayed for $n = 6$, showing that no apparent bias is present in the fits to yield the higher value.

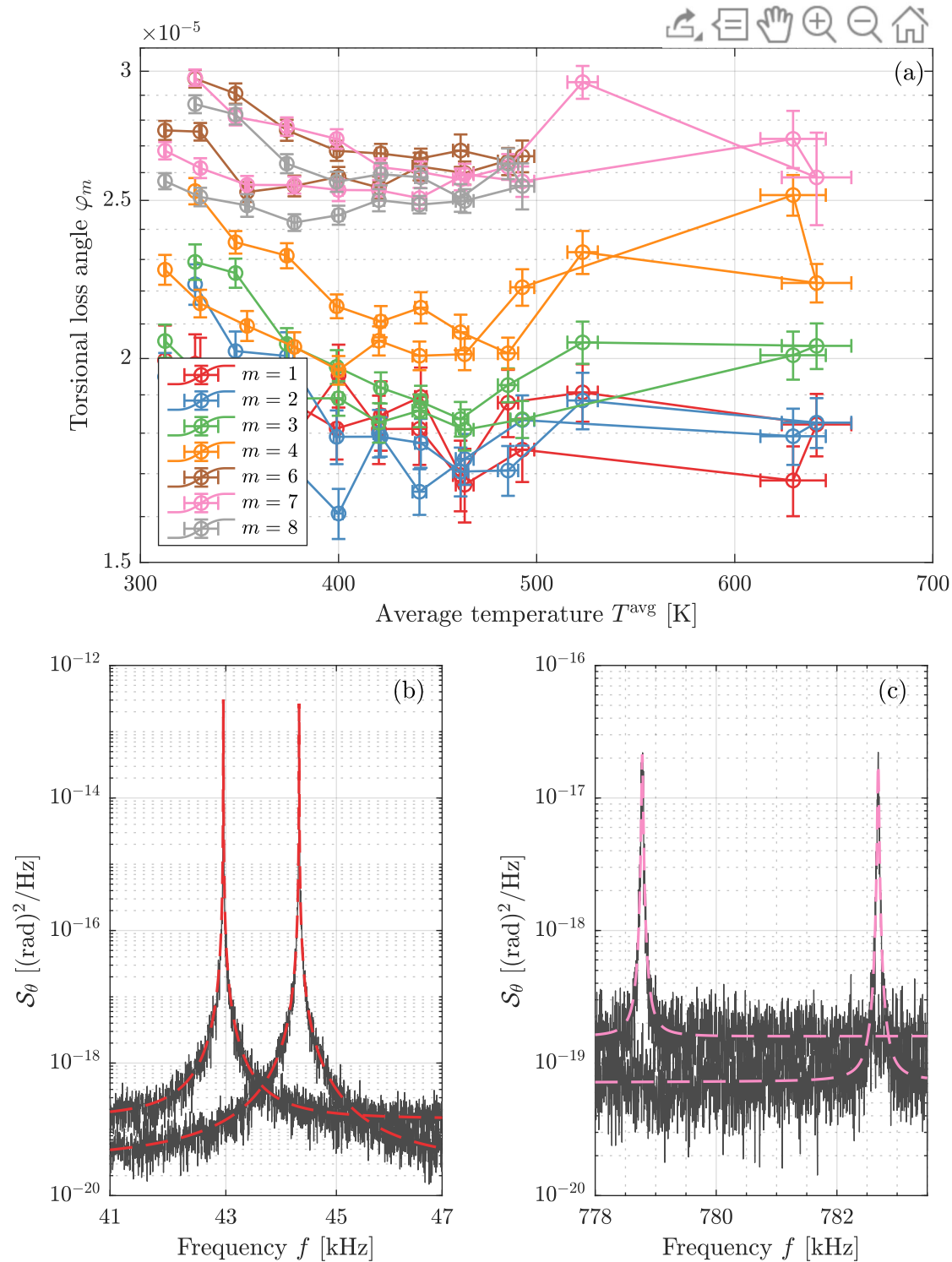


FIGURE 3.4.3: In (a) the torsional loss angles φ_m are shown with respect to the average temperature of the system. The equilibrium value is close to the flexural one at 2.3×10^{-5} , with a tendency to increase with the mode number m . In fact, we note that $m = 6, 7, 8$ are slightly above the first modes. Also in this case, φ_m results roughly independent on the temperature of the system, with changes at most of 15%. As a side note, no fit yields a sufficiently low χ^2 to after $T^{\text{avg}} = 500$ K for modes $m = 6, 8$, so for them no values are available in this range. In (b) and (c) we report the in and out-of-equilibrium spectra for modes $m = 1$ and $m = 7$, respectively.

prediction for T^{fluc} (see eq. 2.81):

$$T^{\text{fluc}} = \frac{1}{L} \int_0^L dx T(x) w^{\text{diss}}(x) \quad (3.15)$$

Since in our case $T^{\text{fluc}} \approx T(0)$, it comes from this relation that $w^{\text{diss}}(x) \approx w(0)$, which means that the mechanical dissipation must be localised at the clamped end of the cantilever, where the only relevant temperature is T^{min} .

This result is further assessed thanks to the measured loss angles φ_n : the dissipation is shown to be roughly independent of the magnitude of the imposed NESS. Two hypotheses can explain this result: either the dissipation can be distributed all along the cantilever, but it is independent of the temperature, or be located at a point with a constant temperature. The former is quite unlikely, thus a damping mainly due to clamping losses seems the right description, since $x = 0$ is always at the temperature of the environment. Our dissipation function then takes the form of a Dirac's delta:

$$w^{\text{diss}} \propto \delta^D(0) \quad (3.16)$$

This conclusion is the same result reached in [42, 40].

In Appendix 2.A, we discuss how a dissipation localised at the clamping can be due to two phenomena: shear stress and defects therein localised. In the first case, in order to assess this, we can compare the flexural loss angles (which are the inverse of the quality factors Q_n) to their theoretical prediction in Table 2.A.1, Q_n^{theo} . The measured quality factor of the second mode $Q_2 = 4.5 \times 10^4$ is 50 times smaller than $Q_2^{\text{theo}} = 2.2 \times 10^6$, and whilst the model forecast a diminishment of Q_n^{theo} for growing n , the highest measured mode $n = 8$ still shows a value half of the theoretical one, $Q_8^{\text{theo}} = 9 \times 10^4$ vs $Q_8 = 4.6 \times 10^4$. Albeit not evident in the flexural modes, the lowering of Q^{theo} at increasing mode number seems to be present in the torsional modes. In fact, in this case we can see that φ_m increases with m , as modes $m = 6, 7, 8$ are roughly 40 % higher than the lower ones. Unfortunately, we do not have a theoretical prediction for the dissipation due to the shear stresses on the torsional modes. While the model represents an approximation, and refinements are possible, the idea that transpires from our measurements is that a pure shear stress-dominated system is not the only answer to explain our measurements. Indeed, the simple presence of this phenomenon prescribes a lower damping in the system than observed, and hence we need another dominant source of dissipation.

The second case described in Appendix 2.A, a preponderant presence of defects close to the clamping, may then be the answer. As previously stated, the cantilever is etched from a single crystal silicon wafer, i.e. in principle devoid of internal defects, and the vacuum removes most of the hydrodynamical damping. The prominent part that can present some defects is thus the clamped end, where the chemically-etched cantilever is attached at the chip.

In conclusion, the simultaneous measurement of both the fluctuation temperatures and the loss angles paints a complete picture of the C100 sample, showing how the fact that $T^{\text{fluc}} \approx T(0) = T^{\text{min}}$ can be explained by the measured $\varphi \approx \varphi(0)$ through our extension of the FDT. It is then important to highlight that these conclusions apply to all the resonances of the cantilever, and thus it is a common property of the sample.

3.4.2 C30C

The coated cantilever C30C is the same sample examined in [42], showing how the thermal noise of the flexural degrees of freedom in a NESS follows closely the average temperature of the system. In this case, the goal of a second measurement is at the same time to strengthen the claims of the previous study for the thermal fluctuations, with the addition of the torsional modes, and to probe the dissipation of the cantilever.

In this measurement, a ramp with 40 laser powers in the 1 – 6 mW range creates a NESS along the length of the cantilever. Two particularities distinguish this measurement from the other measurements presented in this section: firstly, a higher number of power steps is performed instead of an inverse ramp; secondly, the procedure of calibration described in Appendix 3.A is not carried out. Due to this last point, we do not know the evolution of the sensitivity of the photodiode with the increasing power. Nevertheless, since in other measurements this could prompt a bias in the fluctuation temperatures at most 20 %, we can keep in mind that this can be added as an uncertainty. Due to the unknown value of this, though, we decide not to add it to the systematic errors discussed in Appendix 3.A. In this experiment, we can observe up to 4 flexural and 1 torsional resonances, with $n = 1$ being excluded due to self-oscillations.

Thermal fluctuations

In fig. 3.4.4, we show how, with the average temperature T^{avg} of the system increasing, the flexural fluctuation temperatures T_n^{fluc} show values close to T^{avg} , hence close to an equivalent equilibrium system. We note an oscillatory behavior of the T_n^{fluc} at increasing temperature, whose magnitude diminishes with the increase of the mode number. We believe this effect to be due to self-oscillations and self-cooling of the cantilever, which we discuss in Appendix 3.C.3. Since this effect mostly pollutes the first resonances, its magnitude is almost invisible in modes 3 and 4. Indeed, it is for this reason that mode 1 is not significant and not reported. Despite this polluting contribution, the measurement remains significant for two reasons: primarily, de-trending the oscillatory behavior we can see that the most affected resonance, $n = 2$, shows a tendency coherent with the higher modes, being slightly higher than the average temperature of the system; and secondarily, this result is in perfect agreement with the previous measurements performed on this sample [42]. We can therefore believe this to be a minor concern in construing the experimental observations. As a final note, mode $n = 4$ can be observed if the cantilever is shined with a certain amount of power, since before this threshold the shot noise hides the resonance.

The first torsional resonance yields a T_m^{fluc} slightly above the average temperature, showing how its behavior is similar to the flexural modes. Whilst it is possible to retrieve the second resonance mode from a certain laser power onwards, it is hard to assign to it a fluctuation temperature due to the lack of equilibrium measurement with which to confront the NESSes.

Dissipation

In fig. 3.4.5, we report the measured loss angles φ for the C30C sample. The flexural resonances show an equilibrium value around 3.6×10^{-4} , which increases roughly by 50 % at the highest T^{avg} . The same behavior can be observed for the torsional mode. We can approximate the behavior of φ with a second order polynomial in the temperature difference ΔT :

$$\varphi(\Delta T) = a + b\Delta T + c\Delta T^2 \quad (3.17)$$

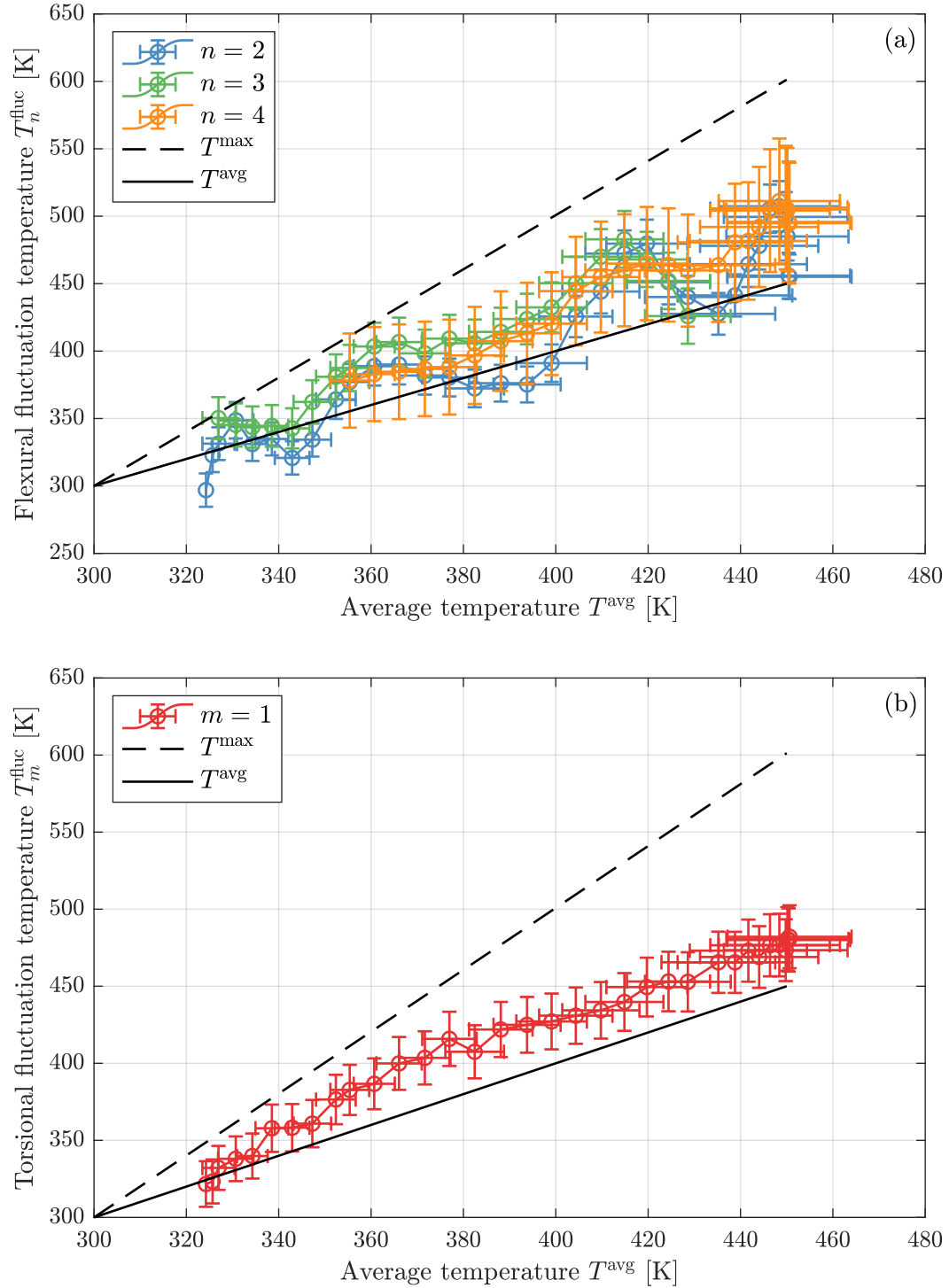


FIGURE 3.4.4: Fluctuation temperature vs. average temperature. In figure (a), the flexural T_n^{fluc} is shown with respect to T^{avg} . The black dashed line represents the maximum temperature T^{max} and the solid one the average temperature T^{avg} . The fluctuation temperatures lie around this value, if not slightly above it. We can notice that the second and third resonance show some oscillations with respect to the average temperature, which we discuss in the text. In (b) the torsional resonance shows a similar behavior, with T^{fluc} being slightly above T^{avg} .

which reasonably fits the experimental data, apart from $n = 4$ for which the lack of points around equilibrium biases the quadratic fit, and it is thus not reported in fig. 3.4.5. Typical fit values (similar for all the analysed modes) range around $a \approx 3.6 \times 10^{-4}$, $b \approx 6 \times 10^{-8} \text{ K}^{-1}$ and $c \approx 2 \times 10^{-9} \text{ K}^{-2}$. In this case, we believe that the system is not dominated by clamping dissipation, but rather that a distributed phenomenon takes place along the cantilever. Indeed, as shown in the previous section, dissipation localised at the clamping end would result in roughly constant loss angles, whilst in this case the damping mechanism is clearly influenced by the temperature increase in the system. We discuss how to link a distributed dissipation with the observed fluctuations in the next section.

Discussion

In order to connect the observed loss angles with the respective fluctuation temperatures, we express T^{fluc} as from eq. 2.84, for example for the flexural modes:

$$\begin{aligned} T_n^{\text{fluc}} &= \frac{\int_0^L dx T(x) k^r(x, \omega_n) \varphi(x, \omega_n) \phi_n''(x)^2}{\int_0^L dx k^r(x, \omega_n) \varphi(x, \omega_n) \phi_n''(x)^2} \\ &\approx T^{\text{min}} + \frac{\int_0^L dx \Delta T(x) \varphi_n(x) \phi_n''(x)^2}{\int_0^L dx \varphi_n(x) \phi_n''(x)^2} \end{aligned} \quad (3.18)$$

where we suppose that the real part of the stiffness is independent of x . Indeed, this is simply the mass times the square of the resonance frequency, which changes range around the percent. We then define $\varphi(x, \omega_n) \equiv \varphi_n(x)$. The measured loss angle corresponds to the quantity at the denominator:

$$\varphi_n(\Delta T) = \frac{1}{L} \int_0^L dx \varphi_n(\Delta T(x)) \phi_n''(x)^2 \quad (3.19)$$

As mentioned, we suppose that the dissipation is distributed along the cantilever, which results in the loss angle being influenced by the increase in temperature. This is due to the presence of the amorphous coating, which has significant internal friction [71, 70]. In this case, we can express the local dissipation as a local loss angle $\varphi(x)$, the form of which is unknown. Since we observe a quadratic dependency of $\varphi_n(\Delta T)$, and the temperature profile can be considered linear, it comes naturally to suppose a quadratic dependency also for $\varphi(x)$:

$$\begin{aligned} \varphi(x) &= \varphi_0 + \alpha \Delta T(x) + \beta \Delta T(x)^2 \\ &= \varphi_0 + \alpha \Delta T^{\text{max}} x + \beta (\Delta T^{\text{max}})^2 x^2 \end{aligned} \quad (3.20)$$

where φ_0 is the equilibrium value of the loss angle at T^{min} and the temperature difference is $\Delta T(x) = \Delta T^{\text{max}} x$ for a linear profile. In this case, thanks to eq. 3.19, we can retrieve the coefficients φ_0, α, β as a function of the experimental a_n, b_n, c_n of eq. 3.17:

$$a_n = \varphi_0 \frac{1}{L} \int_0^L dx \phi_n''(x) \quad b_n = \alpha \frac{1}{L} \int_0^L dx x \phi_n''(x) \quad c_n = \beta \frac{1}{L} \int_0^L dx x^2 \phi_n''(x) \quad (3.21)$$

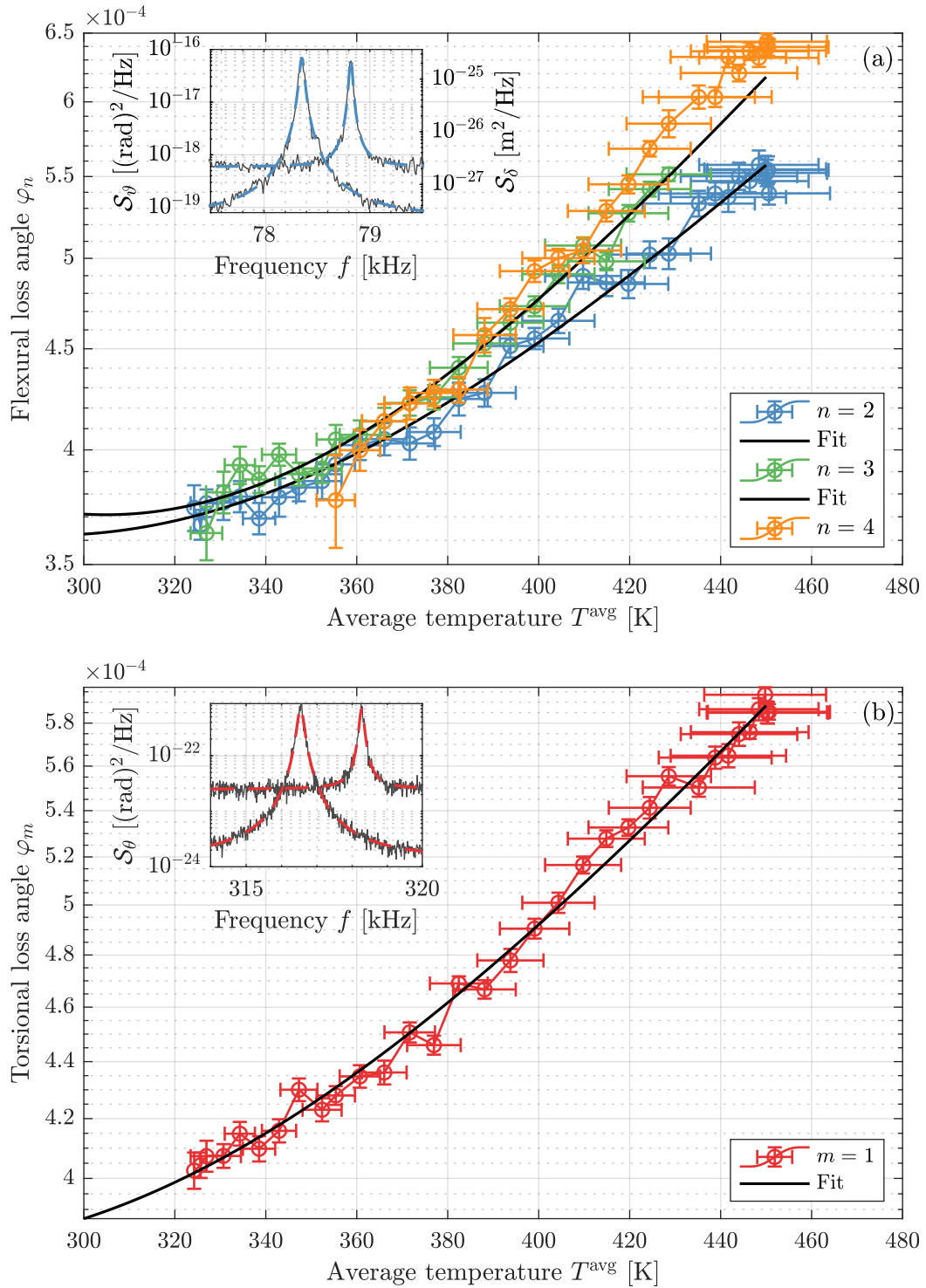


FIGURE 3.4.5: In (a) we report the flexural loss angles φ_n with respect to the average temperature of the system. In general, φ_n increases of about 50 % with T^{avg} rising less than 150 K from room temperature. We note how a second-order polynomial smoothly fits the experimental data for $n = 2, 3$, with $n = 4$ not being considered due to the lack of points close to equilibrium. From these fits, we extract the coefficients used in eq. 3.17. In the inset, we show an in and out-of-equilibrium spectrum of the second mode, with the former at a higher frequency than the latter. From this, we can visually evince how the dissipation process indeed changes with ΔT increasing. In (b), we show the torsional mode loss angle φ_m , which appears to experience a similar 50 % increase. Also in this case, we perform a quadratic fit of the data. Finally, in the inset, we show the equilibrium (higher frequency) and a NESS (lower frequency) spectrum.

In this case, we can express eq. 3.18 as:

$$\begin{aligned}
 T_n^{\text{fluc}} &= T^{\text{min}} + \Delta T^{\text{max}} \frac{\frac{1}{L} \int_0^L dx x (\varphi_0 + \alpha \Delta T^{\text{max}} x + \beta (\Delta T^{\text{max}})^2 x^2) \phi_n''(x)^2}{a_n + b_n \Delta T^{\text{max}} + c_n (\Delta T^{\text{max}})^2} \\
 &= T^{\text{min}} + \Delta T^{\text{max}} \frac{a_n \frac{\int_0^L dx x \phi_n''(x)^2}{\int_0^L dx \phi_n''(x)^2} + b_n \Delta T^{\text{max}} \frac{\int_0^L dx x^2 \phi_n''(x)^2}{\int_0^L dx x \phi_n''(x)^2} + c_n (\Delta T^{\text{max}})^2 \frac{\int_0^L dx x^3 \phi_n''(x)^2}{\int_0^L dx x^2 \phi_n''(x)^2}}{a_n + b_n \Delta T^{\text{max}} + c_n (\Delta T^{\text{max}})^2} \quad (3.22)
 \end{aligned}$$

and we define the theoretical prediction for the fluctuation temperature T^{theo} :

$$T_n^{\text{theo}} = T^{\text{min}} + \iota_n (\Delta T^{\text{max}}) \Delta T^{\text{max}} \quad (3.23)$$

The function ι_n can be understood as follows: if, for certain parameters a_n, b_n, c_n and ΔT^{max} , $\iota_n \leq 0.5$ the theoretical fluctuation temperature is comparable or lower than the average one: $T^{\text{avg}} = T^{\text{min}} + \Delta T^{\text{max}}/2$. Otherwise, the system experiences an excess of fluctuations. It is clear that this procedure can be swiftly extended to the torsional modes, since the T_m^{fluc} can also be expressed with a similar version of eq. 3.18.

We report the comparison between T^{theo} and the measured T^{fluc} in fig. 3.4.6, where we take into consideration only modes $n = 2, 3$ and $m = 1$. For $n = 2$, the theoretical prediction yields a $T_2^{\text{theo}} \lesssim T^{\text{avg}}$, which T_2^{fluc} follows for low $T^{\text{avg}} \leq 400$ K but becomes less accurate at higher values, also due to the pollution of the self-oscillations. Similarly, mode $n = 3$ shows a good agreement (within the error bars) with T^{theo} until the same T^{avg} , then a sudden increase and decrease of the fluctuation temperature hinders a further verification of the theoretical prediction. Finally, the torsional mode $m = 1$ shows different results with respect to the theoretical prediction, which forecasts $T_1^{\text{theo}} < T^{\text{avg}}$. Nonetheless, the prediction correctly describes an increase in the fluctuations with the average temperature.

Let us discuss the possible origins of the slight disagreements between the proposed model and the results at $T^{\text{avg}} \geq 400$ K. As mentioned, self-oscillations hinder a precise verification of the model, due to the oscillations they prompt in the measured T^{fluc} . This may not be the only cause, however. Indeed, at $T^{\text{avg}} = 400$ K, deviations may be due to the loss of the validity of the hypothesis regarding the dependency of φ from the temperature and the position of the cantilever. In fact, a second-order polynomial may not be sufficiently accurate to account for the observed φ . Similarly, the temperature profile slowly departs from linearity when T^{avg} increases. Another concern at high temperatures is finally the absence of a run-time calibration. Indeed, as we show in Appendix 3.A, this effect leads to an underestimation of the fluctuation temperatures up to 20% at around 9 mW for a pure silicon sample, and the effect is unknown in a coated sample.

For typical fit parameters and ΔT , the function ι_n yields values < 0.5 for mode 1, around 0.5 for mode 2, and slowly increasing values for higher mode numbers until around 0.65. The reason for this is that since the dissipation is localised around the curvature of the cantilever (eq. 3.19), the temperature profile is more important in the region close to the origin for mode 1, in the first half for mode 2, and more and more distributed for higher modes. Since in our experiment mode 1 is corrupted, we can see this behavior in fig. 3 of ref. [42], where the fluctuation temperatures of the first three resonances of C30C qualitatively follow the behavior forecasted by our T^{theo} .

The main result of this section is that, with two simple quadratic approximations, we are able to satisfyingly construe the measured fluctuation temperatures of a cantilever with distributed dissipation with the retrieved loss angles. The theoretical framework developed

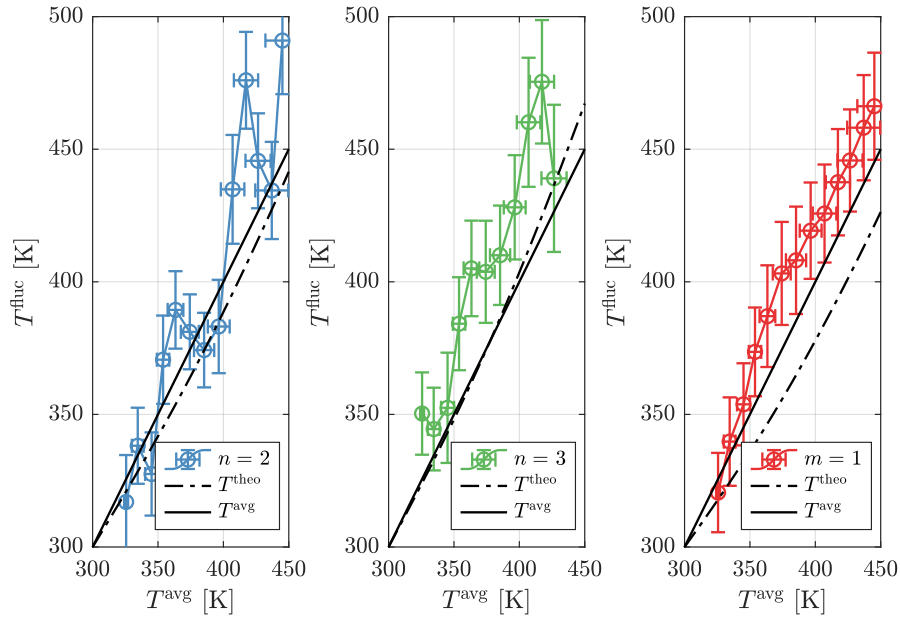


FIGURE 3.4.6: Fluctuation temperatures compared to the theoretical prediction of eq. 3.23. The second flexural resonance shows comparable results between T_2^{fluc} and T^{theo} , with some deviations occurring around $T^{\text{avg}} = 400$ K. It is interesting to note that T_2^{theo} is supposed to be *lower* than the average temperature, so that $\iota_2 < 0.5$. The $n = 3$ mode is similarly in agreement with the theoretical predictions, with the self-oscillations hindering a precise characterisation at high T^{avg} . In this case, ι_3 is lower than 0.5 for low T^{avg} as it surpasses this reference at $T^{\text{avg}} \approx 375$ K. Finally, the torsional fluctuations quite disagree with the forecasted T^{theo} . Indeed, we expect $T_1^{\text{fluc}} < T^{\text{avg}}$, yet the experimental measurements show the opposite behavior. Nonetheless, the deviation is small and T^{theo} still predicts an increase in fluctuations with the temperature. In all the figures, we show an average of the T^{fluc} in bins of 10 K, in order to increase the readability.

here allows us to decouple the measurement of fluctuations and the dissipation to test the validity of our extended version of the FDT, showing a remarkable agreement.

3.4.3 C30

In this section, we analyse the thermal noise measurements on a bare C30 cantilever. Our goal is to see whether the behavior of C30C discussed before is due to the coating, whether it is an intrinsic property of the substrate, or if both of these components contribute to the final result.

In this measurement, 20 laser powers between 0.8 – 9 mW in a double ramp are imposed near the tip of the cantilever, with 40 measurements per power step, which yields a total of 800 measured spectra. Also in this case, a run-time calibration is unfortunately not available; nevertheless, we use the one performed on the C100 as a reference. Two reasons lead us to this choice: firstly, C30 is a pure silicon cantilever just as C100 (with the same crystalline orientation), and secondly the experimental setup is unchanged between the two measurement sessions. Hence, as a first approximation, we can suppose that the power-dependency of the calibration coefficients of the photodiode are independent of any other factor. We record 5 flexural and 1 torsional modes, with the first deflection mode being plagued by self-oscillations and thus discarded.

Thermal fluctuations

The results of the thermal fluctuations are displayed in fig. 3.4.7. Most of the flexural modes increase with the average temperature of the cantilever, with mode $n = 3$ representing an exception. Indeed, this resonance seems less perturbed by the temperature difference than the other modes, the reason for which is unknown. On the other side, mode $n = 2$ shows a $T_2^{\text{fluc}} \lesssim T^{\text{avg}}$ as the higher modes are slightly above T^{avg} . Similarly, the torsional resonance grows close to the average temperature of the system.

We can compare these results with the ones of C30C (fig. 3.4.4). In general, the flexural and torsional resonances of C30 yield smaller values with respect to the ones of C30C for similar T^{avg} . This effect may be further amplified by the corrections to the calibration coefficients for C30C, which may increase the values of T^{fluc} . In order to better construe these results, we discuss the measured loss angles.

Dissipation

The measured loss angles are reported in fig. 3.4.8. As we can notice, the flexural loss angles φ_n significantly vary with respect to the mode number, with the equilibrium value being around $\varphi_2 \approx 10^{-5}$ for mode 2 and around 2.7×10^{-5} for the higher modes. The temperature dependency is similar: all modes roughly triple their initial value at the highest $T^{\text{avg}} = 575$ K. As for the thermal fluctuations, mode 3 represents an exception, with its value increasing by more than 20 times. Since this mode shows bizarre behavior in both the fluctuations and dissipation, we do not discuss it further, as we believe that an external factor is influencing its behavior.

The torsional mode shows a novelty, which is that the loss angle *diminishes* with the temperature of the system increasing. Whilst this effect is minor (the relative change is at most of 30 %), it is interesting to notice how the dissipation process of this torsional mode is slightly less effective with T^{avg} increasing.

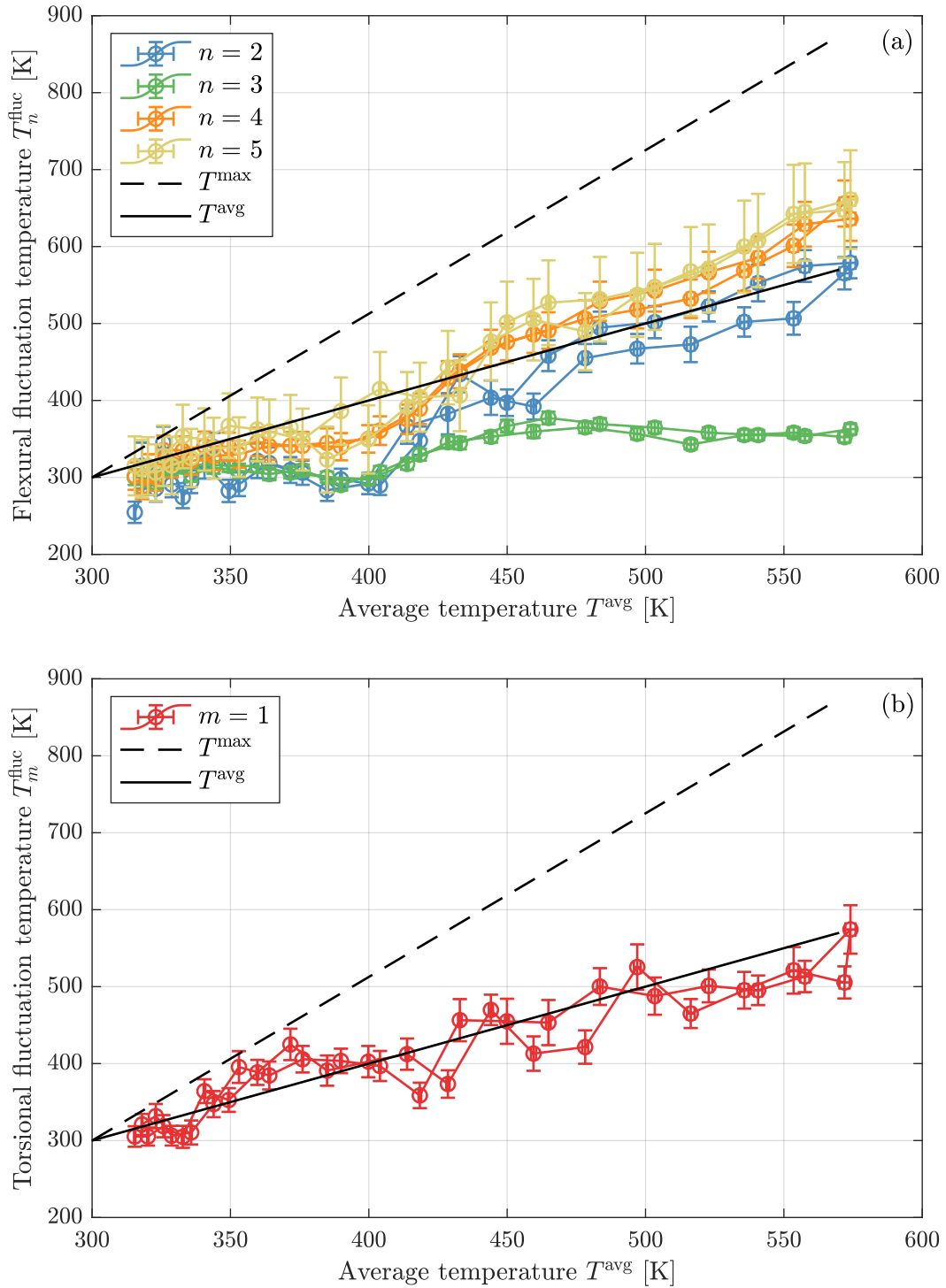


FIGURE 3.4.7: Fluctuation temperature vs. average temperature. In figure (a), the flexural T_n^{fluc} is shown with respect to T^{avg} . The black dashed line represents the maximum temperature T^{max} , and the solid one the average temperature T^{avg} . The fluctuation temperatures are close to this value for all but the third resonant mode. In this case, the fluctuations are in fact almost unchanged with T^{avg} increasing. Modes 4 and 5 become more important than T^{avg} at around 450 K. In (b), the first torsional resonance shows a similar behavior, overlapping T^{avg} .

We can again compare these results with the ones of the C30C sample. Let us start with the deflection. We note that the equilibrium values of φ_n for C30 are roughly 10 times less than the ones of C30C, showing how the coating greatly contributes to the dissipation in the system. Naturally, we cannot quantitatively compare these two results because it is not the same sample before and after coating, but it is nevertheless interesting to see how, whilst the coating is an extremely important source of damping, the bare cantilever still shows a dependency on ΔT .

Regarding the torsional mode, the initial loss angle is roughly 100 times lower than the loss angle of the coated sample, showing how the aforementioned effect of the coating is even more extreme in the present case. Whilst the diminishment of φ_m with the temperature is odd, it is clear that in this case the loss angle is also influenced by the temperature increase of the system. We discuss this in the next section.

Discussion

As in the C30C case, we fit the data with second order polynomials and calculate the theoretical fluctuation temperatures T^{theo} . The results are shown in fig. 3.4.9. Excluding a bump below the theoretical curves around $T^{\text{avg}} = 400$ K for modes $n = 2, 4$, the flexural resonances appear to be well explained by our model. In fact, the model correctly explains the near-equilibrium behavior of mode 2 and the $T^{\text{fluc}} > T^{\text{avg}}$ for mode 4 and 5. Similarly, the torsional mode is quite well represented by this description, where the diminishment of the loss angle (fig. 3.4.5) with the temperature is captured in the $T_1^{\text{theo}} < T^{\text{avg}}$. Also in this case, a bump at $T^{\text{avg}} = 400$ K yields a disagreement between the theoretical prediction and the measurements around this value.

Our conclusion for C30 is then that we have a system with spatially-extended damping, which can be well represented by our model. In addition, in fact, we can compare the fluctuation temperatures against the measured fluctuations, thus further assessing our claims on the theoretical shape of the non-equilibrium fluctuation temperatures. It is nevertheless important to remember that, in order to fully interpret the findings, a reason for the odd behavior of mode 3 and the torsional loss angle would be needed.

3.5 Conclusions

In this chapter, we have shown how we can measure the thermal fluctuations of a micro-cantilever subjected to a heat flux along its longitudinal dimension, thus in a NESS. Depending on the sample under consideration, we can create a large temperature difference between the tip and the clamped end ΔT , which represents the distance of our system from an equilibrium situation. When $\Delta T = 0$, we are in thermal equilibrium, and the EP prescribes the magnitude of the fluctuations of each observable of the cantilever: the normal modes. In this case, $T^{\text{fluc}} = T^{\text{min}}$.

When ΔT increases, the EP needs to be replaced by the extended version of the FDT presented in the previous chapter. In this version of the FDT, T^{fluc} is prescribed by the temperature profile $T(x)$ weighted by the local mechanical energy dissipation of the cantilever w^{diss} :

$$T^{\text{fluc}} = \frac{1}{L} \int_0^L dx T(x) w^{\text{diss}}(x) \quad (3.24)$$

Thus, T^{fluc} depends on where the dissipation is more prominent. In order to prove the validity of our approach, we measure the thermal fluctuations of three different cantilevers, each with its own geometry and characteristics. We summarise the results in fig. 3.5.1, where we

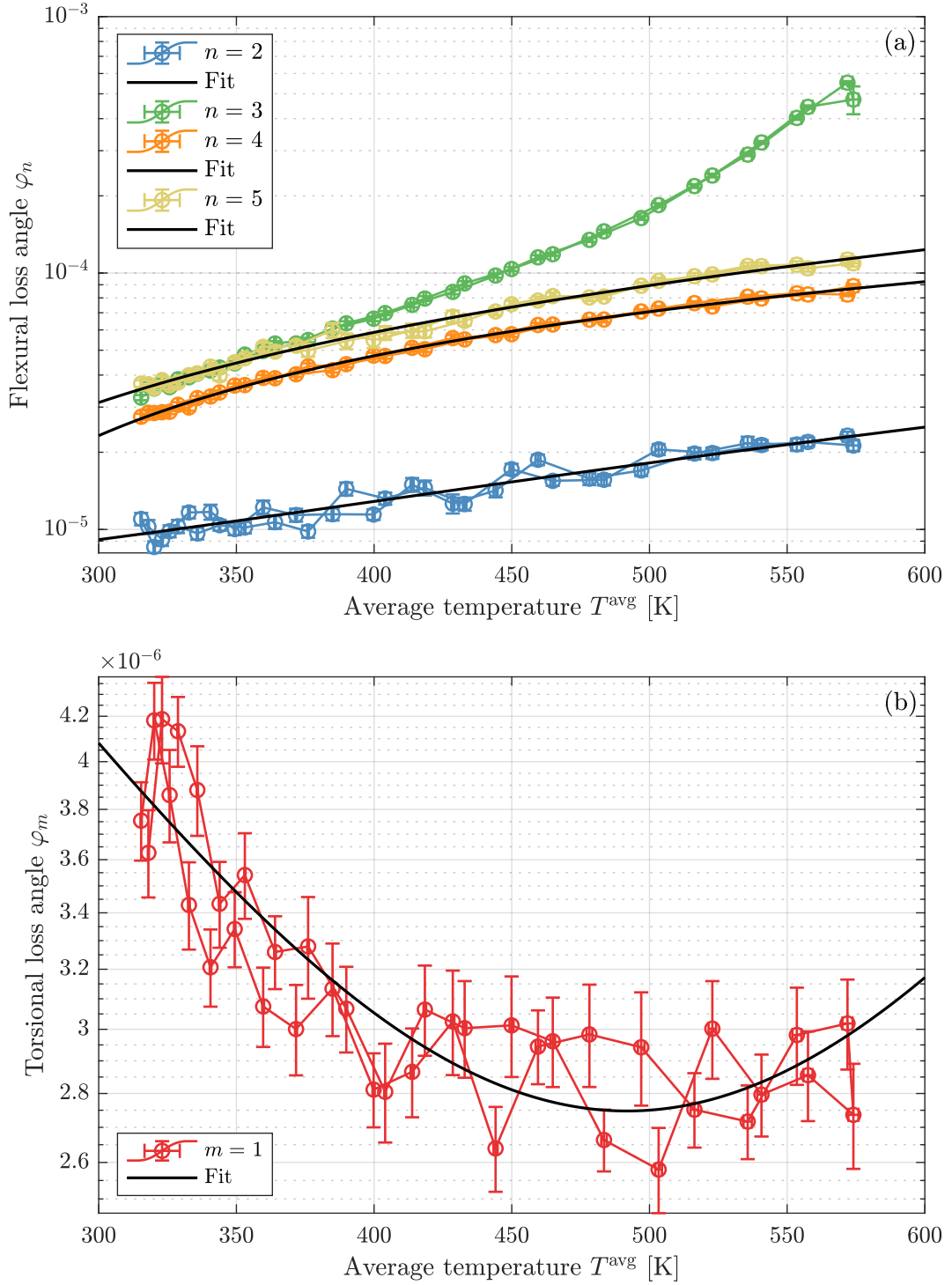


FIGURE 3.4.8: In (a), we show the evolution of the flexural loss angles φ_n with the average temperature of the system. Mode 2 has an equilibrium value around 9×10^{-6} , and it increases at about three times this value at the maximum average temperature explored, $T^{\text{avg}} = 575$ K. Similarly, modes 4 and 5 increase about 3 – 4 times in the same temperature range. We fit these curves following eq. 3.17. Mode 3 represents an exception, increasing more than 20 times from its initial value, the reason for which is not yet understood. In (b), the torsional mode is shown decreasing with increasing average temperature. Whilst the reason for this is still not totally understood, a parabolic fit still well represents the behavior of φ .

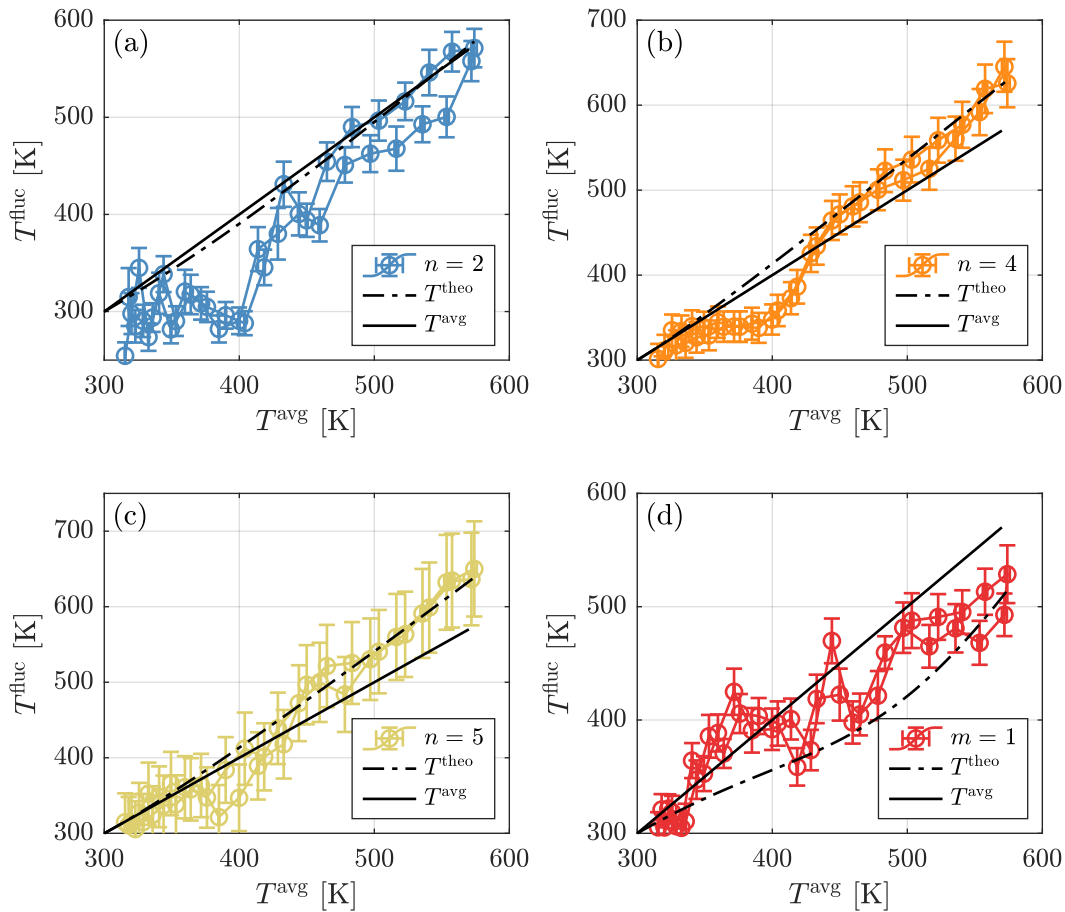


FIGURE 3.4.9: Measured fluctuation temperatures vs their theoretical prediction. In (a,b) we show how for the modes $n = 2, 4$ the T^{theo} appropriately overlaps with the experimental results, apart from a bump around $T^{\text{avg}} = 400$ K. In the first case, we expect a fluctuation temperature slightly below the average temperature, which is the case of the measured fluctuations; in the second, we anticipate higher fluctuations than T^{avg} , and again this is well represented by the measurement. In (c), mode $n = 5$ perfectly overlaps with the theoretical prediction, which dictates that $T^{\text{theo}} > T^{\text{avg}}$, also due to the significant uncertainties. Finally in (d), the theoretical prediction for the torsional mode matches quite well the experimental results after $T^{\text{avg}} = 400$ K.

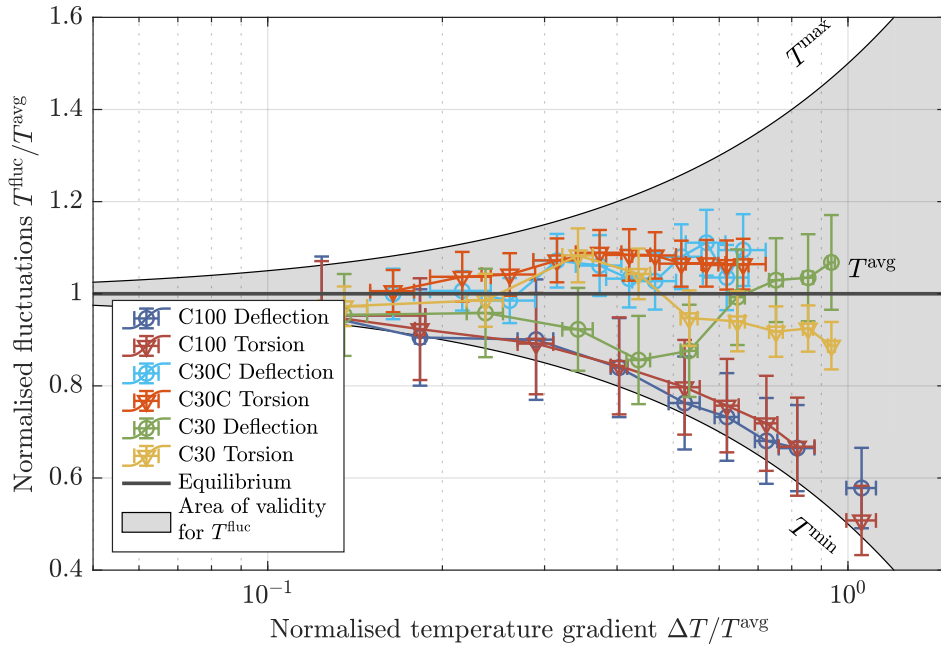


FIGURE 3.5.1: A plot summarising the fluctuations of the cantilevers explored in this chapter. The fluctuation temperature is depicted vs. the temperature difference with both quantities normalised by the average temperature, which is represented by the solid grey line. The grey-shaded area represents our theoretical model for T^{fluc} (eq. 2.81), which is between the minimal temperature of the system T^{min} (lower bound) and the maximal T^{max} (upper bound). We average the fluctuations over the modes not presenting issues (for example excluding mode $n = 3$ of C30) in order to show the global behavior of the sample. We note how the fluctuations of C100 (dark blue and red) are close to T^{min} , those of C30C (cyan and orange) are close but a little above T^{avg} , and those of C30 (green and yellow) show a more erratic behavior but stay close to T^{avg} as well.

show the fluctuation temperatures normalised by T^{avg} vs. the similarly normalised temperature difference for the three cantilevers.

The measurements on C100 show that the fluctuation temperature $T^{\text{fluc}} \approx T^{\text{min}}$ for all the explored temperatures. Furthermore, this behavior is identical for *all* the higher-energy resonances of the sample, showing how this is a universal feature. Our proposal for a non-equilibrium FDT (eq. 3.24) tells us that in order to explain this, dissipation must be located at the clamping end of the cantilever $w^{\text{diss}} = \delta^D(0)$, where $T(0) = T^{\text{min}}$. For this reason, we then expect the dissipation not to be modified by the increasing ΔT , which is the case of the measured loss angles. Indeed, all the resonances are roughly constant throughout the whole experiment. This confirms that we are able to correctly construe the experimental observations of this and the measurement in ref. [42].

The measurements on C30C illustrate a completely different situation: whilst the ΔT increases and the system is increasingly out of equilibrium, the T^{fluc} increase similarly to the average temperature of the system. Thus, always following eq. 3.24, we expect the dissipation to be spread along the cantilever, since the fluctuation temperature resembles the average one. Indeed, the coating distributes the dissipation over the whole length of the cantilever. The measured loss angles confirm this, showing a clear dependency on ΔT . In order to be quantitative, we fit the loss angles and develop a simple model with which to explain the observed fluctuations based on the measured dissipation. Albeit the uncertainties regarding the validity of the hypothesis underlying the model and the self-oscillations polluting the observed T^{fluc} , our description satisfyingly captures the observed behavior

of the fluctuations. Therefore, we are able to verify our extension of the FDT in a system dominated by an unlocalised dissipation, showing how we can not only prove T^{fluc} to be bounded by the borders prescribed by the extension (T^{min} and T^{max}) but also that we can quantitatively predict their value.

The measurements on C30 further assess the previously-developed description. In this case, we ask ourselves whether the behavior of C30C is solely due to the presence of the coating, or if its substrate plays an important role too. As shown, a pure silicon cantilever can present fluctuations that depend on the ΔT , and thus a distributed dissipation. In this case, we show that we are again able to interpret the observed T^{fluc} with the measured loss angles through a parabolic approximation of the dissipation. Whilst the loss angles are much lower with respect to the C30C case, they increase with the ΔT , showing how the *geometry* of the sample can prescribe its fluctuations. Indeed, the C100 and C30 cases are only different for the shape and the manufacturer, being both coatless silicon cantilevers. In this case, it is natural to conclude that C30 presents more defects along its length than C100, the reason for which is possibly that the fabrication techniques are different, and the manufacture of C30 prompts a higher concentration of defects along the cantilever, or a lower concentration at the origin.

To summarise, we believe that we have successfully demonstrated that the extended FDT for out-of-equilibrium systems appropriately explains the three samples presented in this chapter. We then believe that our results have a broad range of applications, owing to the generality of the underlying method. From a manufacturing point of view, we know that normally thermal fluctuations depend on the temperature of the system and therefore, as usual, in order to fabricate a low-noise instrument, it is best to place it at the lowest possible temperature. Our study shows that in the case of a system with highly localised dissipation, it is best to place the high-dissipative parts of it at the lowest available temperature, whereas this constraint can be relaxed for the rest of the system. This possibly simplifies the design of the system which does not need to be kept at a single low temperature. Conversely, a system presenting a distributed dissipation may show higher or lower fluctuations with respect to equilibrium depending on the resonance mode we are interested in and the temperature difference. Indeed, in the case of the cantilever, the first (and the most energetic) mode is less sensitive to the highest temperatures with respect to the higher ones. This may help manufacturers forecast the noise of a non-equilibrium system based on measurements of its dissipation.

From an experimental characterisation point of view, the tools developed in this chapter can be useful in various contexts. For example, noise in nano-mechanical resonators [27] can be predicted when a temperature gradient is present along their length; Johnson noise in non equilibrium samples [10, 79] can be probed and interpreted; the quest for ultra-stable oscillators with cryogenic quartz micro resonators [17] can be facilitated. One of the most straightforward applications is naturally GWs detectors, with the suspension system of the test masses being subjected to a temperature gradient. In this case, the characterisation (and lowering) of thermal noise is paramount [53]. Thus, the non-equilibrium effects that a ΔT may prompt need to be carefully studied. In this chapter, we show how, depending on where the dissipation is located, we do not expect the thermal noise to be much higher than the average temperature of the system, which shows that in the best case scenario (clamping losses at the lowest temperature) the suspension system may be insensitive to the ΔT . Finally, from a theoretical point of view, experiments such as the one described in this chapter are necessary to test the validity of the latest theoretical predictions regarding fluctuation theorems and the relative inequalities [55].

Appendix

3.A Calibration

In this section, we discuss into details how to retrieve the deflection and the torsion of the cantilever from the signals recorded by the photodiode.

Once the laser probe is shined on the surface of the cantilever, it is reflected back to the system with an angle proportional to the slope of the cantilever. As mentioned, we divide this angle in a flexural component ϑ and a torsional one θ . In the next section we show how to retrieve these two quantities, whilst in the following one we present how to convert ϑ into the vertical deflection δ , in meters. We report in fig. 3.A.1 a simplified version of the experimental setup which depicts the quantities involved.

3.A.1 Photodetector

The incoming beam enters the vacuum chamber through a lens CL, which directs the probe towards the cantilever placed at the focal point at distance f_{CL} . Upon reflection, the beam is deviated with an angle double than the slope of the cantilever at the probing point x_0 . The beam, after passing through the lens, is shifted in the $x - y$ plane of:

$$X = 2f_{CL}\vartheta^{\text{meas}} \quad Y = 2f_{CL}\theta^{\text{meas}} \quad (3.25)$$

with X, Y corresponding to the distance from the center of the photodiode, supposing that the beam is in average centered with the sensor. Each quadrant records an incoming power, namely A, B, C, D (top left, top right, bottom left, and bottom right, respectively), from which we evaluate two contrasts:

$$\begin{aligned} C_x &= \frac{(A + C) - (B + D)}{A + B + C + D} \\ C_y &= \frac{(A + B) - (C + D)}{A + B + C + D} \end{aligned} \quad (3.26)$$

These quantities are dimensionless (due to the normalisation) and they are proportional to the spot position (X, Y) on the photodiode for small displacements. Let us imagine that the beam has an irradiance profile at the photodiode in the form:

$$I(X, Y) = I_0 e^{-2(X^2/R_x^2 + Y^2/R_y^2)} \quad (3.27)$$

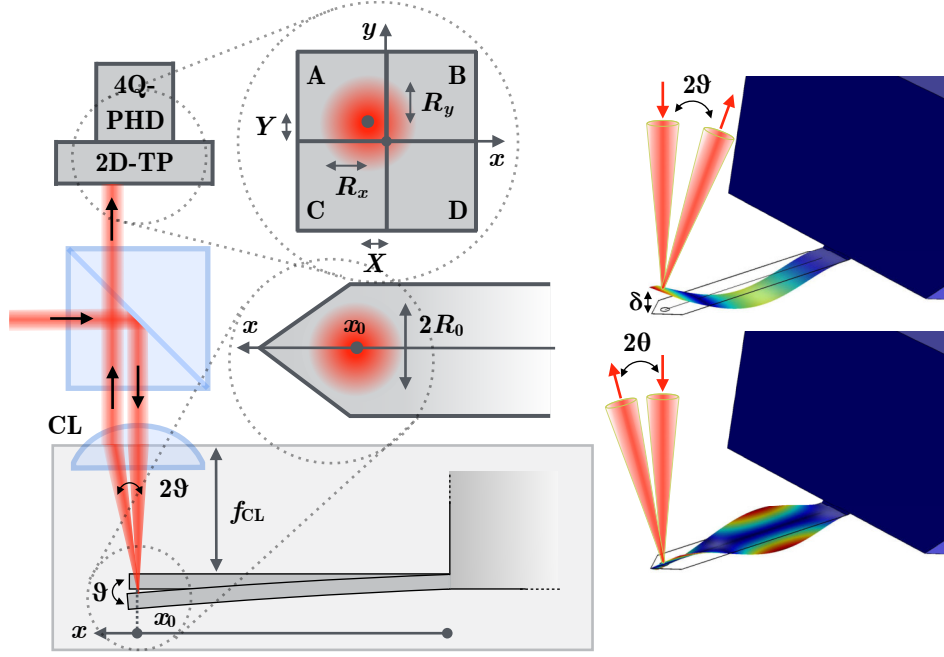


FIGURE 3.A.1: Simplified experimental setup. The probing beam enters the system and it is focused towards the cantilever in the point x_0 with a waist beam radius R_0 . The displacements of the cantilever can be divided in the flexural angle ϑ (proportional to the vertical deflection δ) and the torsional angle θ , such that the beam is reflected back to the focusing lens with the double of this angle. The light then travels towards the photodiode, shining the sensor in the position X, Y , with these quantities proportional to the displacement angles. The radii of this beam are R_x and R_y , in the respective directions.

with $R_{x,y}$ the $1/e^2$ radius of the beam in the respective direction. In this case it is easy to show that:

$$\begin{aligned} C_x &= \text{erf} \left(\frac{\sqrt{2}X}{R_x} \right) \approx \frac{\sqrt{2}X}{R_x} \\ C_y &= \text{erf} \left(\frac{\sqrt{2}Y}{R_y} \right) \approx \frac{\sqrt{2}Y}{R_y} \end{aligned} \quad (3.28)$$

where the approximation is valid for small displacements around the center of the photodiode $X, Y = 0$, i.e. $X, Y \ll R_x, R_y$. In order to retrieve $R_{x,y}$ and thus being able to calibrate the system, we use the 2D translation platform housing the photodetector: keeping fixed the laser beam on the cantilever, we shift the sensor origin and record C_x for a few values of X around 0, then perform a linear fit and directly extract ω_x from the slope. The same is then done in the Y direction, before the photodiode is displaced back to its origin position. As mentioned, this procedure is repeated every time the conditions of the system change, which is mostly due to the heating laser power being modified. Since the calibration coefficients are then experimentally measured, this grants us that we are not introducing a bias in quantifying the displacement of the cantilever. Furthermore, we can account for possible deviations from a gaussian beam.

In fig. 3.A.2 we show an example of measuring the calibration coefficients in an in and out of equilibrium case during the C100 experiment. In addition to this, we show the relative difference of the calibration factors at different powers R/R_{EQ} . This represents how the radii $R_{x,y}$ change from a measurement with low injected power on the cantilever ($P \leq 1$ mW) to

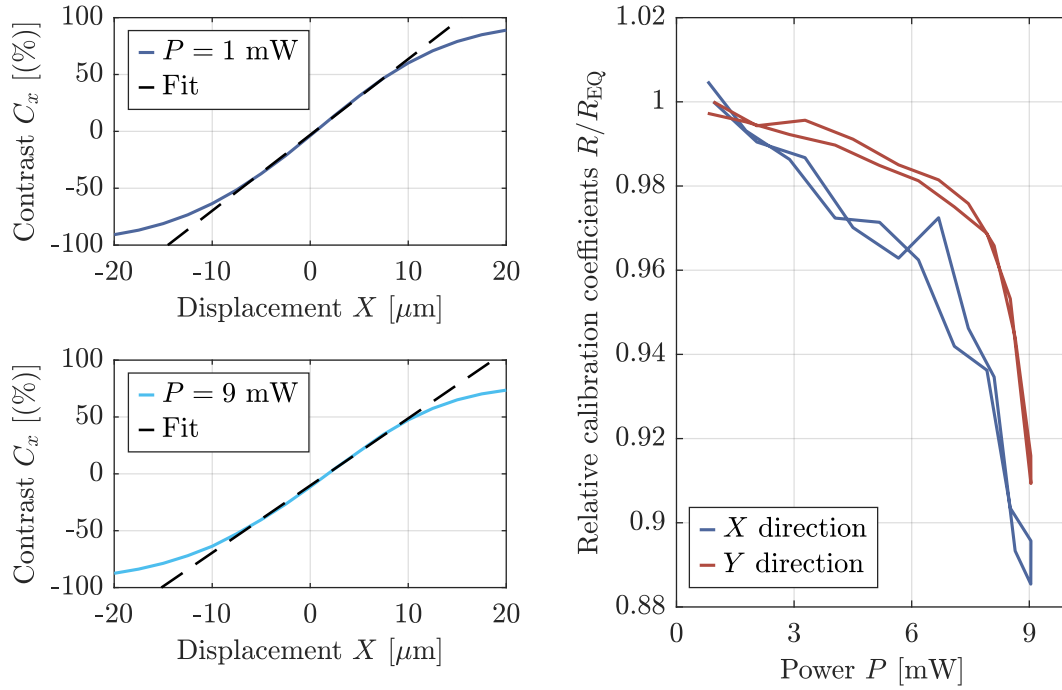


FIGURE 3.A.2: Calibration of the photodiode. In the left panels we show the curves retrieved from moving the sensor through the 2D-TP in the x direction of known steps and measuring the contrast C_x , for an in and out-of-equilibrium case. A linear fit in the region close to $X = 0$ gives us the calibration factor R_x . The same procedure is followed in the y direction, giving R_y . In the right panel, we show the change of these with the laser power with respect to the initial value: at $P = 9 \text{ mW}$, R_x, R_y can be more than 12 % lower than their low power values.

the maximal power, in this case 9 mW. We can see that the radii vary up to 12 %, which results in a 22 % when we consider the thermal fluctuations (which are proportional to the square of the displacement). We can therefore see the importance of a run-time calibration, which ensures that we do not introduce a bias in calibrating the displacements due to the response of the photodiode. Finally, the uncertainty around $R_{X,Y}$ is less than 0.1 % for all the experiments presented in this chapter.

Eventually, we can write:

$$\begin{aligned} \vartheta^{\text{meas}} &= \frac{R_x C_x}{2\sqrt{2}f_{\text{CL}}} \\ \theta^{\text{meas}} &= \frac{R_y C_y}{2\sqrt{2}f_{\text{CL}}} \end{aligned} \quad (3.29)$$

which allows us to retrieve the angles from the measured contrasts $C_{x,y}$ and the relative calibration factors $R_{x,y}$.

3.A.2 Laser spot influence

The thus retrieved angles of the slopes of the cantilever depend on where the laser probes the sample, i.e. the point x_0 , and the resonance mode considered. It is customary to quantify the displacements at the free end of the cantilever $x = L$, thus we can write:

$$\delta_n \equiv \delta_n(x = L) \quad \theta_m \equiv \theta_m(x = L) \quad (3.30)$$

with δ_n measured in meters and θ_m in radians. In order to convert the measured angles to the desired displacement we define the sensitivities:

$$\begin{aligned}\vartheta_n^{\text{meas}}(x_0) &= \sigma_n^\delta(x_0)\delta_n \\ \theta_m^{\text{meas}}(x_0) &= \sigma_m^\theta(x_0)\theta_m\end{aligned}\quad (3.31)$$

We can now distinguish two cases: if the spot size R_0 on the cantilever is much smaller than the typical spatial period of the resonance mode considered, we can suppose that it is point-like and thus the beam probes a single point on the cantilever. In this case, the sensitivity is simply linked to the mode shape:

$$\begin{aligned}\sigma_n^\delta(x_0) &= \frac{1}{\phi_n(L)} \frac{d\phi_n}{dx}(x_0) \\ \sigma_m^\theta(x_0) &= \frac{1}{\phi_m(L)} \phi_m(x_0)\end{aligned}\quad (3.32)$$

such that the calibrated displacements are:

$$\begin{aligned}\delta_n &= \frac{R_x}{2\sqrt{2}f_{\text{CL}}\sigma_n^\delta(x_0)} C_x \\ \theta_n &= \frac{R_y}{2\sqrt{2}f_{\text{CL}}\sigma_n^\theta(x_0)} C_y\end{aligned}\quad (3.33)$$

Conversely, if the laser spot is comparable or larger than the aforementioned length, the laser shines an area where the slope of the mode changes sensibly. We report an example in fig. 3.A.3, where we show how a beam with radius $R_0 = L/10$ probes a surface with a roughly constant slope for mode 2, for which the previous approximation may be considered valid. On the other side for mode 4 we get to the limits of this description, which definitely fails for $n = 8$. Furthermore, it is evident that this classification depends on x_0 . In this cases, we need a description which takes into account the radius of the probing beam, R_0 .

3.A.3 Large spot case

In the following calculation we follow Schäffer [95]. Referring to fig. 3.A.1, the contrasts C_x and C_y are calculated as the difference of irradiance collected by the sectors of the photodiodes in the x and y directions, as reported in eq. 3.28. We start describing the beam before being collimated on the cantilever by the lens CL. We define its irradiance profile:

$$I(x, y) = I_0 e^{-2\frac{x^2+y^2}{R_0^2}} \quad I_0 = \frac{2}{\pi R_0^2} P \quad (3.34)$$

with P the power of the laser. The electric field associated to this is:

$$E(x, y) = E_0 e^{-\frac{x^2+y^2}{R_0^2}} \quad E_0 = \sqrt{I_0} \quad (3.35)$$

Once the beam is focused on the cantilever on the point x_0, y_0 (respectively along the longitudinal and transverse directions) and is reflected back to the sensor, it travels an additional distance $2h(x, y)$ due to the displacement of the cantilever. If this is small, we can express the electric field on the photodiode through the diffraction integral [95]:

$$E_s(X, Y) = \frac{k}{2\pi f_{\text{CL}}} \int_0^L dx \int_0^B dy E(x - x_0, y - y_0) e^{2ikh(x, y)} e^{-ikxX/f_{\text{CL}}} e^{-ikyY/f_{\text{CL}}} \quad (3.36)$$

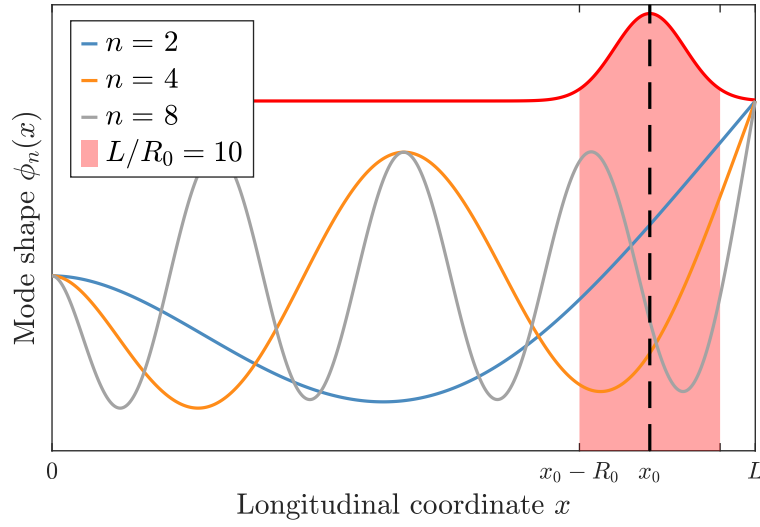


FIGURE 3.A.3: Three different situations for a sensing beam with a waist radius 10 times smaller than the length of the cantilever. For $n = 2$, the beam probes a zone with roughly the same slope, thus it could be considered as point-like and eq. 3.32 is valid in evaluating the sensitivity. For $n = 4$ we are in the limit case, where the beam covers a node of the mode, and for $n = 8$ the beam covers almost a whole spatial period. In these cases, Schäffer's description must be used.

with $k = 2\pi/\lambda$, λ the wavelength of the laser and X, Y the coordinates on the sensor. Taking quadrant A as an example, the irradiance collected is:

$$A = \int_{-a}^0 dX \int_0^a dY |E_s(X, Y)|^2 \quad (3.37)$$

with a the side of the photodiode. If the radii of the laser beam on the photodiode $R_x, R_y \ll a$, we can suppose $a \approx \infty$. Then, we can retrieve the contrasts C_x, C_y , as the difference and sum of signals expressed as eq. 3.37. We start from C_x .

Deflection

Referring to fig. 3.A.1, C_x is the difference between the left and right quadrants, divided by the sum of all four of them. Referring to this difference as D_x , this is:

$$D_x = \left(\frac{k}{2\pi f_{CL}} \right)^2 \int_0^L dx \int_0^L dx' \int_0^B dy \int_0^B dy' E(x, y) E(x', y') e^{2ik(h(x, y) - h(x', y'))} \times \left(\int_0^{+\infty} - \int_{-\infty}^0 \right) dX e^{-ikX(x-x')/f_{CL}} \int_{-\infty}^{+\infty} dY e^{-ikY(y-y')/f_{CL}} \quad (3.38)$$

where to lighten the notation we drop the dependency of the electric fields on x_0, y_0 . The integral over X yields a Cauchy principal part (PP) and the one over Y is a Dirac's delta:

$$\begin{aligned} \left(\int_0^{+\infty} - \int_{-\infty}^0 \right) dX e^{-ikX(x-x')/f_{CL}} &= -\frac{f_{CL}}{k} \text{PP} \frac{2i}{x-x'} \\ \int_{-\infty}^{+\infty} dY e^{-ikY(y-y')/f_{CL}} &= \frac{f_{CL}}{k} 2\pi \delta^D(y-y') \end{aligned} \quad (3.39)$$

Furthermore, for small displacements we can write:

$$e^{2ik(h(x,y)-h(x',y'))} \approx 1 + 2ik(h(x,y) - h(x',y')) \quad (3.40)$$

In this case D_x reads:

$$\begin{aligned} D_x &= \frac{1}{i\pi} \text{PP} \int_0^L dx \int_0^L dx' \int_0^B dy \int_0^B dy' E(x,y) E(x',y') \frac{1 + 2ik(h(x,y) - h(x',y'))}{x - x'} \delta^D(y - y') \\ &= \frac{4}{\lambda} \int_0^L dx \int_0^L dx' \int_0^B dy E(x,y) E(x',y) \frac{h(x,y) - h(x',y)}{x - x'} \end{aligned} \quad (3.41)$$

since the 0th order is zero due to the integrand being antisymmetric with respect to x and x' . Also, the principal part of the integral is dropped since the integrand is not singular in $x = x'$. Now, the flexural displacement for the mode n is:

$$h(x,y) = \delta_n \frac{\phi_n(x)}{\phi_n(L)} \quad (3.42)$$

so that finally:

$$D_x = \delta_n \frac{4}{\lambda \phi_n(L)} \int_0^L dx \int_0^L dx' \int_0^B dy E(x,y) E(x',y) \frac{\phi_n(x) - \phi_n(x')}{x - x'} \quad (3.43)$$

Similarly, the sum of all the photodiodes S can be deduced from eq. 3.38:

$$\begin{aligned} S &= \left(\frac{k}{2\pi f_{CL}} \right)^2 \int_0^L dx \int_0^L dx' \int_0^B dy \int_0^B dy' E(x,y) E(x',y') e^{2ik(h(x,y)-h(x',y'))} \\ &\quad \times \int_{-\infty}^{+\infty} dX e^{-ikX(x-x')/f_{CL}} \int_{-\infty}^{+\infty} dY e^{-ikY(y-y')/f_{CL}} \end{aligned} \quad (3.44)$$

which, expressing the Delta functions, simplifies:

$$\begin{aligned} S &= \int_0^L dx \int_0^L dx' \int_0^B dy \int_0^B dy' E(x,y) E(x',y') (1 + 2ik(h(x,y) - h(x',y')) \delta^D(y - y')) \delta^D(x - x') \\ &= \int_0^L dx \int_0^B dy |E(x,y)|^2 \end{aligned} \quad (3.45)$$

From eq.s 3.43 and 3.45 it is then possible to express the contrast $C_x = D_x/S$:

$$\begin{aligned} C_x &= \delta_n \frac{1}{\phi_n(L)} \frac{4f_{CL} R_0}{\pi R_x} \frac{\int_0^L dx \int_0^L dx' \int_0^B dy E(x,y) E(x',y) \frac{\phi_n(x) - \phi_n(x')}{x - x'}}{\int_0^L dx \int_0^B dy |E(x,y)|^2} \\ &= \delta_n \frac{2\sqrt{2}f_{CL}}{R_x} \sigma_n^\delta(x_0, R_0) \end{aligned} \quad (3.46)$$

expressing the spot size on the detector $R_x = \lambda f_{CL}/(\pi R_0)$ and thus defining the flexural sensitivity as:

$$\sigma_n^\delta(x_0, R_0) \equiv \frac{R_0}{\sqrt{2}\pi} \frac{1}{\phi_n(L)} \frac{\int_0^L dx \int_0^L dx' \int_0^B dy E(x,y) E(x',y) \frac{\phi_n(x) - \phi_n(x')}{x - x'}}{\int_0^L dx \int_0^B dy |E(x,y)|^2} \quad (3.47)$$

where the dependency on the spot position on the cantilever and the radius are embedded in the electric field. Using this definition, we can express the calibrated amplitude of fluctuations as:

$$\delta_n = \frac{R_x}{2\sqrt{2}f_{\text{CL}}\sigma_n^\delta(x_0, R_0)} C_x \quad (3.48)$$

in the same form of eq. 3.33.

Torsion

In order to retrieve the torsional sensitivity we perform the same analysis exchanging $X \Leftrightarrow Y$ and considering the displacement h to be:

$$h(x, y) = \theta_m \frac{\phi_m(x)y}{\phi_m(L)} \quad (3.49)$$

The difference of the upper and lower photodiodes then yields:

$$D_y = \theta_m \frac{4}{\lambda \phi_m(L)} \int_0^L dx \phi_m(x) \left| \int_0^B dy E(x, y) \right|^2 \quad (3.50)$$

and the contrast $C_y = D_y/S$:

$$C_y = \theta_m \frac{2\sqrt{2}f_{\text{CL}}}{R_y} \sigma_m^\theta(x_0, R_0) \quad (3.51)$$

In this case the torsional sensitivity is defined as:

$$\sigma_m^\theta(x_0, R_0) \equiv \frac{R_0}{\sqrt{2}\pi} \frac{1}{\phi_m(L)} \frac{\int_0^L dx \phi_m(x) \left| \int_0^B dy E(x, y) \right|^2}{\int_0^L dx \int_0^B dy |E(x, y)|^2} \quad (3.52)$$

so that the amplitude of the fluctuations is:

$$\theta_m = \frac{R_y}{2\sqrt{2}f_{\text{CL}}\sigma_m^\theta(x_0, R_0)} C_y \quad (3.53)$$

We note that in both flexural and torsional cases, the lateral position does not play a role in the sensitivities. In fact, the deflection does not depend on y_0 and the torsion is linearly dependent on y , hence y_0 (given that it is taken far from the boundaries of the cantilever) is irrelevant on the final result.

In order to express the calibration factors we now need to estimate x_0 and R_0 . These can be often guessed from camera observations, nonetheless in the next section we show how to retrieve these as a post-processing of the experimental data.

3.A.4 Estimation of x_0 and R_0

Eq. 3.31 links the experimentally observed angles to the actual displacements of the cantilever δ_n, θ_n . When the system is in thermal equilibrium at temperature T^{\min} , the EP states:

$$\begin{aligned}\langle (\vartheta_n^{\text{meas}})^2 \rangle &= \sigma_n^\delta(x_0, R_0)^2 \langle \delta_n^2 \rangle = \sigma_n^\delta(x_0, R_0)^2 \frac{k_B T^{\min}}{m \omega_n^2} \\ \langle (\theta_m^{\text{meas}})^2 \rangle &= \sigma_m^\theta(x_0, R_0)^2 \langle \theta_m^2 \rangle = \sigma_m^\theta(x_0, R_0)^2 \frac{k_B T^{\min}}{I \omega_m^2}\end{aligned}\quad (3.54)$$

A single position and beam radius $x_0^{\text{EQ}}, R_0^{\text{EQ}}$ should exist where the quantities η_n, η_m :

$$\begin{aligned}\eta_n(x_0, R_0) &\equiv \frac{\omega_n^2 \langle (\vartheta_n^{\text{meas}})^2 \rangle}{\sigma_n^\delta(x_0, R_0)^2} = \frac{k_B T^{\min}}{m} \\ \eta_m(x_0, R_0) &\equiv \frac{\omega_m^2 \langle (\theta_m^{\text{meas}})^2 \rangle}{\sigma_m^\theta(x_0, R_0)^2} = \frac{k_B T^{\min}}{I}\end{aligned}\quad (3.55)$$

are independent of n, m for all measurements: $\eta_n = \eta^\delta$ and $\eta_m = \eta^\theta$. In figure fig. 3.A.4 we show the functions $\eta_{n,m}$ in the C100 experiment for various x_0 , displaying how these functions overlap in a certain value of x_0 . Let us first consider the flexural modes, the extension for the torsional ones being straightforward. We calculate the error estimator as:

$$\epsilon(x_0) = \frac{\text{std}(\eta_n(x_0))}{\bar{\eta}_n(x_0)}, \quad \forall x_0 \quad (3.56)$$

where the bar indicates the average over n . The minimum of ϵ indicates the probing point with less dispersion between the modes, and thus the most probable value of $x_0 = x_0^{\text{EQ}}$. We can also calculate the effective mass of each mode m^{eff} :

$$m_n^{\text{eff}} = \frac{k_B T^{\min}}{\langle (\vartheta_n^{\text{meas}})^2 \rangle \omega_n^2} \Leftrightarrow m_n^{\text{eff}} = \frac{m}{\sigma_n^\delta(x_0, R_0)^2} \quad (3.57)$$

which represents the distance of the measured fluctuations times the square of the resonance frequency from its "ideal" value set by the sensitivity. In order to better depict this, in fig. 3.A.4 we show the effective masses divided by the one of mode 2, which being the lowest mode available can be taken as a reference. We can see that whilst most of the flexural modes show values close to 1, mode 5 (excluded from the computation of ϵ) yields a much greater value: x_0 is in fact close to one of the nodes of σ_5^δ . Similarly, for the torsional modes we can see how in addition to mode 5 yielding a high effective mass, also modes $m = 4$ and 6 are sensibly higher than 1, x_0 being close to a node of the respective sensitivities.

Next, the minimum of $\text{std}(\eta_n(x_0^{\text{EQ}}, R_0)), \forall R_0$ indicates the experimental value of the beam radius $R_0 = R_0^{\text{EQ}}$. We show this in fig. 3.A.5 for both the flexural and torsional modes.

As we can note, the results for deflection and torsion differ of about 5 % in evaluating x_0 , and about 4.5 % in the case of R_0 . This is not surprising, since the estimations greatly depend on the shape of the cantilever, and its deviations from a pure rectangular beam described by the Euler-Bernoulli and Saint-Venant (or Barr's) models. In fact, the presence of a triangular tip requires an adjustment of the length of the cantilever following the mode, which can be

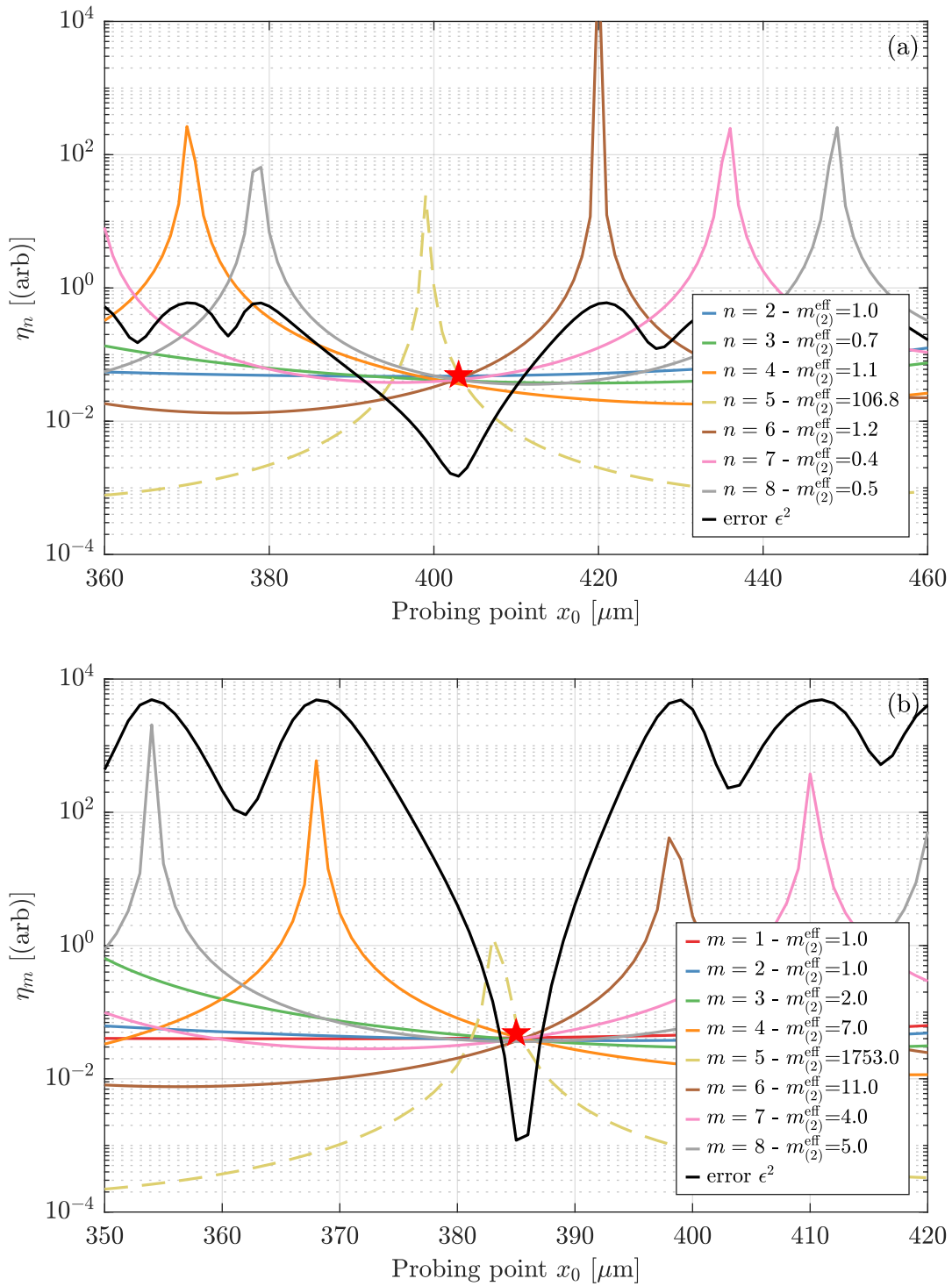


FIGURE 3.A.4: In (a), the sensitivity of the flexural modes is displayed: the quantity η_n is independent of n for a unique value of x_0 close to the end of the cantilever. The black solid line represents the square of the standard deviation over n of η_n divided by its mean, for each x_0 (calculated excluding mode 5). It presents a minimum at the actual measurement point $x_0 = 405 \pm 2 \mu\text{m}$. The effective masses of the modes are given in the graph legends, normalised by the one of the second mode. All the modes but one yield similar m^{eff} , with $n = 5$ being much higher than the others. In (b), we do the same for the torsional modes, also excluding mode 5 from the calculations. In this case, the retrieved probing point is $x_0 = 385 \pm 1 \mu\text{m}$, which shows a discrepancy of about 5 % with the flexural modes. The effective masses hint at the sensitivity of the resonances to a shift in probing position: m^{eff} for mode 5 is hundreds of times higher than the others, as modes 4 and 6 also show high values due to x_0 being close to one of their node in sensitivity.

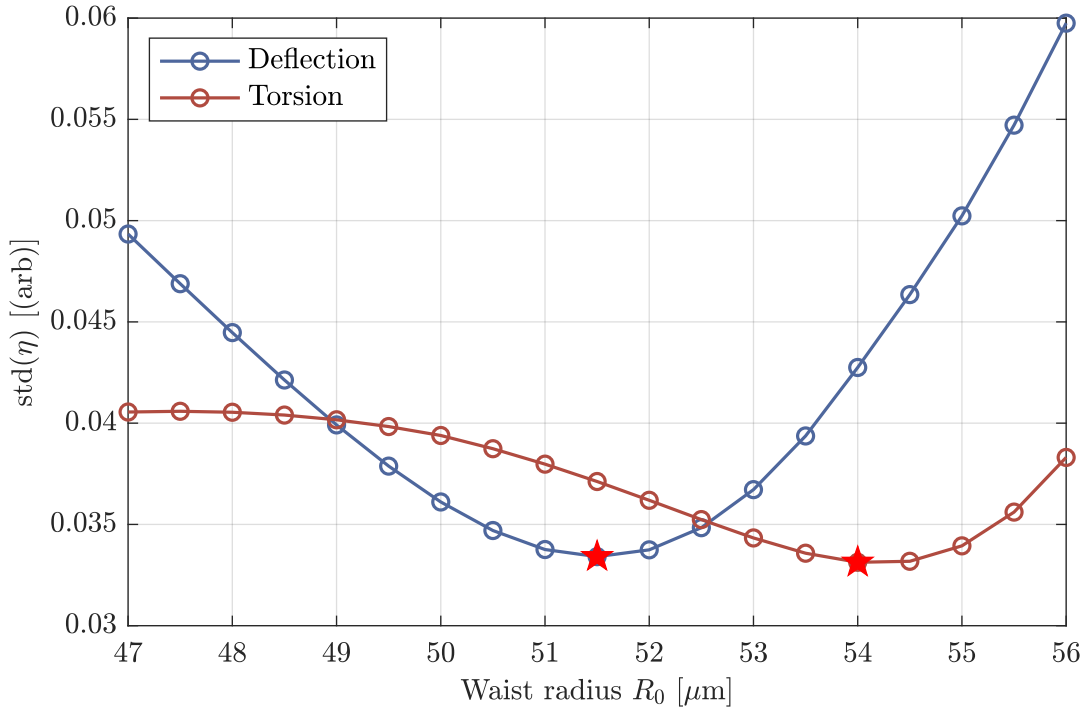


FIGURE 3.A.5: Waist radius evaluation: once a x_0^{EQ} is set, the radius R_0 which yields the least dispersion of the modes is chosen as the representative of the measurement R_0^{EQ} . We can see that the minimum of the curves shows a 5 % difference amongst the flexural and torsional modes.

estimated by an effective length L^{eff} . This can be derived from the dispersion relations:

$$L_n^{\text{eff}} = \sqrt{\frac{YH^2}{12\rho} \frac{\alpha_n}{\sqrt{\omega_n}}} \quad (3.58)$$

$$L_m^{\text{eff}} = \sqrt{\frac{4SH^2}{B^2\rho} \frac{\alpha_m}{\omega_m}}$$

with ρ the density of silicon. It is clear that an incorrect estimation of the geometrical parameters leads to imprecisions in L^{eff} , and thus the estimations of x_0, R_0 . As a side note, since that the Saint-Venant model is not adapted to torsion for modes higher than 2, we use the corrected Barr's equation to retrieve L_m^{eff} which is not reported for the sake of simplicity (see Sec. 2.2.2). For the particular case depicted in fig.s 3.A.4 and 3.A.5, we can partially circumvent the estimation of the geometric quantities using the tabulated values in [15], in which measured values of L_m^{eff} are given.

3.A.5 Calibrated spectra

Once these quantities are correctly estimated, we can use them to estimate the calibration coefficient in eq. 3.31. This allows to finally retrieve the mean square displacements from

the signals retrieved from the photodiodes C_x, C_y :

$$\begin{aligned}\langle \delta_n^2 \rangle &= \left(\frac{R_x}{2\sqrt{2}f_{CL}\sigma_n^\delta(x_0, R_0)} \right)^2 \int_{f_n \pm \Delta f_n} df \mathcal{S}_{C_x}(f) \equiv K^\delta \langle C_n^2 \rangle \\ \langle \theta_m^2 \rangle &= \left(\frac{R_y}{2\sqrt{2}f_{CL}\sigma_m^\theta(x_0, R_0)} \right)^2 \int_{f_m \pm \Delta f_m} df \mathcal{S}_{C_y}(f) \equiv K^\theta \langle C_m^2 \rangle\end{aligned}\quad (3.59)$$

with $f_{n,m}$ the resonance frequencies of the modes and $\Delta f_{n,m}$ the relative frequency interval of integration. This interval is often mode dependent, since it is optimised to encompass the resonance without including any other feature in the spectrum, for example spurious peaks or other modes. It usually spans between $2\Delta f \approx 2 - 6$ kHz. The calibration factors K depend on the radius of the laser probe on the photodiode, which is calibrated in each measurement, and on the spot size and position of the probe on the cantilever.

3.B Fluctuation temperatures and uncertainties

At each power step of the ramp (see Sec. 3.3) we retrieve the spectra of the signals collected by the photodiode C_x and C_y . From this, we compute the fluctuations $\langle C_{n,m}^2 \rangle$, which are averaged between the ones in the same power step (after selecting the data, see Chapter 6). This yields a series of values and the relative statistical uncertainties ϵ^{stat} , which are simply the standard deviations around the mean. Finally, the fluctuation temperatures are computed following eq. 2.88, which we recall for simplicity:

$$\begin{aligned}T_n^{\text{fluc}} &= \beta_n^2 \frac{\langle \delta_n^2 \rangle_{\text{NESS}}}{\langle \delta_n^2 \rangle_{\text{EQ}}} T_{\text{EQ}} = \beta_n^2 \frac{K_{\text{NESS}}^\delta}{K_{\text{EQ}}^\delta} \frac{\langle C_n^2 \rangle_{\text{NESS}}}{\langle C_n^2 \rangle_{\text{EQ}}} T_{\text{EQ}} \\ T_m^{\text{fluc}} &= \beta_m^2 \frac{\langle \theta_m^2 \rangle_{\text{NESS}}}{\langle \theta_m^2 \rangle_{\text{EQ}}} T_{\text{EQ}} = \beta_m^2 \frac{K_{\text{NESS}}^\theta}{K_{\text{EQ}}^\theta} \frac{\langle C_m^2 \rangle_{\text{NESS}}}{\langle C_m^2 \rangle_{\text{EQ}}} T_{\text{EQ}}\end{aligned}\quad (3.60)$$

with the $\beta = \omega_{\text{NESS}}/\omega_{\text{EQ}}$ coefficients representing the change in stiffness of the system when heated, which are measured. In the experiments presented in this chapter, the equilibrium temperature is taken $T_{\text{EQ}} = T^{\text{min}} = 300$ K, which is fixed by the contact of the cantilever with the macroscopic chip. In order to assure T^{fluc} can be computed through eq. 3.60, great care should be taken when estimating the quantities involved.

In the equilibrium step S_{EQ} , in order to retrieve $\langle C_{n,m}^2 \rangle_{\text{EQ}}$, the green laser is set at a low power $P \leq 1$ mW, whilst the red laser (also at a power $P \leq 1$ mW, but on a greater area) probes the displacements. Due to the small but still not negligible injected power, the system cannot be strictly considered in thermal equilibrium. Another difficulty arises for the resonances at high frequency, which sometimes are not visible until a certain heating power is reached. In order to have a general method to correctly estimate $\langle C_{n,m}^2 \rangle_{\text{EQ}}$ we perform a linear fit of the fluctuations for $P \leq 4$ mW so that the ordinate at the origin is taken as the normalisation factor.

Next, we need to make sure that K is unchanged between S_{EQ} and S_{NESS} measurements. Since R_x, R_y are calibrated, this reduces to make sure x_0 and R_0 are constant. If we suppose

that a drift dx_0, dR_0 occurs during the experiment, since $T^{\text{fluc}} \propto 1/\sigma(x_0, R_0)^2$, we find:

$$\begin{aligned} \frac{1}{T_n^{\text{fluc}}} \frac{\partial T_n^{\text{fluc}}}{\partial x_0} &= -2 \frac{1}{\sigma_n^\delta} \frac{\partial \sigma_n^\delta}{\partial x_0} \\ \frac{1}{T_n^{\text{fluc}}} \frac{\partial T_n^{\text{fluc}}}{\partial R_0} &= -2 \frac{1}{\sigma_n^\delta} \frac{\partial \sigma_n^\delta}{\partial R_0} \end{aligned} \quad (3.61)$$

where we limited ourselves to the flexural case for simplicity. The origin of this drift is important: dx_0 can be the result of thermal expansion of the material, which can be computed and confirmed by camera observations. For example, in the C100 experiment we estimate a maximum $dx_0 = 2 \mu\text{m}$. Regarding dR_0 , the leading contribution may come from the thermal expansion of the steel collimator of laser, which nevertheless influences very little the beam radius. We can then suppose $dR_0 = 0$ and thus define the systematic errors for a shift dx_0 as:

$$\begin{aligned} \epsilon_n^{\text{sys}} &= 2 \left| \frac{T_n^{\text{fluc}}}{\sigma_n^\delta} \frac{d\sigma_n^\delta}{dx_0} dx_0 \right| \\ \epsilon_m^{\text{sys}} &= 2 \left| \frac{T_m^{\text{fluc}}}{\sigma_m^\theta} \frac{d\sigma_m^\theta}{dx_0} dx_0 \right| \end{aligned} \quad (3.62)$$

In [40] we report the values of these uncertainties for the C100 case. In this particular case, the higher ϵ^{sys} are given by the modes 4,5,6 for both deflection and torsion, which is due to their higher sensitivity on a change of probing point. This is not surprising, since in fig. 3.A.4 we can see that x_0 is close to a sensitivity node for these mode numbers.

In all the experiments shown in this chapter, ϵ^{sys} constitute a significant source of uncertainty, and depending on the mode number, it can be more important than the statistical one. The final error bar is calculated summing ϵ^{stat} and ϵ^{sys} in quadrature.

3.C Ruling out external noise contributions

Due to the ephemeral nature of thermal fluctuations, usually being unnoticeable due to other sources of noise orders of magnitude higher, we need to take great care in assuring that the measured thermal fluctuations are not biased by the presence of other phenomena. In the experiment we are prudent in excluding any kind of external perturbations, isolating the system from the noise of the environment with a air suspended optical table, removing acoustic contributions and hydrodynamic interactions by placing the cantilever in vacuum.

In the present section, we discuss the action and the magnitude of possible noise sources, and show how we can deal with them.

3.C.1 Background electronic noise contribution

Let us consider one contrast collected by the photodiode, for example C_x . This embeds the actual thermal noise δ and a noise contribution \mathcal{N} :

$$C_x = \frac{\delta}{\sqrt{K^\delta}} + \mathcal{N} \quad (3.63)$$

with K the calibration factor and \mathcal{N} mainly due to the shot-noise of the photodiode. The thermal noise is then evaluated as eq. 3.59:

$$\langle \delta^2 \rangle = K_n^\delta (\langle C_n^2 \rangle - \langle \mathcal{N}^2 \rangle) \quad (3.64)$$

As shown in fig. 3.1.3, \mathcal{N} has a white behavior and it is usually many order of magnitude lower than the resonances, thus it has a very low impact on the fluctuations. Nevertheless, when integrating around a resonance frequency we take care of removing it. This procedure is depicted in fig. 3.C.1. Once we have chosen a suitable frequency range Δf_n around the resonance f_n , we consider a small frequency interval $\Delta_{\mathcal{N}}$ at the left and right sides of the previous one. We then fit the PSD with a linear function of f in the two $\Delta_{\mathcal{N}}$ ranges in order to retrieve the average background level of the resonance \mathcal{N} . Finally, the contribution is systematically subtracted from the integral under the resonance, which is performed in the $f_n \pm \Delta f_n$ frequency interval. In formulas:

$$\langle \delta_n^2 \rangle = \int_{f_n \pm \Delta f_n} df (\mathcal{S}_\delta(f) - \mathcal{N}) \quad \mathcal{N} = a + bf, f \in \{f_n \pm \Delta f_n\} \quad (3.65)$$

with a, b the results of the linear fit of the background in the aforementioned intervals $\Delta_{\mathcal{N}}$.

Another technique in order to eliminate the background contribution is through a cross-correlation method [92]. Two distinct flexural contrast are calculated as:

$$\begin{aligned} C_{x1} &= \frac{A - B}{A + B} \\ C_{x2} &= \frac{C - D}{C + D} \end{aligned} \quad (3.66)$$

Supposing that the signal is the sum of thermal noise δ and shot-noise contribution $\mathcal{N}_{1,2}$, we have $C_{x1,2} = \delta / \sqrt{K^\delta} + \mathcal{N}_{1,2}$. Computing the cross correlation between C_{x1} and C_{x2} leads to:

$$\begin{aligned} \langle C_{x1} C_{x2} \rangle &= K^\delta \langle \delta^2 \rangle + \sqrt{K^\delta} \langle \delta \mathcal{N}_1 \rangle + \sqrt{K^\delta} \langle \delta \mathcal{N}_2 \rangle + \langle \mathcal{N}_1 \mathcal{N}_2 \rangle \\ &= K^\delta \langle \delta^2 \rangle \end{aligned} \quad (3.67)$$

where all but the first contribution are zero due to the noises being uncorrelated. Note that the same strategy applies to torsion by changing the pairs of quadrant to compute $C_{y1} = (A - C) / (A + C)$ and $C_{y2} = (B - D) / (B + D)$. In fig. 3.C.1 this method is used to compute the flexural spectrum and compared to the one calculated through the usual procedure. We can see that the differences close to the resonance are almost inexistent, as the two spectra start to be distinguishable when the PSD is orders of magnitude lower than the maximum. The thermal content obtained integrating the cross-correlated signal through eq. 3.59 and the one retrieved from eq. 3.65 yields a difference $\leq 1\%$ for all the modes in all the experiments presented in this chapter. Therefore, we can conclude that the electronic background noise does not affect our results.

3.C.2 Laser power fluctuations

Due to radiation pressure and photo thermal effects, any fluctuation of the laser power can translate into a force on the cantilever, thus a displacement. In order to estimate the magnitude of this possible disturbance, we show here the study of the laser influence on the measured thermal fluctuations. As usual, we take deflection as an example with the extension to the torsion being trivial.

The first step is the characterisation of the laser transfer function. We add a white noise to the laser power thanks to the Acousto-Optic Modulator (AOM) [1] that is routinely used as the power controller, and measure the laser power P^{driven} and the deflection δ^{driven} . We

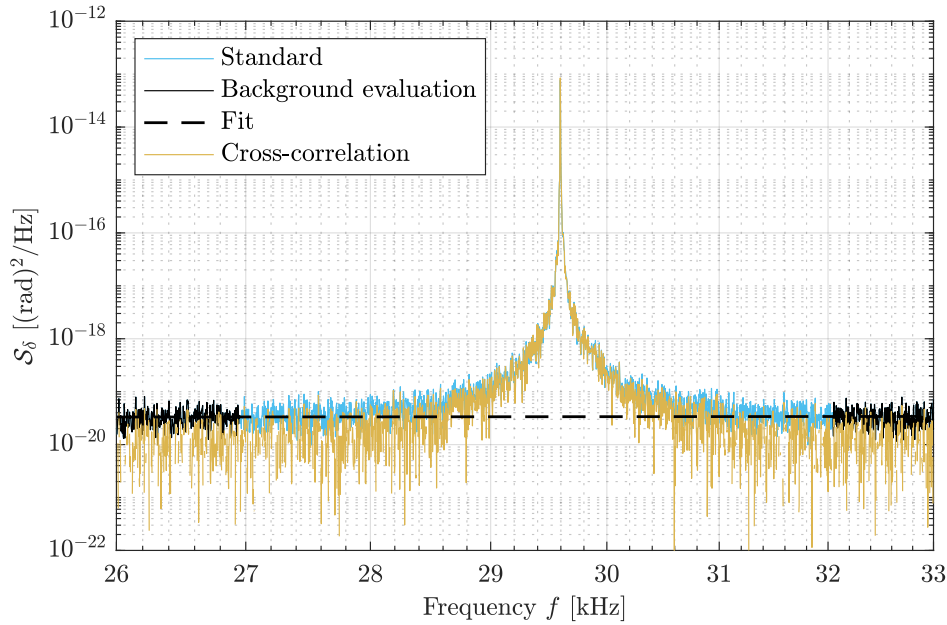


FIGURE 3.C.1: Two different strategies to eliminate the electronic background contribution on the thermal fluctuations. The first consists in selecting a frequency interval for the resonance until the background noise is reached (cyan); then, two small intervals at the sides of the previous one are chosen (black) and a linear fit is performed (dashed black). We then remove the fit of the background from the spectrum, following eq. 3.65. A second method is the cross-correlation technique (yellow): following eq. 3.67, the background noise is automatically subtracted. We note that the two techniques yield very similar results, with differences arising at orders of magnitudes lower than the resonance.

then define the gain of the laser transfer function χ_δ^P :

$$|\chi_\delta^P| = \frac{S_\delta^{\text{driven}}}{S_P^{\text{driven}}} \quad (3.68)$$

We show this function in fig. 3.C.2 for different laser powers for the C100 cantilever. As we can see, χ_δ^P and χ_θ^P can be characterised roughly until 50 kHz, which is the limit of the recording instrument. For this reason, we can probe the effect of the laser for the first two flexural modes and the first torsional one.

Once this transfer function is available, a measurement without any additional noise is performed and the new PSD of laser power is multiplied by the $|\chi_\delta^P|$. We show an example of this function $|\chi_\delta^P|S_P$ in fig. 3.C.3, compared to the measured S_δ . The ratio between these two quantities represents the amount of laser driven fluctuations, which is also shown in fig. 3.C.3 for increasing laser power. We see that the laser oscillations contribute for less than 0.5% for all the considered modes and powers. We can thus affirm that our results are robust against this kind of contribution. For higher order modes, the $|\chi_\delta^P|S_P$ is even weaker and hard to characterize, so the same conclusions apply.

3.C.3 Self-oscillations

In this chapter we have often referred to the "self-oscillations" when excluding the first resonance mode from the analysis. Indeed, we believe that an optomechanical coupling between the cantilever and the laser heating the system may be the source of sudden (and strong) increases and decreases of fluctuations in the system [72]. We show an example of this in

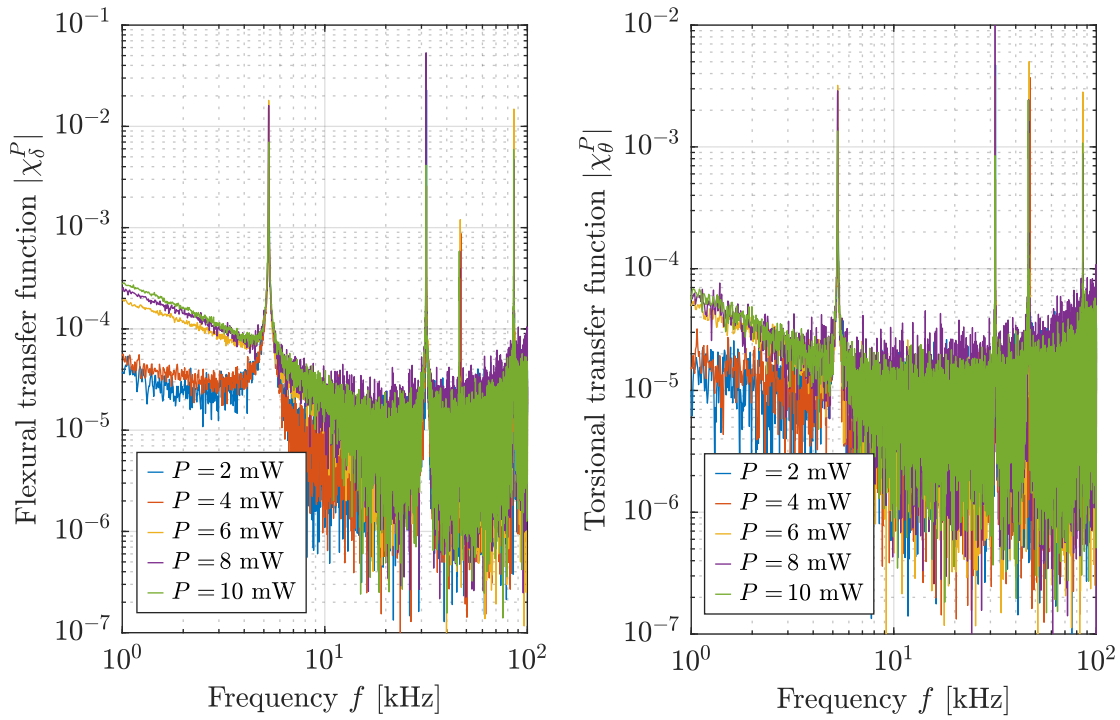


FIGURE 3.C.2: Transfer function gains $|\chi_\delta^P|$ and $|\chi_\theta^P|$ for different laser powers. We limit our description to 50 kHz, since the transfer functions are difficult to characterise at high frequency. This frequency band includes two flexural and one torsional resonances.

fig. 3.C.4, for the C100 example. We can see the PSD of the first flexural resonance in measurements, taken in a time span of less than 1 min. During this time, the PSD changes of 5 orders of magnitude. The same three measurements for the second flexural mode show a comparatively little change, with one PSD roughly two times the others. Taking $n = 2$ as a reference, we know that the amplitude of this mode should yield a PSD roughly 40 times lower than the first mode [23] (the ratio of the PSD goes as the ratio of the relative α_n^4). We can then see that the red curve cannot represent thermal noise. Similarly, we see that the blue curve may represent the opposite behavior: a self-cooling, where the optomechanical coupling in this case removes energy from the resonance. Indeed, the PSD is 10 times lower than the expected value, looking at mode 2.

Whereas the origin and the characterisation of this phenomenon is not trivial, neither is discarding the corrupted data. As in this thesis we often simply discard the modes affected by this phenomenon, in Chapter 6 we discuss the statistical properties of thermal noise, and how we can quantitatively distinguish it from the self-oscillations.

Even considering the aforementioned precautions, it is possible that some spectra are polluted by external factors, with the self-oscillations being a major cause. In order to discard these spectra, we resort to the statistical properties of thermal noise spectra (and the relative quantities) to sort out the proper measurements from the ones which would bias the outcome of the experiment. All the results presented in this chapter (and the following ones) pass through this selection process, each with its particularities. Owing to the generality of the method, we refer to Chapter 6 for the complete description of this process.

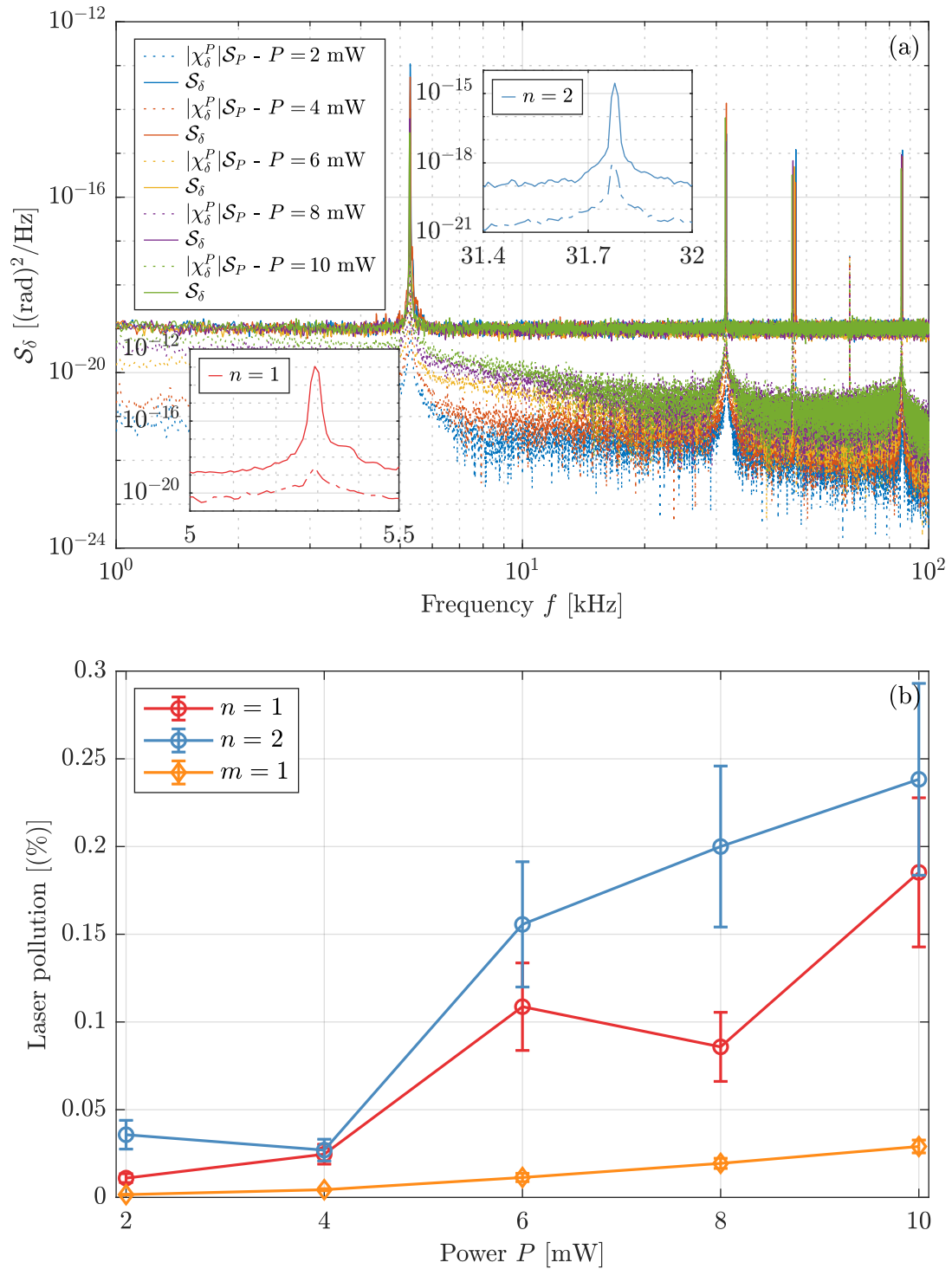


FIGURE 3.C.3: In (a), the laser pollution spectrum, represented by $|\chi_\delta^P|S_P$, is shown with respect to the PSD of the deflection S_δ for different laser powers P . We note that the first quantity is much less important than the second ones, which is exemplified by the two insets showing the first and second resonances and the relative influence of the laser power fluctuations. In both cases, $|\chi_\delta^P|S_P$ is order of magnitude lower than S_δ . In (b), we show this for all the powers, as less than 0.5 % of the amplitude of fluctuations is due to the laser disturbance.

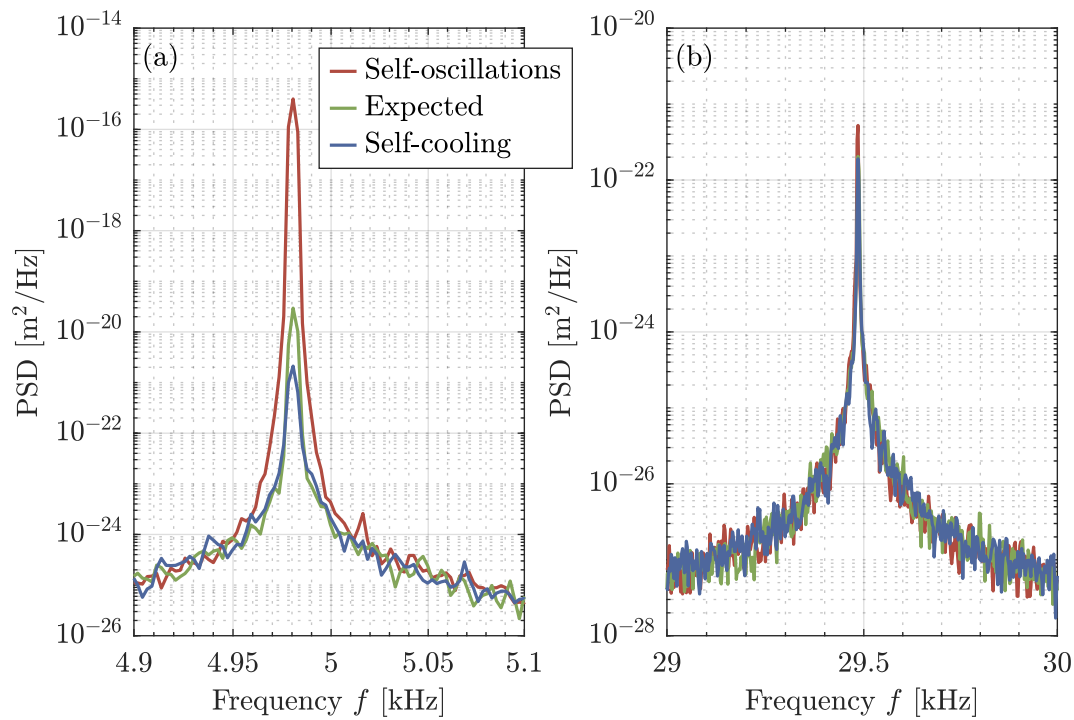


FIGURE 3.C.4: In (a), we show three different regimes for the $n = 1$ resonance more of the C100 cantilever, measured in a 1 min span. The expected value for the PSD (green) is compared to a self-oscillating state (red), where the fluctuations are four orders of magnitude higher. Conversely, a self-cooling state is recognisable thanks to a drastic reduction of the signal, in this case 10 times lower than the expected. As we show in Chapter 6, both these regimes cannot be statistically acceptable as thermal noise. In (b), we show the same measurements for mode $n = 2$. As we can see, the self-oscillating one would barely be identifiable as such, since the PSD is roughly 2.5 times higher than the expected value. Similarly, the self-cooling one shows the same power as the reference. Therefore, in this case, we can say that the self-oscillations pollute the first resonance and leave almost untouched the higher modes.

Chapter 4

Thermal noise of a micro-cantilever in cryogenic environment

In the previous chapter, we studied the thermal fluctuations of a micro-cantilever in contact with a thermal bath at room temperature, showing how these can be linked to the measured mechanical dissipation through a non-equilibrium extension of the FDT. In particular, we test the validity of our model reaching temperature differences about $\Delta T^{\max} = 800$ K between the thermostat and the free end of the sample, depending on the experiment. In the present chapter, we push these concepts towards the limits of their applicability, roughly doubling the aforementioned temperature difference. In this case, we thermalise the cantilever in a cryostat at 10 – 20 K, whilst the tip is heated up to its melting point, $T^{\text{melt}} \approx 1700$ K. We choose a cantilever similar to C100, since we believe this to be an interesting test bench for the measurements shown in the previous chapter and in [42, 40], with the goal of the present section to test whether our description holds up to the physical limits of the system, temperature-wise.

Indeed, in the introduction, we claim that our results could be of particular use in the prediction of noise behavior in the GWs detectors. Whilst we show that this could be the case in the previous chapter, we know that a large effort in the GW community is directed at cryogenics in order to lower the thermal noise of test masses and their suspension system. Therefore, the aforementioned description may help the current instruments to conceive new suspension systems (with silicon as a frontrunner for the possible material) but might not be sufficient in future developments. As previously stated, facilities such as KAGRA [6] and the future proposal of the ET [93] operate (or will operate) at very low temperatures, where whilst the noise level diminishes, other issues arise. In this case, the present study aims to tackle the question of cryogenic non-equilibrium noise, while at the same time probing the behavior of silicon in these conditions.

The first part focuses on the characterization of the experimental setup, describing the cantilever under study. A different detection system with respect to the one in the previous chapter is also displayed.

The second part briefly discusses the temperature of the sample when heated in a cryogenic environment. We make use of a calibration to construe the measured frequency shift of the resonances in order to associate a temperature with the system and to further assess this through a simulation.

The central sections illustrate the experimental procedure and the results obtained in two measurement sessions on the same cantilever. We display the fluctuation temperatures with respect to the average temperature of the system, interpreting the findings with the help of the measured loss angles.

The last part summarises this chapter and discusses the outcome of the experiments. Perspectives for future work and applications are mentioned.

4.1 Experimental setup

The experimental setup is depicted in fig. 4.1.1. The physical systems consists of a $L = 1000 \mu\text{m}$ long, $B = 90 \mu\text{m}$ wide and $H = 1 \mu\text{m}$ thick silicon cantilever (OCTOSENSIS micro-cantilevers arrays [76]) monolithically clamped to a macroscopic chip. We refer to this sample as C90, which is similar to C100, at least in the geometrical specifics.

Contrary to the previous chapter, we recover the displacements of the cantilever through differential interferometry. The measuring system is the CryoQPDI [87], a Quadrature-Phase Differential Interferometer (QPDI) combined with a cryostat assembled at the Laboratoire des Matériaux Avancés (LMA) in Lyon, France. The cantilever is placed in the vacuum chamber at 10^{-7} mbar and $T^{\min} \leq 20$ K, where two laser beams measure its thermal fluctuations and act at the same time as the heater.

4.1.1 CryoQPDI

The principles of operation of a QPDI can be found in [85, 87]. We briefly summarize them here, referring to fig. 4.1.1. As a side note, we report the full functioning of a QPDI in the next chapter, since in that case we aided in its development.

A polarized laser beam is collimated towards the cantilever, which is placed into the cryostat. Before hitting it, a birefringent element (an aberrations-corrected series of Savart plates) divides the probe into two beams. The orientation of this element is 45° with respect to the original axis of polarization, and thus the polarization of each beam is rotated by this quantity, only with opposite signs. The optical path difference (proportional to the vertical displacement of the cantilever along the z -direction) after reflection and recombination results in an optical phase shift ψ , present along both the initial polarization axis and the perpendicular one. The reflected beam is split into the two arms of the QPDI: in the first, the two polarizations are separated, and each yields a power signal $A, B \propto 1 \pm \cos(\psi)$; in the second, a quarter-wave plate adds a phase shift of $\pi/2$, giving two intensity signals $C, D \propto 1 \pm \sin(\psi)$ after the separation of the polarizations. The power signals are thus combined:

$$\begin{aligned} C_1 &= \frac{A - B}{A + B} = \cos(\psi) \\ C_2 &= \frac{C - D}{C + D} = \sin(\psi) \end{aligned} \quad (4.1)$$

We then define the complex contrast $C \equiv C_1 + iC_2 = e^{i\psi}$. The advantage of this setup is that it permits a complete characterization of the phase (modulo 2π): a representation of C in the complex plane completely identifies the phase on the unit circle. The displacement d' , is then recovered through the phase:

$$d' = \frac{\lambda}{4\pi} \psi \quad (4.2)$$

where $\lambda = 532$ nm is the wavelength of the laser. This description is fit for an idealized case, however. Optical misalignments and components' imperfections yield a contrast less than optimal, usually an ellipse smaller than the unit circle. Through a Heydemann's correction [54], it is possible to take imperfections into account: the cantilever is driven at resonance

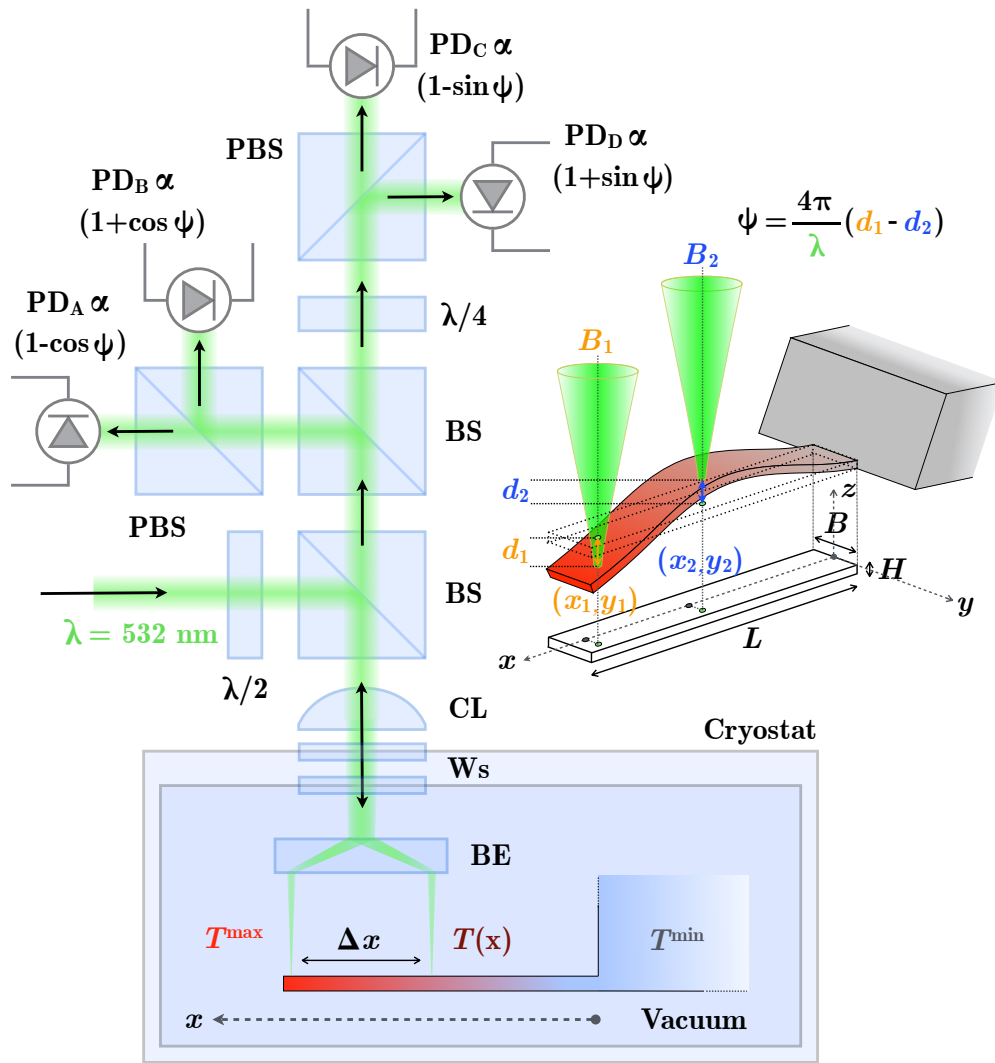


FIGURE 4.1.1: Experimental setup: the deflection and the torsion of a cantilever are captured thanks to a quadrature phase differential interferometer (QPDI). A green laser beam ($\lambda = 532 \text{ nm}$) probes the deformation of the cantilever. The input beam is prepared with a polarization in the figure plane thanks to a half-wave plate ($\lambda/2$), then it is directed towards the cryostat by a Beam Splitter (BS) through a Converging Lens (CL) which focuses the beam on the cantilever. The cryostat is composed of two temperature stages, each presenting a Window (W) on the path of the beam. Light then passes through a Birefringent Element (BE), which is a combination of two Savart plates, the purpose of which is to divide the beam into two, with a spatial separation of $\Delta x = 417 \mu\text{m}$ in the x -direction. The setup being optimized for cantilevers half the length of the considered one, we set one beam B_1 close to the tip of the cantilever at a position x_1 , whereas the second B_2 is close to the middle at x_2 . The difference in optical path of the two beams is shown in the right part, where the second spatial eigenmode of deflection is depicted as an example. B_1 probes a deformation d_1 from a horizontal reference; B_2 measures d_2 . When the beams recombine after reflection, they carry the information in the form of an optical phase: $\psi = 4\pi(d_1 - d_2)/\lambda$. The beam then enters the analysis area, where a BS sends half of the light in each analysis area. In the left area, the signal is further divided by a Polarizing BS (PBS), yielding two power signals proportional to $1 \pm \cos(\psi)$. In the upper branch, the beam first passes through a quarter-wave plate ($\lambda/4$) that adds a phase $\pi/2$, leading to two power signals proportional to $1 \pm \sin(\psi)$ after the PBS. The phase can then be extracted, and the relative displacement $(d_1 - d_2)$ calculated. The cantilever, in vacuum at $5 \times 10^{-6} \text{ mbar}$, is monolithically clamped to its macroscopic chip, which is thermalized at temperature T^{\min} . When the laser power is low ($P \approx 1 \text{ mW}$), we consider the system to be in thermal equilibrium. When the power is raised (10 to 40 mW), a temperature gradient $T(x)$ along the cantilever arises (see Appendix 4.B).

such that d' covers at least one interference fringe. Then, the output of the QPDI C draws the actual contrast, which is fitted to extract the calibration parameters.

4.1.2 Displacements

In fig.s 4.1.1 and 4.1.2, we can see that the cantilever we have chosen is longer than the spatial separation granted by the birefringent element $\Delta x = 417 \mu\text{m}$. The real displacement of the cantilever d , meant as the difference of the displacement at the tip and the one at the base ($x = 0$), is therefore not directly accessible. The measured displacement d' is instead the difference between the displacements at x_1 and x_2 : $d' = d_1 - d_2$. We discuss how to transform d' in d in Appendix 4.A. The QPDI therefore gives access to the displacement temporal signal $d'(t)$, which yields a PSD where the resonances of the cantilever are visible (see fig. 4.1.3).

From d , it is then possible to retrieve the deflection δ and the torsional angle θ of the cantilever, which we again discuss in detail in Appendix 4.A. As discussed in the previous chapter, δ is insensitive to the lateral position y on the cantilever, whilst θ in this case depends on y . Since the torsional modes show no vertical displacement in the center of the cantilever, a probing position y_1, y_2 close to the edge is chosen.

4.2 Temperature of the cantilever

4.2.1 Apparent temperature calibration

As shown in the previous chapter, we can usually link the frequency shift of the normal modes of the cantilever to a temperature T^{app} . If the conditions are favorable, the apparent temperature is a good approximation of the average one, $T^{\text{app}} \approx T^{\text{avg}}$. In the present case, though, we will show that a more careful analysis is required.

Let us start from eq. 3.9, which we report:

$$\frac{\Delta\omega_n}{\omega_n^0} = \frac{1}{2} \frac{\Delta Y}{Y^0} = f(T) \quad (4.3)$$

This equation describes the frequency shift of the flexural resonances if the whole system was to be brought to a uniform temperature T , in equilibrium. The first key difference with a cantilever thermalised at room temperature is that we can no longer rely on the tabulated form of f , specified in eq. 3.10. In fact, since the tabulated values [50] are valid for temperatures $T \geq 295 \text{ K}$ and highly dependent on the geometry and the crystalline orientation of the sample, we cannot assume that f of eq. 3.10 is valid in this case. We thus proceed with a calibration.

This procedure consists of placing the cantilever at the lowest available temperature, $T^{\text{min}} = 10 \text{ K}$, and letting the temperature slowly increase. At the same time we record the frequency of the resonance modes using a low laser power, letting the cantilever be in equilibrium at increasing temperatures. Knowing both T and $\Delta\omega_n/\omega_n^0$, the function $f(T)$ is thus measured. Unfortunately, such a measurement of the cantilever used in this experiment was not possible. We nevertheless use the calibration performed on a similar sample, with the same specifics, but with the length $L = 741 \text{ nm}$ [87]. The experimental data are shown in fig. 4.2.1.

In order to describe $f(T)$, we choose the same ansatz as eq. 3.10 [100]:

$$f(T) \equiv c_1 T e^{-c_2/T} \quad (4.4)$$

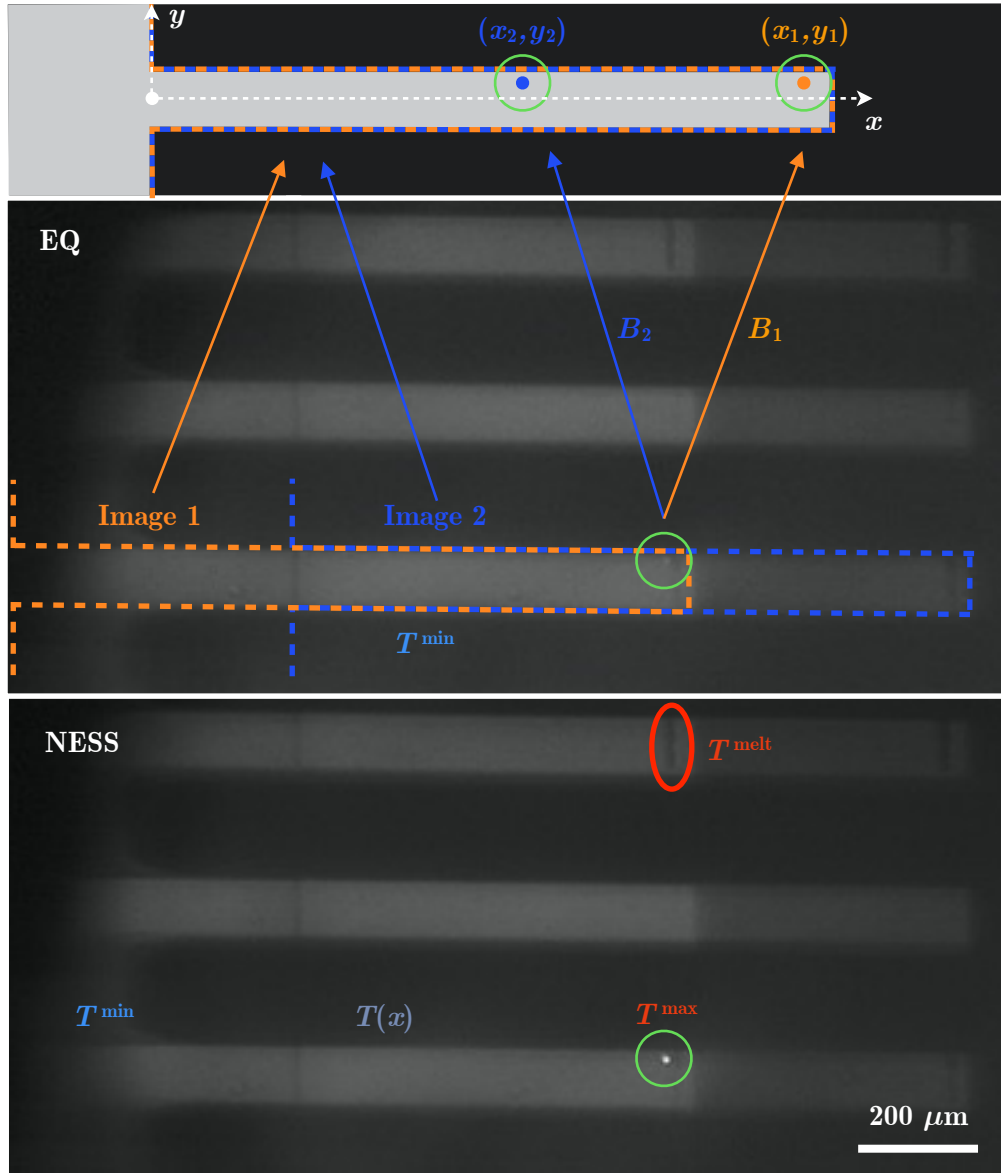


FIGURE 4.1.2: Images of the cantilever during the experiment: an equilibrium measurement is depicted next to a non-equilibrium one. On top, we show a sketch of the cantilever with the two laser beams B_1 and B_2 similar to the one in fig. 4.1.1. Below, two pictures show two superimposed cantilevers with one laser spot reflected on its surface. This is an effect due to the observation through the birefringent element, which merges the two beams into one after reflection but doubles the unpolarized image of the cantilever. In the middle figure, the equilibrium thermal noise of the cantilever is probed by a laser beam of low power P , thus leaving a uniform temperature T^{\min} . In the bottom figure, a NESS case is shown: a higher injected power is visible from the more intense reflected beam, and a temperature profile $T(x)$ is established. We notice how another sample (used for tests) on the top shows signs of surface modifications, most probably melting (see fig. 4.B.3).

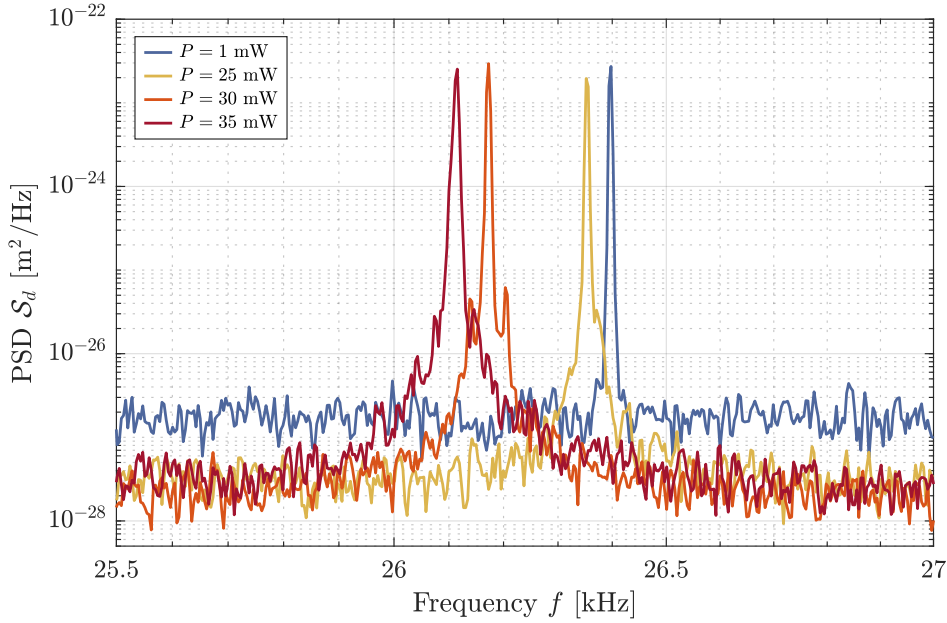


FIGURE 4.1.3: PSD of the displacement signal d' : the third flexural resonance mode is shown at different laser powers P . When the temperature of the cantilever increases, its normal modes get redshifted due to the sample becoming softer. Tracking the frequency shift, it is possible to infer its average temperature T^{avg} , see Sec. 4.2.

with the coefficients now determined by the calibration: $c_1 = 3.6 \times 10^{-5} \text{ K}^{-1}$ and $c_2 = 196.7 \text{ K}$. The curve $f(T)$ in fig. 4.2.1 (dark red) is in remarkable agreement with the experimental data, even if eq. 3.10 is not necessarily valid at low temperatures [50]. Finally, in the same figure, we show how this curve roughly coincides with a linear approximation for the Young modulus (α_Y) for $T \geq 295 \text{ K}$, which is on the other hand not true at lower temperatures.

Now that the function f is calibrated, we can use it to infer the temperature T^{app} of the cantilever in a cryogenic environment from a measured frequency shift :

$$T_n^{\text{app}} \equiv f^{-1} \left(\frac{\Delta \omega_n}{\omega_n^0} \right) \quad (4.5)$$

The key point is now to estimate the distance between this apparent temperature and the average T^{avg} . We discuss this in the next section.

4.2.2 Average temperature from simulated temperature profile

In order to estimate the average temperature of the cantilever and the error we would make using T_n^{app} instead we proceed with a simulation of the temperature profile in this experiment.

The laser acts as a heater on the cantilever: the beam is set to a position x_1 such that B_1 is focused close to the tip of the cantilever, with a waist radius $R_0 \approx 5 \mu\text{m}$. The base of the cantilever is monolithically clamped to a macroscopic chip that serves as a thermostat at temperature T^{min} , set by the cryostat and measured very close to the chip. As in previous experiments [40], we aim to create a temperature difference, and thus a NESS, gradually increasing the laser power at the tip. For a similar cantilever (half the length of the one in this experiment) and $T^{\text{min}} = 300 \text{ K}$, a $\Delta T^{\text{max}} \approx 1400 \text{ K}$ is reached when a laser of $P \approx 12 \text{ mW}$

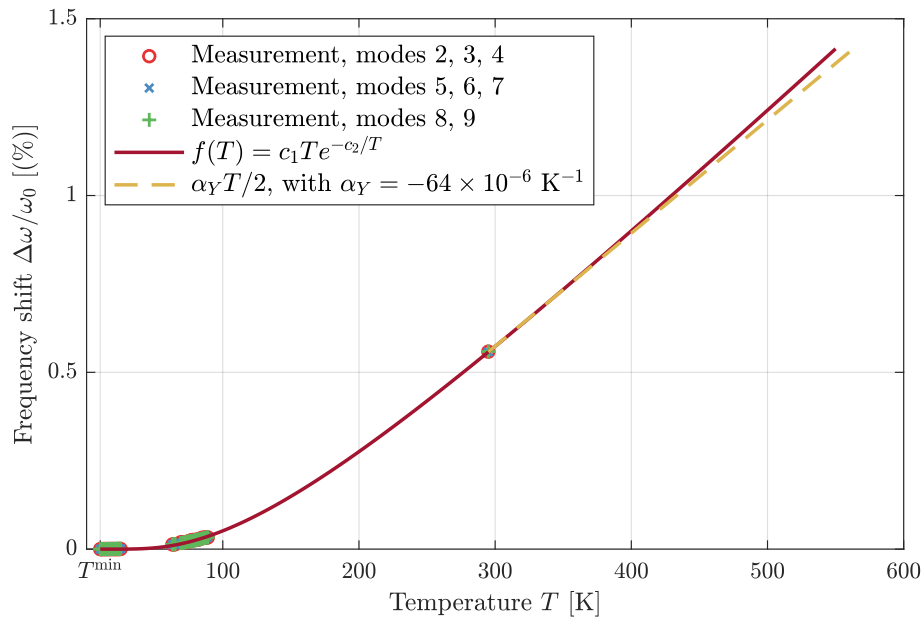


FIGURE 4.2.1: Calibration of $f(T)$: a cantilever similar to the one used in this experiment is used to calibrate the temperature dependence of the frequency shift (eq. 3.9). The calibration points (\circ , \times , $+$) are obtained by measuring the frequency shift $\Delta\omega_n/\omega_n^0$ at equilibrium ($P \leq 1$ mW) of the flexural modes when the temperature of the cryostat slowly increases, until room temperature is attained. The reference frequencies ω_n^0 are taken at 10 K. The figure shows the $\Delta\omega_n/\omega_n^0$ for three groups of modes from $n = 2$ to 9, showing no appreciable difference between them. Therefore, f is experimentally mode-independent. We fit these data thanks to eq. 4.4, yielding the calibration curve (dark red). When the average temperature is higher than room temperature, the slope of this function is in remarkable agreement with a constant temperature dependence of Y (yellow dashed line).

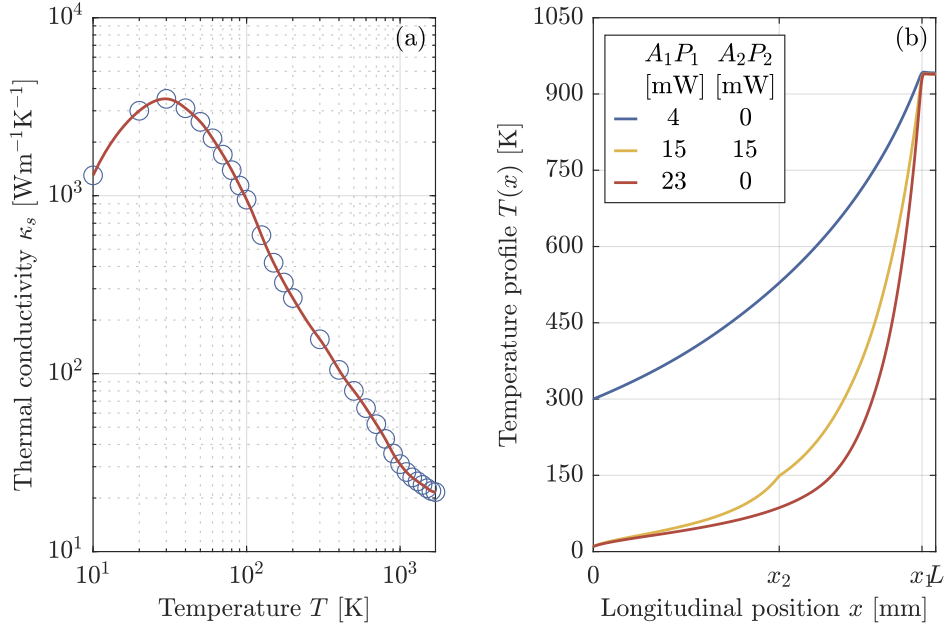


FIGURE 4.2.2: (a) Temperature dependence of the thermal conductivity of silicon $\kappa_s(T)$, tabulated in ref. [102]. $\kappa_s(T)$ is very high at cryogenic temperatures, requiring a strong heat flux to reach a significant temperature difference. (b) A simulated temperature profile reaching $T^{\max} = 950$ K is shown in three different situations: blue curve, the base of the cantilever is at room temperature; red curve, the base is at a cryogenic temperature with one heating source; yellow curve, same but with two heating sources. These are placed at typical values during the experiment: $x_1 = 960 \mu\text{m}$ and $x_2 = x_1 - \Delta x$, with the dimensions of the cantilever the same as the sample of this work. The absorbed power $AP = A_1P_1 + A_2P_2$ is drastically different in the three cases to reach the same T^{\max} : whilst a low power is needed at $T^{\min} = 295$ K, a higher power is required at $T^{\min} = 10$ K, furthermore when AP is divided into two spots.

is shined close to the free end of the sample. When placed at $T^{\min} = 10$ K and irradiated with the same power, though, the yielded ΔT^{\max} is less than 10 K. One difference lies in the very high thermal conductivity of silicon κ_s at low temperatures [45, 102], whilst another difference is due to the presence of two heating sources, after the Savart plates (fig. 4.1.1), possibly with different power.

The thermal conductivity is shown in fig. 4.2.2 (a). Below 100 K, it is one order of magnitude larger than at room temperature. It thus takes a higher heat flux or a longer distance to reach high T^{\max} . To illustrate this behavior, we compute $T(x)$ from $\kappa_s(T)$ in Appendix 4.B, and we report a few examples in fig. 4.2.2 (b). The difference between a situation where T^{\min} is around room temperature vs. a cryogenic situation is remarkable: the temperature profile is significantly more peaked towards the free end of the cantilever, which is mitigated by the presence of the second laser source. At the same total power P , shining all the power in x_1 yields a higher T^{\max} . Nevertheless, this is not experimentally convenient: the interferometer yields the highest sensitivity when the laser power is equally divided between the two beams [87].

We now introduce how to evaluate the temperature profile of the cantilever through a simulation. We write the Heat Law as a Poisson equation:

$$\frac{\partial}{\partial x} \left(\kappa_s(T(x)) \frac{\partial}{\partial x} T(x) \right) + \frac{2\epsilon_s \sigma_{SB}}{H} \left((T(x))^4 - (T^{\min})^4 \right) + B_1(x) + B_2(x) = 0 \quad (4.6)$$

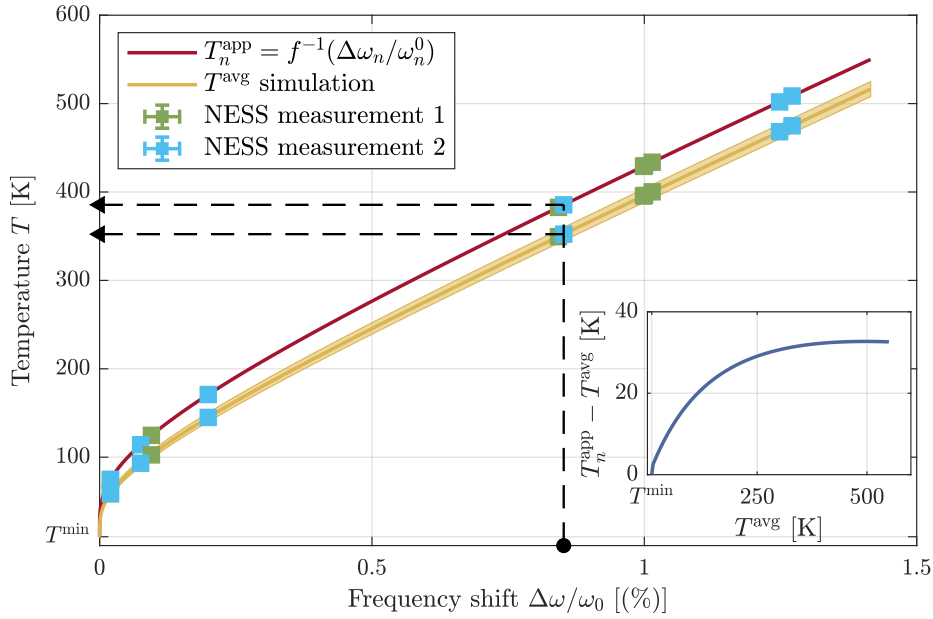


FIGURE 4.2.3: Comparison between T_n^{app} and T^{avg} for the simulated temperature profiles: the apparent temperature T_n^{app} (dark red curve) is inferred from the frequency shift of high modes ($n = 6$ to 9) and the equilibrium calibration (eq.s 4.4 and 4.5). It is very close to the actual average temperature T^{avg} (yellow curve) of the cantilever, which is represented as a yellow shaded area covering all the results of the parametric sweep (see Appendix 4.B). The main source of dispersion is due to the mode number n and is always ≤ 20 K. The temperatures of the NESSs (cyan and green squares) are therefore calculated by projecting the measured $\Delta\omega_n/\omega_n^0$ onto the two temperature curves, in the sense indicated by the dashed black lines. There is a small difference between T_n^{app} and T^{avg} : T_n^{app} overestimates T^{avg} of about ≤ 35 K over the whole temperature range (over 500 K), as depicted in the inset.

where ϵ_s is the emissivity of silicon and σ_{SB} is the Stefan-Boltzmann constant. We suppose the temperature profile unidimensional, condition which is further discussed in Appendix 4.B. The first term represents the conduction, the second the radiation and the others the sources, modeled as a power density:

$$B_i(x) = \frac{A_i P_i}{\sqrt{\pi} H B R_0} e^{-2 \frac{(x-x_i)^2}{R_0^2}} \quad i = 1, 2 \quad (4.7)$$

Here $A_i P_i$ represents the absorbed powers at x_i . Solving this equation yields the temperature profiles shown in fig. 4.2.2 (b). During the experiment several parameters have a high uncertainty or are unknown: the emissivity, the thickness, and the absorbed power at each probing point. Therefore, we sweep the physical value of the most important parameters to generate a family of temperature profiles $\{T(x)\}$, from which the average temperature T^{avg} and a synthetic frequency shift can be calculated (eq. 3.8). Since we expect f_n to be less and less dependent on n with increasing n , we calculate $\Delta\omega_n/\omega_n^0$ for the highest modes available in the experiment: n spans from 6 to 9. From these frequency shifts, we finally compute the apparent temperature of the simulated profile using eq. 4.5. The results are shown in fig. 4.2.3: the average temperature is depicted as a yellow curve, where the shaded area represents the dispersion of the frequency shift between the selected mode numbers, whilst the dark red curve represents the apparent temperature. Therefore, the experimentally measured frequency shifts (cyan and green squares) can be linked to the simulated

average temperature of the cantilever. In the inset, we can see how estimating T^{avg} through T_n^{app} yields an overestimation of the former for up to 35 K.

An interesting result of the simulations is that when $P < 1$ mW the maximum temperature T^{max} differs at most of 8 K from the minimum temperature T^{min} , so that the system in this condition is close to thermal equilibrium.

4.3 Experimental procedure

When a NESS is established, we proceed by measuring the displacement of the cantilever to retrieve its thermal fluctuations. As in the previous chapter, the experiment procedure follows two main steps: S_{EQ} and S_{NESS} .

The first step S_{EQ} corresponds to an equilibrium case, where the cantilever is irradiated with a low power ($P \approx 1$ mW) so that the temperature gradient is small. The second S_{NESS} is a non-equilibrium case, where we shine the sample with high power (up to 40 mW). Each step is further divided into two steps, s_{cal} and s_{meas} .

During s_{cal} , the cantilever is excited through a small hit on the cryostat, prompting relaxation oscillations (ring down) that explore the contrast ellipse C , which is optimized (see [87] for details). The contrast is recorded for a few seconds, in order to properly fit the ellipse to get the calibration coefficients in the post-analysis.

Once the external perturbation has dissipated, the next part s_{meas} consists of measuring the displacement d' of the cantilever. This is repeated as long as the temperature of the cryostat does not change significantly. Indeed, in order to measure the tiny thermal fluctuations of the system, the cryostat has to be turned off. Due to its high thermal capacity, the temperature T^{min} increases slowly, at around 0.18 K/min in our experiment. We repeat the s_{meas} step whilst T^{min} does not change more than 2 K from its value during s_{cal} . This condition is enforced due to the nature of the experiment: we explore how thermal noise evolves with the non-equilibrium average temperature of the cantilever, which can be dependent on T^{min} .

The next step S_{NESS} follows the same principles, with a larger laser power P in order to create a NESS. Unlike in the procedure described in the previous chapter, we do not perform a ramp of increasing and decreasing power, but rather after each S_{EQ} follows one S_{NESS} , and this is repeated for all powers. This way, we have one equilibrium measurement for each non-equilibrium one. Furthermore, the power ramp is randomized, i.e. we do not order the laser powers in any particular way. This is done since T^{min} increases with time, therefore we periodically set it back to the minimum value by turning on the cryostat (always after one complete procedure), such that $T^{\text{min}} \in 9 - 20$ K. Thus, the randomization de-correlates the results from a particular set of parameters $\{T^{\text{min}}, P\}$.

Steps	S_{EQ} ■		S_{NESS} ■	
	s_{cal} ■	s_{meas}^* ■	s_{cal} ■	s_{meas}^* ■
Measured quantities	$T_{\text{cal}}^{\text{min}}, C$	$T_{\text{meas}}^{\text{min}}, d'$	$T_{\text{cal}}^{\text{min}}, C$	$T_{\text{meas}}^{\text{min}}, d'$
Power P [mW]	1		10-40	

TABLE 4.3.1: Experimental procedure. The * steps are repeated while $T_{\text{meas}}^{\text{min}} < T_{\text{cal}}^{\text{min}} + 2$ K.

We summarise the procedure to measure *one* NESS in Table 4.3.1, whilst fig. 4.3.1 illustrates a typical measurement sequence. Once the experiment is concluded, the contrast C

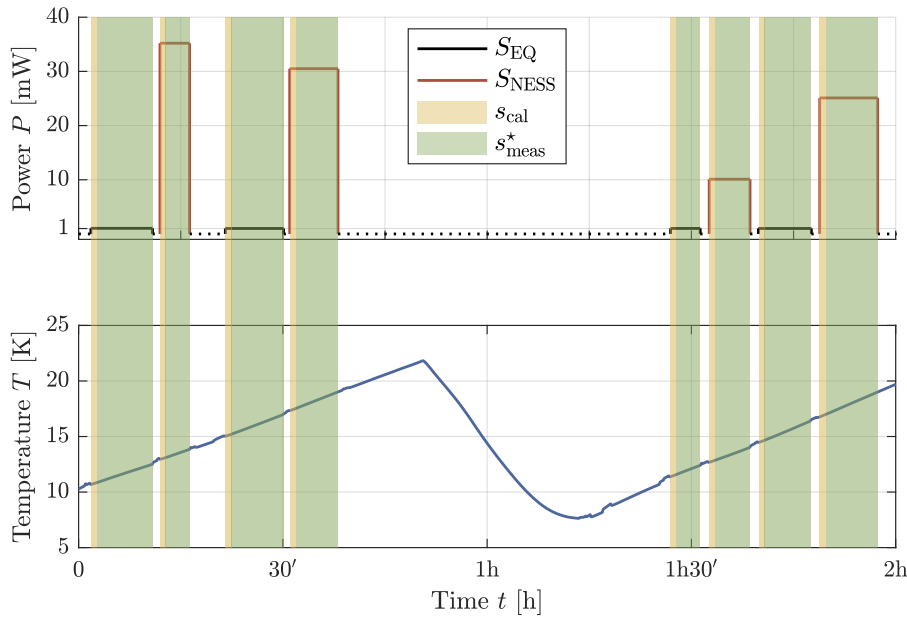


FIGURE 4.3.1: Experimental procedure. In the lower figure, the temperature of the cryostat T^{\min} slowly increases, and it is periodically taken back to its minimum value 10 K. In the upper figure, we show how the equilibrium measurements S_{EQ} ($P = 1$ mW, black) are followed by the non equilibrium ones S_{NESS} ($P = 10 - 40$ mW, red). Each measurement is divided in a calibration s_{cal} (yellow shaded area) and a measurement step s_{meas} (green shade area). In general, s_{cal} lasts less than one minute, whilst s_{meas} lasts between 5 and 10 minutes. The non-colored areas represent the time when no signal is recorded.

measured during s_{cal} is used to calibrate the displacement d' recorded during s_{meas}^* , and the amplitude of fluctuations during S_{EQ} is used to calibrate T^{fluc} during S_{NESS} .

We show a typical camera observation for both S_{EQ} and S_{NESS} in fig. 4.1.2. The upper image depicts the equilibrium measurement, with an almost uniform temperature T^{\min} along the cantilever. In the bottom image, a NESS arises due to a stronger power P injected into the cantilever.

4.4 Results

We now present the experimental observations of two measurement sessions performed on the same cantilever on different days, with different sets $\{T^{\min}, P\}$. We display the fluctuation temperatures and the measured loss angles, then we try to construe these quantities together.

4.4.1 Thermal fluctuations

The results are presented in fig.s 4.4.1 and 4.4.2, showing the output of the experiment in two different runs. Both the flexural and torsional modes demonstrate the same feature: the fluctuation temperatures are *below* the average temperature of the system, therefore showing a lack of thermal noise. We therefore see how C90 presents results very similar to C100, which hints at the possibility of the lack of fluctuation being not only a characteristic of one system, but of a whole class of them. Nevertheless, we note that in both experiments, the fluctuations are not *exactly* constant. They show an increase which looks small with respect to the average temperature T^{avg} , but it is not with respect to T^{\min} . For example, in fig. 4.4.1,

for $T^{\text{avg}} = 350 \text{ K}$, $T^{\text{fluc}} \approx 100 \text{ K}$ for both the flexural and torsional modes, which is roughly 10 times $T^{\text{min}} = 12 \text{ K}$.

It is interesting to discuss the robustness of the results. Firstly, we implement a randomization of the powers and the temperatures of the cryostat within the single experiment, and secondly we repeat the experiment with a different set. The outcome is a similar behavior in the two measurements, and thus we can hereby state that low fluctuations is an intrinsic characteristic of this cantilever.

In Appendix 4.A, we mention the reasons for which some modes are excluded from the results. The figures also show some measurements taken very close to, if not trespassing, T^{melt} : we see a large increase in fluctuations in most modes, as the error bars of the T^{avg} also increase. We know we reach the melting point from camera observations, as well as a smaller light power reflected towards the photodiodes of the QPDI when a hole appears at the spot center. In addition to this, further investigations confirmed structural damage to the material (see fig. 4.B.3). This proves that we are able to reach the $\Delta T^{\text{max}} = T^{\text{melt}} - T^{\text{min}}$.

4.4.2 Dissipation

We show the measured loss angles of the second measuring session in fig.s 4.4.3 and 4.4.4, the first one yielding a similar results. Remembering the measured loss angles of fig.s 3.4.2 and 3.4.3 in the C100 case and judging from the behavior of the fluctuation temperature, we would expect the loss angle to be relatively independent of the temperature increase of the system. However, this is not the case. The retrieved loss angles show a marked increase from the equilibrium case (where they are in the $3 - 6 \times 10^{-6}$ range) and the highest temperature where they are roughly 8-10 times this value. Although there is some mode dispersion, mostly at high temperatures, all the resonances show the same behavior, in both the flexural and torsional cases. It is clear that neither the expected Dirac's delta behavior of C100, nor the parabolic approximation of C30C discussed in the previous chapter can be considered valid anymore, with the loss angles showing a linear increase for $T^{\text{avg}} \leq 100 \text{ K}$ and almost plateauing for higher temperatures. We believe this may be a situation where the loss angle can be described as the sum of the two:

$$\varphi(x) = \varphi_0 \delta(0) + \varphi_1 g(\Delta T(x)) \quad (4.8)$$

with g an unknown function. In the present case, it is hard to imagine linking this function to the shape of the measured loss angles $\varphi_n(\Delta T)$ from the experiment as in the previous chapter, due to few points and the non-trivial shape of $\varphi_n(\Delta T)$. Furthermore, as we discuss in Appendix 4.B, the temperature profile is highly non-linear, rendering a theoretical prediction of T^{fluc} from the experimental data difficult. In the next section, we try to interpret the observed loss angles with the fluctuation temperature in a qualitative manner.

4.4.3 Discussion

As previously shown, in this experiment, we see a drastic dearth of fluctuations for a system as far from equilibrium as possible, with a $\Delta T^{\text{max}} \approx 1600 \text{ K}$. As usual, we interpret this result through a measurement of the loss angle, which somehow unexpectedly shows a drastic dependency on the temperature of the system.

The measurement of φ being extremely delicate, we therefore need caution when construing the results. Firstly, the absorption of the cantilever is highly non-linear, and a small change of laser power can drastically change the temperature of the sample, and thus the position of the resonances. Due to the extremely quick diffusion, this change can happen

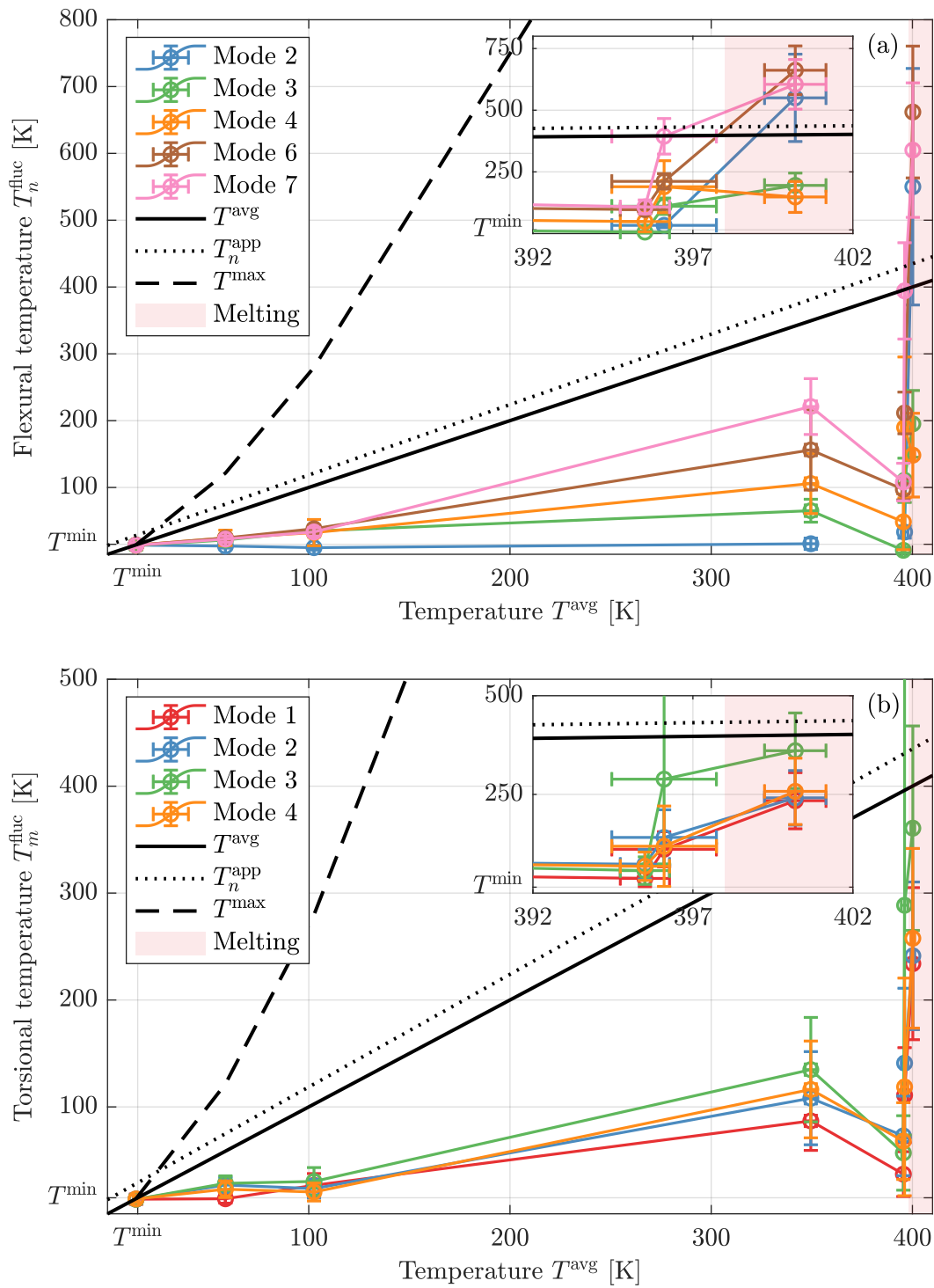


FIGURE 4.4.1: Fluctuation temperature vs. average temperature. In (a), the flexural T_n^{fluc} is shown with respect to T^{avg} . The black solid line represents the "equilibrium" temperature, i.e. the fluctuations an object would show if it was in thermal equilibrium with a thermal bath at T^{avg} , whilst the black dotted line shows the apparent temperature T_n^{app} . All the modes lie below these lines, showing a dearth of thermal noise. It is nevertheless important to note that the noise is not perfectly independent from T^{avg} . For example, T^{fluc} is roughly 10 times the temperature of the clamped end at $T^{\text{avg}} = 350$ K. This effect is even more marked at higher T^{avg} . The modes shown span from 2 to 7, excluding mode 5 because of the laser probe resting on a node. In (b), the same scenario is shown for the torsional degrees of freedom, with modes 1 to 4. Also in this case, the fluctuations are roughly constant below 100 K and then increase, still remaining well below T^{avg} . Finally, the red-shaded area covers measurements where observations suggest that at least a partial melting of the cantilever occurred. It is remarkable that in this area the fluctuation temperature greatly increases for most modes in both motions.

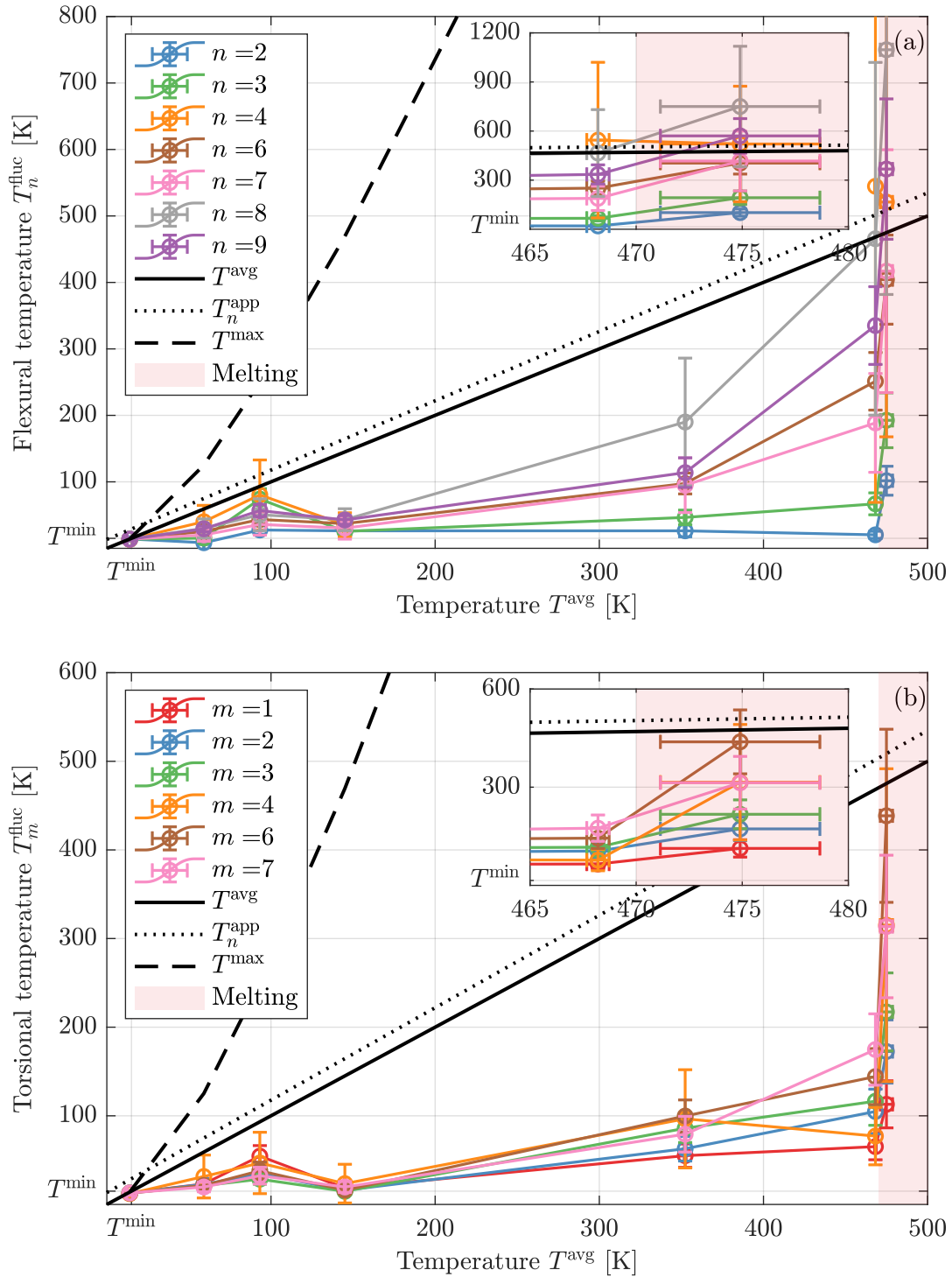


FIGURE 4.4.2: Fluctuation temperature vs. average temperature. In figure (a), the flexural fluctuations temperatures T_n^{fluc} show a behavior similar to the ones in fig. 4.4.1 (a). Indeed, the noise is decidedly below the average temperature of the system, nevertheless showing an increase around $T^{\text{avg}} = 350$ K. This is even more clear in (b) for the torsional resonances, where the dispersion of the modes is smaller. The agreement between this experimental session and the precedent one is remarkable, showing very compatible results. In this case, the flexural modes span from 2 to 9, excluding mode 5 because of the laser probe being close to a node, and the torsional modes from 1 to 7 (where mode 5 is omitted for the same reason).

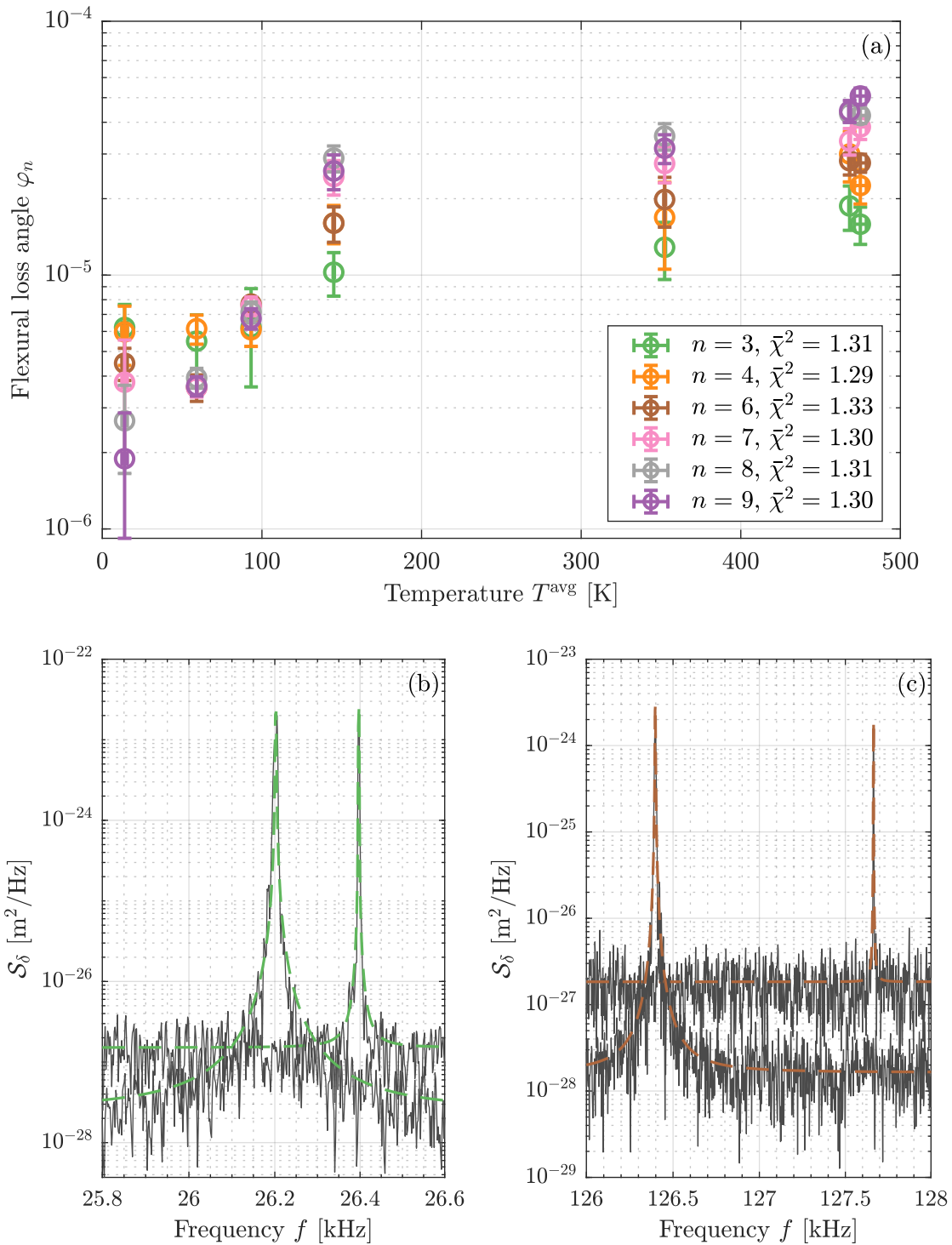


FIGURE 4.4.3: In (a), the flexural loss angles φ_n are shown with respect to the average temperature of the system T^{avg} . We note how they all show a similar behavior, with some dispersion towards the highest temperatures. With an equilibrium value around $3 - 6 \times 10^{-6}$, φ_n increases up to $6 - 8 \times 10^{-6}$ at 100 K, then it is almost unchanged between 150 – 500 K at around $1 - 2 \times 10^{-5}$. We also report the average of the accuracy of the fits at the given temperature, $\bar{\chi}^2$, which is comfortably close to 1. As a side note, mode 2 is not reported due to the poor sample size once the $\chi^2 \leq 2$ sort is made. In (b), the resonance peaks in equilibrium and in a NESS for $n = 3$ are shown, with the former being at higher frequency with respect to the latter. We report also the fits of the data, visually showing how the dissipation looks higher in the NESS, with the resonance peak being broader. In (c), the same is displayed for $n = 6$.

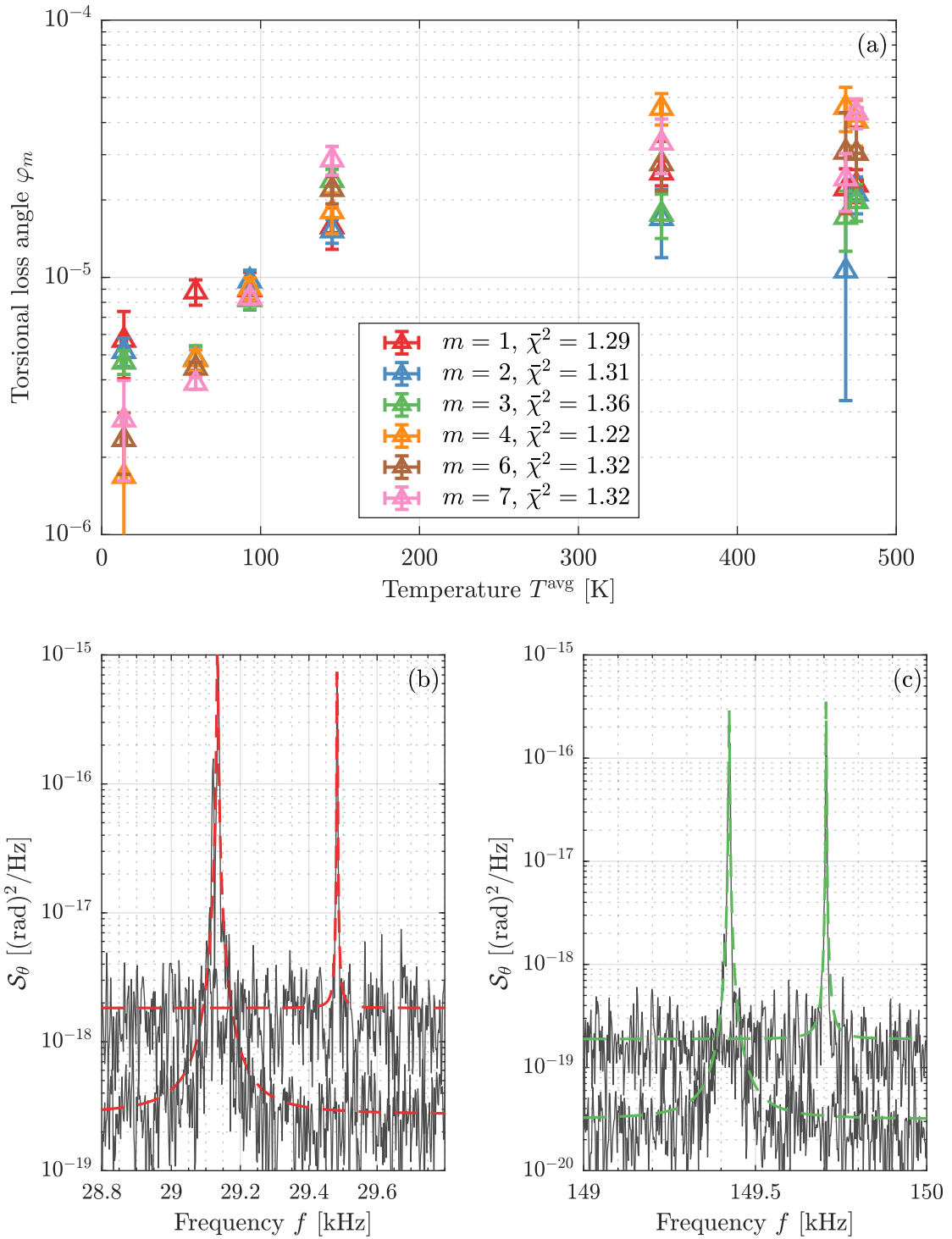


FIGURE 4.4.4: In (a), the torsional loss angles φ_m are reported at increasing T^{avg} . We can notice the same behavior of the flexural loss angles, with roughly the same values at the same temperatures. We can see that mode 1 shows an odd value at $T^{\text{avg}} = 50$ K. Also in this case, it looks like there are two separate regions, until $T^{\text{avg}} = 150$ K with φ_m increasing steadily and a plateau after. In (b), the first resonance mode is shown for an equilibrium (higher frequency) and a NESS case (higher frequency), displaying a clear increase in dissipation. In (c), the same is done for $m = 3$.

during the measurement which hinders a good fit. For this reason, many measurements yield a $\chi^2 \geq 2$ and are thus discarded. This way, the sample size is sometimes reduced, which results in a higher difficulty to assign a precise value to φ . Secondly, the values of the loss angles are extremely low, which would require small frequency bins in the spectra in order to have a fair number of points around the resonance. Nevertheless, this needs to be optimised with respect to the time duration of the displacement signal from which we extract the spectrum (and the relative averages), since the frequency of the resonances is changing with the absorbed power.

Despite these possible issues, we believe the measured damping to be representative of an intrinsic property of the sample. Indeed, all the resonances show the same behavior, which indicates that a phenomenon is indeed occurring in the cantilever when heated. Moreover, the χ^2 of the retained fits is excellent.

As noted, the description valid for C100 cannot be considered strictly valid here. Whilst the fluctuations of C100 are roughly constant at the value of T^{\min} , in this case they increase at more than 10 times this value, which is still considerably less than the average temperature of the system T^{avg} . In this case, it is not odd that φ increases with the temperature. We believe we have a system showing both clamping dissipation and longitudinally-spread dissipation, with the first playing an important role in lowering the value of the fluctuations below the average temperature.

4.5 Conclusions

In this chapter, we test the extended FDT at its physical limits. We impose almost the highest possible temperature difference the system can sustain and measure the out-of-equilibrium fluctuations T^{fluc} . In order to compare them with the temperature of the cantilever, we carefully analyse how to retrieve the average temperature T^{avg} through both an analytical method and simulations. We then show that the cantilever displays a significant lack of fluctuations however out of equilibrium it is. We summarise the results in fig. 4.5.1, where we show the fluctuation temperatures normalised by T^{avg} vs. the similarly normalised temperature difference ΔT .

Whereas in previous experiments $T^{\min} \approx 300$ K, in this chapter we have shown that our extension of the FDT applies when $T^{\min} \approx 10$ K, thus extending the validity of the precedent results and the experiments reported in [42, 40]. Through the measurement of the dissipation, we show that the lack of fluctuations cannot be solely explained by a clamping losses, but rather that the internal dissipation of the sample needs to be taken into account. We thus extend the ensemble of the systems which show lack of fluctuations, until this point represented by C100 and some modes of C30. We demonstrate that a cantilever with distributed dissipation can oscillate less than its average temperature dictates, whatever the temperature profile it is subjected to.

As a consequence, we believe that these results have a broad range of applications. Alongside previously-described experiments, for example nano-mechanical resonators strongly out of equilibrium [27], the GW community could greatly take advantage of our study. Our samples, extremely thin and long silicon cantilevers, might be a testing bench for studies around the suspension systems in cryogenic GW detectors [93, 6]. In these experiments it is customary to assume that a temperature gradient is unwelcome, in order to avoid increasing thermal noise both in the suspension itself and in the test mass. Whereas our results do not affect this statement for the test mass, they suggest that the thermal fluctuations of the suspensions might be unaffected by the temperature gradient. Thus, optimisation

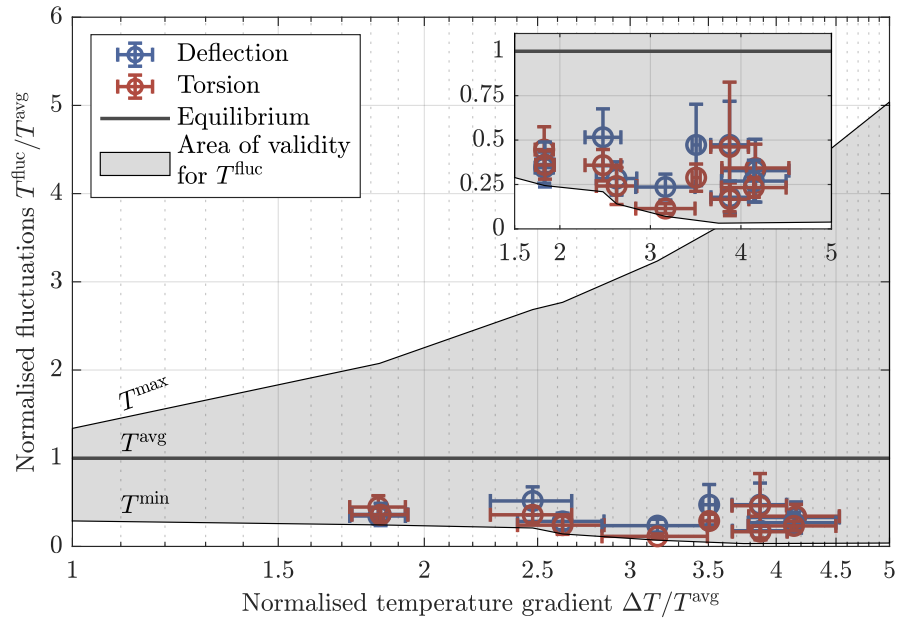


FIGURE 4.5.1: Normalised fluctuation temperature vs. temperature gradient: the non-equilibrium noise is shown in contrast with the meaningful temperatures of the system. The horizontal axis represent the temperature gradient for each NESS normalised by the respective average temperature. The vertical axis displays the average of the flexural modes and the average of the torsional modes for both the experiments, also normalised. We limit ourselves to measurements where no melting occurred. The equilibrium is represented by the horizontal solid line, depicting the value the fluctuations should have in order to mimic a system in thermal equilibrium at $T^{\text{fluc}} = T^{\text{avg}}$. The grey shaded area represents the validity of eq. 2.81: the fluctuations can occur at temperatures between the minimal temperature T^{min} (the lower bound) and the maximal T^{max} (the upper bound). The measured fluctuations are all below the equilibrium line and very close to the lowest available temperature, showing values 10 – 50 times lower than the maximum temperature available.

of suspensions could be facilitated by relaxing the constraint of having no temperature difference along their length, albeit taking great care on the effect of a residual temperature existing in the mirrors. Furthermore, the material used in the current experiment is silicon, one of the main candidates for ET. We probe its thermal fluctuations up to its melting point, showing a remarkable lack of fluctuations that could surely be appealing for the fabrication of the suspension system.

In conclusion, few experiments take into consideration such physical extremes as the ones presented here: cryogenic temperatures are just 1 mm apart from melting ones, probing the very far out-of-equilibrium. This experiment shows how it is possible to have a system oscillating hundreds of degrees less than its average temperature, when one of its end is close to its melting point. We have probed an extension of the FDT to its furthest limits, confirming previous results and improving their robustness. Future work might include studying systems with a non-localised dissipation, or with dissipation localised at a specific point different than the clamping.

Appendix

4.A Sensitivity of the QPDI

As depicted in fig. 4.1.1, the QPDI measures a displacement $d' = d_1 - d_2$. This is proportional to the real displacement d through the sensitivity of the instrument σ , as discussed in the previous chapter. In this experiment we can neglect any contribution from the finite size of the laser spot, since its waist is very small compared to the typical length of the highest measured mode¹. Since the interferometer directly reads the displacement perpendicular to the probing beam, the flexural sensitivity is:

$$\sigma_n^\delta(x_1, x_2) = \phi_n(x_1) - \phi_n(x_1 - \Delta x) \quad (4.9)$$

hence:

$$d(x_1) - d(x_2) = d(x_1) - d(x_1 - \Delta x) = d'(x_1) = \sigma_n^\delta(x_1) \delta_n \quad (4.10)$$

With this, we can estimate the probing point taken during S_{EQ} , which we report in fig. 4.A.1 for the second set of measures (since they present more modes). We notice how all the curves converge towards a single x_1 . Furthermore, the effective masses normalised to that of the second resonance show that modes 5 (not used in the calculation of ϵ) and mode 4 yield high values, due to the closeness of x_1 to one of their nodes. Thanks to this, it is then possible to calibrate the deflection of the cantilever in a similar way as seen in Sec. 3.A.2, and associate the systematic error to the T_n^{fluc} .

During the measurement, the probing point changes for various reasons. One is that when we turn on and off the cryostat, x_1 changes, and even if we place it back at its original place thanks to the camera, this cannot be totally accurate. Another cause are the possible drifts dx , which in this experiment are quantified around $2 \mu\text{m}$ to be conservative. In fact, the two $S_{EQ} - S_{NESS}$ steps are performed in a short time and drifts are less likely. Moreover, the cantilever is two times as long as C100 and due to the extreme conditions it is subjected to, we believe this to still be a meaningful value. A third reason is the melting. As shown in fig. 4.B.3 in fact, this happened several times, so after we move the spot in order to avoid probing the corrupted point. For these reasons, in fig. 4.A.1 we can see that x_1 assumes slightly different values from one measurement to the other.

With an interferometric reading, the torsional sensitivity depends on the transverse position y . The spatial shape of the torsional modes is:

$$\Phi_m(x, y) = y \phi_m(x) \quad (4.11)$$

The sensitivity is thus:

$$\sigma_m^\theta(x_1, x_2, y_1, y_2) = |\Phi_m(x_1, y_1) - \Phi_m(x_2, y_2)| = y_1 |\phi_m(x_1) - \phi_m(x_2)| \quad (4.12)$$

¹With a waist diameter $\approx 10 \mu\text{m}$ the laser beam is 10 times smaller than half the spatial period of the cantilever for the highest available mode, 9: $\lambda_9/2 \approx 100 \mu\text{m}$.

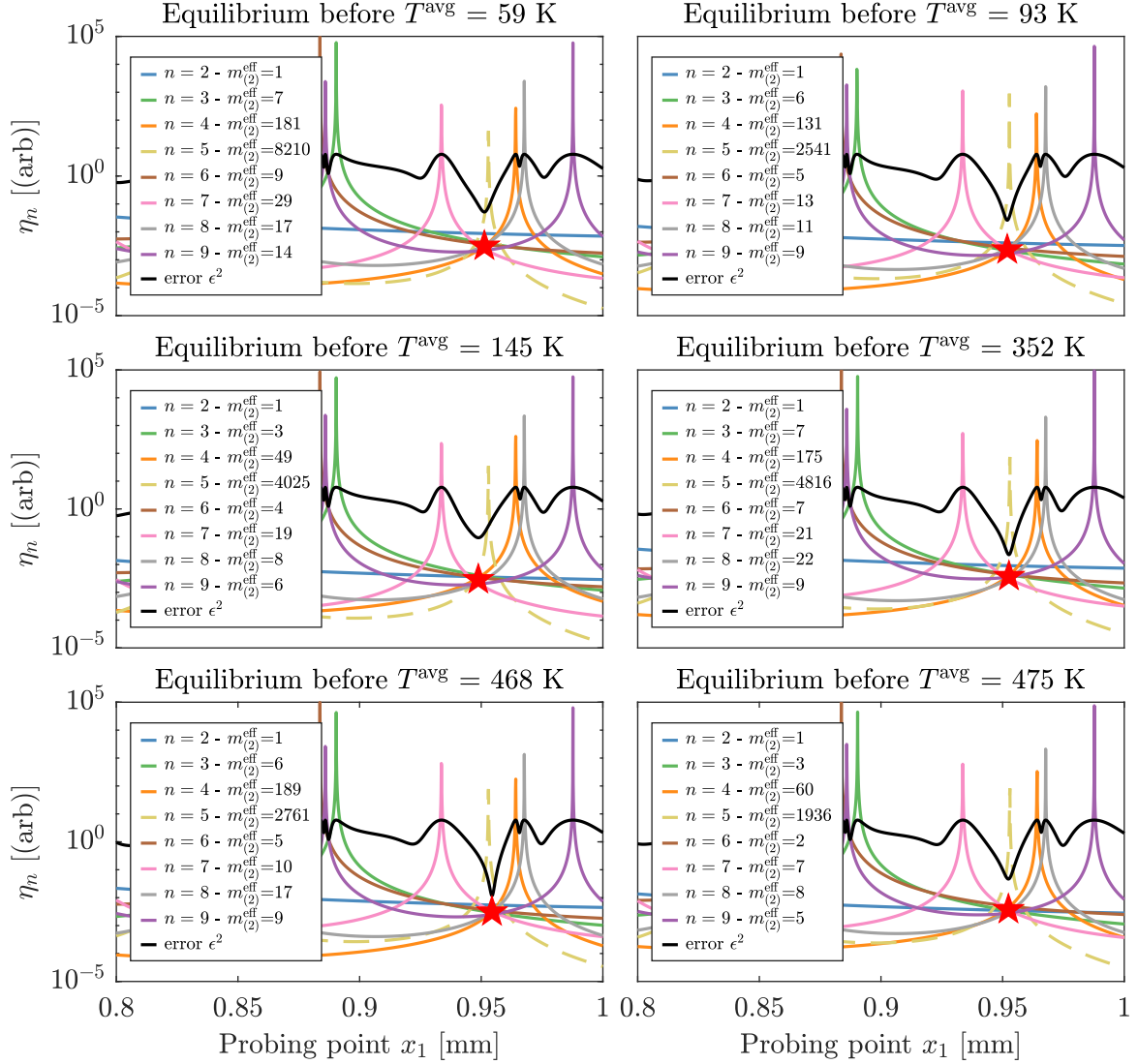


FIGURE 4.A.1: Sensitivity for flexural modes: the quantity $\eta_n(x_1)$ is independent of n for a unique value of x_1 close to the end of the cantilever. The black solid line represents the square of the standard deviation over n of η_n divided by its mean, for each x_1 (calculated excluding mode 5). It presents a minimum at the actual measurement point. The effective masses of the modes are given in the graph legends, normalised by the one of the second mode. We see how modes 4 and 5 have high values, meaning that the respective $\omega_n^2 \langle \delta_n'^2 \rangle$, i.e. the thermal noise, presents a large uncertainty due to the proximity of x_1 to one node of these modes. Also modes from 7 to 9 show a high m^{eff} . We can see that each T^{avg} corresponds to slightly different x_1 , the reasons for which are explained in the text. The average between the actual measurement positions throughout the whole experiment is $x_1 = 952 \pm 1 \mu\text{m}$.

since $y_1 = y_2$ if the spatial separation of the laser spots is purely along x . In fig. 4.A.2 we show the results. We note that the η_m converge towards a slightly different x_1 with respect to the η_n , with a difference around 1%. In this experiment the discordance of the flexural and torsional modes is then lower than the C100 case. We believe this to be due to the shape of C90 which is devoid of a triangular end, being closer to an ideal beam.

We note that this method does not let us estimate y_1 : since both the standard deviation and the average of η_m along y_1 have the same shape (due to the linearity of Φ_m in y), their ratio is independent on y . Nevertheless, since x_1 is precisely known, we can calibrate y_1 thanks to camera images. Finally, from these results, we can calibrate the torsional displacements and calculate the ϵ_m^{sys} .

4.B Temperature estimations

In Sec. 4.2 we have shown how we extract the average temperature information from the the frequency shift of the high frequency modes. Whilst the temperature at the base of the cantilever T^{min} is known, the temperature profile $T(x)$ is unknown and should be estimated through simulations. As mentioned, this is highly non linear due to the shape of the thermal conductivity κ_s and the presence of two thermal sources (fig. 4.2.2). We have already introduced the one-dimensional problem in eq. 4.6, nevertheless let us start considering the problem two-dimensional. In fact, since the cantilever's plane dimensions are much larger than its thickness ($L/H = 10^3$, $B/H = 90$), the correct dimensionality of our cantilever is two. We follow the work of [91] in the next discussion. We write the Heat Law for the 2D temperature field $T(x, y)$ in the shape of a Poisson equation:

$$\nabla \left(\kappa_s(T(x, y)) \nabla T(x, y) \right) + \frac{2\epsilon_s \sigma_{SB}}{H} \left((T(x, y))^4 - (T^{\text{min}})^4 \right) + B_1(x, y) + B_2(x, y) = 0 \quad (4.13)$$

with the first term representing the conduction, the second the radiation and the last two the sources, modeled as a power density:

$$B_i(x, y) = \frac{A_i P_i}{\pi H R_0^2} e^{-2 \frac{(x-x_i)^2 + (y-y_i)^2}{R_0^2}} \quad (4.14)$$

with $i = 1, 2$. Here, $A_i P_i$ represents the absorbed power in each spot (x_i, y_i) , and R_0 is the waist of the focused laser. In the previous equation, ϵ_s is the emissivity of silicon and σ_{SB} is the Stefan-Boltzmann constant.

The function $\kappa_s(T)$ is tabulated [102] and depicted in fig. 4.2.2. The nominal thickness of the cantilever is known, although with an important uncertainty ($H = 1 \pm 0.3 \mu\text{m}$). Nevertheless, we can deduce its value looking at the flexural resonance frequencies and confronting these values with the Euler-Bernoulli prediction. This gives $H = 1.1 \pm 0.1 \mu\text{m}$, which is confirmed by Scanning Electron Microscope (SEM) images. The emissivity is unknown and it varies greatly at high temperatures [57], where the radiation term is more relevant. A first approximation is to consider ϵ_s as free parameter (independent of the coordinates) to be adjusted. Finally, the absorbed power is also unknown: during the experiment we measure the total injected power, with no control over the absorption.

Considering all these free parameters, we do not expect the temperature profile to perfectly match the one in the experiment, therefore the results of the simulation should be taken as an order of magnitude estimation. We report the outcome in fig. 4.B.1. A temperature profile with a particular choice of parameters is presented, showing the bi-dimensional nature of $T(x, y)$, with the temperature peaked around the two laser spots. From it, the

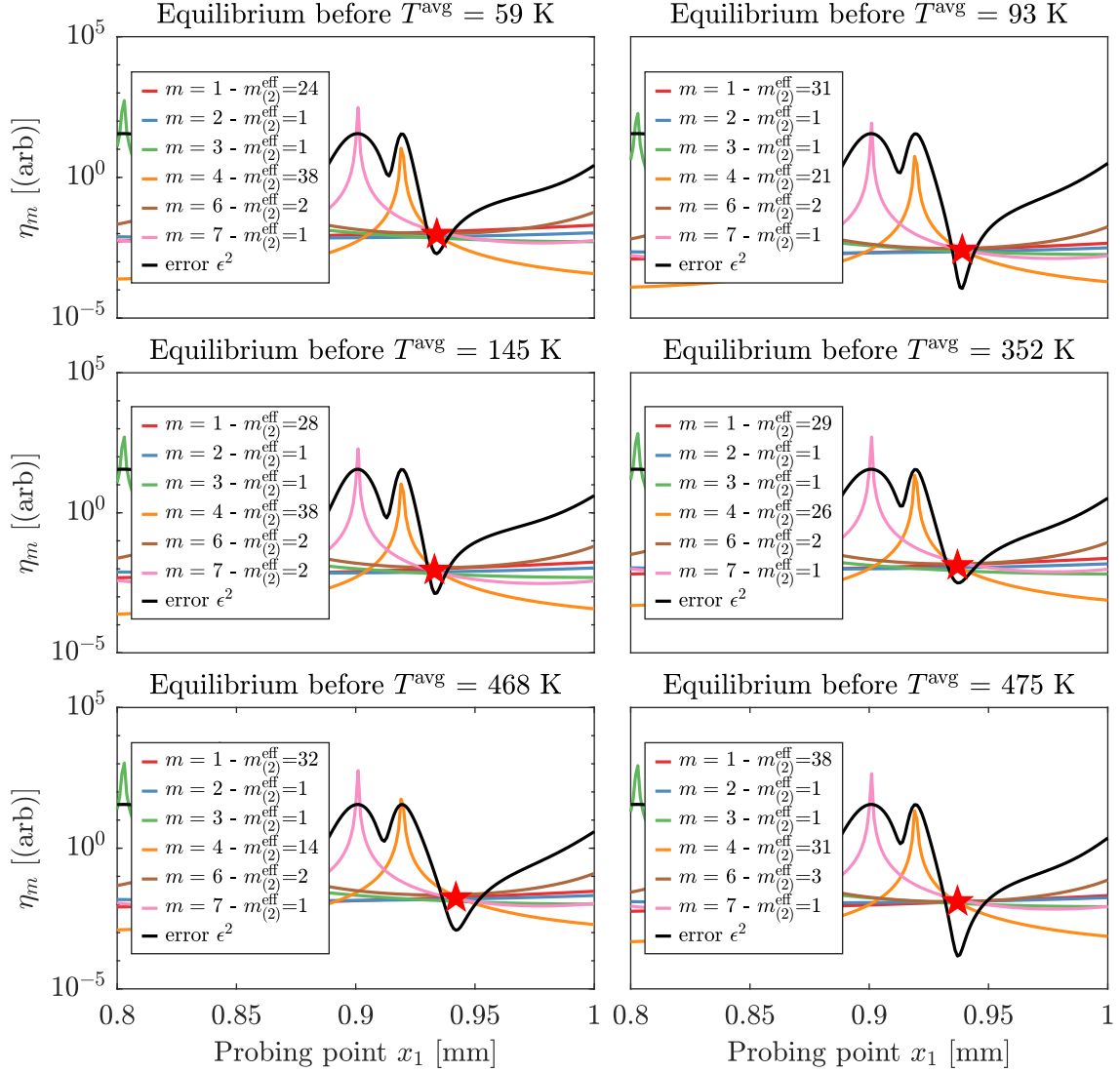


FIGURE 4.A.2: Sensitivity for torsional modes: the quantity $\eta_m(x_1)$ is independent of m for a unique value of x_1 close to the end of the cantilever. Mode 5 is not displayed due to the fact we do not detect it during the experiment. The black solid line represents the square of the standard deviation over m of η_m divided by its mean, for each x_1 . It presents a minimum at the actual measurement point. The effective masses of the modes is given in the graph legends, normalised by the one of the second mode. We see how mode 1 presents high values, which cannot be linked to it being close to a mode. Instead, $\langle \delta_1'^2 \rangle$ is relatively low compared to the value for mode two, yielding a huge m^{eff} . Also mode 4 yields a high effective mass, this time since x_1 is close to a node of sensitivity. The average of the actual measurement positions throughout the whole experiment is $x_1 = 937 \pm 2 \mu\text{m}$, showing a difference of around 1.5 % with respect to the flexural modes. This similarity of predictions in estimating x_1 is decisively better than in the C100 experiment.

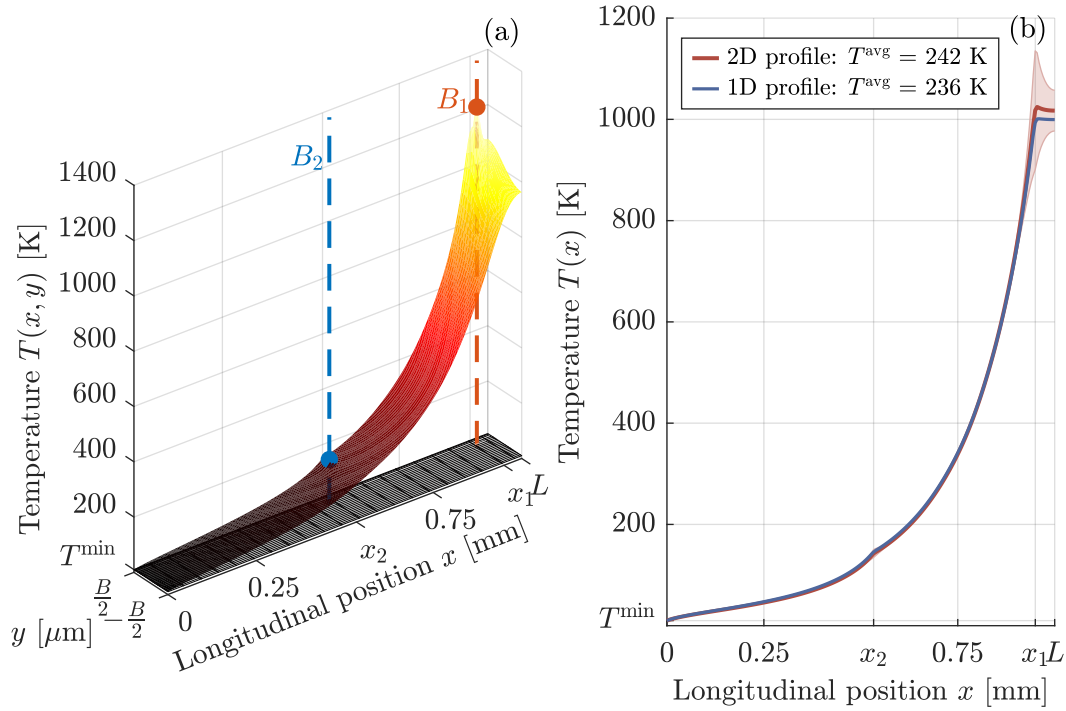


FIGURE 4.B.1: 2D vs 1D temperature profile: a two-dimensional estimation $T(x, y)$ is compared with a unidimensional $T(x)$. In (a) we can see a temperature profile with two beams shining the cantilever at $x_1 = 950 \mu\text{m}$, $x_2 = x_1 - \Delta x$, $y_1 = y_2 = 36 \mu\text{m}$, with equal absorbed power $A_i P_i = 14.5 \text{ mW}$. We consider $\epsilon_s = 0.5$ and $T^{\min} = 10 \text{ K}$. At x_1 (the highest temperature point), we reach a temperature difference of around 200 K along y , showing an important two-dimensional feature. Moreover, a second bump is visible at x_2 . In (b), we see that a one-dimensional profile represents quite well the 2D-one: the dark red solid line represents the average temperature integrated along y , whilst the red shaded area is the standard deviation of its values. The dark blue curve is an unidimensional profile calculated for the same parameters: not only the red and blue curves have a very similar profile, but also they predict similar average temperature T^{avg} . Even for higher power, the 1D T^{avg} differs from the 2D one by 5% at most.

simulated average temperature T^{avg} is calculated as:

$$T^{\text{avg}} = \frac{1}{LB} \int_0^L dx \int_{-\frac{B}{2}}^{\frac{B}{2}} dy T(x, y) \quad (4.15)$$

A simpler choice is to consider the problem unidimensional, thus integrating along the transversal dimension y . Doing this greatly reduces the simulation time, and we can observe the effect in fig. 4.B.1 (b). Albeit the two-dimensional profile integrated along y shows some differences with respect to the one-dimensional one, this effect is relatively small: the calculated average temperatures differ at most of 5% in the whole parameter range. We believe this uncertainty acceptable, therefore we proceed considering 1D profiles $T(x)$.

We then continue with a parametric sweep of the aforementioned meaningful quantities, in order to retrieve the family of temperature gradients $\{T(x)\}$. We report the selection of parameters in Table 4.B.1.

As previously mentioned, equally dividing the light between x_1 and x_2 yields the maximum sensitivity. Nevertheless, the absorbed power of the two beams can differ, since absorption and reflectivity are functions of temperature. Since we cannot measure this, we

	ϵ_s	H [μm]	T^{\min} [K]	a	AP [mW]	n
Parameter range	0 - 1	1-1.2	10-20	0.3 - 0.7	1-35	6-9
Central value	0.5	1.1	15	0.5	1-35	7

TABLE 4.B.1: Parameter range for the temperature profile simulations.

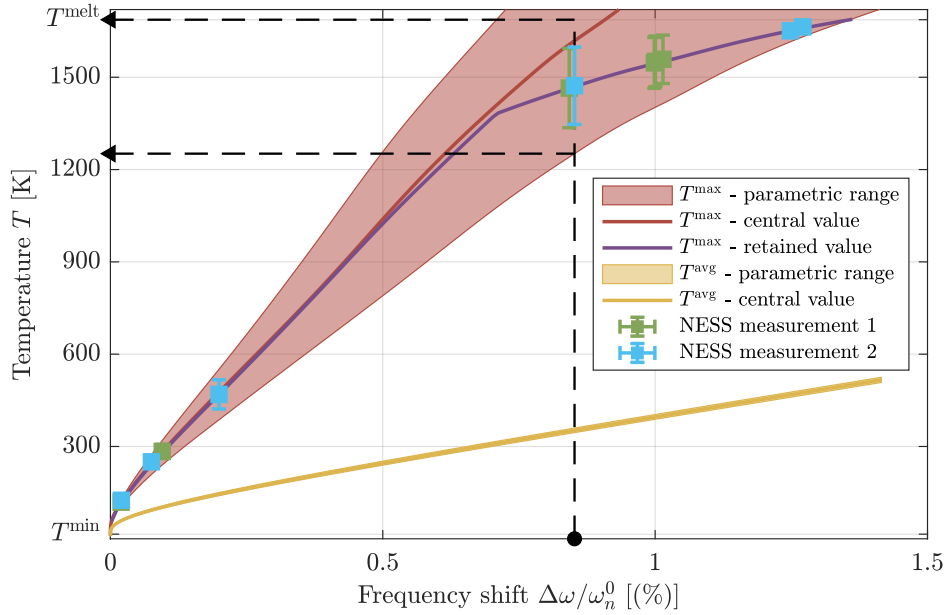


FIGURE 4.B.2: Estimation of T^{avg} and T^{max} : from the parametric sweep reported in Table 4.B.1, we estimate the possible values of the average (yellow curve) and maximum temperature (red curve) of the cantilever, at the same time of the frequency shift for the mode numbers 6 to 9. Whereas for one value of $\Delta\omega_n/\omega_n^0$ the dispersion of T^{avg} (yellow shaded area) is small, this is not true for T^{max} (red shaded area). No bijective relation is possible, thus we estimate T^{max} as the average of a uniformly distributed variable between the possible values (black dashed lines). The purple curve represent the retained value of T^{max} for each frequency shift, and the cyan and green squares are the experimental values.

include in the simulation the possibility of the ratio:

$$a \equiv \frac{A_1 P_1}{A_1 P_1 + A_2 P_2} \quad (4.16)$$

being different from 0.5. As it turns out, this is the most important parameter in prescribing the shape of $T(x)$, and thus T^{avg} . On the other side, smaller H and ϵ_s , and higher total power $AP = A_1 P_1 + A_2 P_2$ yields a higher T^{max} . For each $T(x)$, the relative frequency shift $\Delta\omega_n/\omega_n^0$ is calculated for the mode numbers 6 to 9: we show the results of the sweep in fig. 4.B.2. The solid curve represents the calculated temperature for the central value of the parameters in Table 4.B.1 and the shaded area all its simulated values. Let us discuss T^{avg} and T^{max} separately.

In Sec. 4.2 we made use of this simulation to retrieve the average temperature of the cantilever in the experiments (fig. 4.2.3) and it is the one used throughout this work. The uncertainty is small, mainly given by the standard deviation of the simulated frequency shift, which can be seen in fig.s 4.4.1 and 4.4.2.

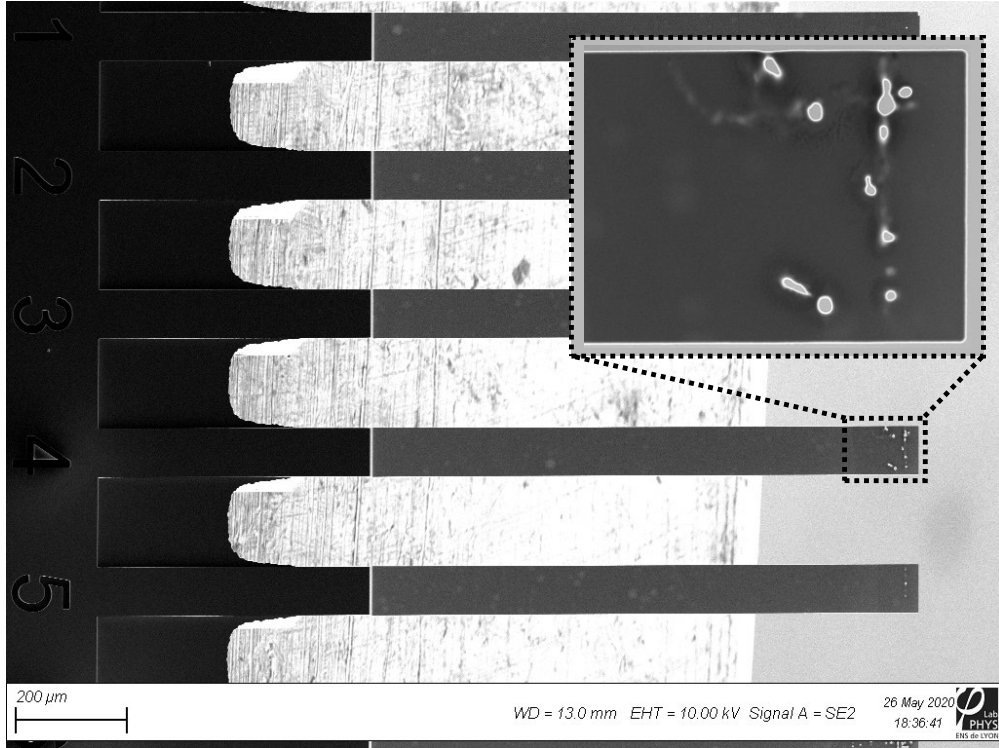


FIGURE 4.B.3: A photo of the cantilever used in the measurements of this chapter, by L. Bellon. As we can see, the sample shows some holes, where the laser melted the material. During the experiment it is easy to evince when this happens from camera observations and the retrieved reflected power. When this happens, we move the probing point x_1 before the next measurement.

On the other side, the maximum temperature varies greatly within the simulation. We set an upper bound to its values at the melting temperature T^{melt} , since we aim to retrieve T^{max} for the measurements where we did not melt the cantilever. In fact, from camera and intensity observations we can discern when we damage the cantilever, hence for the measurements where this is not the case it is reasonable to assume $T^{\text{max}} < T^{\text{melt}}$. Since no other constraint can be safely applied, a whole interval of values of T^{max} can correspond to each measured frequency shift. We therefore assume that the maximum temperature is uniformly distributed, with as average the center of this interval and uncertainty the corresponding standard deviation. It is clear that the upper bound biases the uncertainties for very high values, since the interval is very small. As a side note, in fig. 4.B.3 we show a picture of the cantilever after the whole experimental session, where we can notice the locations where we melted the cantilever. When this happened, we simply moved the probing point.

Let us now briefly discuss the limits of our temperature model. Firstly, corrections on the bulk thermal conductivity due to the low dimensionality of the sample might be necessary. We nevertheless believe that if phonon confinement has some impact, it is small. In fact, a rough estimation of the mean free phonon path λ_p in the cantilever yields $\lambda_p \approx 1 \mu\text{m}$ at room temperature, the same order of magnitude of the thickness H . Thus, if some effects of confinement arise, we do not expect them to be preponderant. Another uncertainty derives from the approximation of constant emissivity, which is nevertheless important solely at high temperatures, where the dispersion of the results is already wide. Finally, we have shown how the influence of the 2D effects on the temperature profile yields an error, although within reasonable limits. All in all, we believe that the results shown in this section represent the physical system in a more than satisfying way.

Chapter 5

Thermal noise of a macroscopic oscillator

In the previous chapters of this thesis, we study the thermal oscillations of micro-cantilevers in a NESS, showing how they are prescribed by the local mechanical energy dissipation function following our extension of the FDT. We mention the importance of this kind of studies in many contexts, spanning from purely theoretical statistical physics to fabrication of mechanical devices. In particular, we discuss the possible uses of our results in one of the most thriving topic of modern physics, GWs detection.

Up until now, we show that it is possible for a microscopic system such as a cantilever to show a dearth of fluctuations with respect to its average temperature if its dissipation is mostly localised where the minimal temperature T^{\min} is. This is true independently of whether T^{\min} is the room temperature one or close to 10 K. Conversely, a distributed dissipation prompts fluctuations on the order of the average temperature of the system. Our formulation of the extended EP, which has proved correct so far, tells us that we can successfully forecast the fluctuations of a microscopic object to be bounded by the minimal and maximal temperature it is in contact with. As discussed, this may be interesting in designing the suspension systems of future GWs detectors.

Nevertheless, these structures are *macroscopic*, and the conclusions we have reached so far could not be applicable. An experiment directly tackling this question is the Non Equilibrium Thermal Noise (NETN) project, located in the Laboratori Nazionali di Legnaro (LNL) in Padua. It is lead by Dr. L. Conti in the VIRGO collaboration, as a mean to investigate the effects of a temperature difference in the thermal noise of test masses of GWs detectors. As shown in [29, 30], an aluminium oscillator is brought in a NESS, and its thermal fluctuations are measured. These depict a picture we cannot explain with our theoretical framework: the non-equilibrium fluctuations not only exceed the average temperature of the system, but also the *maximal* one. In this case, a simple question arises: is our extended FDT valid only for small systems?

In this chapter, we discuss the latest outcomes of this experiment, for which I had the occasion to contribute. I spent one month in the LNL under the supervision of L. Conti and G. Ciani in order to accomplish two goals: first, to modify the existing detection system [90], which finally resulted in a full-scale implementation of a QPDI as the one described in the previous chapter; and second, to set the oscillator in a NESS and to test the aforementioned results.

The first part of this chapter discusses in detail the experimental setup and the physical system, showing how we can retrieve the displacement of the oscillator from the interferometric signal. Further details are given in Appendix 5.A. We then discuss the nature of the

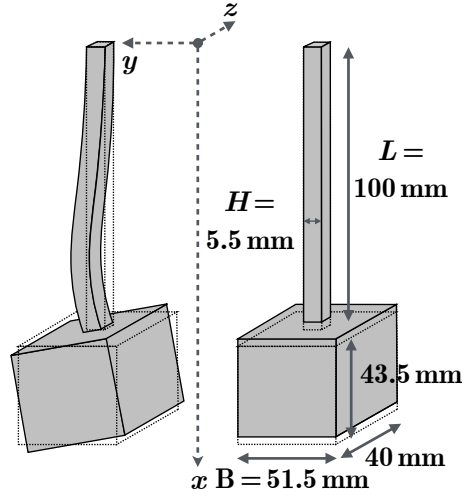


FIGURE 5.1.1: The physical system considered is an aluminium cuboid monolithically clamped to a rod of length $L = 100$ mm and square cross section $H^2 = (5.5 \text{ mm})^2$. The cuboid side is roughly $B = 50$ cm. In the picture, we depict the two motions of the oscillator, a transverse mode (left) and a longitudinal one (right).

two relevant resonances of the oscillator.

The second part briefly focuses on the temperatures of the system and how to retrieve them, whilst the following one describes the experimental procedure.

The following section shows the results, depicting the improvements to the setup and the thermal noise measurements, alongside the measured loss angles. Finally, a discussion concludes this chapter.

5.1 Experimental setup

The physical system is an aluminum cuboid monolithically clamped to a square cross section rod which is suspended at the top end. The mass-rod-suspension is constructed from a single piece of Al5056. The length of the rod is $L = 100$ mm, and its cross section is $H^2 = (5.5 \text{ mm})^2$ [62]. The side of the cuboid is roughly 5 cm (see 5.1.1), where the lower face is polished to be sufficiently reflective. The goal of the experiment is to create a steady temperature difference ΔT between the top end and the mass through a thermal source, hence a NESS. Therefore, the thermal fluctuations of the oscillator are measured following the two motions depicted in fig. 5.1.1. In the past, these were retrieved thanks to a capacitive readout, which is described in [62] (with more details about the oscillator).

Starting with the work of A. Pizzella [90], the experiment moved from the capacitive readout to an interferometric one, which was further developed and completed during my tenure in the laboratory. The choice to move towards interferometric measurements comes from the will to avoid the systematic errors the capacitive readout is afflicted by. Indeed, due to the thermal expansion of the material when the temperature is increased, the sensitivity changes, prompting biases in the calibration.

The current readout is a QPDI, similar to the one used in the previous chapter and described in [85, 87]. A simplified version of the current NETN setup is shown in fig. 5.1.2: the oscillator is mounted in a vacuum chamber at $\leq 5 \times 10^{-2}$ mbar, where one laser beam ($\lambda = 1064$ nm) measures the displacement δx of the test mass with respect to a reference

mirror. This displacement is embedded in an optical phase difference ψ retrieved by the QPDI. The NESS is created thanks to a power source, which creates a temperature profile $T(x)$ along the suspension rod. The temperature difference $\Delta T \equiv T^{\max} - T^{\min}$ is calculated as the difference between the temperature of the mass and the temperature at the top of the rod, both measured by thermopiles.

In the next sections, we show how we can retrieve the displacement of the oscillator starting from the incoming light beam. We divide this section as follows: the Jones calculus is briefly introduced, as a practical way to show the transformations occurring to the electric field of the laser beam, which are later characterized. Then, the power signals retrieved by the photodiodes is transformed into the displacement signal δx after a calibration.

5.1.1 Jones calculus

The Jones calculus [43] is a useful mathematical formalism used to treat the transformations of polarized light when it interacts with optical elements. A light beam propagating along the x -direction can be described as an electric field:

$$\mathbf{E} = E_y \mathbf{y} + E_z \mathbf{z} \quad (5.1)$$

which oscillates in the y and z -directions with respective amplitudes E_y and E_z . These can be written as:

$$\begin{aligned} E_y &= E_{0y} \cos(\omega t - kx + \psi_y) \\ E_z &= E_{0z} \cos(\omega t - kx + \psi_z) \end{aligned} \quad (5.2)$$

where ω and k are the natural frequency and the spatial wavenumber of the light, and each component possesses an amplitude E_{0y} , E_{0z} and a phase ψ_y , ψ_z . Eq. 5.1 can be expressed also as:

$$\mathbf{E} = \text{Re}(\mathbf{E}_0 e^{i(\omega t - kx)}) \quad (5.3)$$

with \mathbf{E}_0 the Jones vector defined by:

$$\mathbf{E}_0 = \begin{pmatrix} E_{0y} e^{i\psi_y} \\ E_{0z} e^{i\psi_z} \end{pmatrix} \equiv \begin{pmatrix} E_{0y} \\ E_{0z} e^{i(\psi_z - \psi_y)} \end{pmatrix} \quad (5.4)$$

The phase at an arbitrary time is arbitrary, so we can always choose to multiply \mathbf{E}_0 by a desired phase without altering the wave. Notice that with the phase convention used here, a decrease in phase indicates retardation, or equivalently $\psi_z < \psi_y$ means that E_z is retarded with respect to E_y .

When the light interacts with an optical element, the Jones vector undergoes a change:

$$\mathbf{E}'_0 = \mathbb{J} \mathbf{E}_0 \quad (5.5)$$

where \mathbb{J} is the 2×2 Jones matrix associated with the optical element. The optical components of the experiments are depicted in fig. 5.1.2. Three different areas are recognizable: i) the *input* area, where the light is prepared in the desired polarization state, ii) the *sensing* area, where the light interacts with the oscillator and the reference mirror, thus creating the interferometric signal, and finally iii) the *analysis* area, where the signal is extracted and read. A Jones matrix depends on the nature of the optical element and its orientation with respect to the chosen coordinate system. It is natural to assume the beam as the reference frame. In this case, referring to fig. 5.1.2, the light beam initially propagates in the x -direction, with the components of the electromagnetic field in the y and z -directions (see eq. 5.2). The z -axis is

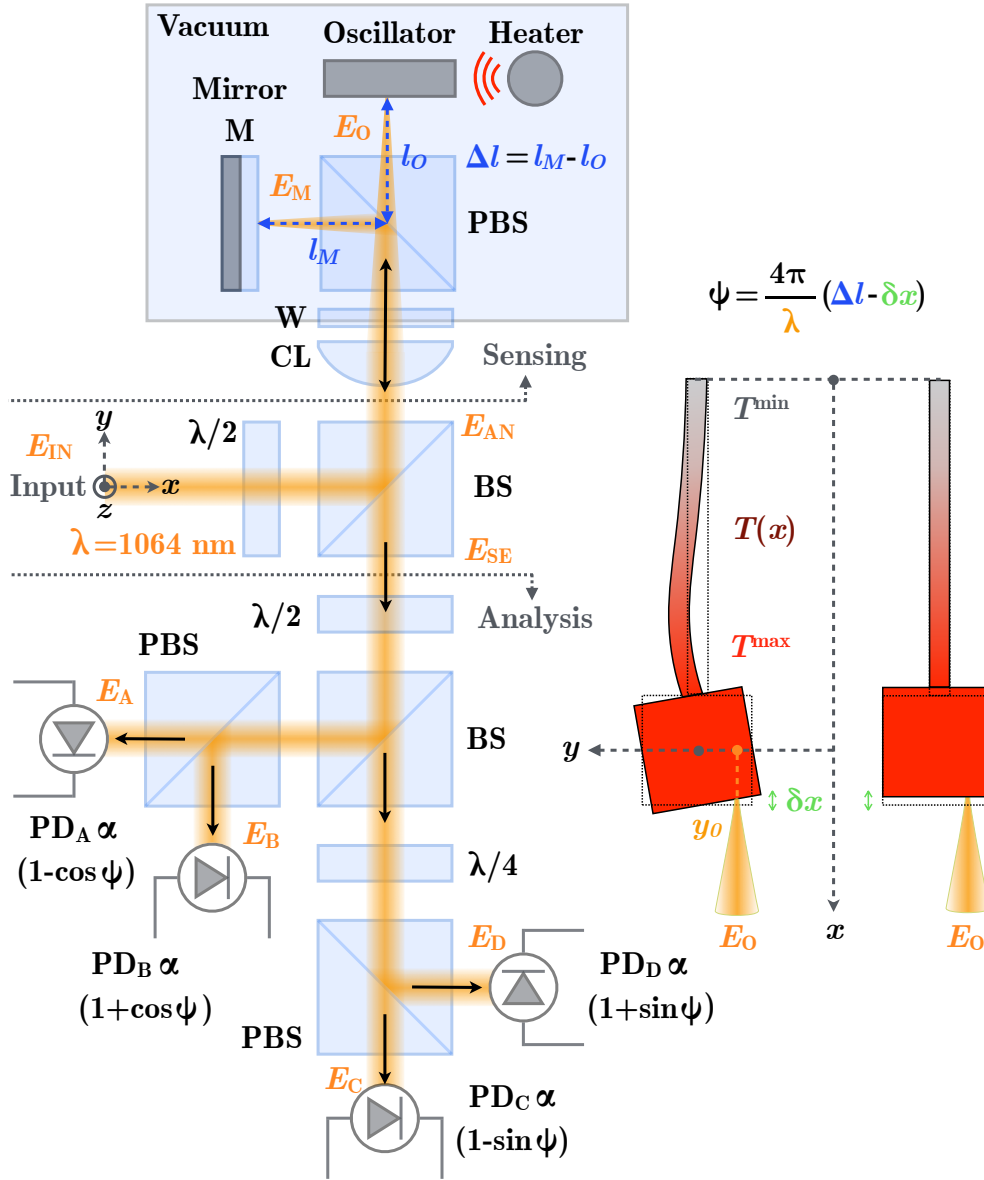


FIGURE 5.1.2: Experimental setup: a QPDI is used to retrieve the displacement of an aluminum oscillator. The laser beam ($I_{IN} = 10 \text{ mW}$ at 1064 nm), focused on the oscillator, is reflected towards the four photodiodes. The interferometer records the temporal signals of the displacements of the oscillator, one transverse and one longitudinal mode depicted on the right. A heater placed close to the cuboid raises the temperature of the mass thus creating the NESS. More details of the optical setup are given in Sec. 5.1. The oscillator, in vacuum at $\leq 5 \times 10^{-2} \text{ mbar}$, is monolithically clamped to a suspension system which is thermalised at room temperature T^{\min} .

fixed pointing out of the page, whilst the other coordinates follow the beam, with x always indicating the propagation of the beam.

We report the Jones matrixes (at the optimal angle ζ with respect to the horizontal axis in case for the wave plates) for the optical elements of the experiment in Table 5.1.1.

Optical component	Symbol	Jones Matrix \mathbb{J}
Half-wave plate ($\zeta = \pi/8$)	$\lambda/2$	$\frac{1}{\sqrt{2}} \begin{pmatrix} 1 & 1 \\ 1 & -1 \end{pmatrix}$
Beam splitter	BS	$\frac{1}{\sqrt{2}} \begin{pmatrix} 1 & 0 \\ 0 & 1 \end{pmatrix}$
Polarizing beam splitter, y	PBS $_y$	$\begin{pmatrix} 1 & 0 \\ 0 & 0 \end{pmatrix}$
Polarizing beam splitter, z	PBS $_z$	$\begin{pmatrix} 0 & 0 \\ 0 & 1 \end{pmatrix}$
Mirror	M	$\begin{pmatrix} 1 & 0 \\ 0 & -1 \end{pmatrix}$
Quarter-wave plate ($\zeta = \pi/4$)	$\lambda/4$	$\frac{1}{2} \begin{pmatrix} 1+i & 1-i \\ 1-i & 1+i \end{pmatrix}$

TABLE 5.1.1: Optical components and respective Jones matrix.

In the following sections, we describe how the light is transformed along the optical path. We do not take into consideration the intrinsic imperfections of the optical element, such as absorption or misalignment.

5.1.2 Input area

The beam can thus be initially described as:

$$\mathbf{E}_{\text{IN}} = E_{\text{IN}} \begin{pmatrix} 1 \\ 0 \end{pmatrix} \quad (5.6)$$

The first element it encounters is a half-wave plate ($\lambda/2$), which is oriented with an angle $\pi/8$ with respect to the y -axis, so that its Jones matrix is the one reported in Table 5.1.1. After this, a beam splitter (BS) directs half of the intensity towards the sensing area. Applying eq. 5.5, the light entering the sensing area is:

$$\mathbf{E}_{\text{SE}} = \mathbb{J}_{\lambda/2} \mathbb{J}_{\text{BS}} \mathbf{E}_{\text{IN}} = \frac{E_{\text{IN}}}{2} \begin{pmatrix} 1 \\ 1 \end{pmatrix} \quad (5.7)$$

The role of the half-wave plate is thus to rotate the polarization of the beam in order to equally divide it in both directions y and z , the first of which interacts with the oscillator and the second with the reference mirror.

5.1.3 Sensing area

The beam goes through a converging lens (CL) and a window (W) before reaching a polarizing beam splitter (PBS). This divides the two polarizations, so that the polarization parallel to y is transmitted to the oscillator and the perpendicular one is deviated towards the reference mirror. The electric field which hits the oscillator and gets back to the PBS is described

as:

$$\mathbf{E}_O = \mathbb{J}_{\text{PBS}_y} \mathbb{J}_M \mathbf{E}_{\text{SE}} = \frac{E_{\text{IN}}}{2} e^{i2k(l_O + \delta x)} \begin{pmatrix} 1 \\ 0 \end{pmatrix} \quad (5.8)$$

where $2(l_O + \delta x)$ is the distance covered by the light, also considering the displacement of the oscillator δx . The beam reflected by the mirror is:

$$\mathbf{E}_M = \mathbb{J}_{\text{PBS}_z} \mathbb{J}_M \mathbf{E}_{\text{SE}} = \frac{E_{\text{IN}}}{2} e^{i2kl_M} \begin{pmatrix} 0 \\ -1 \end{pmatrix} \quad (5.9)$$

with again $2l_M$ the double of the distance between the PBS and M. We can thus refer to the path difference as a phase $\psi \equiv 2k(\Delta l - \delta x) = 2k(l_M - l_O - \delta x)$. After recombination in the PBS, the beam which exits the sensing area and enters the analysis area is:

$$\mathbf{E}_{\text{AN}} = \mathbb{J}_{\text{BS}} (\mathbf{E}_O + \mathbf{E}_M) = \frac{E_{\text{IN}}}{\sqrt{8}} \begin{pmatrix} 1 \\ -e^{i\psi} \end{pmatrix} \quad (5.10)$$

5.1.4 Analysis area

The light is directed towards a second $\lambda/2$, which is oriented as the previous one and thus mixes the polarizations, dividing the information of the optical phase in both directions. The beam then goes through a BS, which divides it into the two analysis arms of the QPDI. For the first one AB we can write:

$$\mathbf{E}_{\text{AB}} = \mathbb{J}_{\text{BS}} \mathbb{J}_{\lambda/2} \mathbf{E}_{\text{AN}} = \frac{E_{\text{IN}}}{\sqrt{32}} \begin{pmatrix} 1 - e^{i\psi} \\ 1 + e^{i\psi} \end{pmatrix} \quad (5.11)$$

A PBS finally separates the two polarizations, so that the two electric fields shine onto the photodiodes A and B:

$$\begin{aligned} \mathbf{E}_A &= \mathbb{J}_{\text{PBS}_y} \mathbf{E}_{\text{AB}} = \frac{E_{\text{IN}}}{\sqrt{32}} \begin{pmatrix} 1 - e^{i\psi} \\ 0 \end{pmatrix} \\ \mathbf{E}_B &= \mathbb{J}_{\text{PBS}_z} \mathbf{E}_{\text{AB}} = \frac{E_{\text{IN}}}{\sqrt{32}} \begin{pmatrix} 0 \\ 1 + e^{i\psi} \end{pmatrix} \end{aligned} \quad (5.12)$$

In the second arm (CD) a quarter-wave plate ($\lambda/4$) adds a $\pi/2$ in both polarizations, yielding:

$$\mathbf{E}_{\text{CD}} = \mathbb{J}_{\lambda/4} \mathbb{J}_{\text{BS}} \mathbb{J}_{\lambda/2} \mathbf{E}_{\text{AN}} = \frac{E_{\text{IN}}}{\sqrt{32}} \begin{pmatrix} 1 - e^{i(\psi + \pi/2)} \\ 1 + e^{i(\psi + \pi/2)} \end{pmatrix} \quad (5.13)$$

and after the PBS, the photodiodes C and D receive:

$$\begin{aligned} \mathbf{E}_C &= \mathbb{J}_{\text{PBS}_y} \mathbf{E}_{\text{CD}} = \frac{E_{\text{IN}}}{\sqrt{32}} \begin{pmatrix} 1 - e^{i(\psi + \pi/2)} \\ 0 \end{pmatrix} \\ \mathbf{E}_D &= \mathbb{J}_{\text{PBS}_z} \mathbf{E}_{\text{CD}} = \frac{E_{\text{IN}}}{\sqrt{32}} \begin{pmatrix} 0 \\ 1 + e^{i(\psi + \pi/2)} \end{pmatrix} \end{aligned} \quad (5.14)$$

Now, the photodiodes capture the power $I = |EE^*|$, with the $*$ denoting the complex conjugated. The four retrieved signals are then:

$$\begin{aligned} I_A &= \frac{I_{\text{IN}}}{16} (1 - \cos \psi) & I_C &= \frac{I_{\text{IN}}}{16} (1 - \sin \psi) \\ I_B &= \frac{I_{\text{IN}}}{16} (1 + \cos \psi) & I_D &= \frac{I_{\text{IN}}}{16} (1 + \sin \psi) \end{aligned} \quad (5.15)$$

where $I_{\text{IN}} = |E_{\text{IN}}E_{\text{IN}}^*|$ represents the input power. We note how the total retrieved power is 1/4 with respect to the initial one, with the remnant being lost in the two passages through the first BS.

5.1.5 Phase and displacement

In order to retrieve the optical phase, we calculate the contrast of each arm:

$$\begin{aligned} C_x &= \frac{I_A - I_B}{I_A + I_B} = \cos \psi \\ C_y &= \frac{I_C - I_D}{I_C + I_D} = \sin \psi \end{aligned} \quad (5.16)$$

We then define the complex contrast C :

$$C \equiv C_x + iC_y = e^{i\psi} \quad (5.17)$$

This formulation has one clear advantage: due to the quadrature, the optical phase is unambiguously determined (modulo 2π). In fact, if we display the contrast C in the complex plane, this is a point on the unit circle, and thus one measurement of the optical phase ψ corresponds to a polar angle in this plane.

Let us interpret the optical phase. As mentioned, this is:

$$\psi = 2k\Delta l = 2k(l_M - l_O - \delta x) = \frac{4\pi}{\lambda}(\Delta l - \delta x) \quad (5.18)$$

where we can distinguish two contributions: the intrinsic optical path difference between the two arms of the interferometer Δl , which may slowly vary with thermal drifts, and the displacement of the oscillator δx , which can be seen as an oscillation around the mean value of Δl . The contributions being summed, the sensitivity of the contrast with respect to δx does not depend on Δl [87]:

$$\left| \frac{dC}{d(\delta x)} \right| = \frac{4\pi}{\lambda} \quad (5.19)$$

Thus, the working point (the position on the interference fringe) does not need to be optimized, since the sensitivity is unaffected by this. Furthermore, if the working point experiences some drifts during the measurement, for example due to the temperature changing, the measured displacement keeps being calibrated. Finally, once the optical phase is determined the displacement of the oscillator is retrieved as:

$$\delta x = \frac{\lambda}{4\pi}\psi \quad (5.20)$$

5.1.6 Real life implementation

As for example reported in [87], this description is not adapted to a realistic interferometer. Imperfections and misalignments, yield a contrast less than optimal, therefore C resembles more an ellipse than a circle (see fig 5.1.3). Through an Heydemann correction [54], though, it is possible to take this into account. We can write a corrected version of eq. 5.15:

$$\begin{aligned} I_A &= \alpha_A - \beta_A \cos \psi & I_C &= \alpha_C - \beta_C \sin(\psi + \varrho) \\ I_B &= \alpha_B + \beta_B \cos \psi & I_D &= \alpha_D - \beta_D \sin(\psi + \varrho) \end{aligned} \quad (5.21)$$

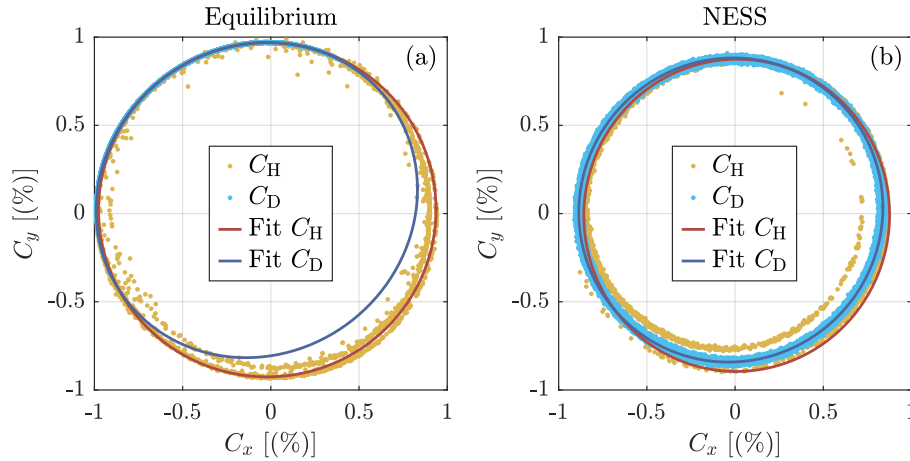


FIGURE 5.1.3: Calibration ellipses. In (a), an equilibrium situation is displayed, where the calibration contrast is generated in two methods: with a small hit (H) on the vacuum chamber (yellow data and red fit) or with the drift (D) throughout the whole measurement (cyan data and blue fit). The first method excites the oscillator through at least one interference fringe, and we notice how the elliptical fit is well overlapped with the experimental points. It is remarkable that the contrast is very close to the ideal unit circle, with fit parameters $X_0 = -2\%$, $Y_0 = 3\%$, $X = 96\%$, $Y = 95\%$, and $\varrho = 10^{-4}$. We also notice how the experimental data do not overlap for displacements larger than $\lambda/2$. Instead, they tend to form a spiral, which is due to the non-linearities of the system. On the other hand, the drift is not significant enough to result in a good fit, yielding a smaller contrast (and hence higher displacement signal). In this particular case, the H method seems to yield the most accurate calibration. In (b), we show a non-equilibrium measurement for the same strategies. In this case, the hit and the drift methods yield more similar results, nevertheless exciting the oscillator results in a more pronounced spiral. The resulting fit is therefore slightly biased, and the best calibration method appears to be the thermal drift. Also in this case, the contrast is close to optimal, with a small degradation with respect to the equilibrium case.

where α is the mean power received by the correspondent photodiode, β is the amplitude of the oscillating component, and ϱ stands for the deviation from a perfect quadrature. A ideal response corresponds to $\varrho = 0$, equal powers on the same photodiode $\alpha = \beta$ and in the same arm $\alpha_A = \alpha_B$, $\alpha_C = \alpha_D$. Using eq. 5.21, the contrasts C_x, C_y can be expressed as:

$$\begin{aligned} C_x &= X_0 + X \cos \psi \\ C_y &= Y_0 + Y \sin (\psi + \varrho) \end{aligned} \quad (5.22)$$

where the coefficients are related to the ellipse: X_0, Y_0 represent the center, X, Y the projection of the semi axes on the axes x, y , and ϱ its precession. If these five quantities are known, eq. 5.22 can be inverted in order to retrieve the optical phase ψ and thus the displacement δx .

The ellipse is also a handy tool to understand the sensitivity of the interferometer during the alignment of the laser probe before a measurement. We give more details in Appendix 5.A.

5.1.7 Calibration

In order to retrieve the parameters of eq. 5.22, a calibration is required before each measurement. As stated, depending on the position on the interferometric fringe, the optical phase lies in one point of the ellipse (working point). If we record the working point whilst it

sweeps at least one entire interferometric fringe, hence the whole ellipse, the optical phase is calibrated and any measured phase can be retrieved as the corrected polar angle on this curve. As seen, the optical phase is composed of two varying quantities: the thermal noise-induced displacement of the oscillator δx and the slow drift in the length of the arms of the interferometer Δl . Modifying either of these quantities changes the working point and in principle should lead to the same calibration. We discuss them separately and report the results in fig. 5.1.3.

In the first case, we inject energy into the system in order to increase δx ; therefore, the ideal strategy would be to drive the oscillator with a piezoelectric device at the resonance frequency and to record the contrast. Unfortunately, in the current setup this is not possible. As such, we hit the suspension system with a plastic hammer, just enough to sweep one interferometric fringe. Consequently, the contrast C is recorded for post-analysis, where we fit the ellipse. Whereas this procedure is quick, and it grants a coverage of the whole contrast, it has some setbacks: as we can see from fig. 5.1.3 (b), the ellipse may not overlap when more than one turn is made, showing a spiraling feature. This effect being almost inexistent when the system is in thermal equilibrium, it becomes preponderant when it is in a NESS. As shown in fig. 5.1.4, the magnitudes of the resonance modes we are interested in are much lower than the noise due to the suspension; therefore, any perturbation feeds energy into all frequencies, and the ellipse may contain these spurious contributions. In order for this method to yield an accurate calibration for the longitudinal mode, the hit must be performed vertically at the center of the suspension system.

The second method consists on waiting for the working point to slowly drift, hence for Δl to change. This method does not require any manipulation of the oscillator and acts as a self-calibration, since the signal itself serves as a calibration. Since we are not injecting energy into the system, we do not expect the ellipse to show non-linearities as strong as the previous method, as we can see from fig. 5.1.3 (b). Nevertheless, the drawback lies in the uncertainty that the drift is significant enough to cover a whole interferometric fringe, as in fig. 5.1.3 (a). In order for this method to yield an accurate calibration, we must ensure the drifts are then significant enough.

We refer to the contrasts calculated with the external perturbation as C_H and the one with the drift as C_D . Due to the ambiguity of these methods, the choice is to use both methods and choose *a posteriori* the more suitable one. Whilst the two strategies can produce different results, for example in the equilibrium experiment in fig. 5.1.3 (a), they usually yield very similar outcomes. In fig. 5.E.1, we show the results following both calibrations, in order to highlight this effect.

5.1.8 Displacements

After calibration, the QPDI yields the temporal displacement signal $\delta x(t)$, from which we can compute the PSD. We show an example of a typical PSD highlighting the two resonance modes we are interested in fig. 5.1.4: a vertical deformation δ of the rod (henceforth called *longitudinal* mode), and a rotation θ of the end mass (henceforth called *transverse* mode). A sketch of these motions is shown in fig. 5.1.2.

The interferometer directly gives access to the longitudinal mode: $\delta = \delta x$. The transverse mode is more complex. It is in fact associated to the first deflection mode of the rod, which, due to the loading at its free end, closely resembles the second deflection mode of a clamped-hinged cantilever [12]. We would expect to measure 2 transverse modes, one oscillating in the $x - y$ plane and the other in the $x - z$ plane. Indeed, the cuboid lateral dimensions are slightly different in order to lift the mode degeneracy. Nevertheless, as shown in fig. 5.1.4,

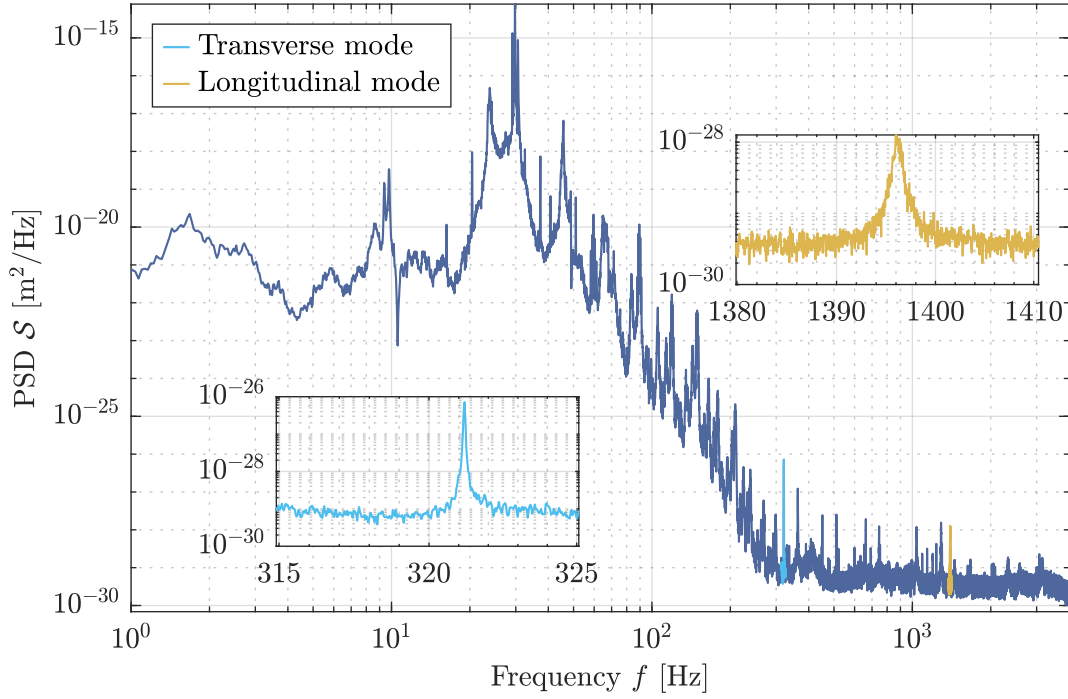


FIGURE 5.1.4: PSD of the displacement signal δx : a typical signal retrieved by the QPDI shows a huge noise bump at low frequencies, which relaxes around $f \approx 200$ Hz. At around 300 Hz, we find the transverse resonance mode (cyan), whilst at 1400 Hz stands the longitudinal one (yellow). Note the extremely low noise floor achieved by the instrument, at $2 \text{ fm}/\sqrt{\text{Hz}}$.

the PSD yields *one* transverse peak. This oddity is not yet explained, as this is also the case in the previous experiments of the group [29]. We then suppose that the measured transverse mode corresponds to a motion in the $x - y$ plane. In this case the transverse angle depends on the position of the laser spot on the oscillator y_0 through the mode shape of the oscillator, which is not trivial [12]. Thus, deriving θ from δx is also not straightforward. Choosing the probing point y_0 before the measurement is also not possible, and any modification *during* it is equally not measurable. Hence, we cannot safely express θ in radians, and thus we keep it as a vertical displacement. We hence call $\theta \equiv \delta x$ the transverse angle expressed in meters.

5.2 Heating

As mentioned, in order to create a temperature difference ΔT between the cuboid and the top end, a heater is placed close to the oscillator. The heating system is precisely described in [62, 29]; we summarize its principle here. The thermal source is placed in front of one face of the cuboid mass, and when it is turned on, some hours are necessary for ΔT to be stationary (see Sec. 5.3.1). The temperatures of the cuboid T^{max} is measured through a thermopile and the one at the top end T^{min} through a thermometer. Furthermore, the temperature of the environment T^{amb} is also measured. The power of the thermal source is at most 5 W, yielding $\Delta T \leq 50 \text{ K}$ along the suspension rod. Since the temperature different is relatively small, we can consider the temperature profile linear: $T(x) \sim x$, with x the longitudinal

coordinate along the rod. Therefore, its average temperature is defined as:

$$T^{\text{avg}} = T^{\text{min}} + \frac{1}{2}(T^{\text{max}} - T^{\text{min}}) = T^{\text{min}} + \frac{\Delta T}{2} \quad (5.23)$$

In fig. 5.3.1 we show an example of the temperature as a function of time during one measurement run.

5.3 Experimental procedure

When a NESS is established, we proceed by measuring the displacement of the oscillator to retrieve its thermal fluctuations. We hence present the experimental procedure, followed by the methods used to retrieve the PDSs of the motions.

5.3.1 Experimental procedure

Let us begin the description of the experimental procedure when the oscillator is placed in the vacuum chamber at a pressure $p \sim 10^{-5}$ mbar, sustained by a turbo pump. The experiment then follows the usual two main steps, S_{EQ} and S_{NESS} .

The first step S_{EQ} corresponds to an equilibrium case, where the oscillator is not heated and its thermal noise is measured. We further divide this step into two steps, a calibration step s_{cal} followed by a thermal noise measurement s_{meas} . The second step S_{NESS} is a non-equilibrium case, where the test mass is heated at various heating powers: $P = 3 - 4.5$ W (see also sec. 5.2). In this case, a heating step s_{heat} precedes the other two s_{cal} , s_{meas} . Let us describe each step in detail, following the procedure of a non-equilibrium measurement and keeping in mind that s_{heat} is simply absent in the equilibrium case.

The first step s_{heat} consists of waiting for the system to reach a steady temperature difference between the top end (T^{min}) and the oscillator (T^{max}) and at the same time creating and maintaining a low pressure in the chamber (around 10^{-5} mbar). The oscillator being macroscopic, it normally takes hours. This step usually begins one day before the following step, in the evening. As we discuss in Appendix 5.B, the measurements are performed at night, where environmental noise is lower. At the end of this step, when the temperature of the top end T^{min} and the temperature of the oscillator T^{max} reach an equilibrium, we turn off the turbo pump. The reason lies in the fact that we cannot leave the pump on in the next steps, since the introduced noise would completely hide the desired signal. It is also important to highlight that the heater is kept on throughout the whole process. As we wait for the vibrations to die out, we see that the pressure rapidly raises (small leaks, degassing).

The next step s_{cal} consists of exciting the oscillator through small hits on the vacuum chamber and retrieving the contrast C through the ellipse. This is optimized if needed (see Appendix 5.A), and it is recorded for some seconds. As shown in Sec. 5.1.7, this allows us to calibrate the displacement in the post analysis.

Once the external perturbations dissipate, the last part s_{meas} consists of measuring the displacement δx of the oscillator. This step lasts all night, around 10 hours of continuous acquisition (see Sec. 5.3.2). Whilst the pressure reaches values up to 5×10^{-2} mbar, the temperature difference $\Delta T \equiv T^{\text{max}} - T^{\text{min}}$ also varies. We test the influence of this phenomenon on the results in Appendix 5.D.

Lastly, a second calibration step s_{cal} is performed in order to verify that the contrast did not vary too much throughout s_{meas} . In all the measurements presented in this chapter, the difference between the calibrations performed before or after s_{meas} is negligible.

In this work, we present one equilibrium measurement and three non-equilibrium ones, i.e. we perform one S_{EQ} and three S_{NESS} . We summarize the procedure in Table 5.3.1, whilst in fig. 5.3.1 we show how one step S_{NESS} is composed.








Steps	S_{EQ}			S_{NESS}			
	s_{cal} 	s_{meas} 	s_{cal} 	s_{heat} 	s_{cal} 	s_{meas} 	s_{cal} 
Measured quantities	C	$\Delta T, \delta x$	C	/	C	$\Delta T, \delta x$	C
Power P [W]	0			3-4.5			

TABLE 5.3.1: Experimental procedure. Firstly we perform one equilibrium measurement S_{EQ} , then the non-equilibrium ones S_{NESS} (just one showed), where the heating step s_{heat} is added.

5.3.2 Analysis procedure

When the measurement is concluded, we proceed with the analysis. With steps s_{cal} (initial and final), we extract from the fit of the ellipse C_{H} the calibrated coefficients, which do not vary more than 1 % during the 10 h acquisition. A second set of coefficients is extracted from C_{D} , which is obtained by decimating the C_x, C_y data drifting during the measurement. Therefore, two continuous displacement signals $\delta x(t)$ are calculated (eq. 5.20), one for each method of calibration. Subsequently, since $\delta x(t)$ is continuous, we can decide the desired frequency resolution. We choose $df_{\delta} = 3 \times 10^{-2} \text{ Hz}$ and $df_{\theta} = 3.4 \times 10^{-3} \text{ Hz}$. The choice is made by balancing various factors: an adequate number of points around the resonance frequency, a time length during which the temperature does not significantly vary and a reasonable amount of final spectra from which to derive averages from.

We then calculate the available number of PSDs for each motion, for both calibration methods. In fig. 5.E.1, we show that the two calibrations yield almost identical results but for the equilibrium measurement, therefore we can choose the method that better suits us. As shown in Sec. 5.1.7, for the equilibrium measurement, the external perturbation contrast fit C_{H} is to be preferred to the drift C_{D} due to lack of calibration points in C_{D} . On the other side, for the NESSes, C_{D} is to be preferred. From now on, we intend $\delta x \equiv \delta x_{\text{H}}$ for the equilibrium measurement and $\delta x \equiv \delta x_{\text{D}}$ for the NESSes.

The spectra are then filtered in order to eliminate signals which show very different behavior with respect to the average (this procedure is carefully explained in the Chapter 6). From the PSDs which pass the selection $\mathcal{S}_{\delta}, \mathcal{S}_{\theta}$, we then calculate the thermal noise as usual (eq. 3.65):

$$\langle \delta^2 \rangle = \int_{f_{\delta} \pm \Delta_{\delta}} df (\mathcal{S}_{\delta}(f) - \mathcal{N}) \quad \langle \theta^2 \rangle = \int_{f_{\theta} \pm \Delta_{\theta}} df (\mathcal{S}_{\theta}(f) - \mathcal{N}) \quad (5.24)$$

taking care to subtract the background noise contribution \mathcal{N} . Here, f_{θ}, f_{δ} are the resonance frequencies and $\Delta_{\theta} \approx 2 \text{ Hz}$, $\Delta_{\delta} \approx 10 \text{ Hz}$ the intervals of integration.

The spectra are then averaged in groups of N in order to be fitted, with $N = 25$ chosen in order to sufficiently smooth the PSDs whilst the temperature does not change significantly. We show an example of the fit in fig. 5.4.3 for both motions in equilibrium and NESS situations. The accuracy of the fit is high, as shown by the reduced χ^2 being always less than 2. For details about the fit procedure, see Chapter 6.

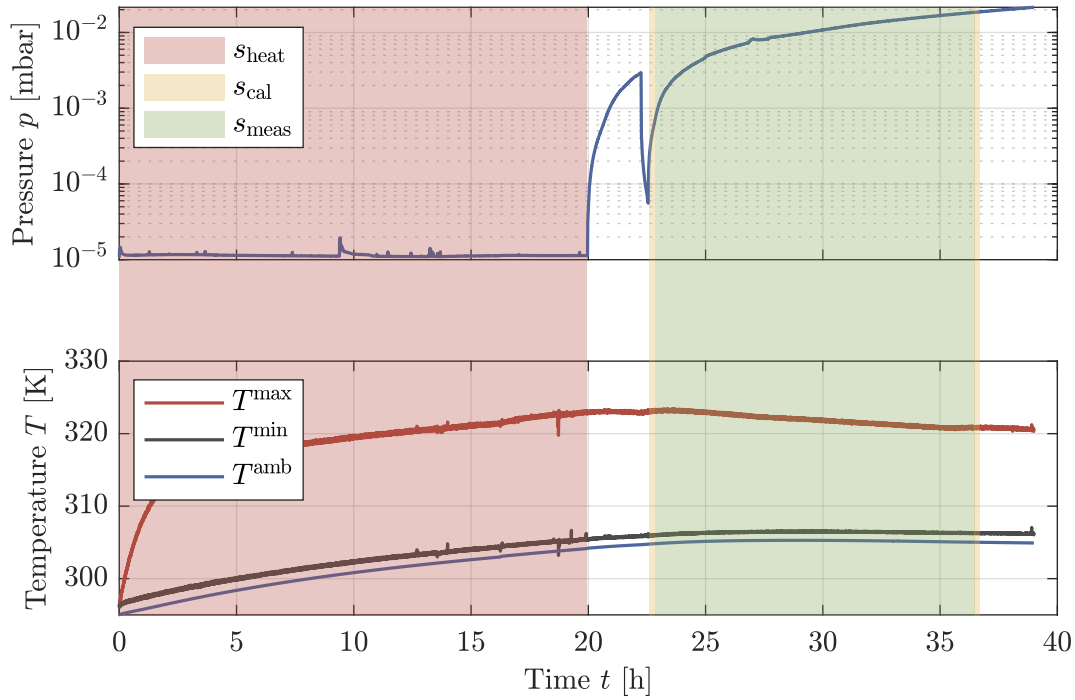


FIGURE 5.3.1: Experimental procedure for a non-equilibrium measurement S_{NESS} . In the upper figure, we can see the time variation of the pressure in the vacuum chamber during the three steps s_{heat} (red shaded area), s_{cal} (yellow shaded area), and s_{meas} (green shaded area). In the first step, the pressure of the chamber is kept around 10^{-5} mbar for almost an entire day by a turbo pump, then it rises quickly when this is turned off. In the non-colored area, the system is prepared for the measurement, and due to a technical issue, the pump is briefly turned on and off. The system is therefore calibrated (s_{cal}), where we exaggerated the width of the shaded area for it to be visible. Thereafter, the thermal noise is recorded as the pressure raises to roughly 2×10^{-2} mbar. Finally, we perform a second calibration in order to check that the contrast C is unchanged with respect to the first calibration. In the lower figure, the temperature of the oscillator is increased by a heater, whilst the temperature of the top end T^{min} and the temperature of the environment T^{amb} are slightly modified. After an entire day, the temperature difference ΔT is roughly constant, and so we proceed with the calibration and the measurement. During this time, ΔT slowly varies because of the increasing pressure.

5.4 Results

In this part, we discuss the experimental results. We first show the improvements of the detection system, then we depict the thermal fluctuations retrieved in the four measurements, represented as usual by the fluctuation temperatures T^{fluc} . We finally display the loss angles of the resonances and interpret the outcome of the experiment.

5.4.1 Improvements of the detection

The NETN experiment as presented throughout this work is the latest advancement of the setup to date. The first version of the experiment with an interferometric readout is described in [90] (we will refer to it as I_1), and the capacitive readout versions are shown in [62]. The principal reason for the passage between the two different readouts is the possibility of reducing the uncertainties regarding the thermal expansion of the material [90].

Whilst the I_1 readout showed the a good sensitivity, with the background noise reaching $10^{-15} \text{ m}/\sqrt{\text{Hz}}$, with the present setup we aim at further increasing it. In fig. 5.4.1, we show the comparison between the I_1 results and the ones presented in this work. We note how we obtain a reduction in the background noise of a factor a little less than 3 around the transverse mode and roughly 1.7 in the longitudinal, depending on the heating power, thus sensibly increasing the SNR. As a reference, we note that the improvements of the detection system leads to a sensitivity close to the one of the capacitive readout, i.e. around $2 \times 10^{-30} \text{ m}^2/\text{Hz}$ for the longitudinal mode [29].

It is worth noting that the improvements are the result of a rearrangement of the previous experimental setup into the new QPDI, without upgrading the hardware such as the optical components or detectors. We believe the increase in sensitivity with respect to I_1 is due to a combination of reasons, spanning from almost optimal interferometric contrast (see fig. 5.1.3) to a different balancing of shot-noise and ADC noise contributions. Unfortunately, due to the short tenure in the laboratory, not many tests regarding the noise sources are available, and quantitative comparisons with I_1 are not possible. We refer to [90] for further details.

5.4.2 Thermal fluctuations

The results are shown in fig. 5.4.2, where we present the fluctuation temperatures calculated numerically and through the fit of the averaged spectra (see Sec. 5.3.2). These two methods yield very similar results, with a difference at most of 3 %, present in just one experimental measurement. The main result is that transverse and longitudinal thermal fluctuations are comparable to the average temperature of the system. The longitudinal mode shows fluctuation temperatures T_δ^{fluc} between the minimal and maximal temperatures in the system $T^{\text{min}} \approx T^{\text{amb}}$ and T^{max} . Since T_δ^{fluc} are very similar to T^{avg} , the thermal noise of this resonance is comparable to the one the oscillator would show if it was heated uniformly at T^{avg} .

The outcome for the transverse mode is more delicate: with more important uncertainties, it is harder to assess how the fluctuations behave with respect to T^{avg} . Nevertheless, we can observe that for all but one measurement, the T_θ^{fluc} is bounded by the aforementioned limits. The measurement at the highest T^{avg} shows fluctuations *below* the lowest available temperature in the system, although with high uncertainty. These are partly due to the choice of a high frequency resolution df_θ (which decreases the number of total spectra) and partly due to these being very noisy (see Appendix. 5.B). We believe that we can interpret the

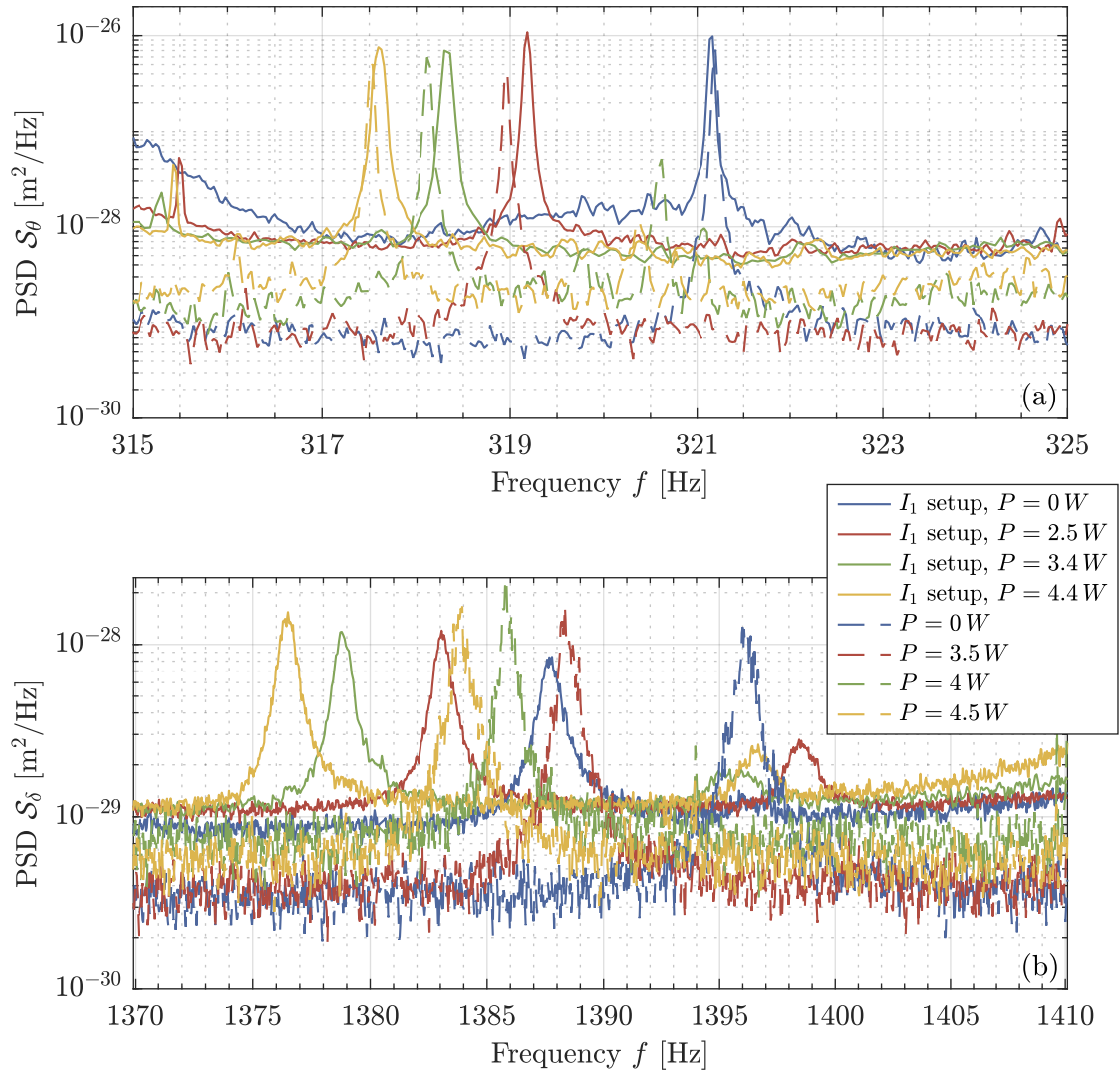


FIGURE 5.4.1: Comparison between some results of the previous setup I_1 (solid lines) and the current one (dashed lines). In (a), we show how the equilibrium resonance frequency of the transverse mode is almost unchanged with respect to the I_1 setup; moreover, for similar heating powers P the resonances are shifted by comparable values. On the other hand, taking the equilibrium measurement as an example, the background noise (in $\text{m}/\sqrt{\text{Hz}}$) is now roughly 3 times lower than the I_1 measurements. In (b), we see how the longitudinal resonance is on average redshifted by 8 Hz for all heating powers. At these frequencies, the background noise is around 1.7 times lower in the present setup.

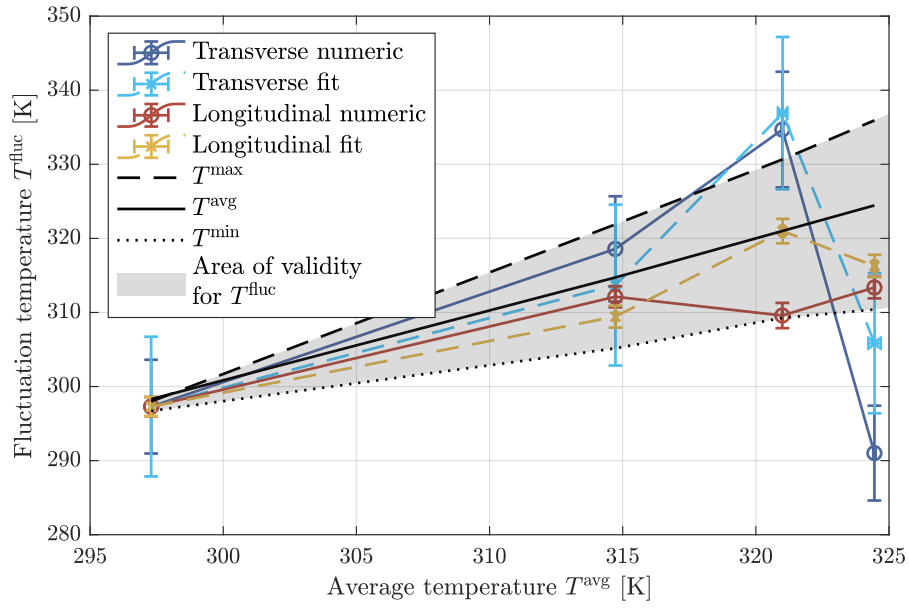


FIGURE 5.4.2: Transverse and longitudinal fluctuation temperatures are depicted against the average temperature of the oscillator for two different calculation methods: numerical integration of the PSD and results of its fit (see Chapter 6 for details). There is a very good agreement between the two methods, showing a difference at most of 3 %. Both longitudinal and transverse temperatures lie between the minimal and maximal temperature of the system, T^{min} and T^{max} (grey shaded area), with one exception likely due to a sensitivity change. While the shown values for T^{fluc} are normalised to room temperature as per eq. 2.88, we show in fig. 5.E.1 how a direct measurement of T^{fluc} leads to a temperature of around 180 K. This is discussed in Appendix 5.E.

odd behavior of T^{fluc} through a change in sensitivity. Indeed, as shown in Appendix. 5.C, a small shift of the probing point y_0 would cause an apparent change in T^{fluc} .

5.4.3 Dissipation

It is difficult to model the spatial and frequency dependence of the dissipation process in the oscillator. We can nevertheless measure it, calculating the loss angle φ from the best fit of the thermal noise spectra. We show the results in fig. 5.4.3. The transverse mode yields a $\varphi_\theta \approx 10^{-4}$, which seems to increase slightly with the average temperature. Due to the important error bars, it is difficult to judge the temperature behavior of φ_θ . The longitudinal loss angles shows an equilibrium value around 6×10^{-4} , which is 5 times higher than the transverse one. Values at higher T^{avg} are scattered, but point towards a smaller φ_δ , up to 20 %. It is important to note that the pressure is not the same throughout the four measurements: as shown in Appendix 5.D, the equilibrium measurement is taken at at least 10 times the pressure of the NESSES. Nevertheless, no correlation between this phenomenon and the measured φ is evident.

5.4.4 Discussion

As discussed, the fluctuation temperatures of the oscillator indicate that the system can be safely compared to an equivalent system in thermal equilibrium at the correspondent average temperature. Albeit the difficulty of assessing this for the transverse mode, it is clear that the longitudinal one supports our extended version of the FDT. Indeed, the retrieved T^{fluc} are compatible to their expected values, between T^{min} and T^{max} . Unfortunately, the

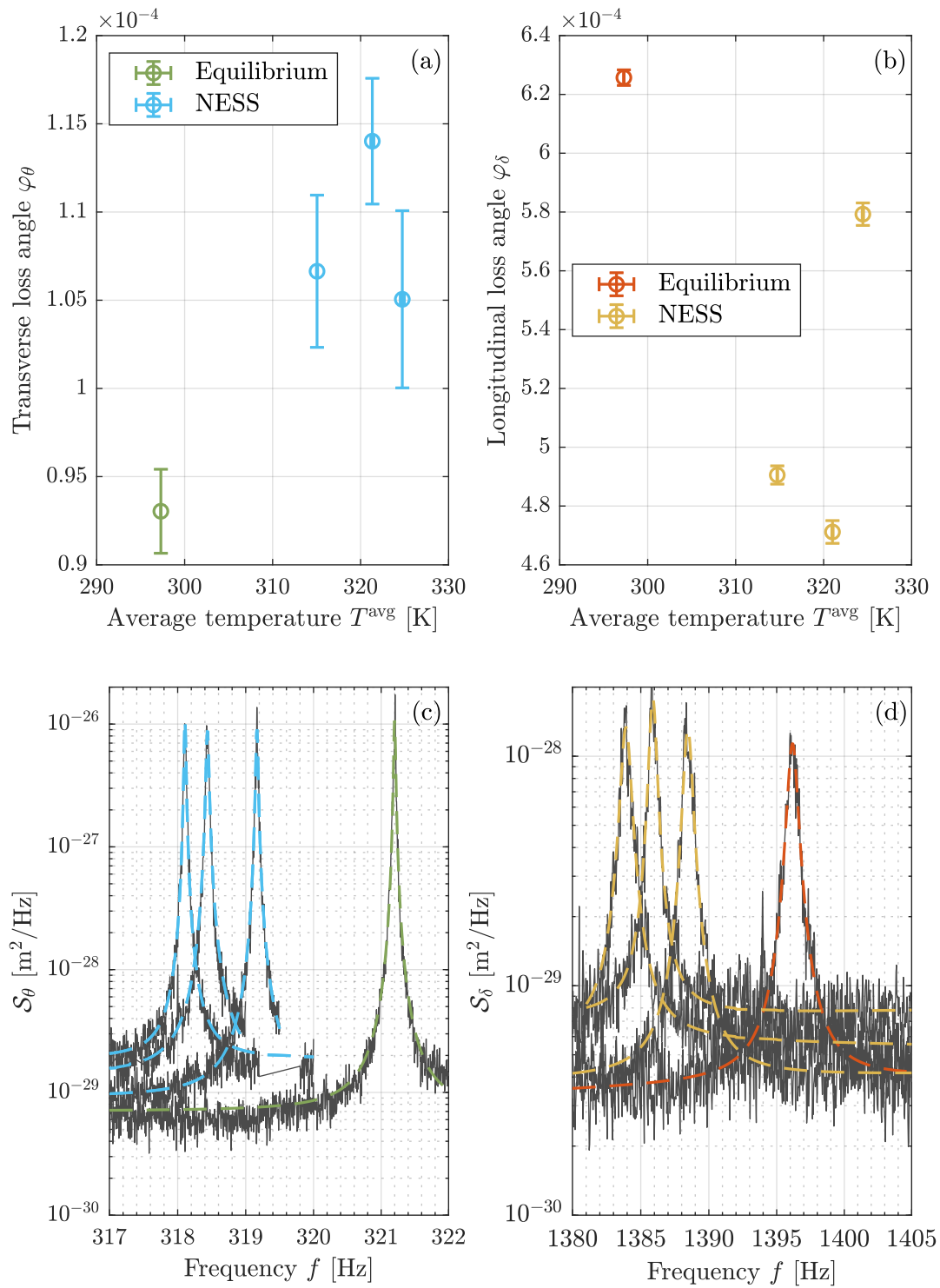


FIGURE 5.4.3: Loss angles of the resonances: the dissipation of the oscillator is estimated through its loss angle in equilibrium and out-of-equilibrium. In (a), though with large uncertainties, we can note how the loss angle φ_θ can be considered roughly constant with T^{avg} , with a difference of at most 20%. It is nevertheless important to note that the NESSes are measured at lower pressure, possibly biasing the result. In (b), φ_δ first decreases and then increases, also with variations of at most 20%. In (c) and (d), we can see an example of the spectra and their respective fits. We note that the shape of the transverse peak looks almost unchanged between the equilibrium measurement (green dashed line) and the NESSes (cyan dashed lines), whilst the longitudinal mode looks broader in the equilibrium measurement (orange dashed line) with respect to the first two non-equilibrium measurements (yellow dashed lines).

limited dataset of the loss angles and their difficult interpretation do not allow us to theoretically predict the fluctuation temperatures of the oscillator. Nevertheless, we note that the dissipation is constant within 20 %, so we do not expect the normalised dissipation function $w^{\text{diss}}(x, \omega)$ to change drastically. For this reason, the results showing $T^{\text{fluc}} \approx T^{\text{avg}}$ are well explained within our theoretical framework. In the next section, however, we show how other measurements on the same oscillator are in contrast with the results presented here, and we discuss a possible interpretation of the differences.

5.5 Conclusions

In this chapter, we show that we can create a NESS in a macroscopic system, and measure the relative thermal fluctuations. The first important outcome of the experiment is the implementation of the new version of the QPDI. Indeed, thanks to the rearrangement of the interferometer and the use of the complex contrast C to maximise its visibility (described in Appendix 5.A), we manage to reduce the background noise of a factor between 1.7-3 around the resonances. Moreover, thanks to the sorting and fitting methods based on the statistical properties of thermal noise described in the next chapter, the results are robust against external factors which may bias the distribution of the fluctuations.

The measured T^{fluc} are approximately what the average temperature of the system would prescribe. Whilst the transverse mode bears some uncertainties regarding its unknown sensitivity, the longitudinal T_{δ}^{fluc} is comfortably comparable enough to T^{avg} to affirm that the oscillations of the system can be described by our extended version of the FDT:

$$T^{\text{fluc}} = \frac{1}{L} \int_0^L T(x) w^{\text{diss}}(x) \quad (5.25)$$

This outcome is extremely interesting, since it shows that our description can be extended to a macroscopic system such as the oscillator.

Unfortunately, no decisive conclusion can be reached for the measured dissipation that would allow us to theoretically predict T^{fluc} . Nevertheless, due to the small change of the loss angles with the temperature (less than 20 %), we expect w^{diss} to similarly change little, thus explaining why $T^{\text{fluc}} \approx T^{\text{avg}}$. Therefore, we believe that these results are perfectly coherent with the rest of the experiments described in this thesis. It follows that our extended version of the FDT is a description applying to both microscopic and macroscopic systems, further expanding its possible applicability.

As mentioned, however, this is not the end of the story. The previous (and new) results of the group [29, 90] on the *same* oscillator are extremely different with respect to the ones presented here. We display a comparison in fig. 5.5.1. In most of the measurements shown, not only is a significant increase of fluctuations with respect to T^{avg} observed (up to 3 times), but also $T^{\text{fluc}} \gg T^{\text{max}}$. This is of particular importance, since most of the measurements shown in fig. 5.5.1 cannot be explained through our extended FDT, and other models need to be taken into account [29]. It is nevertheless puzzling how the same system can show different regimes depending on the measuring setup, and sometimes (as in the new measurements with the QPDI) even using the same one. The reasons for these differences are various and have been long debated; we give a possible insight in Appendix 5.E.

It is important to mention that, if some of the hypotheses explaining this difference and other oddities of the experiment are found to be true, this would partially or completely invalidate the previous conclusions. For the time being, though, we have enough evidence to support the validity of the present results. Firstly, the resulting thermal noise is well

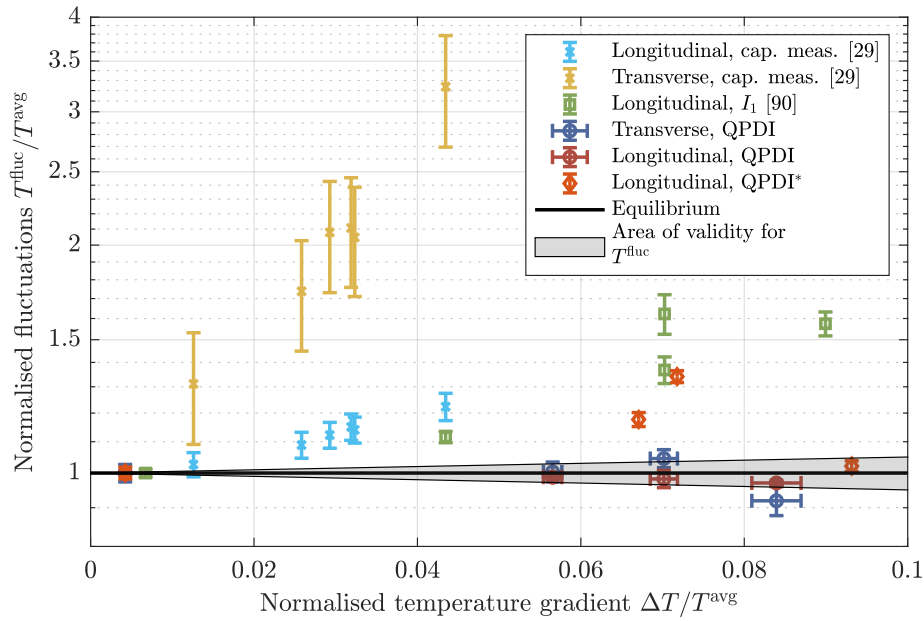


FIGURE 5.5.1: Comparison between the results presented in this work and the other available ones performed on the same oscillator, shown in chronological order. The first measurement set (cyan and yellow stars) is obtained from a capacitive readout [29]: we can see a strong excess of fluctuations with respect to the average temperature of the system, the ratio of which reaches almost 3. Furthermore, since $T^{\text{fluc}} \gg T^{\text{max}}$, we cannot interpret these results with our usual extension of the FDT. The measurements performed with the I_1 setup [90] (green squares) yield results similar to the previous ones, with a marked increase in fluctuations with respect to T^{avg} . We then show our results (blue and red circles), which reveal a clear difference of behavior with respect to the previous outcomes of the experiment. Finally, we display a last set of measurements (orange diamond) taken with the same experimental setup but after my tenure in the laboratory. Surprisingly, this experiment yields mixed results: some measurements are in line with the capacitive and I_1 outcomes, whilst one is in agreement with our theoretical framework.

explained by our models, which in turn do not comprehend the previous results of the group where a different description is needed [29]. Secondly, as we show in the next chapter, the statistical properties of the measured fluctuations are coherent with what we expect from thermal noise.

In conclusion, we show that the out-of-equilibrium fluctuations of a macroscopic oscillator can be explained through the same models describing the behavior of a micro-cantilever. This result, if confirmed, yields important consequences. In general, the applications of forecasting the fluctuations of a micro-resonator knowing the local distribution of the dissipation can be extended to larger systems. Of course, in this case, the form of the dissipation function can be much more complicated to describe, but a naïve extension of a system dominated by clamping losses such as C100 can be conceived. A direct application is clearly in the GW detectors, for which the NETN experiment is conceived. If the fluctuations were similar to the average temperature of the system, no out-of-equilibrium effect should then arise if there is a temperature difference ΔT in the suspension system of the mirrors. The extension towards a cryogenic study such as the experiment of C90, but with a macroscopic setup, is surely an interesting prospect. We finally believe this experiment to be of capital importance in the real-life application of the non-equilibrium tools we have developed, as we encourage future developments in order to understand the open questions and to explore new scenarios.

Appendix

5.A Alignment and optimization of the interferometer

Once the optical path (fig. 5.1.2) is prepared and the bench with the reference mirror is placed inside the vacuum chamber, we need to align the laser beam with respect to the interferometer. At this point the chamber is open and manipulations can be made. In fig. 5.A.1, we show a more detailed version of the input and sensing areas of the optical path. Whilst this new sketch is optically equivalent to the one in fig. 5.1.2, it allows us to better illustrate the alignment process. For this purpose, we impose a fixed set of coordinates (X, Y, Z) , which does not follow the beam as in Sec. 5.1 but instead is fixed at the beam when reflected on the oscillator O. We refer to the caption of the figure to illustrate the optical components of the design. The first step of the alignment is to roughly prepare the optical path as in fig. 5.A.1. All the components but the ones in the vacuum chamber are mounted on the optical table, thus we intend them oriented along the Y axis, exception made for M_3 which has an angle of $\pi/4$ with respect to it. The other mirrors M_1 and M_2 are turned at $\pm\pi/4$ around X . Inside the vacuum chamber, the reference mirror M is mounted with its reflecting face in the same plane of one face of the PBS, which other face is parallel to the oscillator.

We divide the following description in two steps: we first align the laser beam with the interferometer, then we maximise the interferometric signal.

5.A.1 Alignment of the interferometer

The first part is to check whether a signal can be sent and retrieved from the chamber. There are three optical elements which are tunable: the steering mirrors M_1 , M_2 , and the reference mirror M . M_3 being fixed.

A preliminary test is to check whether it is possible to send the laser into the chamber and measure a signal coming back at the entrance of the analysis area, regardless of its polarization. We thus steer M_1 and M_2 in order to find a signal E_{AN} after the BS_{IN} and to try to center this with respect to the Y axis. This can be done placing an optical shutter OS after the BS: a combination of manipulations on M_1 and M_2 should lead to a rough centering of the beam in the OS.

The inclination of the oscillator with respect to the chosen axes is not a degree of freedom, therefore it serves as a reference. While we suppose the surface of the oscillator probed by the laser roughly in the $Y - Z$ plane, we adjust the optical path to its possible misalignments. Changing the orientation of the $\lambda/2_{IN}$ we can turn the polarization of the beam entering the sensing area, E_{SE} . Since we do not precisely know the polarization of the laser after the polarizer P , a simple technique is to cover M and measure the intensity of E_{AN} . We then rotate $\lambda/2_{IN}$ until $|E_{AN}|^2$ is maximal. This means that the $\lambda/2_{IN}$ is shutting off the polarization which goes to M . At this point we can remove the cover on M . Let us call this configuration (a). If now we turn the $\lambda/2_{IN}$ of $\pi/4$ we hide the signal of the oscillator: this is configuration (b). Finally, when $\lambda/2_{IN}$ is turned of $\pi/8$, the optical element equally divides

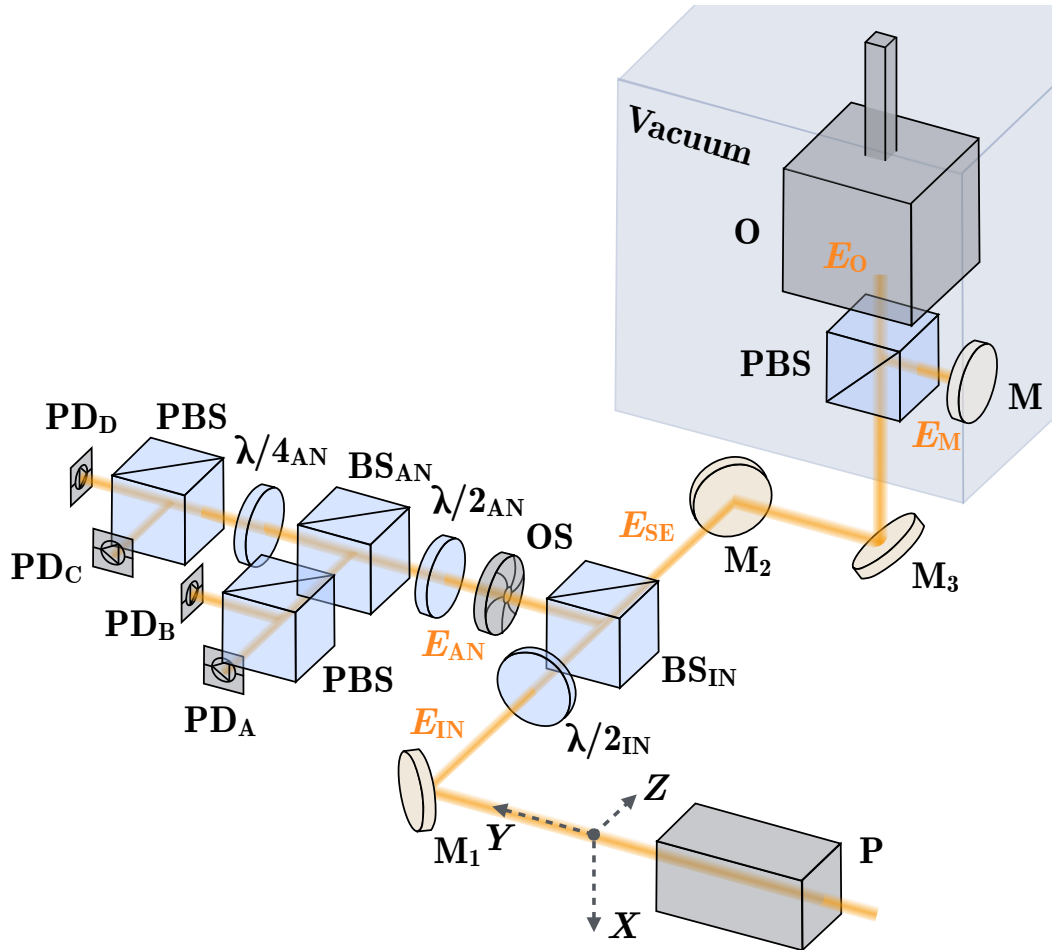


FIGURE 5.A.1: Experimental setup. We show a more detailed version with respect to fig. 5.1.2 of the experimental setup, in order to explain the aligning process. The beam gets inside the system through a polariser P, then it is steered towards the first half-wave plate $\lambda/2_{\text{IN}}$ by a mirror M_1 . Half of the intensity is lost in the beam splitter BS_{IN} (not depicted) whilst the other half is directed towards a second and a third mirror, M_2 and M_3 respectively, which send the probe inside the vacuum chamber. Here, the polarizations are separated by the PBS and one beam probes the reference mirror M whilst the other the oscillator O. Upon recombination the beam follows the same path until it is redirected towards the analysis area by the BS_{IN} . Here the beam goes through an optical shutter OS and a second $\lambda/2_{\text{AN}}$, before being divided in the two analysis areas of the interferometer by a second beam splitter BS_{AN} . Finally, two PBSs separate the polarizations in both arms, whilst in one a quarter-wave plate $\lambda/4$ adds a phase shift in order to create the quadrature of the signals. The converging lenses and the window of the vacuum chamber are not depicted.

the beam in the two polarizations. This configuration, called (c), is the one used during the measurement.

In (a), we can more effectively orient M_1 and M_2 in order to center the returning beam $E_{AN} = E_O$. There are two angles to consider: one is the inclination ($X - Y$ plane) and one is the azimuth ($Y - Z$ plane). Since the longer the path the higher the leverage of a small angle, we can check the orientation looking at the signal returning to the polarizer. The analysis area begins at less than 10 cm with respect to the BS, whilst the polarizer is at roughly 1 m, thus it is more efficient to consider the latter as a reference. Since there is a quarter of the initial laser intensity tracing its way back towards the polarizer, and hence the fiber, it is better to avoid a perfect alignment. We thus steer the mirrors in order to place the returning beam just above the exit hole of P (in the $X - Y$ plane), thus with a small inclination (roughly half a mm above the hole). As mentioned, this misalignment is less influent in the analysis area due to the reduced distance.

When this is done, it is important to test that some intensity reaches at the photodiodes. If this does not happen it means that the analysis area is not aligned with the laser, and we need to adjust the orientation of the elements. Referring to fig. 5.A.1, the most sensitive element is the BS_{AN} , which determines the $Y - Z$ orientation of the E_{AB} probe. The E_{CD} on the other side is independent on the orientation of BS_{AN} . Once we have manipulated BS_{AN} , we can adjust the PBSs in order to center the signals on the photodiodes. Lastly, the position of these can be easily adjusted too. At the end of this stage we ensure that the entering beam E_{IN} is successfully sent to the oscillator and retrieved in the analysis area.

5.A.2 Optimisation of the interferometric signal

We must now create and optimize the interferometric signal, which is retrieved when the reference and the oscillator beams are overlapped. We turn now the $\lambda/2_{IN}$ in the configuration (b). The goal is to steer the laser beam $E_{AN} = E_M$ roughly at the center of the optical shutter, and then test its position above the polarizer. In order to do so, we orient the reference mirror M until an acceptable position is reached.

In order for this to be precise, we switch to configuration (c). At this point the laser probes both the oscillator and the reference mirror, therefore we have two beams going to the optical shutter. In order to verify this, it is practical to cover and uncover quickly the reference mirror to check the presence of E_M on the surface of the shutter. If the spots are separated, one should disappear, whilst if they are well overlapped there should be a lowering in intensity. The next step is then to adjust the orientation of M to refine the overlapping, first at the shutter and then at the polarizer. Whereas the second is more precise, it is also more difficult to test due to the presence of the incoming beam just a millimeter below.

The recombined beams being roughly overlapped, there are two tools to fine tune this: a beam profiler and the contrast C from the interferometer. The first strategy consists of placing a beam profiler in place of the optical shutter, set the $\lambda/2_{IN}$ to the configuration (a), record the beam profile, switch to (b) and overlap the signals. Adjusting the mirror M accordingly and repeating the procedure yields the desired fine-tuning.

The other method is to measure the interferometric signal and maximise the contrast C . In order to do so, we need to prepare the system for a measurement, which is convenient because when this step is completed the QPDI is ready to be used. We thus set the $\lambda/2_{IN}$ in configuration (c), and proceed to find the ideal orientation of the second half-wave plate, $\lambda/2_{AN}$. In order to do so, we acquire the signals of the photodiodes and plot the ellipse C whilst exciting the oscillator with little hits on the vacuum chamber. Whilst prompting

oscillations (the system is exposed to the air and energy is dissipated quickly) we turn the $\lambda/2_{AN}$ in order to find the highest *amplitude* of contrast. In fact, whether or not an ellipse is formed depends on the orientation of the $\lambda/4$: the farther it is from its ideal position (added phase $\psi = \pi/4$), the more the contrast resembles to a line. This happens because if $\psi = 0$, both arms of the interferometer yield the same function, and when plotted one against the other it results in a line. Therefore, some rough adjustments are made between these two optical elements until an acceptable C is visible. Note that if the overlap is not yet good enough, a very small contrast is the probable outcome and it suffices. Subsequently, we modify the orientation of M at very small steps and track the magnitude of the ellipse. When a maximum is reached, the interferometer is aligned with the laser beam.

The last step regards the fine-tuning of the interferometer. The factor that prescribes the sensitivity of the interferometer is how close the contrast C is to a unit circle. Therefore, once the previous steps yield a visible ellipse, this may be improved by little changes in all the degrees of freedom set until now. The mirrors M_1 , M_2 , M can be gently moved around their position, as the optical elements $\lambda/2_{IN}$, $\lambda/2_{AN}$, $\lambda/4$ can be turned. The photodiodes position is important too: if one of them yields a very low signal, the center of the laser beam may be outside or at the border of the detector. This reflects itself in the ellipse's shape or its position in the complex plane.

Once an acceptable contrast is retrieved, the vacuum chamber can be sealed and the interferometer is ready to measure. As a final note, the ellipses shown in fig. 5.1.3 are very close to the unit circle, which shows that we are able to accomplish a quasi-perfect contrast¹

5.B Noise sources

Both the QPDI and the oscillator are extremely sensitive to environmental influences, thus in order to measure the displacement of the cuboid some precautions are necessary. The experimental setup is placed on an optical table, hence suspended from the ground. The only links it has with the environment are the cables of the sensors and the photodiodes, and the pipe of the turbo, which is removed during measurements. In fact, while air is pumped out of the chamber for an entire day (see Sec. 5.3.1), the pump needs to be disconnected during the measuring session due to its vibrations. Owing to a leak in the chamber, the pressure thus increases during the measurement (see fig. 5.3.1), although we show in Sec. 5.D that this does not play a role in the measured thermal noise. The installation of an ion pump was not possible during my tenure at the laboratory due to the leak, which would have crippled the device.

The laser probe used in the NETN experiment is also used in squeezing experiments [14], for which High-Voltage (HV) frequency control is applied. While the power of the incoming laser I_{IN} is relatively stable, the frequency disturbances hinder any NETN measurement during session of the other experiment. Furthermore, we have noticed disturbances in the spectra even when the HV cable connects the laser to the control whilst the control is turned off. In the spirit of limiting external noise sources, we always disconnect it before a measurement.

As mentioned, the NETN sessions are made during the night. In fact, it is preferable to avoid human presence in the laboratory and not hinder the squeezing experiment to work.

¹If the superposition is less than optimal, the signals carrying the displacement information, in the form of sinusoidal functions, never reach the maximum and the minimum in intensity. This happens because complete destructive interference cannot happen, and a residual intensity signal is always retrieved by the photodiodes, thus lowering the visibility of the interferences. The same occurs for the constructive interference, leading to a less than maximum of the function.

Furthermore, the environmental light raises issues: the QPDI optical components being exposed, they capture parasitic light. The effect on the experimental PSDs is an increase of the background noise, usually completely hiding the transverse mode. Since the laboratory is not exposed to natural light, it is sufficient to turn off the artificial lights just before the measurement.

As we can see from fig. 5.1.4, the experimental spectra are dominated by a huge noise bump at low frequency ($f < 200$ Hz). This is mainly due to environmental noise transmitted through the suspension system [62], which is designed to impede this to pollute higher frequencies, where the resonances we are interested in lie (300 – 1500 Hz). In fact, we note that the PSD reaches a plateau around 300 Hz, which previous studies associate with ADC noise [90]. Nevertheless, this part of the spectrum shows various and not completely understood features, such as bumps and peaks, which are sometimes very close to the resonances. This is depicted in fig. 5.B.1, for an equilibrium and an out-of-equilibrium case. We notice how around the transverse resonance the background noise shows some wiggles, which partly disappear in the NESS case. The longitudinal mode is less affected by these features, even if we see the appearance of peaks close to the resonance in the non-equilibrium PSD. We further discuss these characteristics of the spectrum in Appendix 5.E.

5.C Sensitivity and statistical uncertainties on T^{fluc}

As described in Sec. 5.1.8, the QPDI measures the vertical displacement of the oscillator, δx . Whilst this directly gives the longitudinal mode displacement δ , it is not straightforward to convert δx in the transverse angle θ without knowing the probing point y_0 and the precise mode shape of the oscillator. Due to our definition of the fluctuation temperatures T^{fluc} , though, it is not necessary to perform this calibration, proven that we assure y_0 to be constant between the equilibrium and non-equilibrium measurements. Since y_0 is not experimentally accessible, we express the possibility of a shift of probing point $dy_0 \neq 0$ as a systematic error ϵ^{sys} , as usual (see 3.62).

Let us discuss the sensitivities of the two motions to the presence of a dy_0 . As said, the longitudinal mode is independent on the position y_0 (and z_0), therefore its sensitivity σ^δ is constant. On the other side, the angle θ depends on y_0 through the complex mode shape of the oscillator, which can be considered a second deflection mode of the rod with an important load at its end. A full treatment of the sensitivity σ^θ is beyond the scope of this thesis (see for example [12]), nevertheless it is easy to make some qualitative considerations.

If we suppose that a shift dy_0 occurred throughout the four experimental sessions, it affected the measured fluctuation temperatures T_θ^{fluc} . This shift may be due to endogenous causes, such as thermal expansion, which should nevertheless be small due to the small coefficient $\alpha_l = 24.1 \times 10^{-6} \text{ K}^{-1}$ and temperatures ($\Delta T^{\text{max}} \leq 30 \text{ K}$). If a shift occurred, thus, it is more probably due to exogenous reasons, such as small drifts of the optical components directing the laser beam to the oscillator. The measurements spanning 10 days, it is not to be excluded that the beam position moved of a few hundreds of μm . This would then result in a systematic error, thus increasing the uncertainties of the transverse fluctuation temperature in fig. 5.4.2.

5.D Dependency on pressure

Due to the pressure p increasing since the beginning of a measurement session, the system is not strictly in a steady state. As seen in Sec. 5.3.1 in fact, probably due to a leak the pressure

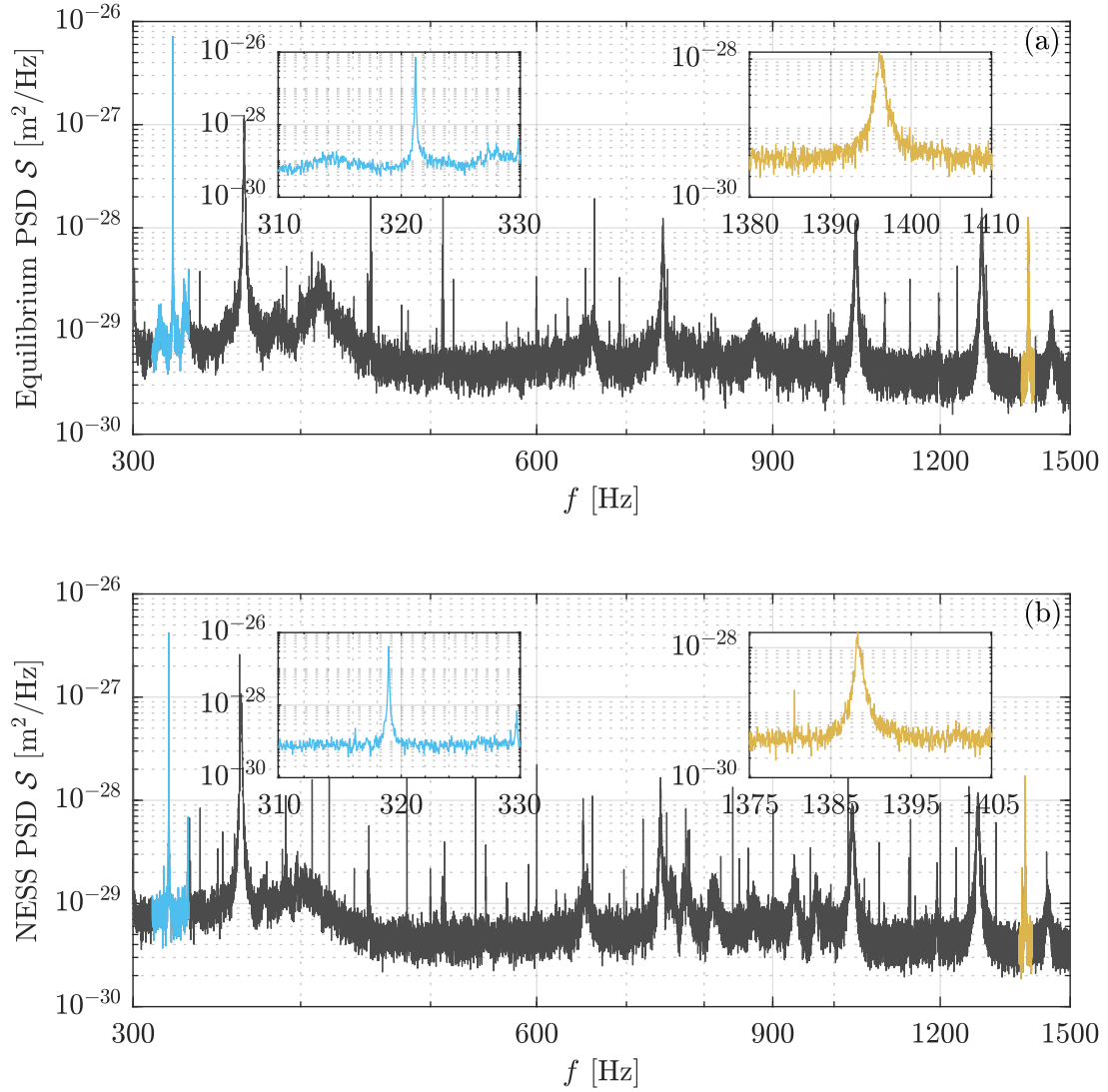


FIGURE 5.B.1: Spurious peaks in the resonance modes frequency range for an equilibrium (a) and non-equilibrium measurement (b). The average of 25 experimental PSDs shows multiple features in the 300 – 1500 Hz frequency band, some of which are extremely peaked and others broader. The most affected resonance is the transverse mode (cyan), where the background around it shows some wiggles. We can notice how the longitudinal mode (yellow) on the other side is relatively unaffected around the resonance frequency. For the NESS example the frequency range around the transverse resonance is less polluted, whilst the longitudinal mode has a spurious peak at its left. When we fit the spectra we remove the frequency bins showing these peaks. As shown in Sec. 6.6, the goodness of the fit is higher for the longitudinal mode, which can be partly understood by these considerations.

increases from roughly 10^{-4} to 10^{-2} mbar, prompting temperature changes. In fig. 5.D.1 (a) we show the average temperature vs. the pressure, displaying how the equilibrium measurement is taken at relatively high pressure with respect to the others.

Since the results shown in Sec. 5.4 are depicted as an average of a whole measurement session, the changes throughout one session are somehow invisible. In particular, we would like to ensure that no dependency on pressure is present in the fluctuation temperatures, which would probably hint at a bias in the measurement. Since our findings suggest that the mass oscillates with the same magnitude of its average temperature, we expect the difference $T^{\text{fluc}} - T^{\text{avg}}$ to be zero in average, as shown in fig. 5.4.2. In fig. 5.D.1 (b-c) we show that this is the case, independently of the pressure the chamber is at. In (d-e) we show how it is hard to find a connection between the pressure and the loss angle too, although it would be expected that dissipation would be more effective at higher p . Due to the reduced dimension of the sample for the transverse mode, it is hard to affirm this for φ_θ , whereas for the longitudinal mode the lack of correlation is more clear.

5.E Open questions and insights

Whilst the new setup shows improvements with respect to the previous version (I_1 [90]), some questions raised by the results of I_1 remain unanswered. Furthermore, as previously stated, there is a clear incompatibility between the measurements presented in this thesis and other measurements of the oscillator. We comment here on these questions.

5.E.1 Open questions

The first question we examine is an issue shown by I_1 and confirmed in this work: an unphysical fluctuation temperature. We discuss only the longitudinal mode, since it is impossible to calibrate the transverse one without knowing y_0 . Since the mass of the oscillator m is well known and the resonance frequencies ω_δ handy to measure experimentally, it should be possible to calculate the temperature of the system through the EP:

$$T_\delta = \frac{m\omega_\delta^2 \langle \delta^2 \rangle}{k_B} \quad (5.26)$$

which can be extended out of equilibrium through eq. 2.77. With the mass being $m = 0.24$ kg, the outcome of measurements in I_1 shows that $T_\delta \approx 150$ K, which is clearly unphysical.

The results of the fluctuation temperatures of the current setup are shown in fig. 5.E.1. We can see that the fluctuation temperatures calculated through eq. 5.26 are well below to $T^{\text{amb}} \approx 295$ K, which shows that the aforementioned issue remains. Furthermore, it is perplexing how its value in equilibrium increases from the 150 K of I_1 to the 180 K of the current setup.

In fig. 5.E.1 we also depict the difference between the calibration through the hit and the drift. Whereas it is not very important for the NESSes, the underestimation of the contrast C_D in the equilibrium measurement yields a difference of roughly 7 % between the two. In both cases the fluctuation temperatures are well below T^{amb} , therefore the calibration process does not explain this feature.

The second question is the difference of these results and the previous ones of the group, which we already commented in Sec. 5.5. We believe these question to be possibly related, so we try to interpret them in the next section.

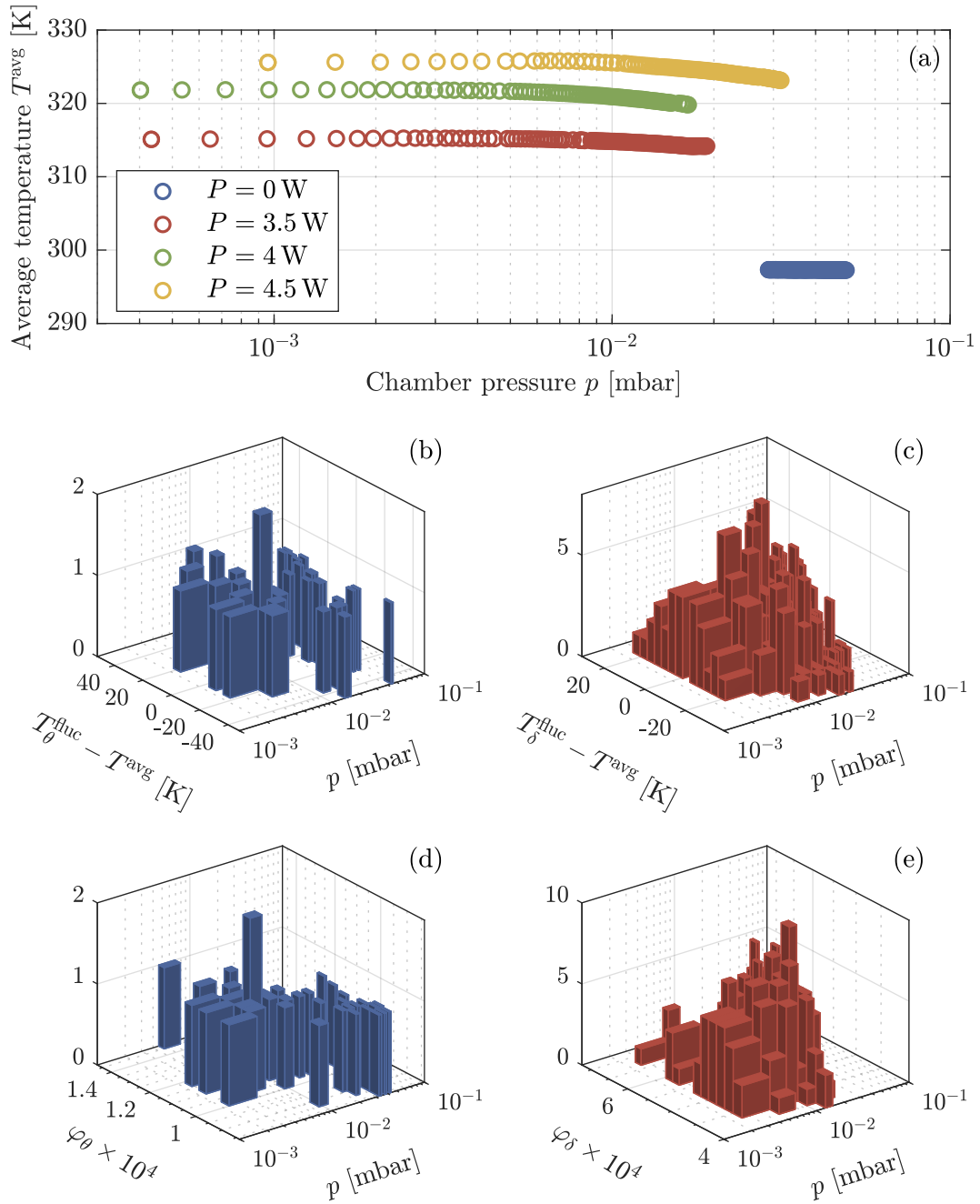


FIGURE 5.D.1: Effect of the pressure changes throughout the experiment. In (a), we show the average temperature of the oscillator T_{avg} with respect to the pressure p of the vacuum chamber. We notice that the equilibrium measurement was taken at relatively high pressure with respect to the non-equilibrium ones. In the latter the average temperature decreases with time. In (b-c) we show the difference between the fluctuation temperature T^{fluc} and T_{avg} vs the pressure. Since our measurements show that $T^{\text{fluc}} \approx T_{\text{avg}}$, this difference should be centered in zero and not depend on the pressure, which is indeed the case from the histograms. In (d-e) we show how the loss angle φ does not have a clear dependency on the pressure either.

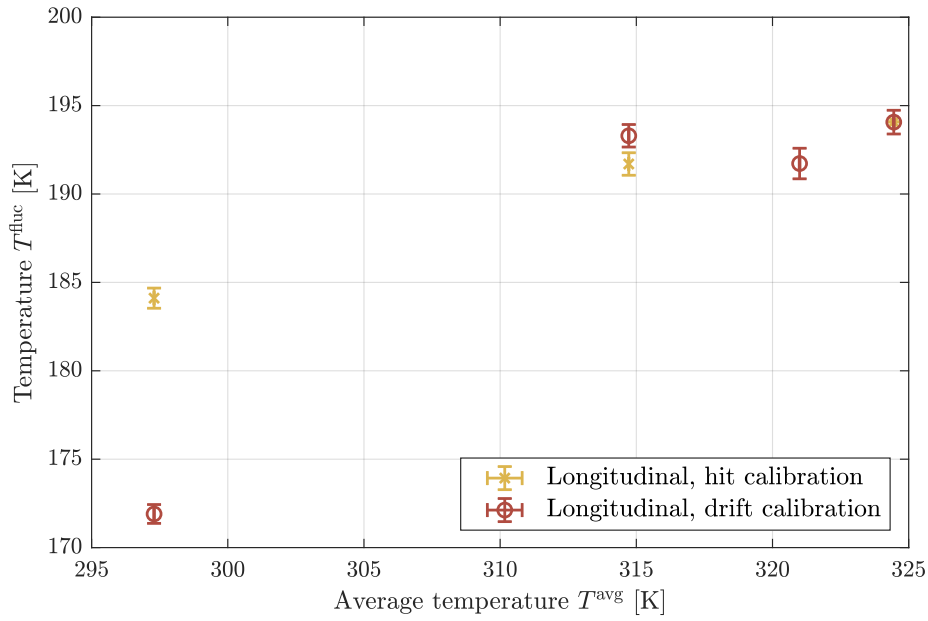


FIGURE 5.E.1: Fluctuation temperatures calculated from eq. 5.26 for the two calibration methods. The longitudinal temperature in equilibrium is lower than the temperature of the environment ($T^{\text{amb}} \approx 295$ K), which is unphysical. The NESS temperatures show the same issue. We cannot expect this to be an issue related to the calibration method used, since with both of them the fluctuation temperature is lower than T^{amb} . Due to the unknown transverse sensitivity $\sigma^\theta(y_0)$, it is not possible to calculate the fluctuation temperatures for this mode.

5.E.2 Insight on possible explanations

Various hypothesis are considered to interpret these issues. The most obvious observation is that we do not understand completely the system, and we may be overlooking some interactions between the oscillator and the measuring devices. For example, the bench where the PBS and the reference mirror are attached (fig. 5.1.2), which is screwed close to the cuboid inside the vacuum chamber, may exchange energy with the oscillator. In fact, when the current setup was changed with respect to the previous one, a considerable weight was removed from the bench, leading to different distribution of the spurious peaks in the PSDs. We show an example of this effect in fig. 5.4.1. Furthermore, the resonance frequency of the longitudinal peak is redshifted of about 8 Hz with respect to its value in the I_1 experiments, which shows that some changes occurred at the oscillator between the two versions of the setup. Explaining this effect thanks to a mass change of the oscillator would yield a mass loss of roughly 1 %, which causes would be unknown.

Due to the high complexity of the experimental setup, this is hard to assess, although tentatives are ongoing. Recently, clues has been found in the displacement of some features around the resonances when some weight was added in different positions of the bench. This would mean that the suspension and detection system may interact with the oscillator, thus perhaps reducing its thermal motion to the point shown in fig. 5.E.1. Furthermore, this could affect the different non-equilibrium behavior of the oscillator presented in this work with respect to previous results.

Chapter 6

Statistical properties of thermal noise

Throughout this thesis, we have studied the evolution of the thermal noise of different cantilevers and a macroscopic oscillator when subjected to a temperature difference along their lengths. We have shown the validity of the extended FDT for all these cases, proving that statistical tools normally defined for systems in thermal equilibrium can be modified in order to include NESS cases. As mentioned, thermal noise is an extremely ephemeral quantity to measure, as it is often orders of magnitudes lower than other possible kinds of perturbations to the considered system. In Appendix 3.C.3, we discuss how we can exclude some of these contributions from polluting the observed signal, namely laser fluctuations and shot noise. Once we rule out all the nuisances we can think of, the reasonable choice is to *assume* we are measuring thermal noise.

In order to be rigorous, though, we can *verify* that this is the case. Indeed, we know that the thermal fluctuations of a system are the expression of randomly-exchanged energy between the system and the surrounding environment through a generalised force $F(t)$. Hence, this quantity is supposed to be a stochastic process for the Central Limit Theorem (CLT). Knowing the Probability Distribution Function (PDF) of the force, it is possible to calculate the expected distribution of the measured thermal fluctuations, and to compare it with the measured one.

In the first part of this chapter, we discuss how the stochastic properties of the force F are inherited by the displacement of the system under study, and how, thanks to a lock-in amplifier technique, we can test whether the measured signals satisfy them. In particular, we demonstrate how there is quantitatively no difference between the PDF of the fluctuations of an equilibrium system and the PDF in a NESS. Furthermore, we shed some light on the self-oscillations of the cantilever (already introduced in Appendix 3.C.3) and how to distinguish them from thermal noise.

In the second and third parts, we discuss the statistical properties of the PSD, showing how an ensemble of spectra are in general Γ -distributed around their average. Thanks to this, we show a method of sorting data based on the expected PDF, demonstrating how doing so can help removing corrupted signals. Since this method is based on an objective principle, it grants us an unbiased tool to sort the experimental spectra. This has been used in every measurement presented in this thesis.

In the next part, we discuss the statistical properties of the retrieved thermal fluctuations, in particular the area under the resonance peak T^{fluc} . Based on the retrieved PDF, a second selection method can be implemented.

Finally, the last section discusses the fitting method used on the thermal noise spectra throughout this thesis. We discuss an unbiased estimator for the parameters of the fit, and

we show a new method in order to associate an uncertainty to the parameters. A discussion then concludes this chapter.

6.1 Statistical properties of noise

As mentioned, we usually refer to thermal noise as a thermal force $F(t)$, through which the environment interacts with the system we are considering. Let us consider the case of the deflection of the cantilever (the extension for the torsion or the NETN oscillator is trivial).

In eq. 2.20, we define the generalised force $F(x, t)$, which pours energy into the cantilever and is converted in its deflection $\delta(x, t)$. We have shown how each mode n of the cantilever can be considered as an independent oscillator, for which the deflection δ_n is coupled with the corresponding F_n (eq. 2.59). In this case, we can simply proceed with our discussion considering a mode n , dropping the index n from δ, F .

6.1.1 Random force F

The average and the variance of the stochastic force $F(t)$ are:

$$\begin{aligned}\langle F(t) \rangle &\equiv \int_{-\infty}^{+\infty} dF F \mathcal{P}(F; t) \\ \langle F^2(t) \rangle &\equiv \int_{-\infty}^{+\infty} dF F^2 \mathcal{P}(F; t)\end{aligned}\tag{6.1}$$

where $\langle \cdot \rangle$ represents the ensemble average, taken over identically prepared systems in different states, at a certain fixed time t . The value of F or F^2 in this instant is weighed by the PDF $\mathcal{P}(F; t)dF$, which quantifies the probability that $F(t)$ lies in the interval $F \leq F(t) \leq F + dF$ at time t .

Since the environment is considered to be in a stationary state, i.e. with constant temperature and pressure, $F(t)$ is said to be stationary and \mathcal{P} does not depend on time: $\mathcal{P}(F; t) = \mathcal{P}(F; t + \tau)$ [66]. For a random process, the probability distribution is thus written:

$$\mathcal{P}(F)dF = \frac{dF}{\sigma_F \sqrt{2\pi}} e^{-\frac{F^2}{2\sigma_F^2}}\tag{6.2}$$

which is the normal distribution with variance σ_F^2 . A quick calculation shows that:

$$\begin{aligned}\langle F(t) \rangle &= 0 \\ \langle F^2(t) \rangle &= \sigma_F^2\end{aligned}\tag{6.3}$$

where the first condition means that the average of the thermal force should be zero.

Let us now observe the stochastic force $F(t)$ in an interval $0 \leq t \leq \mathcal{T}$. This $\tilde{F}(t)$ is a *sample* of the stochastic process $F(t)$. We expand it into its Fourier components:

$$\tilde{F}(t) = \sum_{k=0}^{\infty} \tilde{A}_k \cos(\omega_k t) + \tilde{B}_k \sin(\omega_k t)\tag{6.4}$$

with $\omega_k = 2\pi k / \mathcal{T}$. The stochastic process $F(t)$ is now expanded as:

$$F(t) = \sum_{k=0}^{\infty} A_k \cos(\omega_k t) + B_k \sin(\omega_k t), \quad \text{for } 0 \leq t \leq \mathcal{T}\tag{6.5}$$

The Fourier coefficients \tilde{A}_k, \tilde{B}_k represent a sample of the random variables A_k, B_k , defined by:

$$\begin{aligned} A_k &= \frac{1}{T} \int_0^T dt F(t) \cos(\omega_k t) \\ B_k &= \frac{1}{T} \int_0^T dt F(t) \sin(\omega_k t) \end{aligned} \quad (6.6)$$

We can easily show that when a normally distributed signal $F(t)$ is expressed as the countable sum of coefficients A_k, B_k , these are random variables themselves [19]. As a side note, this is often thought to be the other way around. We can build a random signal *supposing* that all the Fourier coefficients are randomly distributed, and we can show that this property is inherited by their sum, i.e. the signal itself (see [101], sect. 9, (a)). In all cases, the expectation value of A_k, B_k are then defined:

$$\begin{aligned} \langle A_k \rangle &= \frac{1}{T} \int_0^T dt \langle F(t) \rangle \cos(\omega_k t) \\ \langle B_k \rangle &= \frac{1}{T} \int_0^T dt \langle F(t) \rangle \sin(\omega_k t) \end{aligned} \quad (6.7)$$

yielding for $k \neq 0$:

$$\langle A_{k \neq 0} \rangle, \langle B_{k \neq 0} \rangle = 0 \quad (6.8)$$

due to stationarity (every fluctuating component in average is zero), and:

$$\langle F \rangle = \frac{1}{T} \int_0^T \langle F(t) \rangle dt = (\langle A_0 \rangle + \langle B_0 \rangle)/2 \quad (6.9)$$

for the $k = 0$ term¹. In our case, we know that this is zero after eq. 6.3.

Let us imagine we perform a measurement of the average of the sample $\tilde{F}(t)$ in the laboratory, which we call \bar{F}_T :

$$\bar{F}_T \equiv \frac{1}{T} \int_0^T dt \tilde{F}(t) = (\langle \tilde{A}_0 \rangle + \langle \tilde{B}_0 \rangle)/2 \quad (6.10)$$

This is a possible realisation of the expected value $(\langle A_0 \rangle + \langle B_0 \rangle)/2$. Since this is not known, we usually confound \bar{F}_T with the ensemble average $\langle F \rangle$. In general, though, $\bar{F}_T \neq \langle F \rangle$. If, however:

$$\lim_{T \rightarrow \infty} \bar{F}_T = \langle F \rangle \quad (6.11)$$

a process is called *ergodic*. When can a process be considered ergodic? A body of literature exists on the subject [88, 47] from both a physical and a mathematical point of view, and it can be very difficult (if not impossible) to prove a process is ergodic. Often, this is taken as an *assumption*, since during the experiment we are forced to sample the stochastic process, and in principle we cannot access the whole parameter space. It is common then to suppose that for a sufficient sampling time t^{meas} , the system has the time to sample all the possible states; hence, it is ergodic.

We are therefore supposing this to be true, so that we can interchange $F(t)$ and $\tilde{F}(t)$. Let us next go back to the expansion in eq. 6.5. We now know that the random variables in the set $\{A_k, B_k\}$ are normally distributed with zero average (eq. 6.8). We can thus write the

¹In the case of Johnson noise, we can refer to the $k = 0$ term as the DC component of the signal.

probability of finding them in a certain range as [101]:

$$\mathcal{P}(A_k, B_k) = \frac{1}{2\pi\sigma_{F,k}} e^{-\frac{A_k^2 + B_k^2}{2\sigma_{F,k}^2}} \quad (6.12)$$

In this case, we intend that the sum of the variances is the thermal force variance:

$$\sum_{k=0}^{\infty} \sigma_{F,k}^2 = \sigma_F^2 \quad (6.13)$$

Eq. 6.12 can be integrated in order to demonstrate:

$$\begin{aligned} \langle A_k \rangle &= \langle B_k \rangle = 0 \\ \langle A_k^2 \rangle &= \langle B_k^2 \rangle = \sigma_{F,k}^2 \end{aligned} \quad (6.14)$$

and:

$$\begin{aligned} \langle A_i A_{j \neq i} \rangle &= \langle B_i B_{j \neq i} \rangle = 0 \\ \langle A_i B_j \rangle &= \langle B_i A_j \rangle = 0 \end{aligned} \quad (6.15)$$

which shows how the Fourier coefficients are independent from one another and from themselves, unless we consider the same frequency bin k . Using the last property, squaring and averaging eq. 6.5 we obtain:

$$\langle F^2(t) \rangle = \sum_{k=1}^{\infty} \langle A_k^2 \rangle \langle \cos^2(\omega_k t) \rangle + \langle B_k^2 \rangle \langle \sin^2(\omega_k t) \rangle \quad (6.16)$$

where the average of sinusoidal functions yields $1/2$, and the power of each of the Fourier coefficients A_k, B_k at a certain frequency f_k yields $\sigma_{F,k}^2$. The sum at all frequencies is the total power of the thermal force.

If we now consider a frequency range Δ_n around the resonance frequency f_n such that $\Delta_n \equiv \{k \mid f_n - \Delta f \leq f_k \leq f_n + \Delta f\}$, we can define the PSD of the thermal force in this interval as:

$$\mathcal{S}_F(f_k) 2\Delta f = \sum_{k \in \Delta_n} \frac{\langle A_k^2 \rangle + \langle B_k^2 \rangle}{2} = \sum_{k \in \Delta_n} \sigma_{F,k}^2 \quad (6.17)$$

in the form in which we are accustomed to express it (eq. 2.47).

In this section, we thus show how the Fourier coefficients $\{A_k, B_k\}$ are normally distributed with variance $\sigma_{F,k}^2$, how they are independent from each other, and the sum of their variances produces the PSD of the thermal force.

6.1.2 Deflection δ

In the experiment, we retrieve the displacement of the cantilever δ , which we can express in a way similar to eq. 6.5:

$$\delta(t) = \sum_{k=0}^{\infty} X_k \cos(\omega_k t) + Y_k \sin(\omega_k t) \quad (6.18)$$

Inserting eq. 6.5 into the EM for the deflection (eq. 2.20), we can easily connect the force coefficients $\{A_k, B_k\}$ to the flexural ones $\{X_k, Y_k\}$:

$$\begin{aligned} X_k &= \frac{(k^r(\omega_n) - m\omega_k^2)A_k - k^i(\omega_n)B_k}{(k^r(\omega_n)^2 - m\omega_k^2)^2 + k^i(\omega_n)^2} \equiv \alpha A_k + \beta B_k \\ Y_k &= \frac{(k^r(\omega_n) - m\omega_k^2)A_k + k^i(\omega_n)B_k}{(k^r(\omega_n)^2 - m\omega_k^2)^2 + k^i(\omega_n)^2} \equiv \alpha A_k - \beta B_k \end{aligned} \quad (6.19)$$

Since $\{X_k, Y_k\}$ are a linear combination of the random variables $\{A_k, B_k\}$, they too are random variables too. Thus, a PDF $\mathcal{P}(X_k, Y_k)$ similar to eq. 6.12 can be written. We first express:

$$\begin{aligned} A_k &= (k^r(\omega_n) - m\omega_k^2)X_k + k^i(\omega_n)Y_k \equiv \zeta X_k + \rho Y_k \\ B_k &= (k^r(\omega_n) - m\omega_k^2)Y_k - k^i(\omega_n)X_k \equiv \zeta X_k - \rho Y_k \end{aligned} \quad (6.20)$$

The PDF then reads:

$$\mathcal{P}(X_k, Y_k) = \frac{1}{2\pi\sigma_{\delta,k}} e^{-\frac{X_k^2 + Y_k^2}{2\sigma_{\delta,k}^2}} \quad (6.21)$$

with $\sigma_{\delta,k}^2 \equiv \sigma_{F,k}^2 / (\zeta^2 + \rho^2)$. The properties in eq.s 6.14, 6.15 are inherited by $\{X_k, Y_k\}$, therefore they are independent normal variables.

Let us now use the same reasoning of eq. 6.17: squaring and averaging eq. 6.18 in a frequency interval $2\Delta f$ we obtain the PSD of the deflection:

$$\mathcal{S}_\delta(f)2\Delta f = \sum_{k \in \Delta_n} \frac{\langle X_k^2 \rangle + \langle Y_k^2 \rangle}{2} = \sum_{k \in \Delta_n} \sigma_{\delta,k}^2 \quad (6.22)$$

It comes without surprise then that the PSD of the thermal force and the one of the displacement are linked through the susceptibility χ_n (eq. 2.42):

$$\mathcal{S}_{\delta_n}(f_k) = \chi_n^2(\omega_k) \mathcal{S}_F(f_k) = \frac{\mathcal{S}_F(f_k)}{(k^r(\omega_n)^2 - m\omega_k^2)^2 + k^i(\omega_n)^2} \quad (6.23)$$

In this section, we then demonstrate how the Fourier coefficients $\{X_k, Y_k\}$ are also normally distributed with variance $\sigma_{\delta,k}^2$ and are independent random variables.

6.1.3 Lock-in amplifier

Since our goal is to verify whether the retrieved signals respect the aforementioned properties, we use a lock-in amplifier technique applied as a post-processing of the data. We explain this method here.

Following the same principle of eq. 3.63, we can rewrite the deflection taking into consideration a noise contribution \mathcal{N} :

$$\delta(t) = \sum_{k=0}^{\infty} (X_k + M_k) \cos(\omega_k t) + (Y_k + N_k) \sin(\omega_k t) \quad (6.24)$$

with $\{M_k, N_k\}$ the set of Fourier coefficients for the external noise \mathcal{N} .

Let us now consider in a certain frequency f_n . In order to isolate the Fourier coefficients around this frequency bin, a common technique is the lock-in amplifier. It is frequently used in experiments where the SNR of the observed phenomenon is low, since its goal is to

filter out the noise around the desired frequency. This is often done *in real time*, during the experiment; we implement it here as a post-processing.

The procedure is as follows: we multiply the deflection $\delta(t)$ by two sinusoidal reference signals at a frequency ω_r , $\cos(\omega_r t)$ and $\sin(\omega_r t)$, with an amplitude $\sqrt{2}$ in order to have an overall unity gain. Using a trigonometric identity, we obtain two sinusoids $X(t), Y(t)$ at $\omega_k - \omega_r$ and $\omega_k + \omega_r$. We next impose $\omega_r = \omega_n$, the resonance frequency, in order to shift the low-frequency sinusoidal to 0 Hz. We then low-pass filter these signals to discard the high-frequency component, thereby selecting a certain filter interval $2\Delta f$. The locked-in signals end up being:

$$\begin{aligned} X(t) &= \frac{1}{\sqrt{2}} \sum_{k \in \Delta_n} (X_k + M_k) \cos((\omega_k - \omega_r)t) \\ Y(t) &= \frac{1}{\sqrt{2}} \sum_{k \in \Delta_n} (Y_k + N_k) \cos((\omega_k - \omega_r)t) \end{aligned} \quad (6.25)$$

where we recall that $\Delta_n \equiv \{k \mid f_n - \Delta f \leq f_k \leq f_n + \Delta f\}$.

Let us now continue in two steps: first, we proceed by supposing a perfect filter which leaves just one frequency bin $k = n$, then we extend the result for a filter with a bandwidth $2\Delta f$.

Ideal case $\Delta f = 0$

In this case, $\Delta_n = \{k \mid f_k = f_n\}$. The two locked-in signals are simply:

$$\begin{aligned} X(t) &= \frac{1}{\sqrt{2}} (X_n + M_n) \approx \frac{1}{\sqrt{2}} X_n \\ Y(t) &= \frac{1}{\sqrt{2}} (Y_n + N_n) \approx \frac{1}{\sqrt{2}} Y_n \end{aligned} \quad (6.26)$$

Only the Fourier coefficients at $k = n$ survived. As we have seen in the previous chapters, our SNR is usually ≥ 100 , therefore we can suppose that no external noise is polluting this frequency bin.

The signals $X(t), Y(t)$ are random variables because they are a linear combination of random variables X_n, Y_n , after eq. 6.21. We hence proceed to build a statistical ensemble: we sample one value of (X_n, Y_n) every sampling time t_s , the value of which depends on the resonance mode we are interested in. It is in fact fundamental to assure that, after recording one value $(X(t_s), Y(t_s))$, we wait for the system to forget its previous state before sampling $(X(2t_s), Y(2t_s))$. Thus, we should ensure *at least* $t_s \geq \tau_n$, the decay time of the resonance. This is calculated as [81]:

$$\tau_n = \frac{Q_n}{\pi f_n} \quad (6.27)$$

with $Q_n = 1/\varphi_n$. The set $\{X_n, Y_n\} = \{X(t_s), Y(t_s); X(2t_s), Y(2t_s); \dots\}$ is in this way a statistical ensemble for the random variables X_n, Y_n .

General case $\Delta f \neq 0$

When a realistic filter is applied, a certain bandwidth $2\Delta f$ around the resonance is chosen. The selected frequencies are then $\Delta_n \equiv \{k \mid f_n - \Delta f \leq f_k \leq f_n + \Delta f\}$. The signals read:

$$\begin{aligned} X(t) &= \frac{1}{\sqrt{2}} \sum_{k \in \Delta_n} X_k \cos((\omega_k - \omega_n)t) \\ Y(t) &= \frac{1}{\sqrt{2}} \sum_{k \in \Delta_n} Y_k \cos((\omega_k - \omega_n)t) \end{aligned} \quad (6.28)$$

Let's consider $X(t)$. We need to show that it is a random variable. Squaring and averaging it, due to the independence of the Fourier coefficients we have:

$$\langle X^2(t) \rangle = \frac{1}{2} \sum_{k \in \Delta_n} \langle X_k^2 \rangle \langle \cos^2((\omega_k - \omega_n)t) \rangle + \langle Y_k^2 \rangle \langle \cos^2((\omega_k - \omega_n)t) \rangle = \sum_{k \in \Delta_n} \frac{\langle X_k^2 \rangle + \langle Y_k^2 \rangle}{4} \quad (6.29)$$

which are the same coefficients as eq. 6.22. Thus, $X(t)$ is normally distributed with a variance $\mathcal{S}_\delta(f)\Delta f$ and the sum:

$$\langle X^2(t) \rangle + \langle Y^2(t) \rangle = \sum_{k \in \Delta_n} \frac{\langle X_k^2 \rangle + \langle Y_k^2 \rangle}{2} = \mathcal{S}_{\delta_n}(f)2\Delta f \quad (6.30)$$

shows how the variance of the distribution of the set $\{X(t), Y(t)\}$ is the PSD of the resonance n in the bandwidth $2\Delta f$, times this interval. This quantity is then the area under the resonance peak that we calculate in order to retrieve T^{fluc} , following eq. 2.47.

In this section, we showed how $\{X(t), Y(t)\}$ are normally distributed set, and each of the two signals have a theoretical variance of half the area under the resonance peak.

6.2 Experiment

In the present section, we want to use the lock-in amplifier technique in order to test whether the measured signals satisfy the properties described above. Moreover, through this study, our goal is to show that we can isolate the self-oscillating regime from the thermal noise. While this test is not new in equilibrium [65], we will perform it for one non-equilibrium dataset, thus probing whether the equilibrium properties can be extended to this case. We take as an example the C100 measurement, since it is the one with the more pronounced non-equilibrium features, and we consider both the flexural and torsional modes in the analysis.

As mentioned, in this experiment, we perform a double ramp with increasing and decreasing injected power. We thus consider the equilibrium step (the first depicted in fig. 3.3.1) and the one at the highest power $P = 9 \text{ mW}$. In order to apply the concepts developed above, we need to calculate the sampling rate for $\{X(t), Y(t)\}$ for each mode to create the statistical ensemble. As mentioned, this corresponds to sample at least at each decaying time $\tau_{n,m}$. These are shown in Table 6.2.1, where the equilibrium values are given (the non-equilibrium ones are very similar).

The values of τ are then compared to the typical durations of the experiment. In one power step, 74 flexural and torsional signals are collected, each of which lasts $t_s = 2 \text{ s}$, for a total of $t^{\text{meas}} = 150 \text{ s}$, although non-continuous. Indeed, due to the time needed to transfer the data to the disk, after each t_s , a time at least equal to this is needed before another signal is collected. We can then see that mode $n = 1$ shows a coherence time *higher*

Mode n, m	Deflection			Torsion		
	f_n [kHz]	$Q_n/10^4$	τ_n [s]	f_m [kHz]	$Q_m/10^4$	τ_m [s]
1	5.0	≈ 4	≈ 2.5	44.3	4.9	0.36
2	29.6	5.0	0.54	134.0	4.5	0.11
3	80.0	4.8	0.19	232.7	4.4	0.06
4	152.6	4.4	0.09	344.6	3.9	0.04
5	246.2	4.6	0.06	426.8	4.7	0.04
6	360.5	2.3	0.02	619.5	3.4	0.02
7	496.4	3.8	0.02	782.7	3.4	0.01
8	652.6	3.9	0.02	964.5	3.5	0.01

TABLE 6.2.1: Equilibrium decaying times τ for the flexural and torsional modes in the C100 experiment.

than the measuring time t_s , which leads to us to sample just one value of $\{X(t), Y(t)\}$ per t_s . Conversely, all the other resonances grant us at least 3 samples per t_s , which greatly increases with the mode number.

The next step is to calculate the $\{X(t), Y(t)\}$ ensemble for each mode. For the deflection, we multiply the signal $\delta(t)$ for $\cos(\omega_n t)$, $\sin(\omega_n t)$, and then low-pass filter the signal with a bandwidth $\Delta f = 1$ kHz. Doing this for all the available n , we get $\{X_n(t), Y_n(t)\}$. The same is done for the torsional modes, yielding $\{X_m(t), Y_m(t)\}$.

In the next section, we want to check whether the measured $\{X_n(t), Y_n(t)\}$ are randomly distributed around the mean value $(0, 0)$, with $X_n(t)$ independent from $Y_n(t)$. We begin with the deflection case.

6.2.1 Self-oscillations

The first flexural mode is one of the key points of the present chapter. In Chapter 3, we do not show the results for this mode, since we believe the retrieved signals are not the expression of thermal noise, but rather the result of an optomechanical coupling of the cantilever with the incoming light [74]. When the cantilever is heated, it bends, and bending increases its effective thickness, to which the absorption is strongly proportional. Thus, the system heats up and it becomes softer, bending again. We thus expect this phenomenon to leave traces in the bivariate distributions of $X_1(t)$ and $Y_1(t)$. We show the results for $n = 1$ in fig. 6.2.1 (a-b).

While the majority of the points lie in the bin centered on the origin $(0, 0)$, we note some outliers scattered around this value. Due to the magnitude of the corresponding values $\{X_1(t), Y_1(t)\}$, these points cannot be considered thermal noise. Indeed, converting these into fluctuation temperatures T^{fluc} (as in fig. 6.2.1 (c)) would yield values up to the order of 10^5 K, which is completely unphysical. In fact, as a reference, they greatly surpass the melting temperature of silicon, $T^{\text{melt}} = 1684$ K. We then associate this behavior with the self-oscillations of the cantilever.

As we know, in order to calculate T^{fluc} , we normalise the retrieved noise by the equilibrium temperature. In the $n = 1$ case, this is a difficult task due to some of the values spanning 7 orders of magnitude. In calculating T^{fluc} for fig. 6.2.1 (c), we suppose that the points below a certain value are not polluted, and thus we use their average as the equilibrium value, at $T = 300$ K. Nevertheless, this is a double-edged sword, since in the NESS case it appears that most of the points lie *below* 300 K. This can either be due to self-cooling in the

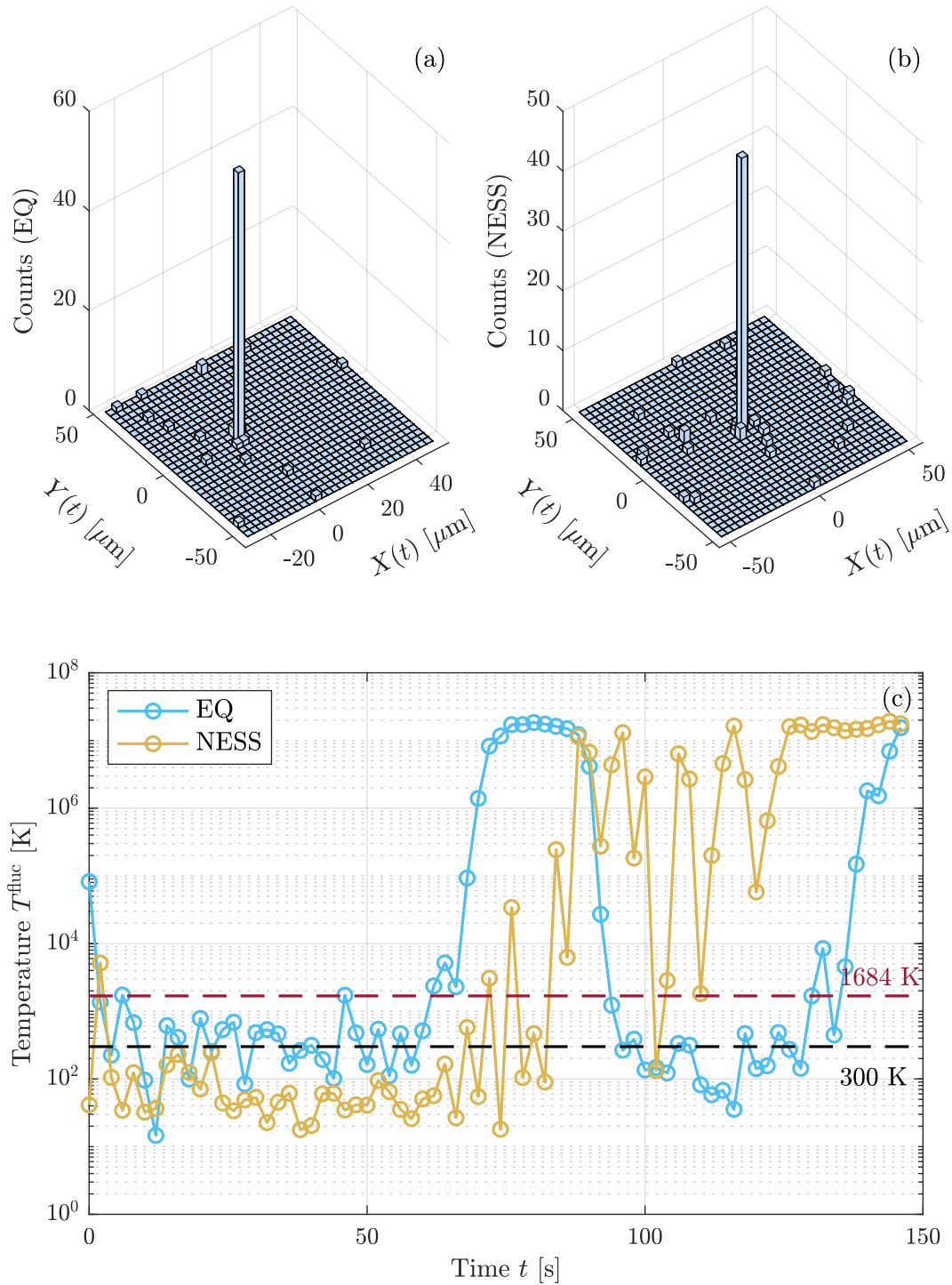


FIGURE 6.2.1: Self-oscillations of mode $n = 1$. In (a), we show the histogram of the locked-in signals $X(t)$ and $Y(t)$ in equilibrium. We can see that whilst the majority of points lie on the origin $(0,0)$, the outliers are significantly far from this point. The same picture is present in (b), for the non-equilibrium measurements. In (c), we convert these fluctuations in T^{fluc} , displaying how they span 7 orders of magnitude. In the equilibrium measurement we can see that part of the points lie around a certain value, which we use as a normalisation in calculating T^{fluc} . Unfortunately, the non-equilibrium T^{fluc} is much below this value. Then, whether the system is self-oscillating in equilibrium or self-cooling in a NESS is difficult to tell. As a side note, we note how there is a maximal value in the self-oscillations amplitude.

NESS case (the opposite of self-oscillations) or conversely to the equilibrium measurements being affected by the self-oscillations.

It is clear that there is a fundamental difficulty in calculating the thermal fluctuations of the first resonance, due to the impossibility of discerning between a purely thermal state and one showing self-oscillating behavior. In fact, no matter where we set a threshold, we cannot be sure whether it is the appropriate one. Furthermore, the statistical ensemble is then too reduced to study the distribution once the outliers are discarded. Since this phenomenon is present in almost all the measurements of this thesis, we believe it is simply best to discard mode $n = 1$.

6.2.2 Equilibrium case

We now focus on the higher flexural modes and the torsional modes, which we believe are not affected by this phenomenon, as reported in Chapter 3. We show the results for deflection in fig. 6.2.2.

Albeit the small sample size, the bivariate histogram of $\{X_2(t), Y_2(t)\}$ for $n = 2$ indicates that these signals are normally distributed around the $(0, 0)$ value, which is confirmed looking at each signal singularly. Moreover, we can test whether any correlation between $\{X_2(t)\}$ and $\{Y_2(t)\}$ exists by transforming them into polar coordinates:

$$\begin{aligned} X(t) &= R(t) \cos \alpha(t) \\ Y(t) &= R(t) \sin \alpha(t) \end{aligned} \tag{6.31}$$

For random uncorrelated signals $\{X_2(t), Y_2(t)\}$ we expect $\alpha(t)$ to be uniformly distributed, which is the case shown in fig. 6.2.2. This means that all the expected statistical properties of thermal noise are satisfied for this mode. Therefore, it is safe to conclude that this resonance is not corrupted by self-oscillations and that the signal is thermal noise. The same can be said for even higher modes, where the increased sample size allows us to further assess this claim: $n = 3, 4$ already shows a better agreement between $\{X_n(t), Y_n(t)\}$ and a normal distribution. In the end, there is no doubt that modes $n = 6$ confirm these results, and the same is valid for modes 7 and 8 (not reported in the figures).

In fig. 6.2.3, we show the results for the torsional modes. In this case, we would need a greater sample size in order for a normal distribution to fit well mode $m = 1$; nonetheless, the result is acceptable. Next, as before, the higher the mode the better the agreement between the expected properties of noise and the measurement.

In conclusion, we can affirm that when the cantilever is in thermal equilibrium, the measured signals satisfy the properties we associate to thermal noise, showing Fourier coefficients that are normally distributed and independent from one another.

6.2.3 Non-equilibrium case

The conclusions reached in the previous section are the ones we hoped for, proving that the measured signals are indeed thermal noise-driven oscillations, since they show the expected statistical properties. When the cantilever is out of equilibrium, though, there is no guarantee that the noise retains these properties. Indeed, out-of-equilibrium statistics might show us a completely different picture, with the PDF departing from a normal law.

In [30], the authors of the NETN experiment (Chapter 5) investigated the statistical properties of the aluminium oscillator. In this work, they demonstrate that no appreciable difference can be detected between the system in equilibrium and in a NESS, using a similar

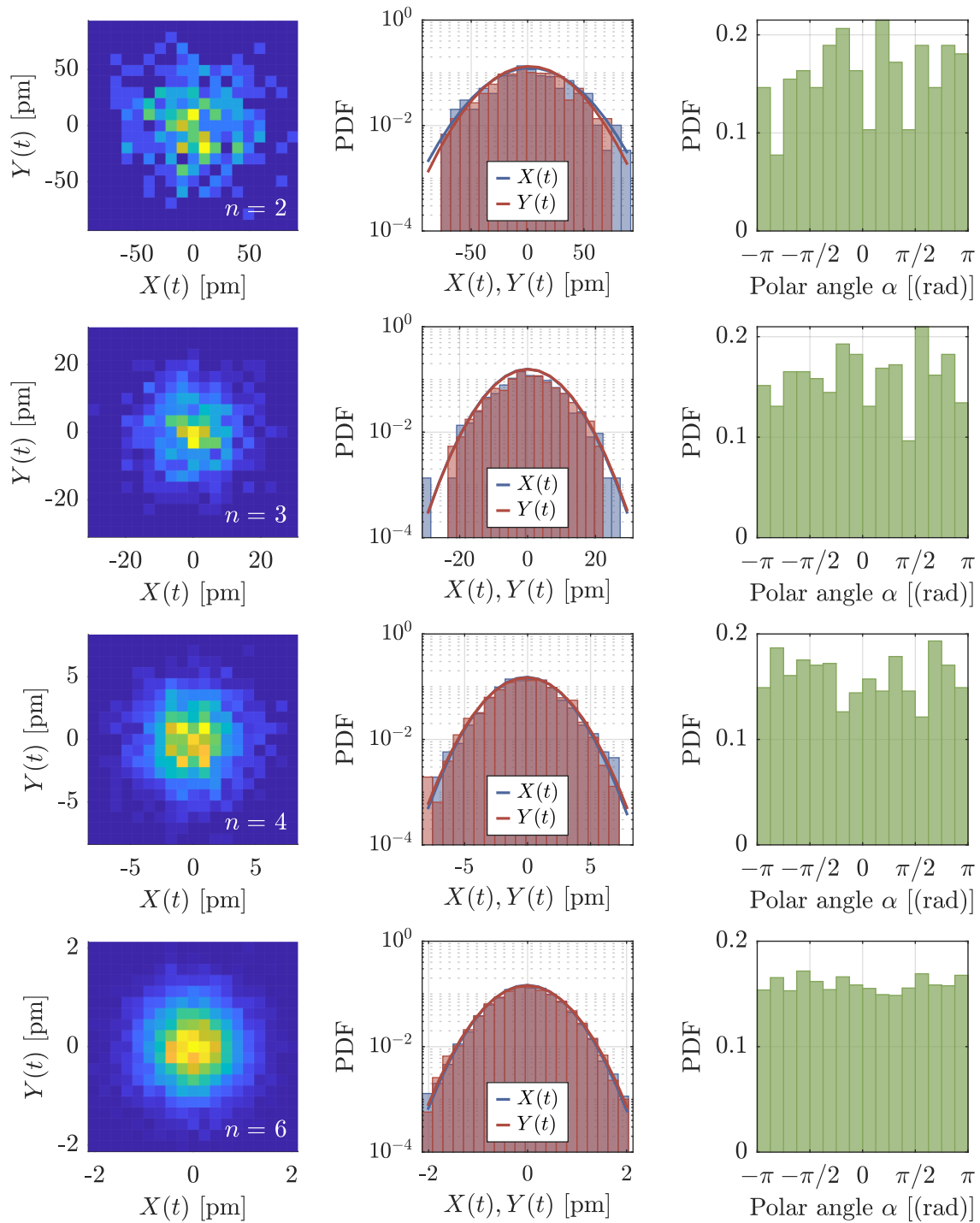


FIGURE 6.2.2: Each row corresponds to a flexural mode n : in the left figure we display the bivariate distribution of the locked-in signals $X(t), Y(t)$, in the center figure the statistical distributions of each signal separately, and in the left figure the polar angle retrieved thanks to eq. 6.31. Starting with $n = 2$, we can see that the signals $X(t), Y(t)$ look randomly distributed around the center $(0,0)$, even though we would need a greater sample size to better test this. Moreover, there are no extreme outliers that can indicate the presence of self-oscillations. Similarly, a normal law fit represents $X(t)$ and $Y(t)$ well. Finally, the polar angle approaches a uniform distribution, hinting that $X(t)$ is not correlated with $Y(t)$. This is even more clear for higher modes (with the sample size increasing), with $n = 6$ showing a perfect agreement between the theoretical prediction and the measurements.

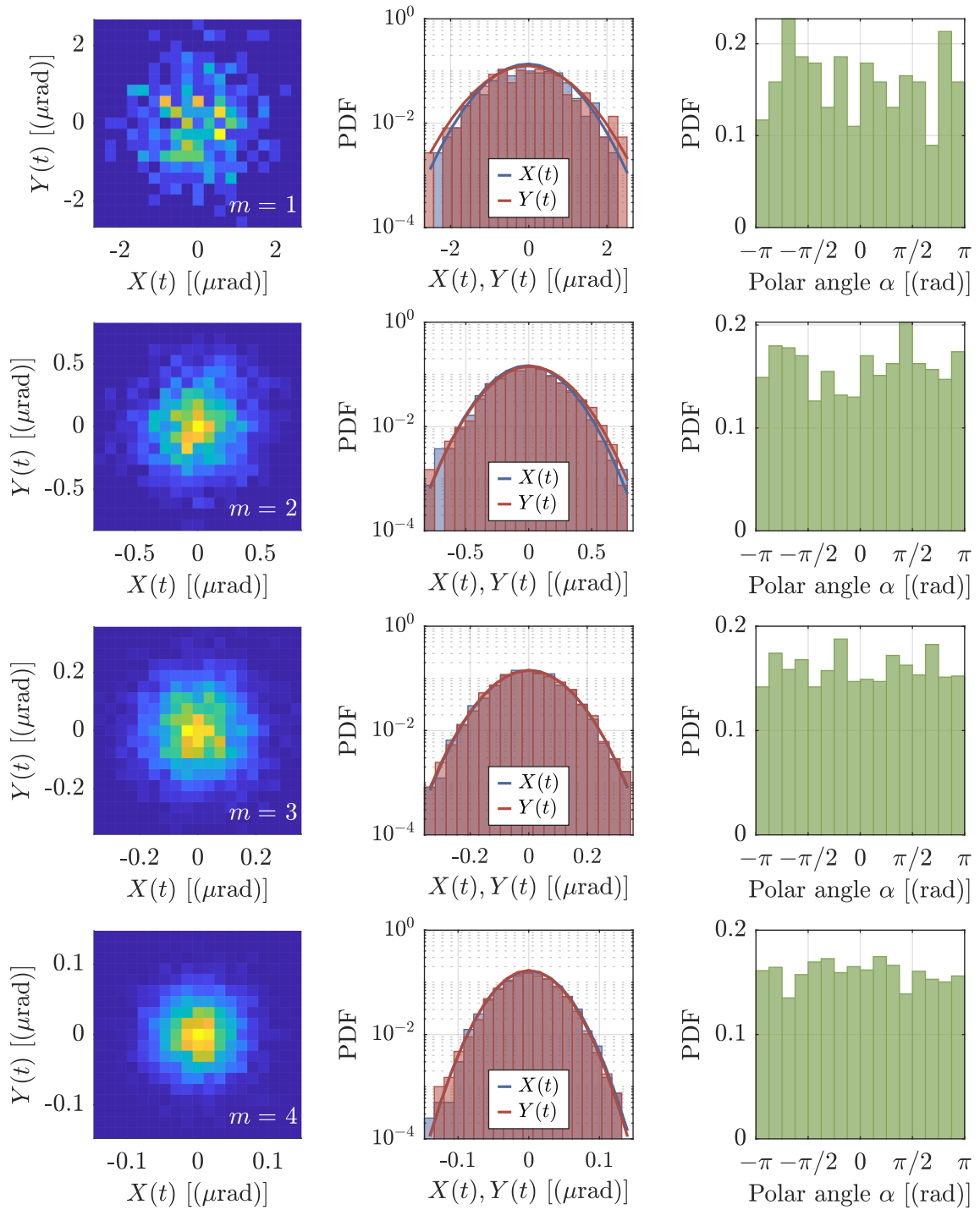


FIGURE 6.2.3: The torsional modes show a behavior similar to the flexural ones. The $X(t), Y(t)$ for mode $m = 1$ can be well fitted by a normal distribution, albeit the sample size being sub-optimal. In addition, the distribution of the polar angle hints that $X(t)$ is not correlated with $Y(t)$. The higher modes $m = 2, 3, 4$ are clearly random independent variables, also not showing traces of self-oscillations.

lock-in method as the one in this chapter. It is interesting to comment on this, following the discussion of Chapter 5: as reported in [30], a strong increase of fluctuation is detected in the oscillator (higher than T^{\max}), still the distribution remains a Gaussian. In this section, we are curious to verify whether this is true also for an object showing a strong *lack* of fluctuations.

The results are shown in fig. 6.2.4, for the flexural modes and in fig. 6.2.5 for the torsional modes. Again, we limit ourselves to the description of the first resonance modes. With the same wariness as in the equilibrium case based on the sample size, we can see that the non-equilibrium data can be well represented by a normal distribution. Indeed, all the shown modes follow the aforementioned properties required by equilibrium thermal noise.

This result is interesting in various ways. Firstly, it confirms the results in [30], showing that also in the case of a dearth of fluctuations, the noise is also still normally distributed. Moreover, in our case the system is even more out of equilibrium, with $\Delta T = 700$ K along its length, thus possibly more prone to perturbations in the distribution. Secondly, it shows that we can safely associate a variance with this distribution, which as seen corresponds to the area under the resonance curve. In fact, the emergence of Lévy behavior [103] for example, i.e. algebraic tails in the PDF, would result in an infinite variance [67]. Thus, it would be mathematical difficult to define an energy content and a fluctuation-dissipation relation itself. It is to be acknowledged that small deviations from a normal distribution are only visible with a huge sample, surely bigger than the one at hand.

6.2.4 Comparison with the measured areas

Now that we made sure that, at least for this example, the noise is indeed normally distributed, we can check whether the variance of the $\{X(t), Y(t)\}$ retrieved from the fits agrees with the integral under the resonance peak, i.e. if eq. 6.30 is verified. We report the relative difference between the area and the variance in Table 6.2.2.

Mode n, m	Deflection		Torsion	
	EQ (%)	NESS (%)	EQ (%)	NESS (%)
1	/	/	0.6	0.1
2	2.7	4.3	0.2	1.3
3	1.9	3.4	1.1	2.3
4	3.8	2.5	2.2	4.3
6	0.9	4.8	4.1	1.4
7	1.7	4.7	4.2	0.6
8	1.5	1.8	3.0	2.2

TABLE 6.2.2: Relative difference between the areas calculated as the integral of the PSD around each resonance and by estimating the variance of $\{X(t), Y(t)\}$.

We see that the results yield very similar values, with differences $\leq 5\%$, which shows the validity of eq. 6.30. Regarding the small disagreement between the area and the variance, we can find two reasons: the first can be traced back to the filter used: an IIR lowpass filter of order 25 is used in the procedure, which can introduce some biases into the original spectrum. In particular, the beginning and the end of each t_s signal is discarded since the filtering creates ripples in this parts. The second is the imperfect Gaussian fit, in particular for the first resonances where the sample size is smaller than the higher modes.

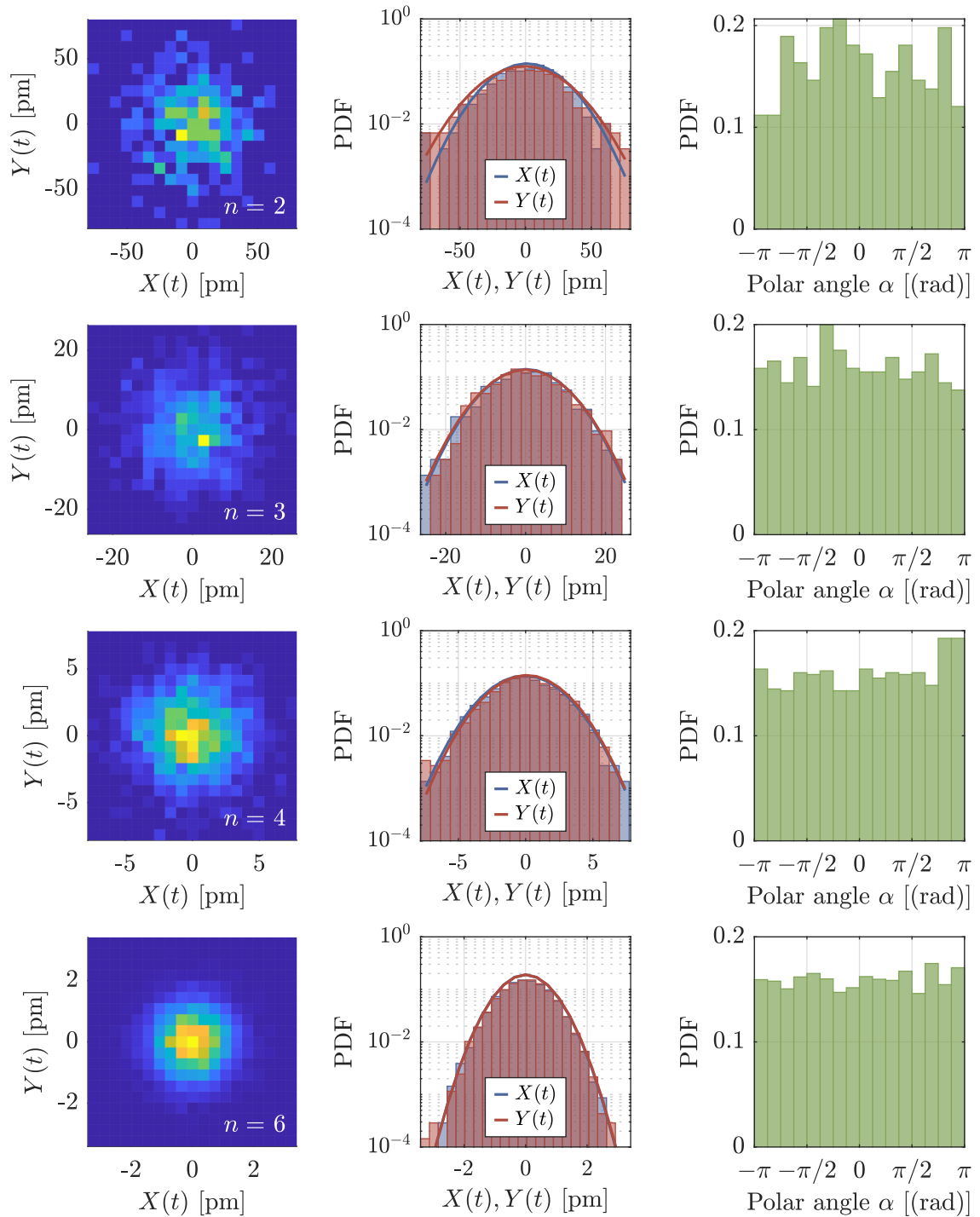


FIGURE 6.2.4: The locked-in signals $X(t), Y(t)$ show no evident deviation from a Gaussian distribution when the cantilever is out of equilibrium. Based on the shape of the PDF, it would be impossible to tell whether the system is in or out of equilibrium. The only thing that might change is the variance of the PDF, since it is the thermal content of the mode.

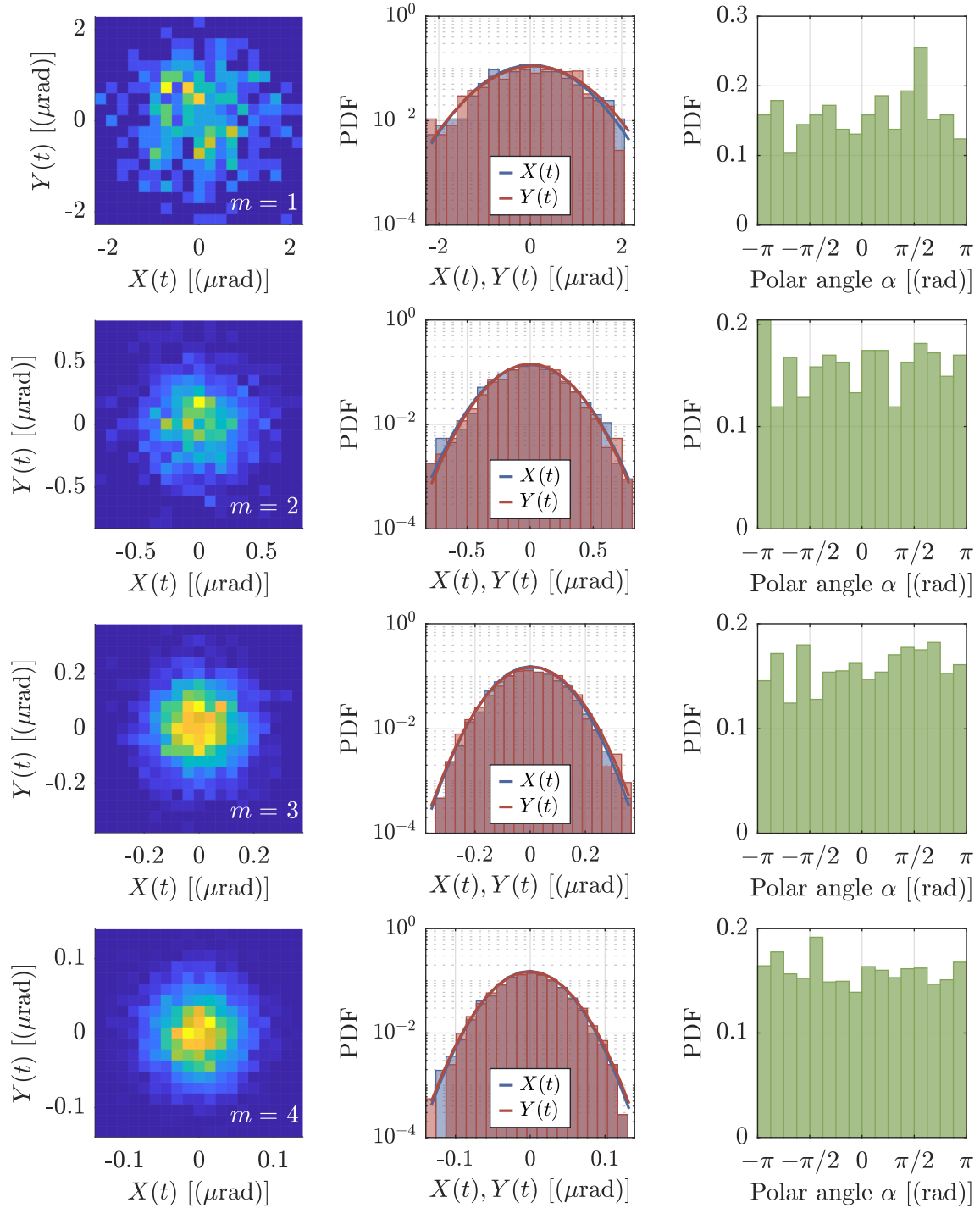


FIGURE 6.2.5: As for deflection, the PDF of the non-equilibrium torsional modes is well fitted through a Gaussian, thus showing that we can safely affirm that the measured signal is caused by thermal noise.

6.2.5 Discussion

In this section, we have tested the statistical distribution of the measured displacement of the C100 cantilever, which we believe is one of the most intriguing experiments presented in this thesis. Indeed, with a huge temperature difference along its length and a strong dearth of fluctuations, it embodies perhaps the clearest example of non-equilibrium behavior.

As mentioned, in this experiment we first encountered the phenomenon we refer to as self-oscillations, which completely hinders the thermal noise measurements for the first flexural resonance. In the previous analysis, we supposed this circumstance to be circumscribed to $n = 1$, leaving the other modes unperturbed. This hypothesis was supported by a reasonable amplitude of the fluctuations, leading to physical T^{fluc} (at least less than the melting temperature of silicon). Whilst a complete characterisation of this phenomenon is not yet available (along with a strategy to counteract it), it is sufficient to verify that self-oscillations do not disturb the higher resonances. For the C100 experiment, we can conclude that this is the case, which means that the fluctuation temperatures are not the expression of this phenomenon. When present, though, we can see that it is not possible to circumvent the manual application of a threshold to distinguish the self-oscillating measurements from the thermal ones. When the magnitude and the frequency of the effect is as extreme as in fig. 6.2.1, it is simply best to discard the considered mode. In the next section, we will show a strategy in case the corrupted signals are rare compared to the total number of available data.

Both the in and out-of-equilibrium measurements respect all the expected properties of stochastic noise, which is paramount for the results of this thesis. In fact, if the non-equilibrium noise were described by another kind of PDF, perhaps a Lévi one, all the concepts of average and variance could be biased. In testing this, we ensure that they are well-defined, with the variance of $\{X(t), Y(t)\}$ being very close to the thermal contents of the modes. Thus, there is no further doubt in regarding the measured fluctuations as *thermal*.

6.3 Statistical properties of the PSD

In the previous section, we discuss how we can make sure that a temporal signal, for example $\delta(t)$, satisfies the properties required for a stochastic noise transferred to the cantilever. With the lock-in amplifier technique we can sample the PDF of the Fourier coefficients of the spectrum \mathcal{S}_δ , which variance is the thermal content of the mode n .

Throughout this thesis, thermal noise is calculated in a different way, i.e. as the integral of the PSD under the resonance peak. While in the C100 case the methods yield comparable results, as we expect, we believe that the lock-in technique is a proof of concept regarding the statistical properties of noise, rather than a way to determine the fluctuations. Indeed, due to post-processing filtering and limited sample size, the fluctuations retrieved thanks to the lock-in amplifier can be misleading. In particular, an error of 5 % may look small, but if it is inserted into the formula for T^{fluc} (eq. 2.88), it can yield to an important bias.

The standard procedure is then to retrieve the signal of the displacement, in this case $\delta(t)$, and calculate the PSD around the resonance n . This is usually the result of N averages (in order to reduce the uncertainty) and it is repeated a certain number of times M in the same experimental conditions (for C100 $M = 74$), in order to have a sufficiently large sample. In this set of M measurements of the spectrum, we would then like to be able to distinguish the signals that represent thermal noise from the eventual presence of external perturbations. An example would be the self-oscillations described in the previous section.

In order to be quantitative, we then proceed to study the statistical properties of the PSD of the displacement. In doing so, we follow [87, 83] in some of the calculations.

6.3.1 Statistical distribution of the PSD

As before, we consider the deflection as an example, with the following results easily extended for the torsion. We recall the definition of the expected value of the PSD, given in eq. 2.5:

$$\langle \mathcal{S}_\delta(\omega) \rangle = \lim_{T \rightarrow \infty} \frac{1}{T} \langle \delta(\omega) \delta^*(\omega) \rangle = \frac{1}{2\Delta f} \langle |\delta(\omega)|^2 \rangle \quad (6.32)$$

As usual, the $\langle \cdot \rangle$ represents the expected value and $2\Delta f$ is the frequency integral around the resonance. In the experiment, we calculate *one* realisation at a time of the PSD, which is simply:

$$\mathcal{S}_\delta(\omega) = \frac{1}{2\Delta f} |\delta(\omega)|^2 \quad (6.33)$$

In order to lighten the notation, in the following description we are going to consider a unitary frequency band $2\Delta f = 1$. Given that we measure N spectra \mathcal{S}_δ , we now want to calculate their PDF. In order to do so, we first decompose the deflection δ in its Fourier coefficients X, Y and second, thanks to eq. 6.22, express the spectrum as the quadratic sum of X and Y in the frequency interval $2\Delta f$. As shown in Sec. 6.1.2, these are normally distributed, so that \mathcal{S}_δ is the quadratic sum of normally distributed variables:

$$\mathcal{P}(X) = \frac{1}{\sigma_\delta \sqrt{2\pi}} e^{-\frac{X^2}{2\sigma_\delta^2}} \quad \mathcal{P}(Y) = \frac{1}{\sigma_\delta \sqrt{2\pi}} e^{-\frac{Y^2}{2\sigma_\delta^2}} \quad (6.34)$$

Then, we can express eq. 6.22 as:

$$\mathcal{S}_\delta(\omega) = X^2 + Y^2 \equiv R^2 \quad (6.35)$$

where the $1/2$ factor disappears since we are not averaging. We then transform X and Y in polar coordinates: $X + iY = R e^{i\alpha}$. Doing so, the PDF of R can be swiftly retrieved:

$$\begin{aligned} \mathcal{P}(R) \mathcal{P}(\alpha) dR d\alpha &= \mathcal{P}(X) \mathcal{P}(Y) dX dY \\ \mathcal{P}(R) \frac{dR d\alpha}{2\pi} &= \frac{R}{2\pi \sigma_\delta^2} e^{-\frac{X^2 + Y^2}{2\sigma_\delta^2}} dR d\alpha \\ \mathcal{P}(R) &= \frac{R}{\sigma_\delta^2} e^{-\frac{R^2}{2\sigma_\delta^2}} \end{aligned} \quad (6.36)$$

with $dX dY = R dR d\alpha$. The PDF of the square of this quantity is then:

$$\begin{aligned} \mathcal{P}(R^2) d(R^2) &= \mathcal{P}(R) dR \\ \mathcal{P}(R^2) &= \frac{1}{2\sigma_\delta^2} e^{-\frac{R^2}{2\sigma_\delta^2}} \end{aligned} \quad (6.37)$$

with $d(R^2) = 2R dR$. This is the PDF of the spectrum \mathcal{S}_δ :

$$\mathcal{P}(\mathcal{S}_\delta) = \frac{1}{2\sigma_\delta^2} e^{-\frac{\mathcal{S}_\delta}{2\sigma_\delta^2}} \quad (6.38)$$

The PSD is then exponentially distributed.

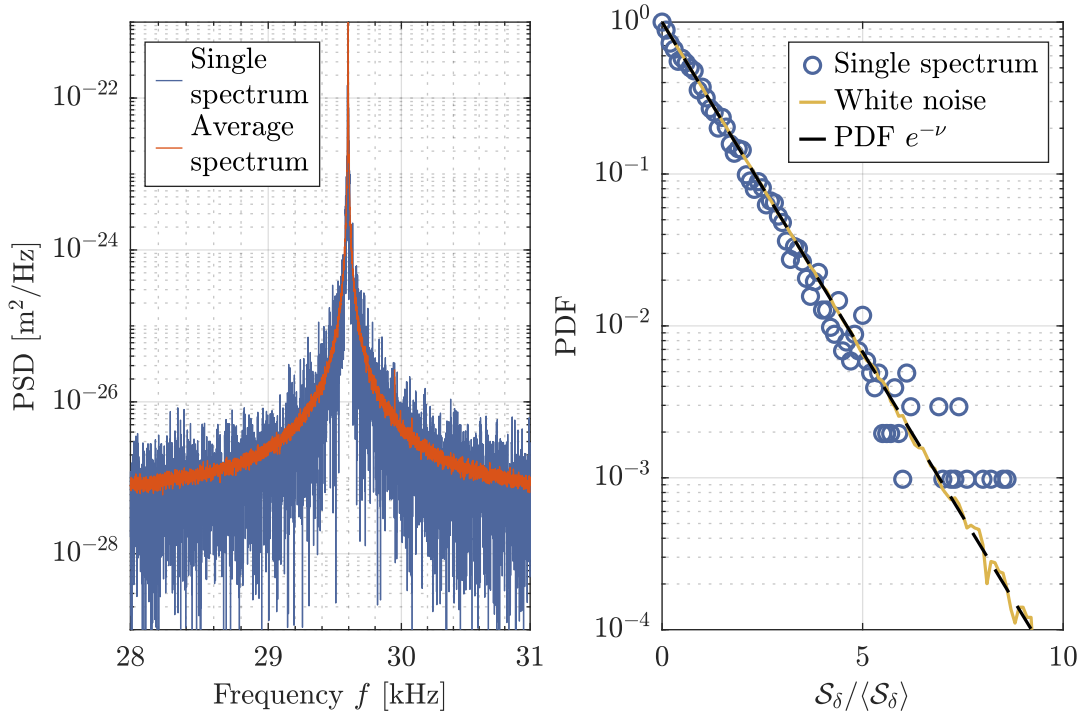


FIGURE 6.3.1: The PSD of the second mode of deflection (in the C100 experiment) is compared to the average of all the $M = 74$ measurements in the same power step. The ratio between these quantities is exponentially distributed, as predicted by eq. 6.41. In addition to this, we simulate a white noise following the same PDF as a comparison. Note that the statistics of the ratio $S_\delta / \bar{S}_\delta$ is independent of the frequency bin, so that the PDF is computed aggregating all frequencies.

Let us now consider the ensemble constituted by N measurements of S_δ , which we call $\{S_\delta\}_N$. Its expectation value and square root of the variance are:

$$\begin{aligned} \langle S_\delta \rangle &= \int_0^\infty dS_\delta S_\delta \mathcal{P}(S_\delta) = 2\sigma_\delta^2 \\ \sigma(S_\delta) &= \int_0^\infty dS_\delta S_\delta^2 \mathcal{P}(S_\delta) = 2\sigma_\delta^2 \end{aligned} \quad (6.39)$$

This shows that the probability distribution of the PSD is:

$$\mathcal{P}(S_\delta) = \frac{1}{\langle S_\delta \rangle} e^{-\frac{S_\delta}{\langle S_\delta \rangle}} \quad (6.40)$$

We can thus see how the PDF of a single spectrum is the expectation spectrum times an exponentially-distributed random number ν :

$$S_\delta = \nu \langle S_\delta \rangle \quad \mathcal{P}(\nu) = e^{-\nu} \quad (6.41)$$

Each Fourier coefficient being independent from the others, eq. 6.41 is valid for all frequencies f_k .

Since the expectation value $\langle \mathcal{S}_\delta \rangle$ is not known, in order to estimate it we calculate the average spectrum $\overline{\mathcal{S}}_\delta$ out of the ensemble $\{\mathcal{S}_\delta\}_N$:

$$\overline{\mathcal{S}}_\delta = \frac{1}{N} \sum_{i=1}^N \mathcal{S}_{\delta,i} \quad (6.42)$$

For the Central Limit Theorem (CLT), we expect that $\overline{\mathcal{S}}_\delta$ tends to $\langle \mathcal{S}_\delta \rangle$ for $N \rightarrow \infty$.

In fig. 6.3.1, we show one example of spectra collected in the equilibrium step of the C100 measurement. In (a), we can see a single PSD (of the second flexural mode) compared to the average performed at the same power step. In (b), we can see that the PDF of the ratio between \mathcal{S}_δ and $\overline{\mathcal{S}}_\delta$ yields an exponential distribution.

Next, we could ask ourselves the nature of the PDF of the average spectrum $\overline{\mathcal{S}}_\delta$. Let us imagine a repeated measurement of ensembles $\{\mathcal{S}_\delta\}_N$, such that we construct a collection $\{\mathcal{S}_\delta\} \equiv \{\{\mathcal{S}_\delta\}_N, \{\mathcal{S}_\delta\}_N, \dots\}$ of M elements. In this case, the expectation value and the square root of the variance of $\overline{\mathcal{S}}_\delta$ are:

$$\begin{aligned} \langle \overline{\mathcal{S}}_\delta \rangle &= \langle \mathcal{S}_\delta \rangle \\ \sigma(\overline{\mathcal{S}}_\delta) &= \frac{\langle \mathcal{S}_\delta \rangle}{\sqrt{N}} \end{aligned} \quad (6.43)$$

As expected, the variance of the average spectrum is inversely dependent on N . In this case, its statistical distribution is the Erlang distribution $\mathcal{P}(N, \lambda)$ [56]:

$$\mathcal{P}(\overline{\mathcal{S}}_\delta, \lambda) = \frac{\overline{\mathcal{S}}_\delta^{N-1}}{\langle \mathcal{S}_\delta \rangle^N} \frac{N^N}{\Gamma(N)} e^{-N\overline{\mathcal{S}}_\delta / \langle \mathcal{S}_\delta \rangle} \quad (6.44)$$

with rate parameter $\lambda = \langle \mathcal{S}_\delta \rangle / N$ and $\Gamma(N) = (N-1)!$. The Erlang distribution is a Gamma distribution $\Gamma(N, \lambda)$ with integer N , and it is known that this converges to a normal distribution for large N .

As we are going to show in this chapter, this distribution recurs often in the quantities we measure in the experiments. For example, the PSD is not usually the result of a Fourier transformation of the whole $t_s = 2$ s signal (which is the case reported in fig. 6.3.1), but rather the average of parts of it (also through a 50 % overlap). We show an example in fig. 6.3.2, for which $N = 8$. In this case, the PSD of the third resonance mode is in perfect agreement with an Γ fit, which yields a number of averages N similar to the expected value.

As a final step, we might wonder which is the PDF of the average of M spectra which are themselves averages of N spectra. Calling this quantity $\overline{\overline{\mathcal{S}}}_\delta$, this is:

$$\overline{\overline{\mathcal{S}}}_\delta = \frac{1}{M} \sum_{i=1}^M \overline{\mathcal{S}}_{\delta,i} \quad (6.45)$$

Thus, $\overline{\overline{\mathcal{S}}}_\delta$ is the summation of M Γ -distributed variables, each with a PDF $\Gamma(N, \lambda)$. The resulting variable is also Γ -distributed, with a PDF $\Gamma(N \times M, \lambda)$, as expected.

In this section we have shown how to retrieve the PDF of a spectrum, be it the result of one or more averages, and tested this against experimental signals. As in the previous parts of this chapter, we can then use this information to sort the measurements, detecting spectra that are statistical outliers of the PDF set by the average spectrum. We discuss this in the following section.

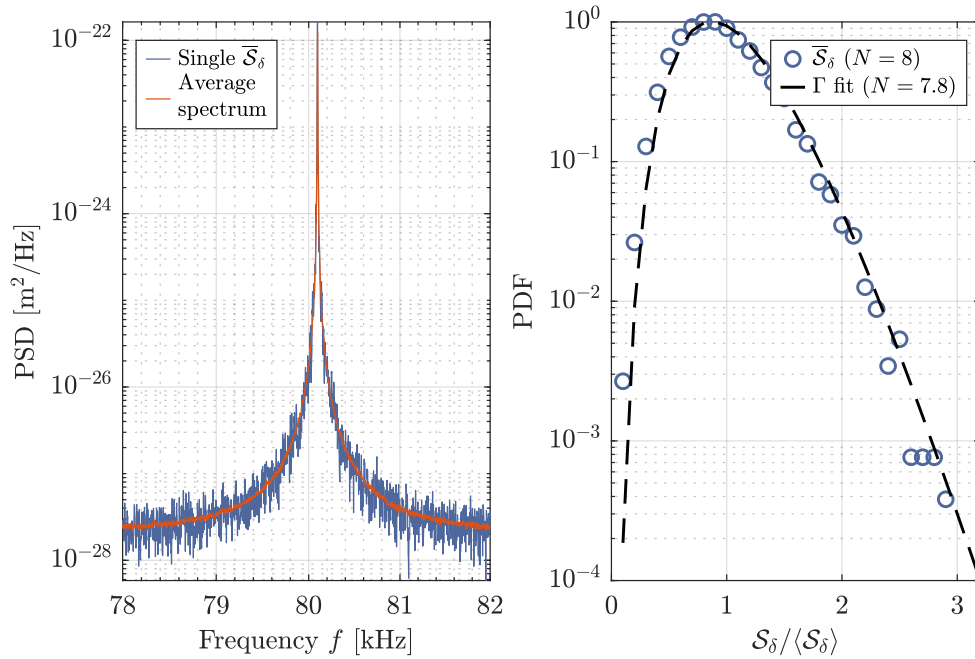


FIGURE 6.3.2: A single PSD which is the result of $N = 8$ averages is shown alongside the average of M PSDs in the same power step (for the third flexural resonance of the C100 experiment). With respect to fig. 6.3.1, since all the spectra are the result of N averages, the final average has a lower variance. The ratio of these two quantities is Γ -distributed, with the fit yielding $N = 7.8$, similar to the expected value.

6.4 Spectra selection

Once the PDF of an experimental spectrum is known, be it the result of N averages or a single PSD, we can create a selection protocol based on the needs of the experiment. In Sec. 6.2.1, we discussed the self-oscillations, which result in the spectrum being greatly enhanced (or reduced) with respect to its expected value. Furthermore, some external noise sources can sometimes create wiggles and spurious peaks in the PSD, as seen for example in the NETN experiment (see Chapter 5).

In order to discard the problematic spectra without being forced to check each one manually, we can decide to exclude the outliers of the distribution of the experimental spectrum \bar{S}_δ , with the bar indicating that it is the result of N averages. As usual, we confound its expectation value $\langle S_\delta \rangle$ with the average spectrum amongst all the measurements $\{S_\delta\}$ in the same experimental conditions. For all the experiments in this thesis, this ensemble corresponds to all the M measurements in the same heating power P , since the system is considered in a stationary state (refinements of this method based on possible heating power changes are discussed later). Referring to the ratio $\nu \equiv \bar{S}_\delta / \langle S_\delta \rangle$, we can then express eq. 6.44 in a more handy way:

$$\mathcal{P}(\nu) = \frac{N^N}{\Gamma(N)} \nu^{N-1} e^{-N\nu} \quad (6.46)$$

Our goal is then to set a threshold $\mu(N)$ so that if one value of ν lies outside this limit it is discarded. Since the PSD is composed of K frequency bins, this corresponds to compare *all* the bins with μ .

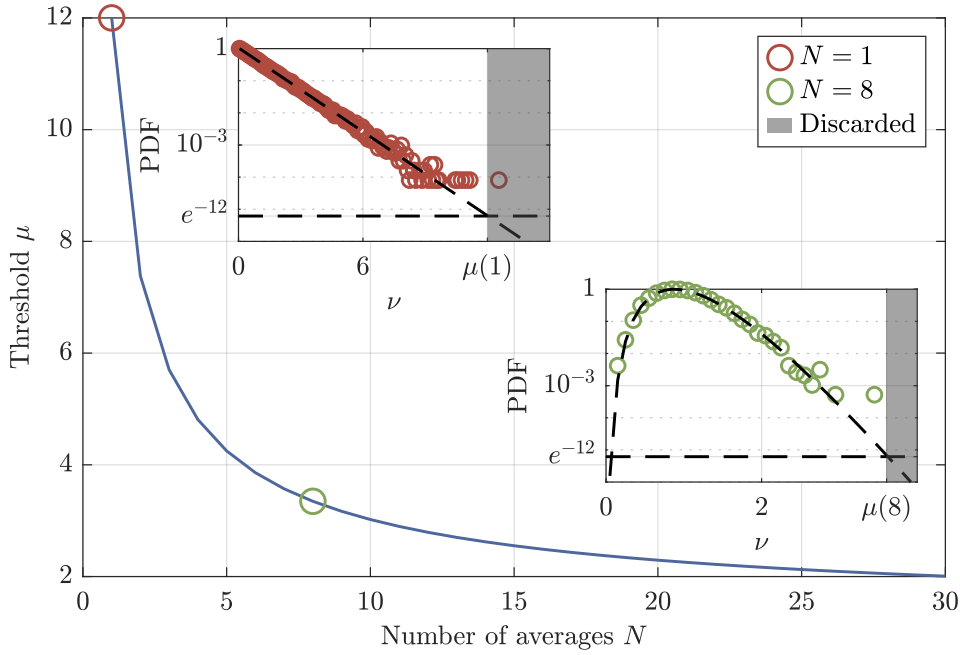


FIGURE 6.4.1: In order to sort the experimental data, we can set a threshold μ which excludes a certain percentage of upper outliers. Choosing $\mu(1) = 12$, this corresponds to e^{-12} . We then derive $\mu(N)$ from eq. 6.49, which for $N = 8$ yields $\mu(8) = 3.2$.

6.4.1 Threshold

In the case $N = 1$, in [87] it is shown that setting $\mu(1) = 12$ is a reasonable choice. This means that if a spectrum is 12 times greater than the average is discarded. The percentage of discarded bins is:

$$\int_{\mu(1)}^{\infty} d\nu e^{-\nu} = e^{-\mu(1)} = 6 \times 10^{-6} \quad (6.47)$$

This quantity needs to be then multiplied by K . In all the experiments presented in this thesis $K \in [1000 - 2000]$, so that the total number of *a priori* discarded PSDs is around 1%. As we show later, if a higher percentage of spectra are discarded we can conclude that they are not part of the expected distribution, and they are thus rightfully rejected.

When $N > 1$, we can adapt $\mu(N)$ in order to conserve the same percentage of discarded spectra, e^{-12} . In this case, we write:

$$\int_{\mu(N)}^{\infty} d\nu \frac{N^N}{\Gamma(N)} \nu^{N-1} e^{-N\nu} = \frac{N}{\Gamma(N)} \gamma(\mu(N), N) \equiv g(\mu(N), N) \quad (6.48)$$

with γ the incomplete gamma function. Imposing the right hand-side to be equal to e^{-12} and inverting the equation gives the threshold:

$$\mu(N) = g^{-1}(N, e^{-12}) \quad (6.49)$$

In fig. 6.4.1 we show the results for the threshold for various values of $\mu(N)$. As we can see, the dependency on N is important for small N whilst the PDF quickly converges towards a normal distribution for $N \rightarrow \infty$.

In this section, we set a higher threshold but not a lower one. Nevertheless, it is clear that this concept can be extended for these events too, at least for $N > 1$.

6.4.2 Analysis procedure

The sorting of the data following the expected PDF is applied systematically in all the datasets shown in this thesis. We discuss here the procedure.

Once we have the statistical ensemble of interest $\{\mathcal{S}_\delta\}$, in order to retrieve the experimental PDF we first need to associate to this an expectation value $\langle \mathcal{S}_\delta \rangle$. As said, for a sufficient number of spectra ($M \geq 40$ in all the experiments presented), the average of these is the main candidate. Depending on whether this is possible or not, various strategies are set in place.

Representative average

If we believe that the average of $\{\mathcal{S}_\delta\}$ is representative, it means that we suppose that the eventual outliers are a strong minority of the total *and* their magnitude is not too different from the rest. Indeed, we need the signals containing spurious effects not to bias the average, which is for example the case with the self-oscillations, since one PSD can be orders of magnitude higher than the others. If the average is representative then, we proceed as follows. For each spectrum, we test whether the power of each frequency bin is above the threshold μ times the average: if in one frequency bin the PSD is above the threshold the spectrum is discarded, if not it is retained. Next, we re-compute the average with the spectra passing the first selection, and we repeat the procedure until no spectrum is discarded in the last iteration.

We show an example for the C100 experiment in fig. 6.4.2, with the third flexural mode from a NESS measurement. The whole $M = 74$ spectra at $P = 9$ mW are averaged to give $\{\mathcal{S}_\delta\}$ and a threshold $\mu(8) \approx 3.2$ is set, since each spectrum is the average of $N = 8$ spectra. The PSDs lying above the average times μ are then discarded. When the sorting is done, the spectra passing the selection are most of them, in this case 84 %. Whilst we attend a refusal rate of roughly 1 %, due to the $2\Delta f = 1.6$ kHz, the actual value is much higher than this. This proves that some of the PSDs are not part of the statistical distribution of thermal noise spectra, thus to be discarded.

Non-representative average

In some cases, the average can be misleading. In this thesis, this is the case for two experiments in particular: the self-oscillations of the $n = 1$ mode of the cantilever, which we have discussed above, and the cryogenic measurements on C90. As also shown in [87], the experimental system experiences some "jumps" when the temperature increases, thus creating odd features in the spectrum. Moreover, the self-oscillations are more severe than the ones at room temperatures, with the harmonics of the first mode being visible in the higher modes too. We show this example in fig. 6.4.3 for the second flexural resonance in a NESS. With a sample size of $M = 60$, we can see that most of the spectra show odd features, such as spurious peaks. Two of these (located at $f_2 \pm 1.5$ kHz) are the harmonics of the first resonance mode.

In such situations, in order to sort the spectra we proceed in the opposite direction with respect to the algorithm above. We first elect one spectrum as the representative one, choosing it as the one showing the lowest mean background noise around the resonance. This criterium comes from experimental evidence: since the spurious peaks tend to increase the mean background noise, we select the one that *a priori* shows the less pollution. Then, we find all the spectra within μ from this and we compute the average between them. We thus find the signals within μ of the new average, therefore *adding* spectra to the ensemble $\{\mathcal{S}_\delta\}$.

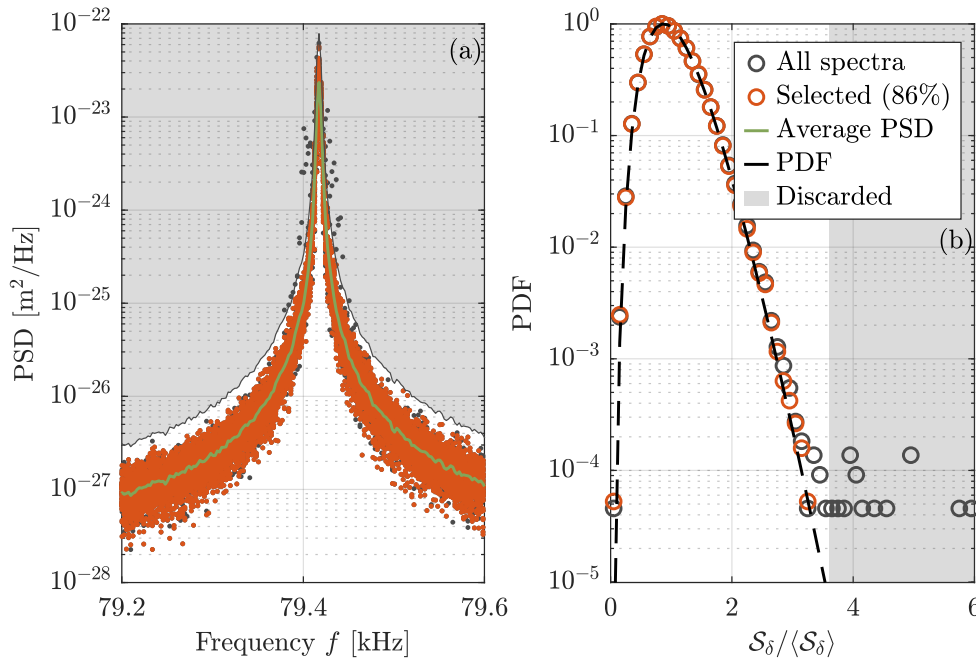


FIGURE 6.4.2: In (a), we show the PSDs of the third flexural mode in the C100 experiment with their average spectrum. As we can see, 14 % of the spectra are do not pass the selection since they are $\mu(N)$ times higher than the average, with $N = 8$. In (b), the experimental PDF for the selected spectra follows the theoretical prediction (a Γ distribution), whilst the discarded ones show some non-compatible values with the distribution. For this reason, we deem them as non-representative, and discard them.

Once the last iteration does not increase the sample size, we have our sorted spectra. In the example reported in fig. 6.4.3, the signals passing the selection are roughly 14 %, which is very low compared to the expected value. Luckily, this represents an extreme case, with the success rate increasing for the higher modes. Since the $n = 1$ mode is always excluded, in this work we apply this procedure solely in the C90 experiment.

Frequency dependent average

A third scenario arises when the spectra are not polluted as in 6.4.3, but still an average over all $\{S_\delta\}$ cannot be applied straightaway. This is the case of the laser power fluctuating during a power step, prompting changes in the temperature and thus in the resonance frequencies of the modes. This effect is more and more important with the mode number increasing. In this case, the average of the ensemble $\{S_\delta\}$ is biased towards the spectra representing the average temperature. Therefore, spectra that could be accepted if the power was constant are discarded.

In order to prevent this, we decide to divide the $\{S_\delta\}$ in a number J of a sub-ensembles, based on the resonance frequency. This way, we get various averages each better representing the temperature of the system. We exemplify this in fig. 6.4.4 for mode $n = 7$ in the C90 experiment. As we can see, although small, the laser fluctuations in the cryogenic environment prompt changes of the resonant frequency for more than 50 Hz. In this way, the average of all the spectra would yield just 11 % of them to pass the selection. Conversely, setting $J = 2$ already doubles this number. Albeit J can be further increased, with the sorting giving higher and higher yield, it is important to conserve a meaningful amount of spectra

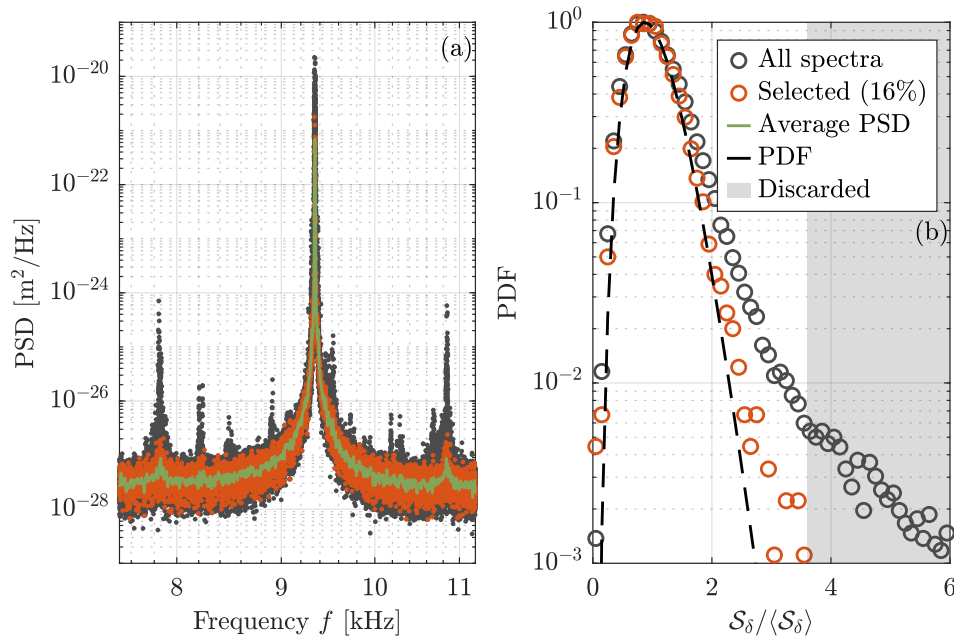


FIGURE 6.4.3: In (a), we show a NESS measurement of the second flexural resonance in the C90 experiment. We notice various features in the spectrum, with two symmetric peaks around the resonance frequency being identified as the higher harmonics of the first (self-oscillating) mode at ± 1.5 kHz. Since the average of all the spectra would yield a biased average, we consider the PSD with the lowest background noise as representative and construct the ensemble of selected spectra from this. Only 16 % of the spectra are then accepted, which PDF is shown in (b). As this follows the expected Γ distribution, the other spectra clearly do not.

per bin in order for the average to be representative. In the experiment this is usually set between 4 and 6.

6.4.3 Discussion

In the last two sections we discuss the statistical properties of the experimentally measured spectra. We first show how the PDF of a spectrum when it is not averaged is an exponential distribution, then that the average of N spectra follows a Γ distribution. We compare our prediction with the experimental data, finding perfect agreement. This result further assesses how our measurements satisfy the statistical properties of thermal noise.

In particular, this knowledge grants us a powerful tool to recognize whether a measured PSD represents the thermal fluctuations of the system or it is corrupted by an external factor. As seen, self-oscillations and other sources can create some features in the spectrum, which, if not forsaken, might bias the final result. We then set an average number-dependent threshold μ which eliminates roughly the 1 % of the signals with the higher amplitude. Next, we show how to systematically sort the spectra based on the value of μ , first in the case the spectra average is significative and then when it is not. We finally test the method against experimental spectra, showing how it helps us discarding corrupted signals, and how the selected PSDs satisfy the predicted distribution.

While in the first part of this chapter we have shown another strategy aimed at finding irregularities in the distribution of the signals, it requires to act on the temporal signals through filters and possibly subsampling. The tools developed in this section represent a handy way to find spurious signals directly in the spectra and discard them. At the end of

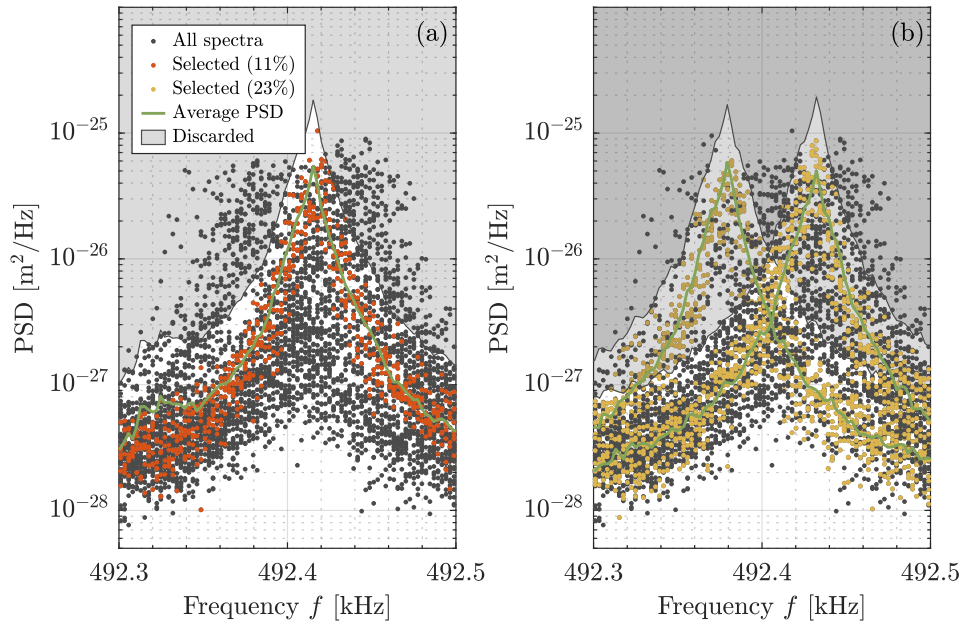


FIGURE 6.4.4: In (a) we depict mode $n = 7$ in a NESS measurement on the C90 cantilever. Due to tiny fluctuations in the laser power, the temperature of the cantilever can change sensibly, prompting important variation in the resonance frequency. Therefore, the average of all the spectra in the power step leans towards the mean temperature, excluding normally acceptable signals. Indeed, just 11 % of them are within μ from the average. In (b) we show that this technique can be refined simply dividing the ensemble in J resonance frequency bins, and applying the sorting algorithm in each of them. With $J = 2$ we roughly double the accepting rate.

the procedure, only spectra satisfying the expected distribution are selected, thus in theory zeroing the possibility of the measured fluctuations to be biased.

Until now we have discussed two faces of the same coin, the PDF of the Fourier coefficients of the spectrum, first with a lock-in amplifier and then through the spectrum. In the next sections we apply the concepts discussed in these sections for the *derived* quantities, such as the area under the resonance peak which gives us the fluctuation temperature T^{fluc} and the fit procedure that gives us the loss angle φ .

6.5 Statistical properties of the area

The step that follows the spectra selection is the calculation of the areas under the resonances, which then leads to the fluctuation temperatures T^{fluc} . We will refer to the area as A :

$$A = \frac{2\Delta f}{K} \sum_{k \in \Delta_n} \mathcal{S}_{\delta,k} \quad (6.50)$$

with the frequency interval $2\Delta f$ containing a total of K frequency bins f_k . Let us be in the most general case, where the PSD \mathcal{S}_{δ} is the result of N averages. As in eq. 6.45, the area is a summation of K independent Γ -distributed variables with parameters $\Gamma(N, \lambda)$. The resulting variable is then also a Γ -distributed variable, with parameters $\Gamma(N \times K, \lambda)$. The PDF of A is then:

$$\mathcal{P}(A) = \frac{A^{NK-1}}{\langle A \rangle^{NK}} \frac{(NK)^{NK+1}}{\Gamma(NK)} e^{-NK A / \langle A \rangle} \quad (6.51)$$

where we define the expectation value:

$$\langle A \rangle = \frac{2\Delta f}{K} \sum_{k \in \Delta_n} \langle \mathcal{S}_{k,\delta} \rangle \quad (6.52)$$

Since in the experiment $K \in [1000 - 2000]$, we expect the PDF (eq. 6.51) to be very close to a Normal law.

Similarly, when we calculate the area we subtract the background noise \mathcal{N} level from the area, as seen in Appendix 3.C.3. In order to do so, we calculate the mean of the PSD in a small interval $\Delta_{\mathcal{N}}$ at the sides of the resonance:

$$\mathcal{N} = \frac{1}{K'} \sum_{k \in \Delta_{\mathcal{N}}} \mathcal{S}_{k,\delta} \quad (6.53)$$

with K' the total number of bins in the interval. Also in this case then, it is easy to show how \mathcal{N} follows a Γ distribution $\Gamma(N \times K', \lambda)$, and since $K' \in [50 - 100]$ we expect the PDF to also closely resemble a Gaussian.

6.5.1 Area selection

Once we know that we expect the retrieved area and background noise to be normally distributed, we can then sort the retrieved values based on their PDF. It is in fact possible to decide to discard values that are for example outside $\mu = 4\sigma$ from the average. In fig. 6.5.1, we show an example taken from the NETN experiment, for a NESS measurement. We note that the PDFs closely resembles a Normal law, with a Γ distribution following slightly better the data. The average value of the area and the noise are also very close.

We then see that in this case not many values lie outside the threshold, with a discarding rate of just 0.2 % for the areas and < 0.1 % for the background. The expected value for a normal distribution for $\mu = 4\sigma$ corresponds to roughly 0.01 % of the total, which is 20 times smaller than the case shown. Therefore, at least some of these spectra are statistically not acceptable and are thus discarded as outliers. Conversely, the same concept applied to the background noise yields a discarded rate within the expected value.

6.5.2 Distribution of T^{fluc}

As the final result of this part, we derive the PDF of the fluctuation temperature T^{fluc} . As seen in Section 2.3.2, we calculate T^{fluc} as:

$$T^{\text{fluc}} = \frac{A}{\langle A \rangle} T^{\text{EQ}} \quad (6.54)$$

with $T^{\text{EQ}} = 300$ K and forgetting the resonance frequency changes with the temperature. As usual, we set $\langle A \rangle = \bar{A}$, the average of the M measurements. In addition to this, we know that the background noise has little if no influence on our results, so we set $\mathcal{N} = 0$. The two variables in eq. 6.54 are both Γ -distributed, with:

$$\mathcal{P}(A) = \Gamma\left(NK, \frac{\langle A \rangle}{NK}\right) \quad \mathcal{P}(\bar{A}) = \Gamma\left(NKM, \frac{\langle A \rangle}{NKM}\right) \quad (6.55)$$

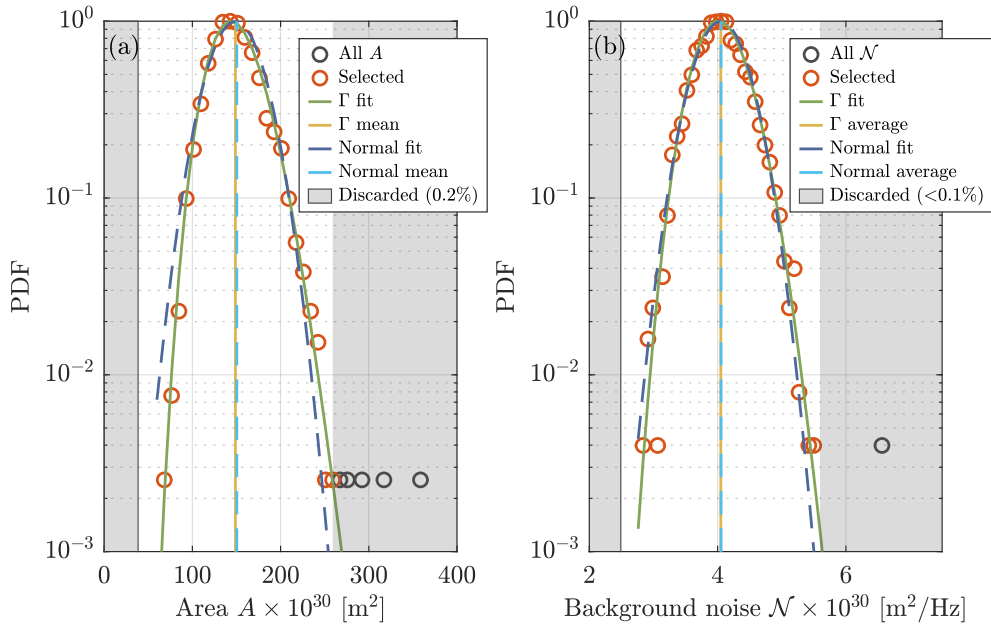


FIGURE 6.5.1: In (a), we show how the distribution of the area A closely approaches a Normal law, although a Γ distribution (eq. 6.51) follows slightly better the data. The averages of the two distribution fits are indeed very close, and the same goes for the variances. We can thus decide to eliminate the spectra that lie outside 4σ from the average, which in this case corresponds to the 0.2% of the total. In (b), the same analysis is performed on the background noise \mathcal{N} , which follows the same distribution. In this case the spectra lying outside the 4σ is only one, which is within the expected value.

The ratio of two Γ -distributed variables with different scale factors is a Beta prime distribution β' :

$$\mathcal{P}(T^{\text{fluc}}) = \beta' \left(NK, NKM, 1, \frac{1}{M} \right) = M \frac{(MT^{\text{fluc}})^{NK-1} (1 + T^{\text{fluc}})^{-NK-NKM}}{\beta(NK, NKM)} \quad (6.56)$$

with β the beta function. As usual, it is possible to show that for large values this distribution approaches a gamma distribution, and thus a normal distribution. Since usually $N \geq 8$, $M \geq 50$ (depending on the sorting) and $K \in [1000 - 2000]$, we can safely approximate the β' distribution with a Gaussian. This can be seen in fig. 6.5.1 (a), since the fluctuation temperature is simply the area normalised by its average.

6.6 Statistical properties of the fit

As shown in the previous chapters, in order to interpret the measured fluctuations of the system under study, the estimation of the dissipation is paramount. This quantity is embodied in the loss angle φ , which is retrieved thanks to a fit of the spectra. In this section, we give the details of the fit procedure, showing how we can estimate the Goodness Of the Fit (GOF) and associate an uncertainty to the fit parameters.

In order to prepare the experimental spectra for the fit, two different strategies are followed (depending on the experiment). When we measure the thermal noise of the cantilever, we fit singularly each spectrum. For example, in the C100 experiment our ensemble is constituted of 74 (minus the discarded) fit results. Conversely, in the NETN experiment we average $N = 25$ spectra and then perform the fit on it. Since we have seen that the number

of averages does not change the nature of the PDF but only its parameters, the following discussion can be applied in the two cases.

Let us call the spectrum we want to fit \mathcal{S}_δ . As seen in eq. 2.44, the function that represents \mathcal{S}_δ for the mode number n can be written as:

$$\mathcal{S}_\delta(f) = \frac{2k_B T}{\pi k_n^r f} \frac{\varphi_n}{(1 - (f/f_n))^2 + \varphi_n^2} \quad (6.57)$$

with k_n^r the stiffness and φ_n the loss angle. While this description is valid for the n flexural mode of the cantilever, it can be easily adapted to its torsional modes and to the motions of the macroscopic oscillator. Rewriting the previous equation while adding the contribution of the background noise \mathcal{N} yields:

$$\mathcal{S}_\delta^{\text{fit}}(f) = p_1 \frac{2}{\pi f} \frac{p_3}{(1 - (f/p_2)^2)^2 + p_3^2} + p_4 \quad (6.58)$$

where the free parameters of the fit p_i are the thermal content of the mode $p_1 = A = k_B T / k_n^r$, the resonance frequency $p_2 = f_n$, the loss angle $p_3 = \varphi_n$ and the background noise $p_4 = \mathcal{N}$.

According to [83], the unbiased method to estimate these parameters through a fit of the experimental spectra $\mathcal{S}_\delta(f)$ is to minimise, with respect to p_i , the expression:

$$\sum_{k \in \Delta_n} \frac{\mathcal{S}_\delta(f_k)}{\mathcal{S}_\delta^{\text{fit}}(f_k)} + \log(\mathcal{S}_\delta^{\text{fit}}(f_k)) \quad (6.59)$$

with Δ_n the usual frequency interval around the resonance which contains a total of K frequency bins f_k . The initial values for $p_1 = A$, $p_2 = f_n$ and $p_4 = \mathcal{N}$ are estimated from the numerical integration of the spectrum, whilst the initial $p_3 = \varphi_n$ is usually set at a constant 10^{-4} .

Let us now imagine to fit the spectrum \mathcal{S}_δ and retrieve the parameters p_i , which define the best fit function $\mathcal{S}_\delta^{\text{fit}}$. In order to quantify how well this function describes the experimental PSD, we estimate the GOF, to which we refer as χ^2 . Since we know the distribution of \mathcal{S}_δ , we can calculate χ^2 as the distance between the experimental data and the fit:

$$\chi^2 = \frac{1}{\Delta_n} \sum_{k \in \Delta_n} \left(\frac{\mathcal{S}_\delta(f_k) - \mathcal{S}_\delta^{\text{fit}}(f_k)}{\sigma(\mathcal{S}_\delta(f_k))} \right)^2 = \frac{N}{\Delta_n} \sum_{k \in \Delta_n} \left(\frac{\mathcal{S}_\delta(f_k) - \mathcal{S}_\delta^{\text{fit}}(f_k)}{\langle \mathcal{S}_\delta(f_k) \rangle} \right)^2 \quad (6.60)$$

where in the second passage we insert eq. 6.43. As usual, the expectation value is unknown and its evaluation depends on the N we consider. If N is small, we cannot expect the experimental spectrum to be representative of the expectation value, and its estimation is thus difficult. This case, however, is not one we encounter often: we indeed wish the PSD to have a small uncertainty, and thus we then usually consider at least $N = 16$ when calculating the fit. We can thus approximate $\langle \mathcal{S}_\delta \rangle$ with \mathcal{S}_δ [83]. We note that in the NETN experiment this value is even higher, $N = 25$. Eq. 6.60 then simplifies:

$$\chi^2 = \frac{N}{\Delta_n} \sum_{k \in \Delta_n} \left(1 - \frac{\mathcal{S}_\delta^{\text{fit}}(f_k)}{\mathcal{S}_\delta(f_k)} \right)^2 \quad (6.61)$$

If the fit is a perfect representation of the experimental measurement, the χ^2 is be equal to 1, since the distance between the fit and the measurement is equal to the uncertainty of the experimental spectrum. Usually a $\chi^2 \leq 2$ represents a good result, with the higher value

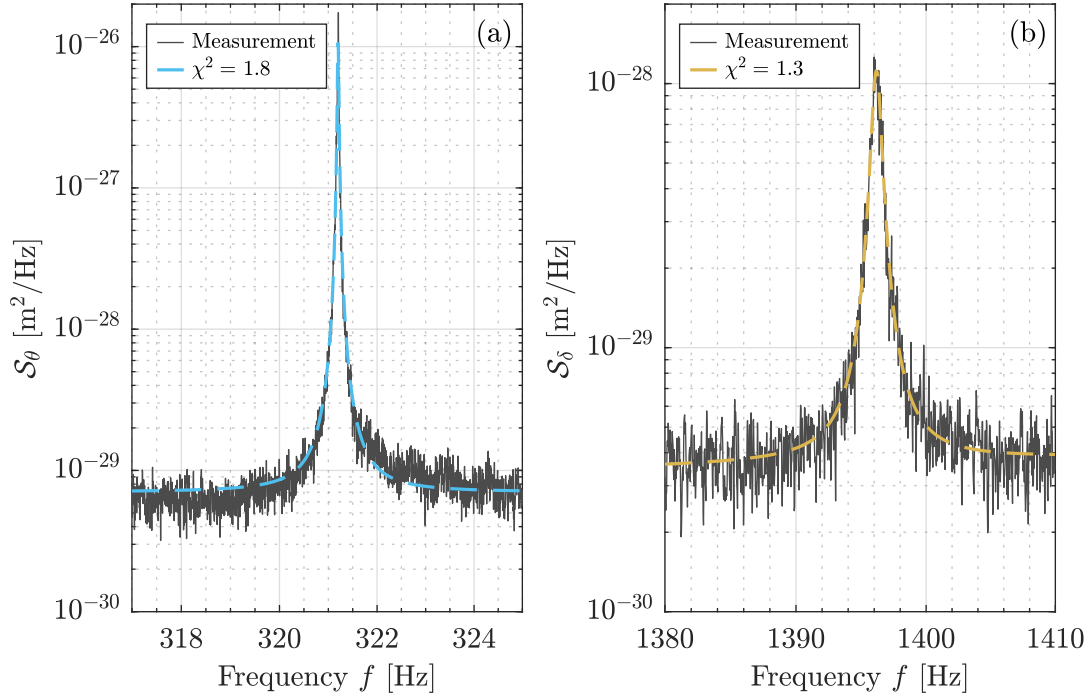


FIGURE 6.6.1: In (a) we show an example of fit for the transverse mode and in (b) for the longitudinal modes in the NETN experiment. For the former the goodness of fit χ^2 is slightly higher than for the latter, which is due to the asymmetrical shape of the background noise.

possibly due to the model not perfectly representing the experiment. In this thesis, $\chi^2 = 2$ is the threshold we use in accepting the data. As an example, in fig. 6.6.1, we show a fit of the two resonances in the NETN experiment.

6.6.1 Uncertainty of the fit parameters

The χ^2 tells us the accuracy of the fit with respect to an experimental spectrum, hence the reliability of the parameters p_i . In order to be more rigorous, we now show how we can estimate the uncertainties of the single parameters, $\sigma(p_i)$. The p_i are drawn from a certain statistical distribution of the ensemble $\{p_i\}$, with expectation value and square root of the variance:

$$\begin{aligned}\bar{p}_i &= \langle p_i \rangle \\ \sigma(p_i) &= \sqrt{\langle (p_i - \langle p_i \rangle)^2 \rangle}\end{aligned}\tag{6.62}$$

where the estimation of these is our objective. The PDF of p_i depends on the nature of the parameter i , the theoretical model used for the fit and the minimization method used in order to estimate the best fit. Even if it is probably possible to reconstruct the PDF of the p_i , it is more handy to sample it.

In order to do so, we consider the best fit curve \mathcal{S}^{fit} . Since, given an average number N , we know that \mathcal{S} is a Γ -distributed number ν (eq. 6.46), we can generate a synthetic noisy spectrum \mathcal{S}^{syn} from \mathcal{S}^{fit} simply as:

$$\mathcal{S}^{\text{syn}}(f_k) = \nu_k \mathcal{S}^{\text{fit}}(f_k)\tag{6.63}$$

where v_k are random numbers drawn from the distribution:

$$\mathcal{P}(v_k) = \frac{N^N}{\Gamma(N)} v_k^{N-1} e^{-Nv_k} \quad (6.64)$$

The fit of this curve yields a new set of synthetic parameters p_i^{syn} , which are samples of the population $\{p_i\}$. Repeating this procedure then builds the statistical ensemble of the parameters, from which we can then deduce the average \bar{p}_i^{syn} and the variance $\sqrt{\sigma(p_i^{\text{syn}})}$ (eq. 6.62).

Next, we can then test whether the values drawn from the initial fit p_i are statistically correct, i.e. they do not differ from the average \bar{p}_i^{syn} more than the uncertainty $\sigma(p_i^{\text{syn}})$. This study is of particular importance, since it allows us to make sure that the parameters p_i we estimate from the experimental spectrum are statistically unbiased. We show an example in fig. 6.6.2, with the fit being performed on the longitudinal mode of the NETN experiment. In this measurement, we can see that the initial value of p_i and the average value of the synthetic distribution of p_i^{syn} are within the statistical uncertainty, thus demonstrating how the fit is indeed unbiased.

Once the fit of one spectrum \mathcal{S}_δ gives its values $p_i \pm \sigma(p_i)$, another spectrum is fitted and the parameters with the respective uncertainties are calculated, and so on and so forth. This way, we get as many estimations of the parameters $\{p_i\}$ as the available spectra, let us say M . As always, in the experiments with the cantilever, M correspond to all the PSDs (which passed the sorting) in the same power step. In order to extract *one* single value \bar{p}_i we calculate the average:

$$\bar{p}_i = \frac{1}{M} \sum_{j=1}^M (p_i)_j \quad (6.65)$$

Regarding the uncertainty $\sigma(\bar{p}_i)$ to associate to this value, since the PDF of $\{p_i\}$ may not be Gaussian, an error propagation of the single $\sigma(p_i)$ is not strictly possible. Therefore, the meaningful uncertainty of \bar{p}_i is the dispersion of the $\{p_i\}$:

$$\sigma(\bar{p}_i) = \sum_{j=1}^M \sqrt{\frac{1}{M} ((p_i)_j - \bar{p}_i)^2} \quad (6.66)$$

6.6.2 Discussion

In the last two sections we discussed the statistical properties of the quantities derived from the experimental signals. In particular, we retrieve the PDF of the area under the resonance curve A , which leads to our calculation of the fluctuation temperature T^{fluc} . We show how A is Γ -distributed, and compare this prediction with the experiment, showing a remarkable agreement. The same study is performed for the background noise \mathcal{N} , with similar results.

Based on the PDF of A and \mathcal{N} , we then define a second sorting of the experimental data. Since the distribution is usually the result of a large number of samples, we can safely approximate the PDF with a Gaussian, and thus decide that areas and noises lying outside 4σ from the average are discarded. As shown, it is possible to retrieve a higher discarded rate than the forecasted one, showing that some of measurements do not belong to the same distribution as the others and are rightfully rejected.

In the second part we discuss the fitting of the data. We retrieve the fit parameters p_i from the unbiased estimator described in [83], and calculate the GOF χ^2 thanks to our knowledge

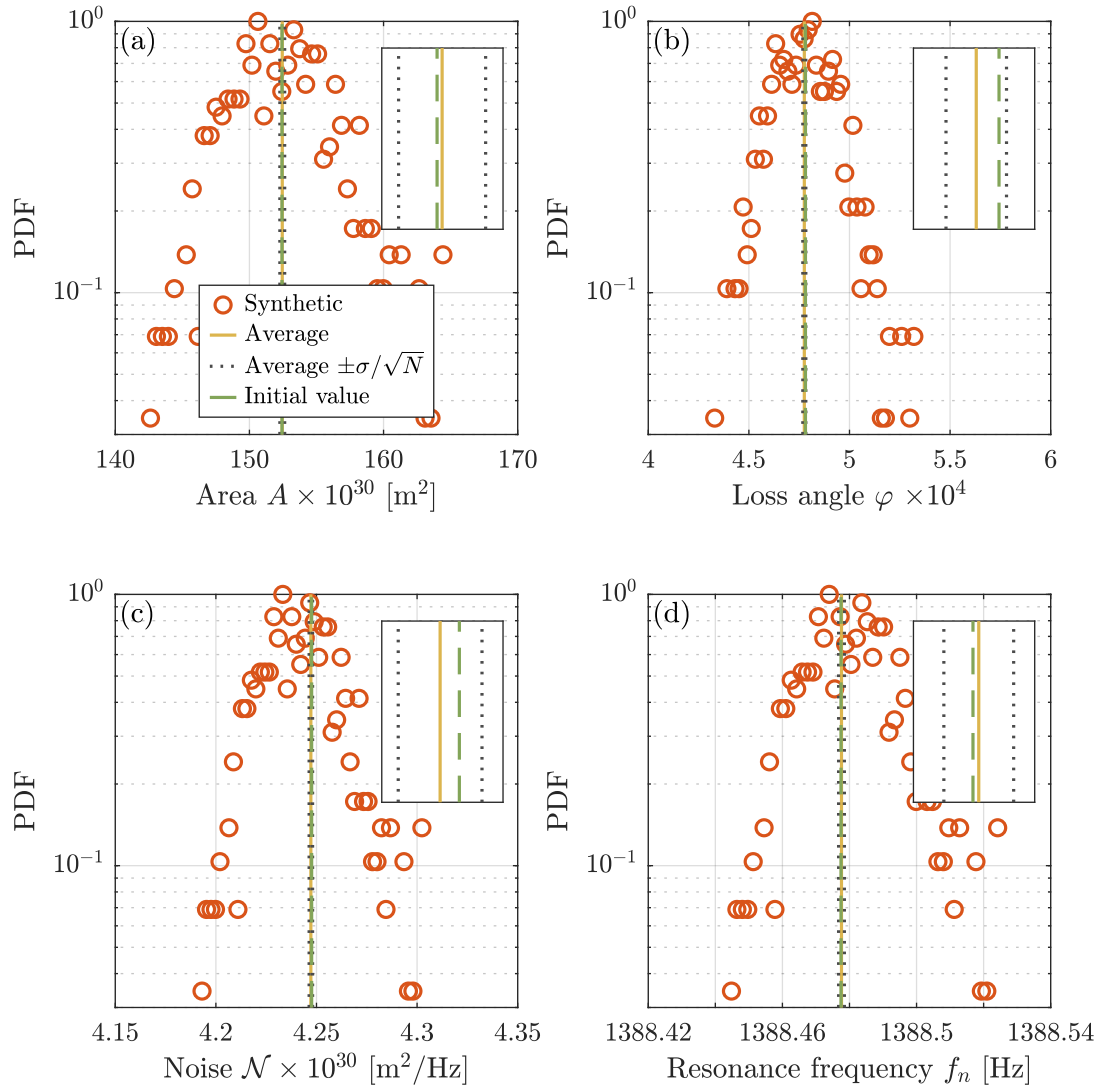


FIGURE 6.6.2: For each experimental spectrum \mathcal{S}_δ we extract the fit parameters, from which we generate 500 synthetic noisy spectra. These are then fitted and the synthetic parameters (orange circles) are retrieved. From these, the average (yellow line) and the the square root of the variance (grey dotted lines) are obtained. We can see that the original value (green dashed line) is within the uncertainties for all parameters, showing that the fit is not biased. The width of the distribution of the synthetic fit parameters is used to estimate the uncertainty of the fit parameters of the experimental spectrum.

of the PDF of the spectra. This result is of particular importance for estimating the loss angle of the resonance φ , used in the estimation of the dissipation.

Whilst χ^2 is an objective way to estimate how well our parameters fit the experimental data, we show that it is possible to directly associate an uncertainty to each p_i . Indeed, we demonstrate a method based on the PDF of the spectra that allows us to sample the parameter distribution, with the double result of yielding the interval of confidence of p_i and test whether our fit results are statistically unbiased.

These two results allow us to sample the distribution of the area and the loss angle - thus the T^{fluc} and the dissipation w^{diss} -, two central quantities of this thesis. Knowing the statistical distribution of these two quantities, we can not only distinguish the corrupted measurements from the statistically acceptable ones, but also associate the correct uncertainty to T^{fluc} and φ . Regarding the fluctuation temperatures, due to the large number of averaged spectra, the PDF resembles a Gaussian, so we can confidently assume the standard deviation to be correct uncertainty. For the loss angle, though, we cannot calculate the PDF so a theoretical value for the uncertainty is not available. Nevertheless, thanks to a simulation we can sample it and thus retrieve the desired quantity. Throughout this thesis, the error bars for φ are calculated following the approach described in this section.

6.7 Conclusions

In this chapter we tackle the question related to the statistical properties of thermal noise signals, thus the relative spectra and related quantities. The importance of the present description is paramount for two reasons: it allows us to assess that the measured signals are thermal-noise driven, and it gives a method to eliminate the ones that are not expression of this phenomenon. These are two sides of the same coin, since testing the PDF of the noise naturally leads to the exclusion of the points not following the predicted behavior.

The first test we propose is a proof of concept: thanks to the lock-in technique, we directly sample the statistical distribution of the Fourier coefficients of the resonances. This leads to a first verification of the expected properties of the thermal noise-driven displacement of the cantilever, which proves that it is the result of a stochastic force acting on the system. Thanks to lock-in technique, we shed light to the self-oscillating state of the first resonance, showing how it cannot be linked to thermal noise. More importantly, the other resonances are not affected by this phenomenon, as they show the expected Gaussian behavior. It also is very interesting how we cannot distinguish the NESS from an equilibrium state solely from a statistical point of view. Confirming the results of [30], we believe this to be of fundamental importance: it lets us suppose that the equilibrium properties of noise can be extended for the non-equilibrium systems we analyse. We thus insist on the leitmotiv of this thesis: testing whether we can extend equilibrium tools for out-of-equilibrium ones.

Since in the experiment we often retrieve directly the spectrum, it is then compelling to discuss its statistical properties, in particular its PDF. We show that spectra are Γ -distributed, and so is their average. We then propose a practical sorting algorithm, based on the PDF set by the average spectrum, distinguishing between possible issues in calculating the latter. Thanks to this strategy, we set a statistically independent threshold that allows us to assure that the selected signals satisfy the properties we associate to thermal noise, and they do not contain spurious exogenous signals.

Once this selection is done, we briefly show how to retrieve the PDF of the derived quantities, the area and the dissipation. The first follows a Γ distribution, which in the experiment closely approaches a Normal one. We can then set a second sorting algorithm, eliminating

the outliers of the distribution. This allows us to further reduce the possibility of the final results containing contrived values. Regarding the dissipation, thanks to an *a priori* unbiased fit, we retrieve the loss angle from the experimental spectra. We then take advantage of knowing the PDF of the spectra in order to estimate the uncertainty on the fit parameters thanks to a simulation.

The tools we develop in this chapter are used throughout the whole thesis in all the presented experiments. The two-step selection of the spectra and the area grants us the confidence to claim that the results of the T^{fluc} shown in the previous chapters are valid and unbiased. Furthermore, the fit procedure we apply allows us to be confident of the estimations of the dissipation.

We believe these results could be useful in many applications. The sorting of spectra can be applied in possibly every experiment aimed at measuring or characterising thermal noise, spanning from micro-mechanical systems [44], RC circuits [10] or coatings for the GW community [70]. We believe it could be an important part in the analysis of the thermal noise in the NETN experiment, also in light of the still-standing issues in construing the results. In a similar way, these experiments could take advantage of the fit procedure too. Firstly, we believe that the excellent analysis of [83] in describing an unbiased fit procedure for spectra is not yet as generally known as it should perhaps be. Applying this technique to our experimental data and combining it with our innovative way to compute the uncertainties of the fit parameters shows that the procedure is indeed unbiased. Therefore, experiments where the estimation of the dissipation is important ([97, 38] for example) could make good use of this technique, if a similar one is not already implemented.

Chapter 7

General conclusions

The quest for a predictive non-equilibrium statistical physics has existed since the beginning of the thermodynamics. Indeed, equilibrium systems represent but an exception in physics, with most of our surroundings (and ourselves) being in a constant dance with the law of thermodynamics around equilibrium. In many cases, thermal equilibrium can be considered a valid approximation, and centuries of studies have given us impressive statistical tools in order to describe the reality in this situation. Nevertheless, sometimes non equilibrium is so preponderant that we need to find new theoretical frameworks in order to predict the behavior of the systems in such a state.

Non-equilibrium is a topic as old as equilibrium, with K. Thompson first addressing the subject in 1854. After him, many authors contributed to the subject, with non-equilibrium statistical physics being nowadays an important branch of research. Applications span physics, biology, finance, and much more, as we believe it is a rich field with much left to discover. In particular, thermal fluctuations have become more and more important with technology pushing its limits to the micro and nanoscale, where the interactions of the systems under study with the surrounding environment become salient. A salient example is the GWs detectors, one of the most precise instruments built by human kind, whose developments require careful thermal noise considerations. Often, these systems are in a NESS, and thus a non-equilibrium characterisation is paramount.

In this thesis, we try to add our piece of the puzzle in this vivid world that is non-equilibrium. We embrace a project which has already yielded impressive results [42] and push it forward, both from an experimental and a theoretical point of view.

The main protagonist of this thesis is the Fluctuation Dissipation Theorem. Its importance in physics is deservedly celebrated, as under this formalism the thermal fluctuation of an observable in thermal equilibrium can be easily quantified through the temperature of the thermal bath and the dissipation processes involved. Whereas the FDT validity is normally limited to thermal equilibrium, we combine the approaches of [42, 64] in order to show an elegant and simple way to extend it for systems presenting a temperature difference along their lengths, i.e. in a NESS. The outcome is that the fluctuations are prescribed by the temperature profile weighted by the local mechanical energy dissipation function. This leads to the definition of a non-equilibrium temperature T^{fluc} , which reflects where the dissipation is more preponderant. We reiterate once again its shape:

$$T^{\text{fluc}} = \int dx T(x) w^{\text{diss}}(x)$$

We then proceed with the experiments, imposing a strong temperature difference along some silicon micro-cantilevers and an aluminum macroscopic oscillator, and measure their

thermal fluctuations. We thus construe the results with the extended FDT. We summarise here the main results of this work:

- We carefully show how we can derive the equilibrium FDT for both the flexural and torsional modes of a cantilever, and then extend this result for NESSes. In doing so, we calculate the dissipated energies of the motions, including high-modes corrections to the Saint-Venant model through Barr's description. In order to do so, we derive expressions for the internal dissipation of a crystal, which is later compared to other sources of damping such as clamping losses.
- We test the validity of the extended FDT in the case of a thin silicon micro-cantilever (C100) subjected to a strong heat flux. The measured fluctuations are insensitive to the temperature difference, which is a strong evidence of non-equilibrium behavior. Through our theoretical interpretation, we construe these findings with a clamped-located dissipation, where the temperature of the cantilever is kept constant at room temperature. This is confirmed through the measured loss angles, which are also roughly independent from the temperature. Since we verify these properties for all the measurable resonances, we conclude that this system shows a lack of fluctuations as a general feature.
- The same study is performed on a coated cantilever (C30C), which conversely shows an increase in the fluctuations at increasing temperature, on the order of the average temperature. The measured loss angles similarly depend on the temperature, which can be fitted with a second order polynomial. Thanks to this, we propose a theoretical prediction for the fluctuations, which satisfyingly represents our measurements. Thus, with the measurement of the dissipation, we are able to forecast the evolution of the noise. Our conclusion is then that the dissipation is spread along the whole cantilever, causing an increase in the fluctuations, and the extended FDT perfectly captures the experimental results.
- A third sample (C30) is studied to verify whether the distributed dissipation is solely due to the coating, or if the substrate plays a role. We show that the latter is the case, with the non-equilibrium fluctuations being sensitive to the temperature profile. Also, in this case the measured dissipation helps us explain the results, showing how we can predict the thermal noise through the extended FDT. In addition to this, we demonstrate how purely silicon cantilevers with different geometries and manufacturers can be dominated by different kinds of dissipation (C100 at the clamping and C30 distributed).
- We carefully demonstrate how to convert signals retrieved with the optical lever technique to calibrated displacements. We take into consideration many factors: modifications of the beam's waist on the detector through a run-time calibration; the different methods needed to compute the sensitivity depending on the spot's size on the cantilever, in particular showing the limit for large ones; the influence of modifications of the spot's size and position on the cantilever during a measurement, which leads to a systematic uncertainty on the fluctuations. In order to compute the spot's size and position on the cantilever, we show a simple method based on the equilibrium EP, which is more precise than camera observations. Through this, the sensitivity can then be easily computed.
- We test the extended FDT to its physical limits, probing it at cryogenic temperatures. We impose the highest temperature difference the cantilever (C90) can sustain, and we measure its thermal fluctuations. Through a robust experimental protocol, we show how the noise is much lower than what the average temperature of the system

would indicate. Since all the resonances show similar behavior, we can conclude that similarly to C100, this sample displays a lack of fluctuations as a common trait. Despite the extreme experimental conditions do not allow a prediction of the fluctuations as in the previous cases, the measured dissipation agrees with the thermal noise observations. The takeaway is then that the non-equilibrium FDT is valid up to its physical limits.

- The next sample is an aluminum oscillator of the NETN experiment. In this case, the experimental conditions and the physical system are radically different with respect to the previous ones, as we aim at testing the extended FDT in the case of a macroscopic object. Since the previous measurements of this group cannot be explained in our framework, we aim at testing whether our approach is valid only for microscopic systems. During the time spent at the LNL, a new version of the detection interferometer is installed, sensibly increasing the SNR around the resonances. Next, non-equilibrium thermal noise measurements show that the fluctuations are compatible with the average temperature of the system, perfectly in line with our theoretical prediction. Also in this case, the dissipation cannot allow us to quantitatively predict the fluctuations; nonetheless it indicates a distributed dissipation which fits with the observed noise. We then conclude how the extended FDT can be considered valid also in the case of a macroscopic system.
- We study the statistical properties of thermal noise, from the statistical distribution of the Fourier coefficients of a stochastic force to the PDF of the spectrum of the displacement. We show how one resonance is polluted by self-oscillations, which bias the distribution. However, this does not perturb the higher modes, which satisfy the predicted properties. We demonstrate how there is no difference between an equilibrium and an out-of-equilibrium noise from the statistical point of view.
- Thanks to the retrieved statistical properties, we propose an innovative sorting algorithm which excludes signals showing higher values than a certain threshold. We show how this method can be applied in both low and high-polluted ensembles and can be adapted to the fluctuations of the laser power. This is then experimentally tested. Furthermore, thanks to the PDF of the area being close to a Gaussian, we can set a second threshold to exclude extreme outliers.
- We discuss an unbiased fitting method in order to estimate the loss angle, which then is experimentally tested yielding in general a very good GOF $\chi^2 < 2$. We then show a method to retrieve the uncertainty of the fit parameters and at the same time to test the absence of biases in the procedure.

In this thesis, we discuss the results of various experiments, each with its particularities and outcomes. In each chapter, we then suggest some possible applications, which span from the fabrication of MEMS to GWs detection. One omnipresent application is nevertheless embedded in the common thread linking the experiments of this thesis: the quest for a non-equilibrium characterisation of statistical physics. Micro-cantilevers truly represent a perfect testing bench for non-equilibrium properties, the study of which we hope this thesis will help encourage. Perspectives range from a deeper study of the statistical properties of noise, with possible scaling properties [37], measurements of the entropy and the work of the cantilevers [16], and second-order effects in the temperature profile [73], to give a few examples.

So far, we have proven that our theoretical models explain all the systems we have studied, hinting at the possible generality of the extended FDT. Additional experiments are nevertheless possible to further strengthen its validity: we can imagine a system with dissipation localised at a specific point, say the last antinode of a given mode of the cantilever. In this case, it would be interesting to check whether the fluctuations evolve following the high temperature at this point, as the extended FDT predicts. Such a system can be fabricated for example by adding a coating at this point. This kind of experiment would pave the way for thermal engineering or for thermal noise operated systems. Indeed, the evolution of the thermal noise would then be mode-dependent, and it would be the signature of the dissipation processes at stake: the presence of target molecule increasing damping, radiation increasing temperature or creating defects, etc.

Another application of this extended FDT is to use it as a tool to characterise dissipation: since T^{fluc} is the convolution of the temperature with the dissipation field, scanning the former could lead to a better knowledge of the latter. This has already been demonstrated when we conclude from the out-of-equilibrium measurement of the fluctuations that the dissipation is localised at the clamp. This method could be extended to other MEMS and NEMS, such as nanowires, to better understand their mechanical dissipation and spatial distribution.

Bibliography

- [1] AAPTOELECTRONIC. <https://.aaoptoelectronic.com>.
- [2] J. AASI, B. P. ABBOTT, AND R. A. ET AL., *Advanced LIGO*, Classical and Quantum Gravity, 32 (2015), p. 074001.
- [3] F. ACERNESE, M. AGATHOS, AND K. A. ET AL., *Advanced virgo: a second-generation interferometric gravitational wave detector*, Classical and Quantum Gravity, 32 (2014), p. 024001.
- [4] R. X. ADHIKARI, O. AGUIAR, AND K. A. ET AL., *A cryogenic silicon interferometer for gravitational-wave detection*, 2020.
- [5] F. AGUILAR SANDOVAL, M. GEITNER, E. BERTIN, AND L. BELLON, *Resonance frequency shift of strongly heated micro-cantilevers*, Journal of Applied Physics, 117 (2015).
- [6] T. E. A. AKUTSU, *First cryogenic test operation of underground km-scale gravitational-wave observatory KAGRA*, Classical and Quantum Gravity, 36 (2019), p. 165008.
- [7] A. AMATO, *Low Thermal Noise Coating for New Generation Gravitational-Wave Detectors*, PhD thesis, 2019. Thèse de doctorat dirigée par Cagnoli, GianpietroCanepa, Maurizio et Granata, Massimo Physique des matériaux Lyon 2019.
- [8] A. AMATO, S. TERRENI, M. GRANATA, C. MICHEL, L. PINARD, G. GEMME, M. CANEPA, AND G. CAGNOLI, *Effect of heating treatment and mixture on optical properties of coating materials used in gravitational-wave detectors*, Journal of Vacuum Science & Technology B, 37 (2019), p. 062913.
- [9] S. M. ASTON, M. A. BARTON, A. S. BELL, N. BEVERIDGE, B. BLAND, A. J. BRUMMITT, G. CAGNOLI, C. A. CANTLEY, L. CARBONE, A. V. CUMMING, L. CUNNINGHAM, R. M. CUTLER, R. J. S. GREENHALGH, G. D. HAMMOND, K. HAUGHIAN, T. M. HAYLER, A. HEPTONSTALL, J. HEEFNER, D. HOYLAND, J. HOUGH, R. JONES, J. S. KISSEL, R. KUMAR, N. A. LOCKERBIE, D. LODHIA, I. W. MARTIN, P. G. MURRAY, J. O'DELL, M. V. PLISSI, S. REID, J. ROMIE, N. A. ROBERTSON, S. ROWAN, B. SHAPIRO, C. C. SPEAKE, K. A. STRAIN, K. V. TOKMAKOV, C. TORRIE, A. A. VAN VEGGEL, A. VECCHIO, AND I. WILMUT, *Update on quadruple suspension design for advanced LIGO*, Classical and Quantum Gravity, 29 (2012), p. 235004.
- [10] M. BAIESI, S. CILIBERTO, G. FALASCO, AND C. YOLCU, *Thermal response of nonequilibrium rc circuits*, Phys. Rev. E, 94 (2016), p. 022144.
- [11] M. BAIESI, C. MAES, AND B. WYNANTS, *Fluctuations and response of nonequilibrium states*, Phys. Rev. Lett., 103 (2009), p. 010602.
- [12] B. BALACHANDRAN AND E. B. MAGRAB, *Vibrations*, Cambridge University Press, 3 ed., 2018.
- [13] A. D. S. BARR, *Torsional waves in uniform rods of non-circular section*, Journal of Mechanical Engineering Science, 4 (1962), pp. 127–135.

- [14] M. BAWAJ, M. BARSUGLIA, M. BAZZAN, E. CALLONI, G. CIANI, L. CONTI, B. D'ANGELO, M. D. LAURENTIS, R. D. ROSA, S. D. PACE, V. FAFONE, B. GARAVENTA, G. GEMME, A. GENNAI, L. GIACOPPO, J. HARMS, I. KHAN, E. MAJORANA, L. NATICCHIONI, C. NGUYEN, D. PASSUELLO, G. PRODI, F. RICCI, A. ROCCHI, V. SEQUINO, F. SORRENTINO, M. VARDARO, AND J. ZENDRI, *Study and experiment on the alternative technique of frequency-dependent squeezing generation with EPR entanglement for virgo*, Journal of Physics: Conference Series, 1468 (2020), p. 012215.
- [15] L. BELLON, *Exploring nano-mechanics through thermal fluctuations*, habilitation à diriger des recherches, Ecole normale supérieure de lyon - ENS LYON, Nov. 2010. 176 pages format A5.
- [16] L. BELLON, J. R. GOMEZ-SOLANO, A. PETROSYAN, AND S. CILIBERTO, *Measuring Out-of-Equilibrium Fluctuations*, John Wiley & Sons, Ltd, 2013, ch. 4, pp. 115–153.
- [17] J. BON, L. NEUHAUS, S. DELÉGLISE, T. BRIANT, P. ABBÉ, P.-F. COHADON, AND S. GALLIOU, *Cryogenic optomechanic cavity in low mechanical loss material*, Journal of Applied Physics, 124 (2018), p. 073104.
- [18] V. BRAGINSKY, M. GORODETSKY, AND S. VYATCHANIN, *Thermodynamical fluctuations and photo-thermal shot noise in gravitational wave antennae*, Physics Letters A, 264 (1999), pp. 1 – 10.
- [19] D. R. BRILLINGER, *Time Series: Data Analysis and Theory*, Classics in Applied Mathematics (Book 36), SIAM: Society for Industrial and Applied Mathematics, 1 ed., 2001.
- [20] R. BROWN, *A brief account of microscopical observations made on the particles contained in the pollen of plants*, London and Edinburgh philosophical magazine and journal of science, 4 (1828), pp. 161–173.
- [21] BUDGETSENSORS. <https://www.budgetsensors.com/multipurpose-afm-probe-no-tip-all-in-one-tipless>.
- [22] L. BUISSON, M. CICCOTTI, L. BELLON, AND S. CILIBERTO, *Electrical noise properties in aging materials*, in Fluctuations and Noise in Materials, D. Popovic, M. B. Weissman, and Z. A. Racz, eds., vol. 5469, International Society for Optics and Photonics, SPIE, 2004, pp. 150 – 164.
- [23] H. J. BUTT AND M. JASCHKE, *Calculation of thermal noise in atomic force microscopy*, Nanotechnology, 6 (1995), pp. 1–7.
- [24] G. CAGNOLI, L. GAMMAITONI, J. HOUGH, J. KOVALIK, S. MCINTOSH, M. PUNTURO, AND S. ROWAN, *Very high Q measurements on a fused silica monolithic pendulum for use in enhanced gravity wave detectors*, Phys. Rev. Lett., 85 (2000), pp. 2442–2445.
- [25] H. B. CALLEN AND T. A. WELTON, *Irreversibility and generalized noise*, Phys. Rev., 83 (1951), pp. 34–40.
- [26] M. CERDONIO, L. CONTI, A. HEIDMANN, AND M. PINARD, *Thermoelastic effects at low temperatures and quantum limits in displacement measurements*, Phys. Rev. D, 63 (2001), p. 082003.
- [27] A. N. CLELAND AND M. L. ROUKES, *Noise processes in nanomechanical resonators*, Journal of Applied Physics, 92 (2002), pp. 2758–2769.
- [28] S. COMSOL AB, STOCKHOLM, *Comsol multiphysics®*. <https://www.comsol.com>. v. 5.4.

- [29] L. CONTI, P. D. GREGORIO, G. KARAPETYAN, C. LAZZARO, M. PEGORARO, M. BONALDI, AND L. RONDONI, *Effects of breaking vibrational energy equipartition on measurements of temperature in macroscopic oscillators subject to heat flux*, Journal of Statistical Mechanics: Theory and Experiment 2013, 12, P12003 (2013).
- [30] L. CONTI, C. LAZZARO, G. KARAPETYAN, M. BONALDI, M. PEGORARO, R.-K. THAKUR, P. DE GREGORIO, AND L. RONDONI, *Thermal noise of mechanical oscillators in steady states with a heat flux*, Phys. Rev. E, 90 (2014), p. 032119.
- [31] L. F. CUGLIANDOLO, *The effective temperature*, Journal of Physics A: Mathematical and Theoretical, 44 (2011), p. 483001.
- [32] A. V. CUMMING, A. S. BELL, L. BARSOTTI, M. A. BARTON, G. CAGNOLI, D. COOK, L. CUNNINGHAM, M. EVANS, G. D. HAMMOND, G. M. HARRY, A. HEPTONSTALL, J. HOUGH, R. JONES, R. KUMAR, R. MITTLEMAN, N. A. ROBERTSON, S. ROWAN, B. SHAPIRO, K. A. STRAIN, K. TOKMAKOV, C. TORRIE, AND A. A. VAN VEGGEL, *Design and development of the advanced LIGO monolithic fused silica suspension*, Classical and Quantum Gravity, 29 (2012), p. 035003.
- [33] B. DE SAINT-VENANT, *Mémoire sur les vibrations tournantes des verges élastiques*, Comptes Rendus, 28 (1849), pp. 97–109.
- [34] A. EINSTEIN, *Über die von der molekularkinetischen theorie der wärme geforderte bewegung von in ruhenden flüssigkeiten suspendierten teilchen*, Annalen der Physik, 322 (1905), pp. 549–560.
- [35] V. S. EKEL'CHIK, *Torsional vibrations and dispersion of torsional waves in orthotropic composite rods*, Mechanics of Composite Materials, 44 (2008), pp. 109–120.
- [36] G. FALASCO, M. V. GNANN, D. RINGS, AND K. KROY, *Effective temperatures of hot brownian motion*, Phys. Rev. E, 90 (2014), p. 032131.
- [37] E. FALCON, S. G. ROUX, AND B. AUDIT, *Revealing intermittency in experimental data with steep power spectra*, EPL (Europhysics Letters), 90 (2010), p. 50007.
- [38] X. L. FENG, R. HE, P. YANG, AND M. L. ROUKES, *Very high frequency silicon nanowire electromechanical resonators*, Nano Letters, 7 (2007), pp. 1953–1959.
- [39] E. FERMI, J. PASTA, AND S. ULAM, Los Alamos Scientific Laboratory report, LA-1940 (1955).
- [40] A. FONTANA, R. PEDURAND, AND L. BELLON, *Extended equipartition in a mechanical system subject to a heat flow: the case of localised dissipation*, 2020.
- [41] M. GEITNER, *Température effective d'un système hors équilibre : fluctuations thermiques d'un microlevier soumis à un flux de chaleur*, PhD thesis, 2015. Thèse de doctorat dirigée par Bellon, Ludovic Physique Lyon, École normale supérieure 2015.
- [42] M. GEITNER, F. AGUILAR SANDOVAL, E. BERTIN, AND L. BELLON, *Low thermal fluctuations in a system heated out of equilibrium*, Physical Review E, 95 (2016).
- [43] A. GERRARD AND J. BURCH, *Introduction to Matrix Methods in Optics*, Dover Books on Physics Series, Dover Publications, Incorporated, 2012.
- [44] F. GITTES AND C. F. SCHMIDT, *Thermal noise limitations on micromechanical experiments*, European Biophysics Journal, 27 (1998), pp. 75–81.
- [45] C. J. GLASSBRENNER AND G. A. SLACK, *Thermal conductivity of silicon and germanium from 3° k to the melting point*, Phys. Rev., 134 (1964), pp. A1058–A1069.

- [46] M. GRANATA, A. AMATO, L. BALZARINI, M. CANEPA, J. DEGALLAIX, D. FOREST, V. DOLIQUE, L. MERENI, C. MICHEL, L. PINARD, B. SASSOLAS, J. TEILLON, AND G. CAGNOLI, *Amorphous optical coatings of present gravitational-wave interferometers*, Classical and Quantum Gravity, (2020).
- [47] R. M. GRAY, *Probability, Random Processes, and Ergodic Properties*, Springer Verlag, 2 ed., 2010.
- [48] S. K. GUPTA AND M. GUO, *Equilibrium and out-of-equilibrium mechanics of living mammalian cytoplasm*, Journal of the Mechanics and Physics of Solids, 107 (2017), pp. 284 – 293.
- [49] M. G. L. GUSTAFSSON AND J. CLARKE, *Scanning force microscope springs optimized for optical beam deflection and with tips made by controlled fracture*, Journal of Applied Physics, 76 (1994), pp. 172–181.
- [50] U. GYSIN, S. RAST, P. RUFF, E. MEYER, D. W. LEE, P. VETTIGER, AND C. GERBER, *Temperature dependence of the force sensitivity of silicon cantilevers*, Phys. Rev. B, 69 (2004), p. 045403.
- [51] Z. HAO, A. ERBIL, AND F. AYAZI, *An analytical model for support loss in micromachined beam resonators with in-plane flexural vibrations*, Sensors and Actuators A: Physical, 109 (2003), pp. 156 – 164.
- [52] T. HARADA AND S.-I. SASA, *Energy dissipation and violation of the fluctuation-response relation in nonequilibrium langevin systems*, Phys. Rev. E, 73 (2006), p. 026131.
- [53] G. M. HARRY, H. ARMANDULA, E. BLACK, D. R. M. CROOKS, G. CAGNOLI, J. HOUGH, P. MURRAY, S. REID, S. ROWAN, P. SNEDDON, M. M. FEJER, R. ROUTE, AND S. D. PENN, *Thermal noise from optical coatings in gravitational wave detectors*, Applied Optics, 45, 7 (2006).
- [54] P. L. M. HEYDEMANN, *Determination and correction of quadrature fringe measurement errors in interferometers*, Appl. Opt., 20 (1981), pp. 3382–3384.
- [55] J. M. HOROWITZ AND T. R. GINGRICH, *Thermodynamic uncertainty relations constrain non-equilibrium fluctuations*, Nature Physics, 16 (2020), pp. 15–20.
- [56] O. C. IBE, *Markov Processes for Stochastic Modeling*, Elsevier, 2013.
- [57] S. C. JAIN, S. K. AGARWAL, W. N. BORLE, AND S. TATA, *Total emissivity of silicon at high temperatures*, Journal of Physics D: Applied Physics, 4 (1971), pp. 1207–1209.
- [58] H. J. JOHNSON AND M. PAVELEC, *Thermal noise in cells. a cause of spontaneous loss of cell function*, Am J Pathol., 69 (1972), pp. 119–130.
- [59] J. B. JOHNSON, *Thermal agitation of electricity in conductors*, Phys. Rev., 32 (1928), pp. 97–109.
- [60] R. V. JONES, *Some developments and applications of the optical lever*, Journal of Scientific Instruments, 38 (1961), pp. 37–45.
- [61] S. JOUBAUD, N. B. GARNIER, AND S. CILIBERTO, *Fluctuation theorems for harmonic oscillators*, Journal of Statistical Mechanics: Theory and Experiment, 2007 (2007), pp. P09018–P09018.

- [62] G. KARAPETYAN, D. AGGUIARO, M. BONALDI, L. CASTELLANI, R. HAJJ, C. LAZZARO, D. MAZZARO, M. PEGORARO, C. POLI, R. THAKUR, AND L. CONTI, *Non-equilibrium "thermal noise" of low loss oscillators*, Journal of Physics: Conference Series, 363 (2012), p. 012011.
- [63] A. KHALAIDOVSKI, G. HOFMANN, D. CHEN, J. KOMMA, C. SCHWARZ, C. TOKOKU, N. KIMURA, T. SUZUKI, A. O. SCHEIE, E. MAJORANA, R. NAWRODT, AND K. YAMAMOTO, *Evaluation of heat extraction through sapphire fibers for the GW observatory KAGRA*, Classical and Quantum Gravity, 31 (2014), p. 105004.
- [64] K. KOMORI, Y. ENOMOTO, H. TAKEDA, Y. MICHIMURA, K. SOMIYA, M. ANDO, AND S. W. BALLMER, *Direct approach for the fluctuation-dissipation theorem under nonequilibrium steady-state conditions*, Phys. Rev. D, 97 (2018), p. 102001.
- [65] T. KOUH, U. KEMIKTARAK, O. BASARIR, C. LISSANDRELLO, AND K. L. EKINCI, *Measuring gaussian noise using a lock-in amplifier*, American Journal of Physics, 82 (2014), pp. 778–784.
- [66] R. KUBO, M. TODA, AND N. HASHITSUME, *Statistical Physics II: Nonequilibrium Statistical Mechanics*, Springer Series in Solid-State Sciences, Springer-Verlag Berlin Heidelberg, 1 ed., 1985.
- [67] L. KUSMIERZ, A. CHECHKIN, E. GUDOWSKA-NOWAK, AND M. BIER, *Breaking microscopic reversibility with lévy flights*, EPL (Europhysics Letters), 114 (2016), p. 60009.
- [68] L. LANDAU AND E. LIFSHITZ, *Theory of Elasticity*, no. v. 7 in Course of theoretical physics, Elsevier Science, 1970.
- [69] Y. LEVIN, *Internal thermal noise in the ligo test masses: A direct approach*, Phys. Rev. D, 57 (1998), pp. 659–663.
- [70] T. LI, F. A. AGUILAR SANDOVAL, M. GEITNER, L. BELLON, G. CAGNOLI, J. DEGALLAIX, V. DOLIQUE, R. FLAMINIO, D. FOREST, M. GRANATA, C. MICHEL, N. MORGADO, AND L. PINARD, *Measurements of mechanical thermal noise and energy dissipation in optical dielectric coatings*, Phys. Rev. D, 89 (2014), p. 092004.
- [71] T. J. LI AND L. BELLON, *Dissipation of micro-cantilevers as a function of air pressure and metallic coating*, EPL (Europhysics Letters), 98 (2012), p. 14004.
- [72] R. LIFSHITZ AND M. ROUKES, *Thermoelastic damping in micro- and nanomechanical systems*, phys. rev. b 61(8), 5600-5609, Physical Review B, 61 (2000), pp. 5600–5609.
- [73] O. S. LUMBROSO, L. SIMINE, A. NITZAN, D. SEGAL, AND O. TAL, *Electronic noise due to temperature differences in atomic-scale junctions*, Nature, 562 (2018), pp. 240–244.
- [74] C. METZGER, M. LUDWIG, C. NEUENHAHN, A. ORTLIEB, I. FAVERO, K. KARRAI, AND F. MARQUARDT, *Self-induced oscillations in an optomechanical system driven by bolometric backaction*, Physical review letters, 101 (2008), p. 133903.
- [75] G. MEYER AND N. M. AMER, *Novel optical approach to atomic force microscopy*, Applied Physics Letters, 53 (1988), pp. 1045–1047.
- [76] MICROMOTIVE. <https://www.micromotive.de>.
- [77] MINUTELABS.
- [78] F. MOHD-YASIN, D. J. NAGEL, AND C. E. KORMAN, *Noise in MEMS*, Measurement Science and Technology, 21 (2009), p. 012001.

- [79] B. MONNET, S. CILIBERTO, AND L. BELLON, *Extended nyquist formula for a resistance subject to a heat flow*, (2019).
- [80] NANOWORLD. <https://www.nanoworld.com/array-of-8->.
- [81] A. S. NOWICK AND B. S. BERRY, *Anelastic Relaxation in Crystalline Solids*, Academic Press, 1972.
- [82] H. NYQUIST, *Thermal agitation of electric charge in conductors*, Phys. Rev., 32 (1928), pp. 110–113.
- [83] S. F. NØRRELYKKE AND H. FLYVBJERG, *Power spectrum analysis with least-squares fitting: Amplitude bias and its elimination, with application to optical tweezers and atomic force microscope cantilevers*, Review of Scientific Instruments, 81 (2010), p. 075103.
- [84] P. PAOLINO, *Thermal noise and dissipation of a micro-cantilever*, theses, Ecole normale supérieure de lyon - ENS LYON, Nov. 2008.
- [85] P. PAOLINO, F. A. AGUILAR SANDOVAL, AND L. BELLON, *Quadrature phase interferometer for high resolution force spectroscopy*, Review of Scientific Instruments, 84 (2013), p. 095001.
- [86] P. PAOLINO AND L. BELLON, *Frequency dependence of viscous and viscoelastic dissipation in coated micro-cantilevers from noise measurement*, Nanotechnology, 20 (2009), p. 405705.
- [87] R. PEDURAND, *Instrumentation for Thermal Noise Spectroscopy*, PhD thesis, Universite Claude Bernard Lyon 1.
- [88] P. Z. PEEBLES JR., *Probability, random variables and random signal principles*, McGraw-Hill series in electrical engineering, 2 ed., 1987.
- [89] J. B. PERRIN, *Les atomes*, Nouvelle collection scientifique, 1 ed., 1913.
- [90] A. PIZZELLA, *A homodyne quadrature interferometer for the study of thermal noise in solids in non-equilibrium steady states*, Master's thesis, Unverisity of Padua, 2019.
- [91] B. POTTIER, F. AGUILAR, M. GEITNER, F. MELO, AND L. BELLON, *Resonance frequency shift of silicon cantilevers heated from 300 k up to the melting point*, 2020.
- [92] B. POTTIER AND L. BELLON, *"noiseless" thermal noise measurement of atomic force microscopy cantilevers*, Applied Physics Letters, 110 (2017), p. 094105.
- [93] M. PUNTURO ET AL., *The third generation of gravitational wave observatories and their science reach*, Classical and Quantum Gravity, 27 (2010), p. 084007.
- [94] J. E. SADER, *Frequency response of cantilever beams immersed in viscous fluids with applications to the atomic force microscope*, Journal of Applied Physics, 84 (1998), pp. 64–76.
- [95] T. E. SCHÄFFER, *Calculation of thermal noise in an atomic force microscope with a finite optical spot size*, Nanotechnology, 16 (2005), pp. 664–670.
- [96] K. SOMIYA, *Detector configuration of KAGRA—the japanese cryogenic gravitational-wave detector*, Classical and Quantum Gravity, 29 (2012), p. 124007.
- [97] A. TAVERNARAKIS, A. STAVRINADIS, A. NOWAK, I. TSIOUTSIOS, A. BACHTOLD, AND P. VERLOT, *Optomechanics with a hybrid carbon nanotube resonator*, Nature Communications, 9 (2018), p. 662.

- [98] C. A. VAN EYSDEN AND J. E. SADER, *Frequency response of cantilever beams immersed in viscous fluids with applications to the atomic force microscope: Arbitrary mode order*, Journal of Applied Physics, 101 (2007), p. 044908.
- [99] G. VINCZE, N. SZASZ, AND A. SZASZ, *On the thermal noise limit of cellular membranes*, Bioelectromagnetics, 26 (2005), pp. 28–35.
- [100] J. B. WACHTMAN, W. E. TEFFT, D. G. LAM, AND C. S. APSTEIN, *Exponential temperature dependence of young's modulus for several oxides*, Phys. Rev., 122 (1961), pp. 1754–1759.
- [101] M. C. WANG AND G. E. UHLENBECK, *On the theory of the brownian motion ii*, Rev. Mod. Phys., 17 (1945), pp. 323–342.
- [102] H. WARLIMONT AND M. W., *Springer Handbook of Materials Data*, Springer Handbooks book series, Springer, Cham, 2018.
- [103] D. H. ZANETTE AND M. A. MONTEMURRO, *Thermal measurements of stationary nonequilibrium systems: a test for generalized thermostatics*, Physics Letters A, 316 (2003), pp. 184 – 189.
- [104] C. ZENER, *Internal friction in solids 1, theory of internal friction in reeds*, Phys. Rev., 52 (1937), pp. 230–235.